INTRA-SEASONAL CONVECTION DYNAMICS OVER SOUTHWEST AND NORTHEAST TANZANIA: AN OBSERVATIONAL STUDY

Emmanuel Jonathan Mpeta

Department of Oceanography,

University of Cape Town

A Thesis Submitted in fulfilment of the degree of Master of Science

September 1997

Abstract

Intraseasonal convection oscillation over the northeastern and southwestern Tanzania during MAM and DJF seasons respectively are examined using December, 1979 to May, 1994 pentad (5-day mean) Outgoing Longwave Radiation (OLR) as an indicator of convective cloud distribution. Area-averaged OLR indices are derived for the two areas. Time series of OLR indices for MAM and DJF indicate large quasi-periodic OLR fluctuations in some years and small fluctuations in other years. Periodogram analyses results reveal that dominant periodogram values for the oscillations were different in different years over both areas. Dominant periodogram peaks with periods more than 6 pentads (30 days) occurred 40% of the time on the average. Based on the pentad OLR time series plots deep convection and their precursors are composited. The time evolution of composite OLR maps reveal that patterns of low OLR values (indicating deep convection) shift northeastwards coupled with low OLR values associated with mid-latitude troughs and linked to the ITCZ.

Composite of kinematic and thermodynamic parameters associated with deep convection and precursors are composited. The analyses results show that deep convection is associated with the following characteristics:

-Simultaneous geopotential height falls over the Indian Ocean and geopotential height rises over the Atlantic Ocean and northwest Africa;
-Convergence of westerly (integrated between 1000 hPa and 500 hPa Water Vapour Flux) WVF and northeasterly WVF in the case of southwestern areas and northeasterly WVF and southeasterly WVF in the case of northeastern areas;
-Expansion and strengthening of easterlies at the 200 hPa level. Southeasterly cross-equatorial flow is also observed;
-Increase in equivalent potential temperatures in the mid-troposphere;
-Increase in integrated precipitable water over the target sub-regions.

Time-longitude or Hovmoller diagrams of 4-12 pentad (20-60) days band filtered OLR, zonal winds at 850 hPa and 200 hPa, and integrated pricipitable water anomalies averaged in the 2.5°-5°S and 7.5°-10°S latitude bands for the period November to May (1980-1993) are analysed. Some of the findings are similar to those of previous researchers. Eastward, westward and non-propagating convective features are revealed in the two sub-regions. Organised eastward convective propagating features simultaneously transits the two latitude bands indicating that the intraseasonal convective features are of large scale. The phase speed of the convective features is found to be between 2 and 8 m s^{-1} while the period of oscillation is between 5 to 11 pentads. The eastward propagating negative (positive) OLR anomaly features are coupled with positive (negative) zonal wind at 850 hPa, negative (positive) zonal winds at 200 hPa and positive (negative) integrated water anomalies. Time evolution of kinematic and thermodynamic parameters associated with non-propagating and propagating convective features are analysed. The analyses show that in both cases the convective systems are closely linked to the ITCZ. The geopotential height results at 850 hPa level indicate that before the eastward propagation starts the southern sub-tropical anticyclone ridge axes are meridional and during the propagation phase the mascarene anticyclone ridge axis is zonal. Based on these results it is shown that convective oscillations over the northeastern and southwestern areas of Tanzania have some of the characteristic features of intraseasonal oscillations observed elsewhere.

CONTENTS

CHAPTER 4: DYNAMICS OF THE PENTAD CONVECTIVE SEQUENCE: SOUTHWESTERN AREA

CHAPTER 5: DYNAMICS OF THE PENTAD CONVECTIVE SEQUENCE: NORTHEASTERN AREA

CHAPTER 6: ANALYSIS OF SYSTEM PROPAGATION

List of Tables

PREFACE

The mainstay of the economy of Tanzania is rainfed subsistence agriculture. Hydroelectricity is one of the cheapest and environmentally friendly power sources utilised in Tanzania. However, large spatial and temporal rainfall variability is common. For the proper agricultural planning and utilisation of water resources therefore, an understanding of rainfall variability in all time scales is required. A number of studies have been made to understand rainfall variability at synoptic and inter-annual scales, but little work has been done at the intraseasonal time scale. In order to lay a groundwork for the proper monitoring and prediction of intraseasonal rainfall, an understanding of kinematic and thermodynamic processes associated with the oscillation is required.

Utilisation of weather or climatological information in the planning of farming effort is becoming popular in Tanzania. It is common nowadays to come across a question from a farmer, within a rainy season, as to when there will be a dry or wet spell. This is because some agricultural activities require dry or wet interludes e.g. spraying of pesticides or application of fertilisers requires dry weather interludes. The study of intraseasonal rainfall variability is most appropriate in this regard.

In this thesis the intention is to examine the intraseasonal convection oscillation, inferred from OLR variability, over the northeastern and southwestern areas of Tanzania during MAM and DJF respectively. Kinematic and thermodynamic features associated with the oscillation will be investigated for monitoring and predictive purposes.

The general aim of this thesis is to contribute to an understanding of the intraseasonal oscillation operating over the two areas of Tanzania and forcing mechanisms such as kinematic and thermodynamic processes that are responsible for generating wet/dry spells associated with the oscillations. The main objectives of this study are to:

(i) identify and describe the nature of convective variability over the northern and southwestern areas of Tanzania during MAM and DJF seasons respectively in both the frequency and spatial domains.

(ii) identify kinematic and thermodynamic features associated with active convection both in the horizontal and vertical sections.

(iii) identify propagating convective systems over the two areas together with their associated kinematic and thermodynamic features.

The study is divided into seven chapters. Chapter 1 presents the motivation, some climatological background of Tanzania with an emphasis over the northeastern and southwestern areas and provides a literature review of intraseasonal studies done by researchers elsewhere. The hypothesis to be tested is presented at the end of the chapter. The data and methodology are discussed in chapter 2. Observed and derived parameters are discussed in this chapter. Chapter 3 presents the results of characteristics of convective variability based on time series analyses (spectral and time plot analyses of pentad OLR indices) and spatial analyses of pentad OLR. Results of composite analyses of kinematic and thermodynamic parameters associated with the time evolution of convection results obtained in chapter 3 are discussed in chapters 4 and 5. Chapter 6 presents and discusses Hovmoller results of OLR, zonal wind components at 850 hPa and 200 hPa levels, and precipitable water anomalies over near equatorial bands. Temporal spatial sequence analyses of kinematic and thermodynamic parameters associated with selected propagating and non-propagating convective features are also presented and discussed in the chapter. The thesis summary and conclusion is given in chapter 7.

CHAPTER 1

INTRODUCTION AND LITERATURE REVIEW

1.1 Introduction

1.1.1 Motivation

Drought and floods in Tanzania are common but their frequency and severity varies from one area to another and also from year to year. Long interludes of dry or wet spells, which are always bothersome to farmers, are not uncommon over these areas. Long dry spells can lead to withering or complete failure of some crops while prolonged wet spells can lead to flooding of farms thus destroying crops. In some years rains start very late and withdraw early thus shortening the growing season. Severe drought or flood covering extensive areas of the country means a drop in cash and food crop production which normally leads to a deficit of foreign exchange and famine respectively. In order to acquire the capability to predict extreme climate variability a thorough understanding of the meteorological mechanisms is needed. The predictions will help farmers, hydroelectricity firms, water resources planning and development, and decision makers in the government.

Studies of rainfall variability in Tanzania have mainly focused on the long-time scale, i.e. seasonal and inter-annual variability. Attempts have been made to establish statistical models for forecasting seasonal rains over the country. Seasonal rainfall over northern Tanzania has shown some relationship with global Sea Surface Temperature anomalies (SSTs), the ENSO (El Nino/southern oscillation) (Hastenrath et al., 1993), and QBO (Quasi-biennial Oscillation).

This research work provides an understanding of within season convective variability in Tanzania and assists development of intraseasonal rainfall prediction. Presently weather prediction models provide reasonable forecast guidance up to 5 days. The current study aims at filling the gap in the understanding of weather phenomena at intraseasonal time scale. Intraseasonal, i.e. 10-20 day rainfall forecasts can assist farmers in decisions regarding planting, fertilising, pesticide application, irrigation demand, etc. Forecasts can also assist dam management authorities in regulating levels. Kabanda (1995) has analysed seasonal and intra-seasonal rainfall variability over the bi-modal areas for the ‘short’ (vuli, OND) rains. Further work is necessary on the long rains (masika, MAM) at the intra-seasonal scale.

The study area lies between 2.5°S to 10.0°S and 30°E to 40°E (figure 1.1). Lake Victoria and Tanganyika and the Indian Ocean lie to the North, west and east of the study area respectively. Two areas sub-regions, i.e. northeastern area in the box 35°S-40°E, 2.5°-5°S and southwestern area in the box 30°-35°E, 7.5°-10°S are selected for detailed study. The northeastern part is mountainous containing the ranges of the Usambaras, Pare mountains, Kilimanjaro, and then extending westwards to Mount Meru, the Monduli and Ngorongoro hills. In the eastern area the coastal plains extend some 60 to 70 km inland with an average height of 200 m above MSL. The northeastern sub-region experiences two rainy seasons, the 'long' rains (Masika) from March to May and the 'short' rains (vuli) from October to December. The southwestern sub-region is also mountainous containing the Ufipa plateau to the west and the Livingstone mountain ranges to the South. The southern sub-region has one main season. Rains over the southwestern area usually begin in November and continue until April (EAMD, 1963a; Alusa et al., 1973, Mhita, 1990 among others); with the highest totals in January and February.

Synoptic features and wind flow patterns which produce rain in the tropics are complex, especially in East Africa which includes Tanzania, where orography complicates the situation. Many authors have done studies of rainfall patterns in East Africa including those of Griffiths, (1959); Ogallo, (1989); and Nyenzi, (1988). Their results show that the Inter-Tropical Convergence Zone (ITCZ) is the major source of rainfall in the region as it moves North and South of the Equator lagging behind the solar angle. Some detailed descriptions of weather systems are given by Hills, (1979) and Nyenzi, (1984). The two authors suggest that the space and time characteristics of the rainfall over East Africa including Tanzania includes:

(a) Monsoon wind system; i.e., the Southeast monsoon which blows on the coast from April to October and the Northeast monsoon which blows from November to March.

(b) Sub-tropical anticyclones (Arabian ridge, Mascarene and St. Helena)

(c) The ITCZ which is the Convergence zone of the inter-hemispheric winds

(d) Orography and thermally induced mesoscale systems associated with large water bodies.

1.2 Literature Review

1.2.1 Climatic Seasons of Tanzania

The seasons of Tanzania climate are controlled by the apparent southward and northward movement of the sun. The area of greatest heating and therefore lowest pressure occurs where the sun is nearly overhead and this is known as the Heat Trough or the ITCZ (Inter-Tropical Convergence Zone). There is normally a lag of four to six weeks behind the time of the sun's maximum elevation (EAMD, 1963b). Despite the fact that Tanzania lies within the tropics considerable variations of climate occur throughout the country on account of topography. The seasons will be described below, with some brief explanation of important variations.

The sun is approximately overhead in Tanzania at the end of March, and again at the end of September so the ITCZ can be expected to be most effective about a month later, that is late April/May, and late October/November. These are the two main rainy seasons in northern Tanzania. During these times the pressure is high in the subtropical latitudes of northern and southern Africa, and there is a general movement of airmass from these high pressure belts towards the trough of low pressure in the equatorial region. At times this may result in organised south-easterly and northeasterly winds meeting in a zone of convergence or more often, winds which are not well organised converging locally. Both types of convergence result in vertical upward motion of air, condensation and precipitation. As the sun is moving South in October and North in April southern areas of Tanzania can expect a late onset of rain in October and early cessation of rains. Southern Tanzania at 10° South has only one rainy season. However, there are frequently considerable jumps in the position of the rain belt and large day to day variations in amount and distribution of rain caused by changes in the area of convergence.

In July the sun reaches the tropic of Cancer. During this time high pressure is in southern Africa and low pressure to the North. With this pressure pattern the wind flow over Tanzania is south-easterly. These winds cross the Indian Ocean and are moist in the lower layers. The circulation is mostly divergent in the austral winter. The large area of low pressure over Arabia and India has a controlling influence so that the south-east Trade winds recurve across the equator into the south-west Monsoon over the Indian Ocean, and along the coast of East Africa and Somalia. Although little precipitation falls in Tanzania, a considerable amount of stratiform clouds forms on the eastern slopes.

During January, the sun reaches the tropic of Capricorn so that the pressure is high to the North of the equator and low pressure to the South, giving the rainy season in Zimbabwe. The wind flow over Tanzania, and East Africa in general, at this time of the year is northeasterly, and since the air usually originates over the deserts of Arabia, dry, almost cloudless conditions, with high temperatures normally prevail over all areas, except the southern parts of Tanzania. Very hazy conditions affect parts of northern Tanzania at this time of the year largely caused by fine particles. Haze also affects central and southern Tanzania in the long dry season of June-October.

November to April is also the season of tropical cyclones in the southern Indian Ocean, but as they rarely come within 10° degrees of the equator, and normally recurve southward in the areas of Mauritius and Madagascar, Tanzania is seldom affected. Small cyclones very occasionally cross the extreme southern coast of Tanzania, causing severe damage over a small area.

1.2.2 Intraseasonal Oscillation Research

Intra-Seasonal Oscillations (ISO) in the atmosphere are generally defined as fluctuations with periods longer than synoptic scale but shorter than the seasonal time scale. They are mostly of the order of 10-60 days (Makarau, 1994). Madden and Julian (1971) discovered a 40-50 day oscillation in the equatorial region. In their pioneering work they described the oscillations as a global-scale eastward-propagating zonal circulation cells along the Equator. The Madden and Julian Oscillation or MJO, as sometimes called, was discovered when studying a time series of zonal winds at Canton island in the tropical Pacific and other individual tropical rawinsonde stations. Since then, the low frequency oscillations have been studied by many researchers, including, Wang et al., (1990); Murakami et al., (1985); Lau et al., (1987); Weickmann et al. (1990); Vincent et al., (1991).

Various methods have been used to study intraseasonal oscillations. Common methods are spectral and cross spectral analysis, Empirical orthogonal functions (EOF), composite and hovmoller analysis i.e. longitude-time or latitude-time analysis on daily or 5-day pentad data. Modelling have also been used in studying intraseasonal oscillations.

Madden and Julian, (1971) noticed coherence between surface pressure, zonal winds, and temperature at various levels over a period range from 41 and 51 days. They also noted that surface pressure was coherent and in phase with the 850 hPa level zonal wind and with temperatures from 700 to 150 hPa. The 850 hPa level zonal wind component was coherent and out of phase with the zonal wind component from 300 to 100 hPa level. Little evidence that the meridional wind played a role in the variation was found. Madden and Julian, (1972) subjected to spectral analysis long time series (5-10 years) of station pressure and upper air data from stations located in the tropics, to investigate the spatial extent of the oscillation. The cross-spectral analysis suggested that the oscillation was of global scale but restricted to the tropics and possessed features of a eastward-moving wave whose characteristics changed with time. A mean wave disturbance, constructed with additional data from the International Geophysical Year (IGY), provided descriptive material on the spatial and temporal behaviour of the oscillation. They found that the station pressure consisted of anomalies which appear between 10°N and 10°S in the Indian Ocean region and propagating eastward to the eastern Pacific. Zonal winds participate in the oscillation and, in general, were out of phase between upper and lower troposphere. The sum total of evidence indicated the oscillation was the result of an eastward movement of large scale circulation cells oriented in the equatorial (zonal) plane.

The behaviour of these Intra-Seasonal Oscillation (ISO) perturbations have been documented, as they move around the globe. Characteristics like phase speed, variation of frequency with season and region, changes in amplitude with season and region etc. Also efforts are being made to know the source of energy of these perturbations as well as the mechanism driving them.

Observational as well as modelling studies are being used in studying intraseasonal (low-frequency) oscillations.

Murakami et al. (1985) detected 40-day oscillations travelling in a SW-NE direction in the southern hemisphere. The perturbation seemed to commence in the mid-latitude and moved northeastward crossing the sub-tropics in the vicinities of 30°S, 160°W, 15°S, 150°W to the equatorial regions (5°S, 120°W). In addition, another 40-day wave was noted originating in the South West Indian Ocean off the coast of South Africa and propagating towards the North Pacific Ocean.

Niita et al., (1985) studied the global characteristic features of the lower troposphere in the tropics using the FGGE level III-b wind data during the northern summer of 1979. They found disturbances with periods shorter than 10 days and others with periods between 50-60 days. Variations with longer periods (>13.3 days) predominate in the Asian monsoon region extending from the Indian Ocean through Southeast Asia to western Pacific. Spectral analysis results of winds were compared with those of the outgoing longwave radiation (OLR) data. The spatial distribution of the time variation of OLR was quite similar to those of winds indicating that the convective activity was coupled with the large-scale lower tropospheric circulation in the tropics. From Asnani, (1993), it is believed that a 16-day globally travelling wave was first detected by Kuboto and Lida, (1954). Anyamba, (1992) observed a 20-30 day oscillation in global OLR data over the western Indian and Pacific Oceans.

Using two years of ECMWF analyses (1984-1986), Vincent et al., (1991) examined the intraseasonal (40-50) day oscillation in convection over the tropical southern hemisphere (0°-15°S). They used Velocity Potential at 200 hPa (χ_{200}) and OLR to indicate oscillatory behaviour of convective activity. Spectral peaks at 33 and between 50-67 days were found in the data. Intraseasonal oscillations propagated eastward and convective activity was intense over the maritime continent. They also found that the χ_{200}-wave could be followed continuously around the world, but the convection (OLR) associated with the intraseasonal oscillation was weak and difficult to track over much of the western hemisphere. The same was observed by Murakami et al., (1986). Rui and Wang, (1989) investigated the development and dynamical structure of intraseasonal (low-frequency) convection anomalies in the equatorial region using 10 years (1975-85) of outgoing longwave radiation (OLR) and 7 years (1979-85) of 200 hPa and 850 hPa wind data. The composite OLR anomalies, they formed, for 36 cases revealed a four-stage development process: initiation over the equatorial Africa, rapid intensification when passing through the Indian Ocean, mature evolution characterised by a weakening in the maritime continent and redevelopment over the western Pacific, and dissipation near the date line in moderate events and emanation from the equator toward North America and southern Pacific in strong events. Their vertical structure revealed that the 850 hPa convergence leads convection and mid-tropospheric upward motion by about 30 degrees of longitude in both developing and mature phases. Equatorial upper- (lower-) level easterly (westerly) anomalies and associated twin anomalous anticyclonic (cyclonic) circulation anomalies couple with equatorial convection anomalies. The wind anomalies, however, generally lagged convection anomalies in development and early mature phases, but nearly overlap in late mature phase and slightly led convection anomalies in dissipation phase. Similar results were found by Knutson and Weickmann, (1987). Jury et al., (1991) described wave-organised convective features in the Southwest Indian Ocean using hovmoller composites of satellite imagery, OLR anomalies and ECMWF precipitable water departures during the southern summer. They distinguished intra-annual trends in zonal propagation speed in the 10°-15°S latitude band: Transient convective waves moved westwards in the years 1970, 1972, 1974, 1976, 1977, 1988; convective systems were quasi-stationary in the summers of 1971,1975, 1978, 1979,1983 and 1984; and transient convective waves during the summers of 1970, 1972, 1973, 1976, 1977, and 1981 had short convective wavelengths that coincided with more rapid westwards propagation. Using hovmoller analysis of some meteorological variables between 1987 and 1992, Levey (1993) noted that of 175 convective systems achieving status over southern Africa; 50% propagated eastwards, 21% were stationary, 18% had an ambiguous pattern and the rest propagated westward.

Modelling studies by Lau et al., (1987) have shown that the observed eastward propagation of intraseasonal oscillation in the tropical atmosphere arises as an intrinsic mode of oscillation resulting from an interaction of convection and dynamics via the so called "mobile" wave-CISK mechanism. Through this mechanism it is suggested that, the heat source feeds on the east-west asymmetry of forced equatorial waves. As a result, Kelvin waves are selectively amplified, which in turn causes the heat source to propagate eastward. The "mobile" wave-CISK establishes a new dynamical equilibrium state between convection and the wind field to form a wave packet or collective motion with relatively fixed horizontal and vertical structure. Their results also suggested that the periodicity of oscillation was determined by the time taken for the Kelvin wave to complete one circuit around the world in the equatorial region. The speed and growth rate, it was found, were dependent on the static stability of the basic state. In addition to the eastward propagation, other observed features, such as pressure and wind distribution, amplitude modulation by SST, and dominance of low wave-number response, were well simulated in the idealised experiment. Carrying out a linear theoretical analysis of the β-plane wave-CISK with a focus on the Kelvin modes, Chang et al., (1988) suggested that a possible mechanism for the 30-50 day oscillations propagating Kelvin waves are maintained by cumulus heating and not interactions with stationary oscillations of the basic state. Their results show that two types of CISK modes may arise from an interaction of vertical modes. They found that for heating with maximum in the lower troposphere, the instability was due to the lowest internal mode which gave a stationary, east-west symmetry structure. But, when heating was maximum in the mid-troposphere, eastward propagating CISK mode resembling the observed and the numerically-simulated oscillation occurred. Their results further imply that in the absence of wave-CISK, the observed oscillations cannot be excited by stationary oscillations.

Several studies have shown an association between intraseasonal oscillation with both northern and southern summer monsoons. While studying the onset of the Australian summer monsoon in each year of (1957-87) using the wind and rainfall record at Darwin, Hendon et al., (1990) found that the composite onset coincided with the arrival of an eastward propagating convective anomaly. The anomaly was found to originate in the southern Indian Ocean, propagating eastward at 5 m s^{-1} and was detectable as far as the date line. Madden, (1986) studied the annual variations of the 40-50 day oscillations by applying spectral and cross-spectral analysis on daily rawinsonde data from 19 near-equatorial stations. The zonal wind variance was in a relatively broad band centred on the 47-day period during December, January and February (DJF) at stations in the Indian and western Pacific Oceans. The results, coupled with composited wind and outgoing longwave radiation data, led them to conclude that in the Indian and western Pacific Oceans the eastward-moving regions of the enhanced convection associated with the 40-50 day oscillation force a Kelvin-like wave to the east and anticyclonic, Rossby-like wave to the west. They found that anticyclonic eddies were found in the summer hemisphere during solstice seasons and cause local surges in the upper-level southeasterlies (northerlies) during DJF (JJA). Wang and Rui, (1990) studied the synoptic climatology of transient intraseasonal convection anomalies: 1975-1985 using OLR data. They found 122 Transient Intraseasonal Convection Anomalies (TICA) during the period of study. Of the 122 events studied, 77 moved eastward, 27 were northward propagating and 18 moved westward. Their study further showed that the major formation region was the west equatorial Indian Ocean and a secondary source equatorial Africa. The researchers also showed that the maximum intensification rates of the TICA were in the central equatorial Indian Ocean, with secondary areas of intensification near 160°E North of the equator and one extending from Australia to the date line South of the equator. The areas of intensification were associated with the ITCZ (Wang and Rui, 1990). Applying spectral analysis on surface and rawinsonde time series from several locations in the western Pacific and Indian Oceans, Hartmann et at., (1992) investigated the seasonal dependence of the frequency and intensity of tropical oscillations with intraseasonal time scale. Though their evidence was weak, they were able to show that the Madden-Julian oscillation (MJO) in the Indian Ocean region revealed a seasonal variation in its preferred period from 50 days during Northern Hemisphere winter to about 35 day during summer. In the western tropic Pacific during the September-December season, a pronounced spectral peak with a central frequency between 20 and 25 days was observed.

Murakami, (1987, 1988), studying teleconnection patterns during MJO eastward propagation phase, indicated that a succession of upper level cyclonic and anticyclonic disturbances develop over both the northern and southern subtropics mainly downstream of the convection anomalies, while at 850 hPa, strong 30-60 day meridional wind anomalies surge from the cold mid-latitude.

According to Chen and Tzeng, (1990), for intra-seasonal oscillations to occur, positive (negative) precipitable water anomalies and negative (positive) OLR anomalies couple with convergent (divergent) centre of the potential function of the water vapour transport anomalies and divergent (convergent) centre of the upper-level divergent circulation anomalies.

Composite intraseasonal seasonal oscillation life cycle studies suggest that the Equatorial Indian Ocean is the most favourable geographic location for the development of low-frequency convection anomalies. Besides the warm Ocean surface condition, the interaction between Walker circulation and transient intra-seasonal disturbances and the interaction between monsoon circulation and equatorial intra-seasonal mode may be important factors in determining favoured locations for convective development. Interaction between the tropics and extra-tropics, evidenced by equatorward meridional flow, may activate equatorial convection in those favoured regions (Murakami 1987,1988).

Below a the summary of some of the properties and characteristic features of intraseasonal oscillations in the tropics as revealed by different studies:

-the period of oscillation varies between about 16 to 76 days;

-the oscillations consists of an eastward propagating, wave number one, Kelvin wave with an average speed of 10 m s^{-1};

-the convection anomalies are smaller over the Atlantic, tropical Africa and South America than over the western Pacific and Indian Ocean;

-there is coherence between areas of upper-air divergence and areas of convection;

-the oscillation has strong amplitude and slowest propagation speed (5 m s^{-1}) from about 60°E to 180°E

1.3 Hypothesis

(a) Convection over Tanzania is modulated by low frequency oscillations of periods ranging from 10 to 60 days (ISO);

(b) meteorological features influencing convection over Tanzania:

(i) the Arabian ridge, Mascarene and St. Helena anticyclones,

(ii) orographic and thermally induced circulations of a local nature,

(iii) the ITCZ- the inter-hemispheric wind convergence zone

(iv)remnants of tropical cyclones

(c) the dynamics of DJF (MAM) rains are influenced by the NE (SE) monsoons of the adjacent Indian Ocean

(d) there is some coupling between the intra-seasonal and inter-annual variability.

We require an understanding of rainfall variability over Tanzania with associated local and regional dynamic and thermodynamic processes influencing such variabilities. The knowledge gained can be used in forecasting weather phenomena at the intraseasonal time scale.

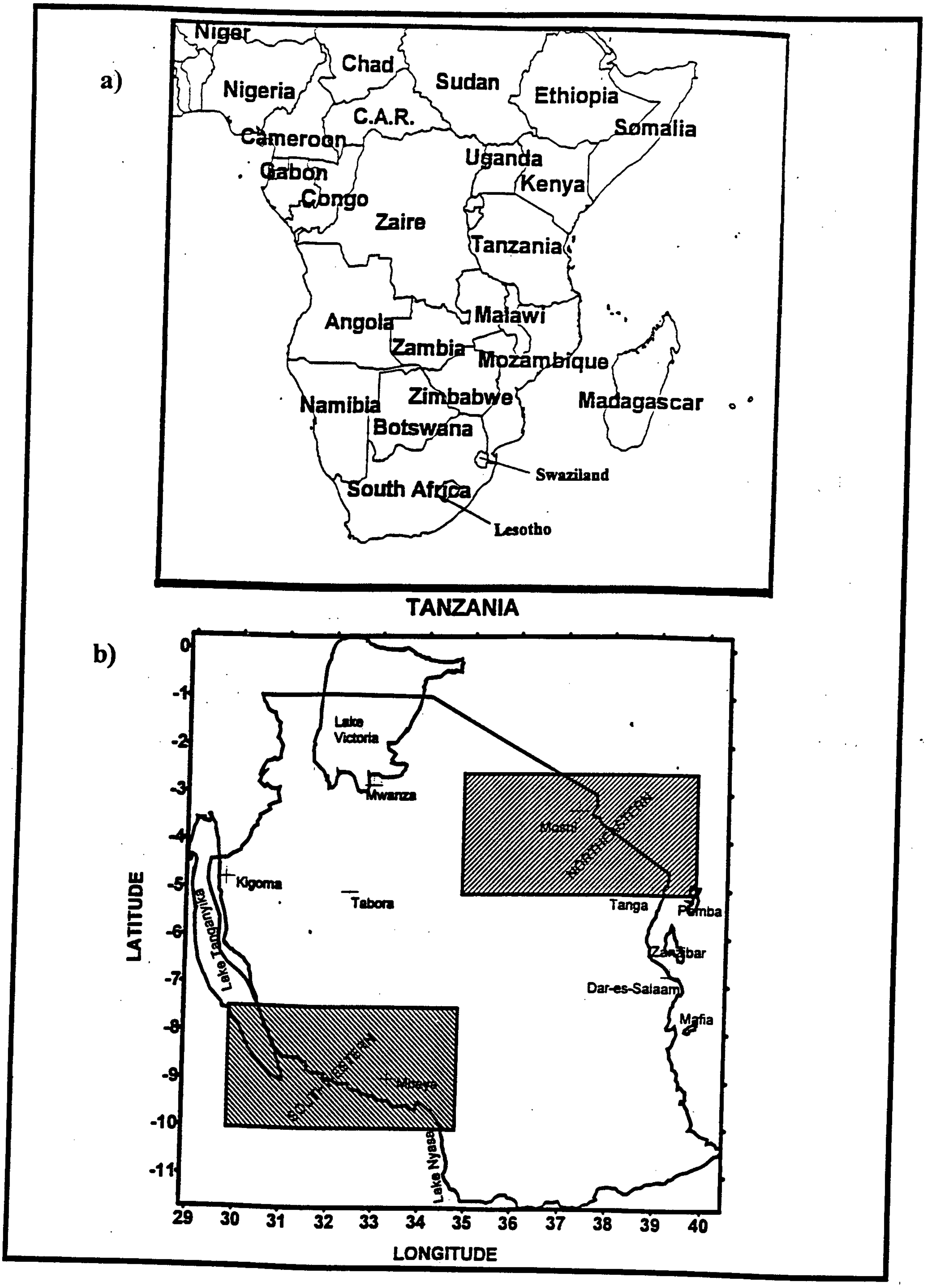

Figure 1.1: (a) Part of the map of Africa (with political boundaries) and the domain of study; (b) Map of Tanzania showing areas selected for study.

CHAPTER 2

DATA AND METHODOLOGY

2.1 Data

2.1.1 Introduction

The model data used in this study is from two main sources. Model-based global data sets of atmospheric circulation from ECMWF (European Centre for Medium Weather Forecasting) and OLR (Outgoing Longwave Radiation) data from the National Centre For Environmental prediction (NCEP) in Washington D. C. These data sets have been widely used by many researchers for studying dynamical and physical processes and for describing the nature of the general circulation of the atmosphere. A lot of research have been undertaken to assess the currently available model-based global data sets of atmospheric circulation. Studies recently made by Bengtsson and Shukla, (1988) have shown that not all the available model based global data sets are suitable for studying regional climatic variability. They state reasons such as limitations in the early data assimilation systems and inconsistencies caused by numerous model changes. However, the data set can be used in the current study to address intraseasonal oscillations. Satellite derived Outgoing Longwave Radiation (OLR) is utilised as a proxy for synoptic scale cloudiness and convective activity over Tanzania. Warm, shallow clouds, land masses and ocean bodies within the tropics radiate high values of OLR while cold, deep clouds radiate low values of OLR.

2.1.2 ECMWF Data

The ECMWF data assimilation system has undergone improvements over the last ten years. Hoskin et al. (1989) undertook a diagnostic of the global atmospheric circulation based on ECMWF analyses 1979-1989 and discussed various changes in the data set during the period. The ECMWF analyses system undergoes continual revision and development in order to provide better forecasts and reliable data. Some of the changes which have been implemented in the last ten years include:

-03/1986: better humidity analyses, including the use of satellite precipitable water content data;

-09/1986: introduction of new model levels and further refined structure functions;

-01/1988: improved analysis of divergent wind;

Since the mid 1980's the data resolution has increased and new basic or advanced data sets are available at different resolutions.

Considerable effort in the quality control of observations through frequent correspondence with the data producers to improve the quality of observation has been undertaken by ECMWF. Of concern to ECMWF has been the quality and availability of satellite observations, especially in areas where few conventional observations are available, e.g. over the oceans and remote areas.

The ECMWF weather data are modelled from observations made from rawinsondes, satellite temperature and moisture soundings, pilot balloons and cloud tracked winds, surface observations from ships, oceanic buoys and land stations, aircraft reports and occasional bogus inputs. Comparisons of ECMWF FGGE analyses up to 1994 with analyses by other centres have shown that the ECMWF data:

- gave realistic circulation features in the southern Hemisphere;

-more closely fit the data;

-had more balanced mass and wind fields;

-had less random error than analyses by the other centres, such as the National Meteorological Centre (NMC) USA

Here, pentad (5-day mean) ECMWF data have been used to study intraseasonal convection variability over Tanzania. The basic parameters obtained are geopotential height, zonal wind components (u), meridional wind component (v) and vertical motion (ω), specific humidity (q), etc. ECMWF model data set was available at 12 UTC, i.e. 15h00 local, at standard pressure levels up to 100 hPa. The data were extracted for the months November, December, January, February, March, April and May from 1979 to 1994. The data encompasses 15°N to 35°S and 0° to 100°E domain at a resolution of 2.5 by 2.5. From the above retrieved data other parameters were derived (derivation methods are shown in section 2.2.6)

Other derived parameters include:

vorticity and Divergence;

precipitable water;

water vapour flux and

Equivalent Potential Temperature.

Parameter	Pressure Surface (hPa)							Units
Geopotential height	850				200			gpm
Zonal wind	1000	850	700	500	300	200	100	m s^{-1}
Meridional wind	1000	850	700	500	300	200	100	m s^{-1}
Vertical motion			500					Pa s^{-1}

Table 2.1: Primary ECMWF parameters used in this study.

Derived parameters	Pressure levels (hPa)						Units
Divergence	850				200		s^{-1}
Vorticity	850				200		s^{-1}
Precipitable Water	Integrated from 1000 hPa to 300hPa						mm
Water Vapour Flux	Integrated from 1000 hPa to 500hPa						kg m^{-1} s^{-1}
Equivalent Potential Temperature	850	700	500	300	200	100	°K

Table 2.2: Derived parameters used in this study

2.1.3 National Centre For Environmental Prediction (NCEP)

The main aim of this work is to study rainfall variability at intraseasonal time scale. However, rainfall data is not going to be used to study the variability because of the following reasons:-

-few and uneven distribution of rainfall stations over the study areas;

-irregular recording of data and

-poor quality of the data.

An indirect measure of rainfall variability, i.e. convection, will be used instead. OLR and SSM/I data have been used by many researchers as a proxy of convection within the tropics. Zipser et al., (1997) used SSM/I as a proxy measure to infer convection intensity. In this study we will use Outgoing Longwave Radiation (OLR). OLR data has been used as a proxy for cumulus convection/cloud variability particularly over convectively active regions of the tropics by Wang and Rui, 1989; Chen and Tzeng, 1989; Lyons, 1990 and many others. Low (high) values of OLR indicate greater (less) cloudiness and hence increased (decreased) depth of cumulus convection. Caution should be exercised when interpreting Outgoing Longwave Radiation as convection/rainfall, since thick, high clouds can produce identical OLR signature as convective clouds, while substantially different productions of rainfall occur between the two type of clouds (Lyons, 1990). OLR data used here encompass the 15°N-35°S and 0°-100°E domain with 2.5° degree resolution. The data set extended from November, 1976-May, 1994. The data were analysed in the form of pentads (non-overlapping 5-day means) starting at pentad 1 for each year (1-5 January) and ending at pentad 73 (27-31 December). Leap years within the data set include one 6 day mean "pentad" at the end of February.

2.2 Methodology

2.2.1 OLR Index Formulation

The aim is to investigate intraseasonal convective oscillations over southwestern and northeastern Tanzania in mid-summer and autumn respectively. In order to achieve the above aim OLR indices for the two areas were created. To represent the northeastern area a box which extends from 2.5°S to 5°S and from 35°E to 40°E was used. The box include parts of Tanga, Kilimanjaro, and Arusha regions in Tanzania and the south-eastern part of Kenya. The box which extends from 7.5°S to 10°S and from 30°E to 35°E represents the southwestern areas and includes some parts of Mbeya, Ruvuma and Rukwa regions and northeastern parts of Zambia. The indices were defined as pentad averaged OLR values within a box, that is, OLR pentad values at grid points were added together and divided by the number of points. For example, for southwestern areas the index was created by adding OLR pentad values for 6 grid points and dividing by the sample size. Time series of the pentad OLR index was produced for MAM (March-April-May) season for 1980 to 1993 for northeastern areas and DJF (December-January-February) season for southwestern areas. Comparisons with rainfall stations area averages are shown below.

YEAR	SW- r_{18}	YEAR	NE- r_{18}
76/77	-0.41*	76	-0.19
77/78	-	77	-0.79*
78/79	-	78	-
79/80	-0.60*	79	-0.32
80/81	-	80	-0.18
81/82	-0.46*	81	-0.63*
82/83	-0.34	82	-0.76*
83/84	-0.50*	83	-0.51*
84/85	-0.65*	84	-0.41*
85/86	-0.23	85	-0.85*
86/87	-0.18	86	-
87/88	-0.46*	87	-0.46*
88/89	-0.21	88	-
		89	-0.63*
AVE.			

Table 2.3: OLR correlation with area averaged rainfall (Figure 1.1). SW=Southwestern NE=Northeastern (Correlation values with * are significant at 95%; (with 16 degrees of freedom: [Sample size is 18]- 2), according to Underhill, 1981)

Station		Station Location	Elavation (meters)
SW	Mbeya	9832001	1758
SW	Mbimba	9932005	1524
SW	Igawa Maji	9834006	1067
SW	Luponde Farm	9934013	2134
NE	Moshi	9337004	813
NE	Selian Coffee Estate	9336011	1402
	Ngorongoro	9335033	2286
NE	Kondoa Maji	9435025	1372
NE	Oldeani	9335020	1676
NE	Langasani	9337028	701
NE	Same	9437003	860

Table 2.4: Stations used to calculate area averages of rainfall (1980-1989). NE- northeastern, SW- Southwestern

Various analysis methods are used depending on temporal and spatial resolutions of the data to be analysed. Since medium term (20 day) temporal resolution is desired in this study pentad (5-day mean) data are ideal. Different analysis techniques have been utilised to understand the cyclic nature of the intra-seasonal oscillation. A detailed account of each technique is discussed.

2.2.2 Analysis techniques

Spectral analysis is performed on pentad OLR indices created in section 2.2.1 above. Composites of individual case studies were used. Longitude-time analysis (Hovmoller plots) of various meteorological parameter anomalies have been used to identify characteristics and direction of propagating systems.

2.2.2.1 SPECTRAL ANALYSES

The idea behind spectral analysis of a time series is to explore the existence of cyclical patterns of data. The features of spectral analysis is to decompose a time series with cyclical components into a few linear combinations of sine and cosine functions of different frequencies, in order to determine those that appear particularly strong or important. To do so a multiple regression is developed as follows:

for k = 1 to q:

$$x_t = a_0 + \sum_{k=1}^{q}\left[a_k * \cos(\lambda * t) + b_k * \sin(\lambda * t)\right] \qquad \text{Eq. 2.1}$$

where $\lambda = 2*\pi*f$ frequency expressed in radians

$f = 1/T$ T is period of oscillation

$q = \frac{n}{2} - 1$

a_k and b_k are regression coefficients of cosine and sine parameters respectively and tell the degree to which the respective functions are correlated with the data. Periodogram values were then computed as follows:

$$P_k = \left(a_k^2 + b_k^2\right) * \frac{n}{2} \qquad \text{Eq. 2.2}$$

where P_k is the periodogram value at frequency f_k, and n is the overall length of the series. The periodogram values can be interpreted in terms of variance (sum of squares) of the data at the respective frequency or period. Periodograms were then plotted against the frequencies.

Spectral analysis was performed on different OLR time series using the STATISTICA software package. Before the spectral analysis was done the following steps were performed:

(i) removal of mean,

(ii) Trend removal,

(iii) The data series were padded in order to obtain finer mesh of frequencies as the original data length were small (18 pentads). The padded data were tapered at 10% to enhance spectral estimates (BMDP Statistical package). Tapering also reduces the influence of estimates calculated in one frequency band upon those in another frequency band.

2.2.2.2 COMPOSITE ANALYSES

Rui and Wang, (1990), Chen and Tzeng (1989) and many others have used composite analyses techniques extensively in the field of meteorology. Composites are better at indicating common features, trends and patterns in the various variables than individual cases. This method reduces the total number of maps and figures associated with each case study. Various ways are used in selecting cases to composite. It is important however, to select cases with similar characteristics to composite. We have selected our cases from OLR-time plots. Our focus in the selection is deep convection cases with their precursors, i.e. a pentad during deep convection and one pentad before deep convection. Deep convection pentads is denoted by P0 and the precursor pentad is denoted by P-1. The Deep convection pentads were selected when OLR index values were lower than 190 W m^{-2} and onset or precursor pentads were picked when OLR index values were between 210-240 W m^{-2}. Mean composites for deep convection were obtained by adding together the selected cases and dividing by the number of cases. The same was done for the onset pentad. Pentad anomalies were obtained for onset and deep convection cases by subtraction of seasonal means. Anomaly analysis is useful in studying weak tropical features (Asnani, 1993).

SOUTHWEST TANZANIA		
YEARS	P-1 (210-240W m^{-2})	P0 ($\leq$ 190 W m^{-2})
1980	P 01	P 02
1980	P 05	P 06
1981	P 71	P 72
1982	P 72	P 73
1983	P 07	P 08
1985	P 03	P 04
1986	P 01	P 02
1987	P 73	P 01
1989	P 72	P 73
1990	P 02	P 03
1991	P 72	P 73
1991	P 04	P 05
1992	P 70	P 71

NORTHEASTERN TANZANIA		
1981	P 17	P 18
1984	P 20	P 21
1985	P 17	P 18
1986	P 23	P 24
1988	P 15	P 16
1989	P 19	P 20
1991	P 17	P 18

Rable 2.5: Case selection. P0 = Pentad number (see pentad calendar in appendix A)

2.2.2.3 Hovmoller Analysis

Longitude-time (hovmoller) plots are useful in identifying zonal moving meteorological systems. Anomalies of some meteorological parameters, from which we can infer convection, are used in the analysis in order to identify propagation of intraseasonal convection oscillation anomalies. Mean values of meteorological parameters between 2.5° and 5°S and 7.5° and 10.0°S latitude bands for northeastern and southwestern Tanzania respectively were calculated along each longitude from longitude 0° to 100°E. This was done for pentads 62-73 and 1-30, from November to May of the following year e.g. November, December, January, February, March, April, and May. The latitude band and pentad averaging has the effect of filtering the high frequency oscillatory small scale systems. Hovmollers for individual seasons are plotted e.g. Nov., 1992 to May., 1993. Anomalies were calculated by subtracting the historical mean array for the respective latitude bands, at longitudes 0° to 100°. This has the effect of removing the annual cycle or seasonal signal. Subsequently hovmollers for each year from 1980-1994 were plotted.

2.3 Derived Parameters

The reason for producing secondary derived parameters, is that such values when used in combination with primary parameters yield results which describe meteorological kinematics and thermodynamic structure (Parker, 1994)

2.3.1 Divergence and Vorticity

Divergence is defined as the acceleration and diffluence experienced by the air in the local horizontal plane. A region of divergence on an isobaric surface is one from which there is a net outflow of airmass. The component of divergence in the total two dimensional field is as follows:

$$\text{Divergence} = (\nabla_h . V)$$

$$= \frac{\partial u}{\partial x} + \frac{\partial v}{\partial y} \qquad \text{Eq. 2.3}$$

Vorticity is defined as the measure of relative spin about the local vertical. In the southern hemisphere negative relative vorticity is one in which there is a tendency for the air to rotate in a clockwise (cyclonic) sense. The components of vorticity in the two dimensional field are as given below:

$$\text{Vorticity} = \xi = (\nabla \times V)$$

$$= \frac{\partial v}{\partial x} - \frac{\partial u}{\partial y} \qquad \text{Eq. 2.4}$$

where

u = zonal wind component

v = meridional wind component

x = longitudinal distance

y = Latitudinal distance

2.3.2 Precipitable Water

Precipitable water is a useful parameter which depicts the moisture content of the atmosphere calculated between two points situated vertically above each other. Precipitable water is theoretically defined as the depth of water in millimetres that would be obtained if all the water vapour in the column were condensed onto a lower horizontal surface of unit area. Precipitable water (PW) is therefore the measure of the atmospheric vertically integrated water content. It is defined quantitatively using the following formula:

$$PW = \frac{1}{g}\int_{p1}^{p2} x\delta p \qquad \text{Eq. 2.5}$$

Where: x is the mean humidity mixing ratio between pressure levels,

p1 is 1000 or 850 hPa and p2 is 300 hPa

and g = 9.80665 m s^{-2}

PW is usually integrated between 1000 to 300 hPa (Chen and Tzeng, 1990). For purposes of this study PW is expressed in mm and the integration starts from 1000 hPa over sea or 850 hPa over land (P_1) to 300 hPa for (P_2).

2.3.3 Water Vapour Flux (Q)

Water vapour flux (Q) can be defined as the advection of precipitable water by horizontal wind. Water vapour flux, Q, is obtained through vertical integration. In this study, integration is between the 1000 hPa and 500 hPa levels (except over the African plateau). A sizeable amount of horizontal transfer of water vapour in the tropics is near 700 hPa.

$$Q = \frac{1}{g}\int_{p1}^{p2} qV\delta p \qquad \text{Eq. 2.6}$$

where $g = 9.80665$ m s^{-2}, gravitational constant,

q = specific humidity (g kg^{-1}),

V = velocity at a particular level (m s^{-1}).

p1 and p2 are 1000 hPa and 500 hPa respectively, however over the African plateau the surface is taken as 850 hPa. The individual qu and qv components of the moist flow are combined to give a water vapour flux vector, Q, which has both magnitude and direction. The magnitude is represented by:

$$\sqrt{(qu)^2 + (qv)^2}$$

and the direction by:

$$\arctan(qu/qv)$$

Since the concentration of atmospheric moisture is highest in the lowest levels of the atmosphere and Walker and Hadley overturning results in upper flows often opposing lower levels, it was felt that incorporating the horizontal wind above 500 hPa may distort results. Integration was thus carried out up to 500 hPa. Since moisture in the atmosphere is concentrated in the lowest levels of the atmosphere, the weighted vector average often reflects flow below 500 hPa, and is similar to the 700 hPa level.

2.3.4 Equivalent Potential Temperature

Equivalent Potential Temperature (EPT, θ_e) can be defined as the final temperature which a parcel of air attains when it is lifted dry adiabatically to its lifting condensation level, then pseudo-wet adiabatically (with respect to water saturation) to a great height (dropping out condensed water as it is formed). Finally the parcel is brought down dry adiabatically to 1000 hPa level. Useful references are Holton, (1973); Bolton, (1980) and Peixoto and Oort, (1992). EPT eliminates problems associated with local temperature changes like cooling (warming) due to adiabatic expansion (compression), thereby enabling compression to be made at various atmospheric levels. Equivalent potential temperature, $\theta_{e,}$ is a useful parameter for studying cumulus convection, as it combines temperature and moisture variables (Preston-Whyte and Tyson, 1988). With, the definition above it is apparent that if $\partial\theta_e/\partial z$ is negative the atmosphere is potentially unstable. Malkus and Riehl, (1960) showed that the warmest possible column consisting of air which ascends from the surface at 1000 hPa, under moist adiabatic condition would have a value of θ_e as 350°K. As a quasi-conservative parameter, it can be used for investigating the stability of the atmosphere. Quantitatively EPT can be expressed as follows (Bolton, 1980),

$$\theta_e \quad = \theta \exp\left[\left(3.376 / T_l - 0.00254\right) * r\left(1 + 0.81 * 10^{-3} r\right)\right] \qquad \text{Eq. 2.7}$$

T_L is the lifting condensation level, expressed as

$$T_L = \frac{2840}{\left(3.5 \ln\left(T - 273.15\right) - \ln\left(e\right) - 4.805\right)} - 55$$

where $e = T\left(P_0 / P_s\right)^{\kappa}$ and $\kappa = R^d / C_p$

e is the water vapour pressure, T, temperature and r the mixing ratio

CHAPTER 3

ANALYSIS OF CONVECTIVE OSCILLATIONS OVER TANZANIA FROM OLR

3.1 Introduction:

The tropical atmosphere is convectively unstable. For production of clouds and rainfall vertical motion and moist air are required. Within the tropics vertical motion can be induced by forced ascent of air over high ground, horizontal velocity convergence and unequal heating of land and water mass. Large temporal and spatial variations of convection are normally observed within the tropics. There are diurnal variations due to insolation and seasonal variations which are due to the North and South movement of the ITCZ in sympathy with the overhead sun. There are also inter-annual variations which may be linked to ENSO (El Nino Southern Oscillation), Nicholson, (1983); Ogallo et al., (1988); Hastenrath, (1993). Deep convection within the tropics is modulated by zonal moving waves from the east at higher frequency (easterly waves) and from the west at low-frequency (Madden and Julian Oscillation). Tanzania being within the tropics is expected to experience this type of convective variability.

Two areas of Tanzania have been picked to study the intraseasonal convection oscillations and these are the northeastern and the southwestern sub-regions. The areas have been selected for study because of their importance to agriculture and hydroelectricity generation potential. The seasonal cycle of convection is optimum over southwestern Tanzania during mid-summer: December-January-February, and over northeastern Tanzania during the autumn season: March-April-May (known as the long rains or Masika). The short rainy season has been covered by Kabanda, (1995). The northeastern area experiences two rainy seasons October-December and March-May. The southwestern area experiences one rainy season (December-April). Through this distribution the behaviour of intraseasonal oscillations during the Northeast Monsoon and the Southeast Monsoon over East Africa can be studied. An understanding of the circulation features and thermodynamic processes associated with the intraseasonal convective oscillation will enable forecasts of drought and flood events.

The purpose of this chapter is to analyse the intraseasonal convective variability over southwestern and northeastern Tanzania with the aim of understanding dominant convective periodicities and also the spatial evolution of convection in the selected domain. Dynamics and thermodynamic features associated with the OLR spatial sequence shall be covered in chapter 4 and 5

Time series analysis of the area averaged OLR data for the southwestern and northeastern areas of Tanzania will be performed in order to establish intraseasonal variability. Two methods of time series analysis shall be used.

The first is area-averaged pentad OLR index time plots. This is done for individual seasons. Spectral analysis is also used in order to reveal periodicity in the pentad OLR index data. From the time series plots different events of convection, inferred from OLR, were selected and composited as described in section 2.24 of chapter 2. Composite maps were then made for a pentad before deep convection (P-1), the onset phase, and a pentad during deep convection P0, the active phase. Deep convection (P0) cases selected for compositing are indicated by arrows in figures 3.1 and 3.4.

3.2 Southwestern Tanzania (DJF).

3.2.1 Intraseasonal OLR time variability

Pentad OLR index time series plots are illustrated in figure 3.1. For plotting purposes pentad 68-12 are represented as pentad 1-18 in figure 3.1. The plots reveal that the highest pentad OLR value was 274 W m^{-2} and this was in 1993 pentad 68, while the lowest was about 154 W m^{-2} and occurred in 1984 pentad 69. The plots also show that the OLR index varies differently in each season. Some seasons have larger OLR variability than others. A subjective count of deep convective cases in each season shows that there are about 3 to 4 cases and the dominant period of oscillation of deep convection is between 4 to 6 pentads. Seasons with pronounced OLR variability are 1979-80, 1981-82, 1982-83, 1984-85, 1989-90, 1990-91, 1992-93, and 1993-1994. In some years the period of oscillations are shorter than others. It is also revealed that in some seasons the OLR index values are persistently about 200 W m^{-2} or below 200 W m^{-2} for a longer period of the season, with small OLR variability. A good example of such type of variability is revealed in 1983-84. A season with delayed seasonal onset is 1993-94 DJF season (figure 3.1p). The lowest value of OLR occurred at pentad 4 of 1994.

3.2.2 OLR Spectral Analysis

Results of periodogram analysis of OLR index for individual seasons over southwestern Tanzania are presented in figure 3.2. Due to the shortness of the data window (18 pentads) care should be exercised in interpreting the periods. Periodogram results reveal that relatively high peaks at different periods in different seasons. Some seasons have peaks at shorter periods (e.g. 1982/83, 1990/91; figures 3.2b and 3.2j) while in other years high periodogram peaks occurs at longer periods (e.g. 1987/88, figure 3.2g). Other years reveal mixed peaks at both shorter and longer periods. Seasons with large OLR index variability, as revealed in pentad OLR time series plots, produce large periodogram peaks in comparison with years with small OLR index variability as expected. The average period was found to be about 4 pentads (20 days) with periods of relatively high periodogram peaks ranging from 2-pentads (10-days) to 16-pentads (80-days). As pointed by Madden, (1994) the intraseasonal oscillation has a broad band nature with periods spreading from 22 days to a whole season. The broad band nature has also been confirmed by other researchers like (Weickmann et al., (1985); Vincent et al. (1991); Murakami et al., (1986) and others). A period of 85-day was noted by Hendon and Liebmann, (1990) in OLR data at Darwin. However, in Order to confirm the existence of periods longer than 6 pentads (>30-days) in the OLR oscillation we need to perform spectral analyses using area averaged daily data for the same area. Using the results of periodogram analyses of individual seasons, we subdivide the periods into three ranges, i.e. 2 to < 4 pentads; 4 to < 6 pentads and greater than 6 pentads. Table 3.1 show the distribution of relatively dominant periodogram peaks within the period ranges selected. This illustrates that, in the period 1981-1994 for the DJF season, dominant spectral peaks with period from 2 to < 4 pentads occurred 21% of the time, and those with periods from 4 to < 6 pentads occurred 34% of the time. Spectral peaks at periods longer than 6 pentads, the MJOs, were also indicated.

SOUTHWESTERN TANZANIA				NORTHEASTERN TANZANIA			
YEARS	$2 \leq P < 4$ Pentads	$4 \leq P < 6$ Pentads	$P > 6$ Pentads	YEARS	$2 \leq P < 4$ Pentads	$4 \leq P < 6$ Pentads	$P > 6$ Pentads
1981/82	W	4.57	10.67*	1980	2.28	W	10.67*
1982/83	W	4.57	W	1981	W	W	8
1983/84	W	4.57	8	1982	3.56	W	10.67*
1984/85	2.67 2	5.33	10.67*	1983	3.2	4.57	8
1985/86	2.46	4	6.4	1984	2	W	10.67
1986/87	3.2	4	6.4	1985	3.2	W	8
1987/88	W	W	6.4	1986	▨	▨	▨
1988/89	W	W	8	1987	2.91 2.13	5.33	10.67
1989/90	W	W	10.67*	1988	▨	▨	▨
1990/91	W	4.57	W	1989	2	4	8
1991/92	3.2	W	10.67*	1990	W	5.33	6.4
1992/93	W	5.33	6.4	1991	3.56	4.57	8
1993/94	W	W	16*	1992	W	4	16*
				1993w	2	5.33	W
Percentage	21%	34%	46%		36%	25%	39%

Table 3.1: Periods of dominant spectral peaks. Periods with * have been resolved after padding the data with zeros to 32 data points.

3.2.3 OLR Spatial analysis for southwest Tanzania

Composite pentads will be described in this section to show the evolution of pentad OLR pattern from pentad P-1 (onset of convection) to pentad P0 (deep convection). Figures 3.3a and 3.3b represent mean composite values for pentad P-1 and P0 respectively. The two figures reveal that high values of OLR (less cloudiness/convection) are located over the desert areas and low values of OLR (deep clouds/convection) are located mainly over the equatorial tropics. Figure 3.3a reveals that lowest values of OLR, of less than 200 W m^{-2}, are centred at about 10°S, 25°E at P-1 while figure 3.3b shows that the lowest values, of less that 190 W m^{-2}, are located at 10°S, 31°E at P0. This indicates that there is a northeastward shift of convection of about 6° of longitude and decrease of pentad OLR values (increase of convection) over the index area within 5 days. The northeastward shift of low OLR values from southern Africa has been observed by Lyons, (1991). Figures 3.3c and 3.3d reveals spatial OLR anomalies at pentad P-1 and P0 respectively following subtraction of the seasonal mean. At pentad P-1, figure 3.3c, positive anomalies are located over southwest and northeast Africa, southwest and southern Indian Ocean and over Mozambique, Malawi, Zambia and western Tanzania. Negative OLR anomalies are located off the coast of Tanzania, central Indian Ocean, central west Africa and west Africa. At P0, figure 3.3d, negative OLR anomaly values are located over east Africa, central Indian Ocean, Zambia and Zimbabwe and also over eastern South Africa. Negative OLR anomaly values which were observed at P-1 over North and northwest Africa have been replaced by positive OLR values. Generally there is an eastward shift of OLR anomaly values.

3.3 Northeastern Tanzania (MAM)

3.3.1 OLR time series Analysis

Pentad OLR index time series plots for the 'masika' rainy seasons of individual years 1980 to 1994 inclusive are shown in figure 3.4. Pentad OLR index time plots reveal considerable variability. Large fluctuations are observed in some years while small fluctuations are observed in others. The maximum OLR index is shown to be 297 W m^{-2} in pentad 17 of 1982 (indicative of less convection) while the minimum OLR index is 176 W m^{-2} on pentad 20 of 1989.

The OLR index mean time series plot reveals that low OLR values occur between pentad 17 and pentad 24, which fall in April. This is the most rainy part of the season. Generally the plots reveal that there is an average of about 2 to 3 cases of OLR values below 220 W m^{-2} deep convection per season. 1993 MAM season was different from the rest as it shows that all pentads had pentad OLR index values above 220 W m^{-2}. The average number of deep convective cases is about 2 to 3 per season. 1987 was the year with more relatively deep convective (about 4) cases. Longer periods with low OLR values (deep convection) are observed in 1981 with three consecutive pentads below 220 W m^{-2} and 1991 with two pentads. The average oscillation period of active convection is subjectively counted to range between 3 to 6 pentads.

3.3.2 OLR Spectral Analysis

The northeastern OLR index data was subjected to FFT to establish periodicity. Periodogram values were calculated for each season MAM (March-April-May); 1986 and 1988 were not considered because of missing data points). Periodograms for each season reveal relatively high periodogram values (spectral peaks) at different periods. From the periodogram analysis figure 3.5, relatively high periodogram peaks are found in the period range of 2-pentads (10-days) and 16-pentads (80-days). As stated in section 3.2.2 we need to analyse area averaged daily OLR data to confirm the existence of periods greater than 6 pentads (> 30-days). Relatively large dominant peaks were found to have an average period of about 4 pentads (20-days). From the results of periodogram analyses of individual seasons, we subdivide the periods into three ranges, that is 2 to < 4 pentads, 4 to < 6 pentads and greater than 6 pentads. From table 3.1 (right panel) we see that spectral peaks with periods 2 to < 4 occur 36% of the time, while those with periods from 4 to < 6 occur 25% of the time. Pronounced spectral peaks with periods greater than 6 pentads occur 39% of the time.

3.3.3 OLR Spatial analysis for northeastern Tanzania.

Composite evolution of spatial pentad OLR (convection) from pentad P-1 to pentad P0 for the northeastern areas are presented in figures 3.6a and 3.6b. Figure 3.6a reveals low values of OLR centred at about 02°S, 28°E with central values less than 190 W m^{-2}. High values are found North of latitude 10°N and over southwestern Africa. At pentad P0, figure 3.6b, the low values have shifted for 10° of longitude to the east in 5 days. High OLR values seem to have spread over the whole of southern Africa. While in the North values higher than in figure 3.6a are noted. Deep convection is noted over the index region at pentad P0 than pentad P-1 as expected.

Figure 3.6c and 3.6d shows the evolution of OLR anomalies from pentad P-1 to pentad P0. At P-1 positive OLR anomaly values are located North of 10°N, over the South Atlantic ocean and the extreme southern tip of Africa. Negative

OLR anomalies cover the rest of the study area with large negative anomalies over central west Africa and at 10°S, 47°E. At P0, figure 3.6d, negative values cover the whole central and northeastern Africa with high negative values located at 4°S, 37°E. The pattern indicates that subtropical pressure forces play important roles.

3.4 Summary

The purpose of chapter 3 was to investigate the characteristic nature of convection over southwestern and northeastern areas, through the temporal and spatial analyses of pentad OLR data. Convection was inferred from OLR variability. Based on the time series plots and spectral analyses of the defined pentad OLR indices and spatial pentad OLR maps for P-1 and P0 for the two areas the temporal and spatial variabilities of convection were investigated over the two areas. The above analysis has demonstrated inter-annual variability of convection over southwestern Tanzania, during DJF and northeastern Tanzania, during MAM through spectral cycles of OLR indices. It is interesting to note that pentad OLR index values representing deep convection over the southwestern area are generally lower than those over northeastern Tanzania. This may indicate that clouds are shallower over the northeastern area than over the southwestern area. It has also been shown that there exits pronounced peaks in the 2-6 pentad ranges. The spatial analyses have revealed that low OLR values over central equatorial shifts eastwards coupled with the low OLR pattern in the South associated with frontal troughs; in agreement with Lyons, (1991). The results of the analyses can be summarised as follows:

-large fluctuations of convection do exist over the two areas in respective seasons. The analysis have shown that deep convection varies from season to season or from year to year. Season to season large amplitude variation of OLR have also been noted by Murakami et al., (1987) and suggested that they are associated with the low frequency oscillations. The analysis has shown that there exists spells of active and weak convection over Tanzania. Prolonged weak convective spells can lead to drought while prolonged active spells can lead to flood. These events can have adverse consequences for agricultural activities depending on the extremity of the events. The average number of deep convection cases per season was found to be about 3.

-spectral analyses results show that periods of dominant peaks varies from year to year. The periods of dominant peaks ranges from 2 pentad to about 10 pentad (10-50 days). However, the (20-50 days) period band had the highest occurrence of dominant periodogram peaks. This comes not as a surprise as dominant spectral bands, in various meteorological parameters, in the period range 20-60 days have been detected by other researchers like (Weickmann et el., 1985; Vincent et al., 1991; Madden, (1971); Murakami et al., (1986) and many others). Care should be exercised however, when discussing the periods above 6 pentads because of the length of the time series used in analysing periodograms. To confirm the presence of periods greater than 6 pentads (30 days) in the convection oscillation over the two areas we need to perform spectral analysis on area averaged daily OLR data for each season. Large amplitude of periodogram values were found during seasons with large OLR variability and small amplitude of periodogram values in seasons with small OLR variability as expected.

-the spatial analyses for P-1 (The precursor to deep convection phase) and P0 (the deep convection phase) have revealed that low OLR values patterns over central southern Africa shifts northeastward (for the case of DJF season) and eastwards (for the case of MAM season). The shift of low OLR patterns are coupled with low OLR patterns in the South associated with frontal troughs; in agreement with Lyons, (1991); Weickmann et al., (1985). The shift of low OLR patterns are also linked to the Shift of the ITCZ. This is similar to the findings of Knutson and Weickmann, (1987).

Based on the analyses done in this chapter we have been able to reveal the nature of convective variabilities. It is difficult to say with confidence the convection periodicity operating over the two areas, due to the short data window, but indications are there to show that periodicties in the MJO band (i.e. 30-60 days) do exist. Also we have been able to show the temporal spatial patterns of convection affecting the two areas. In chapter 4 and 5 we shall analyse kinematics and thermodynamic parameters associated with the temporal spatial convective patterns at P-1 and P0 for southwestern and northeastern areas. In these two chapters we shall be finding whether the convection oscillation over the two areas behave the same way as those observed in intraseasonal oscillations discussed elsewhere.

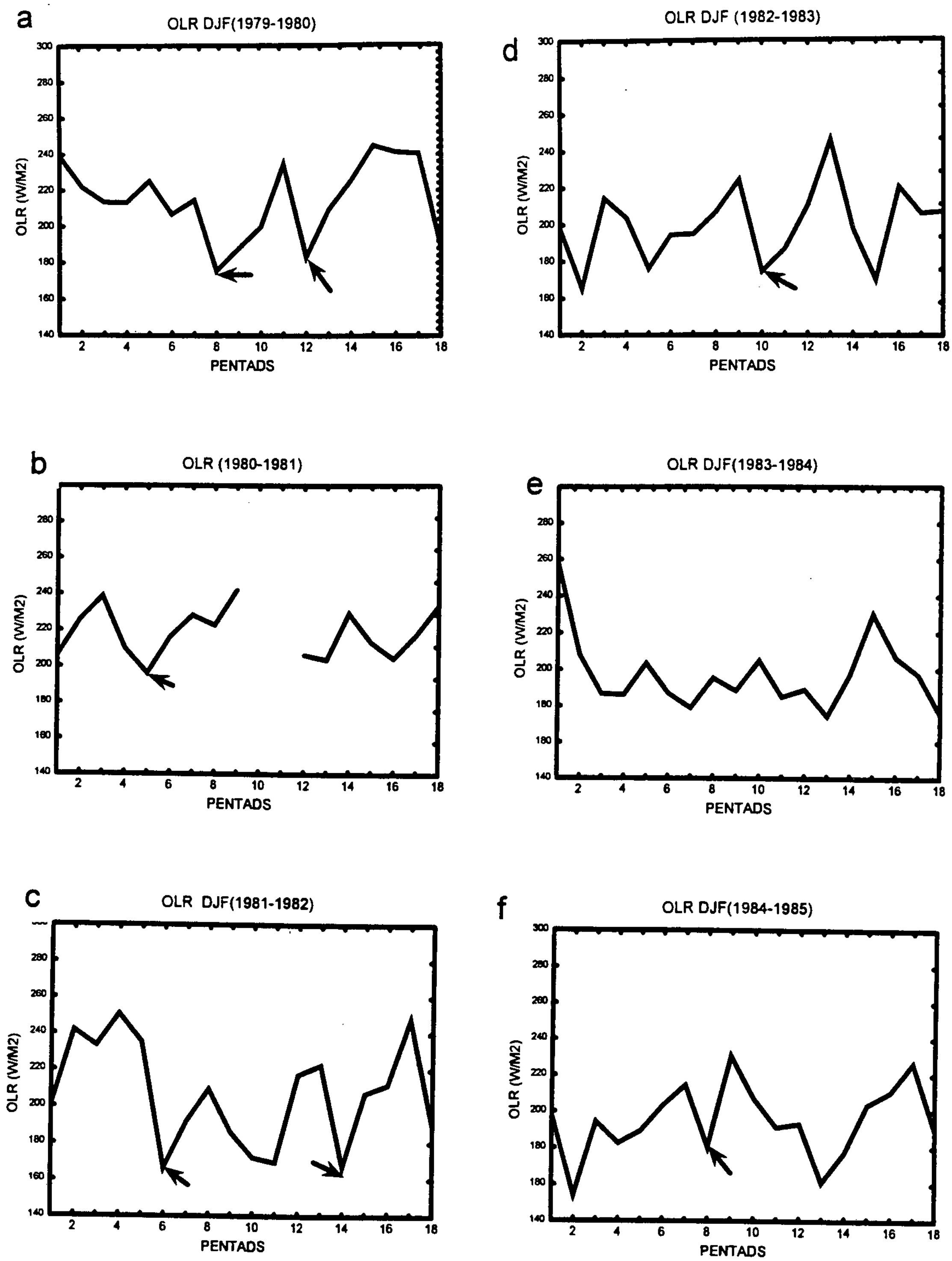

Figure 3.1: Time series of pentad OLR (W m $^{-2}$) for Dec-Feb. for 1979/80 to 1993/94. Selected P0 cases for compositing are indicated by arrows. In this diagram pentad 68 to

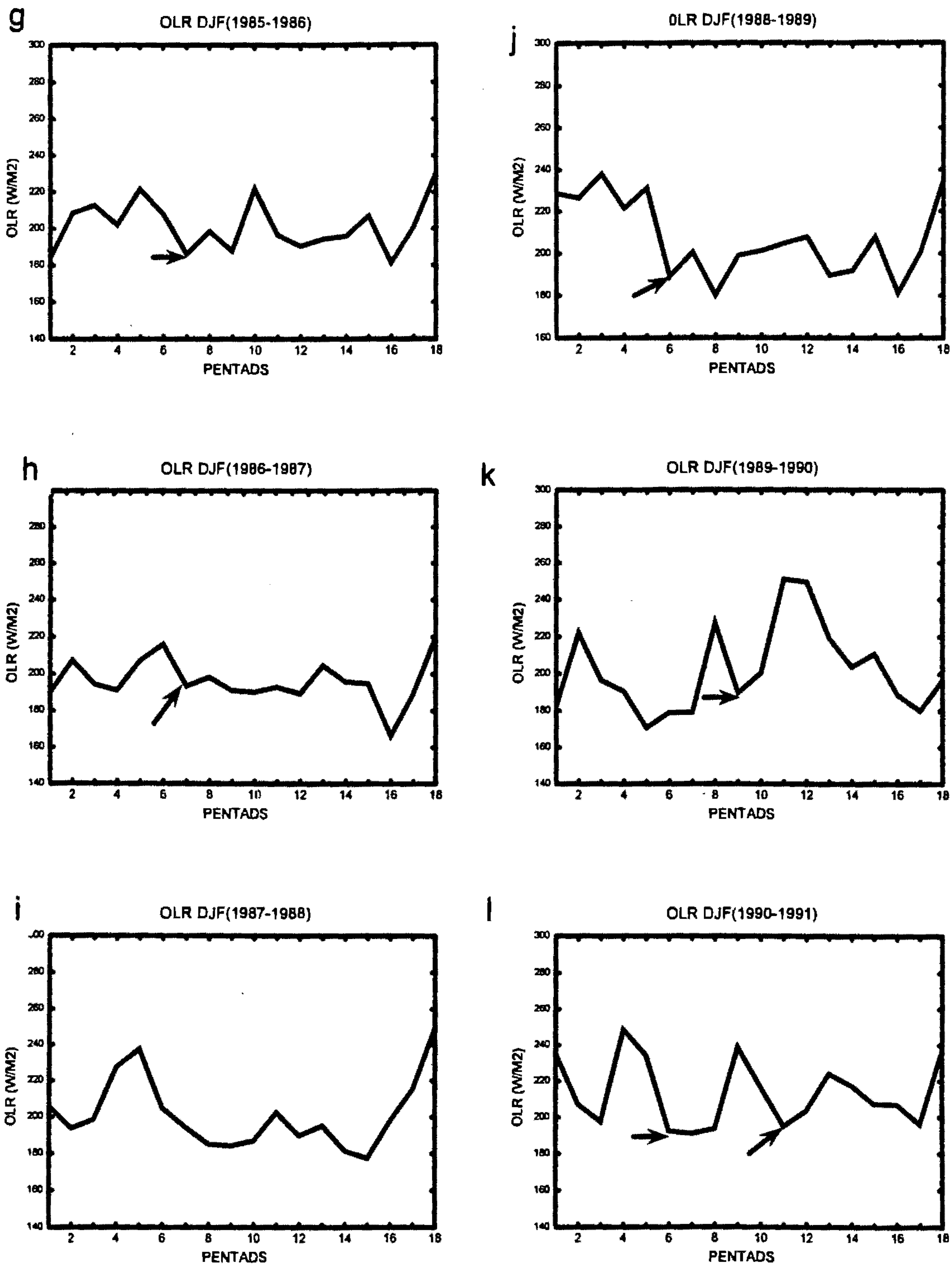

Figure 3.1 Continued: pentad 12 are represented by 1 to 18.

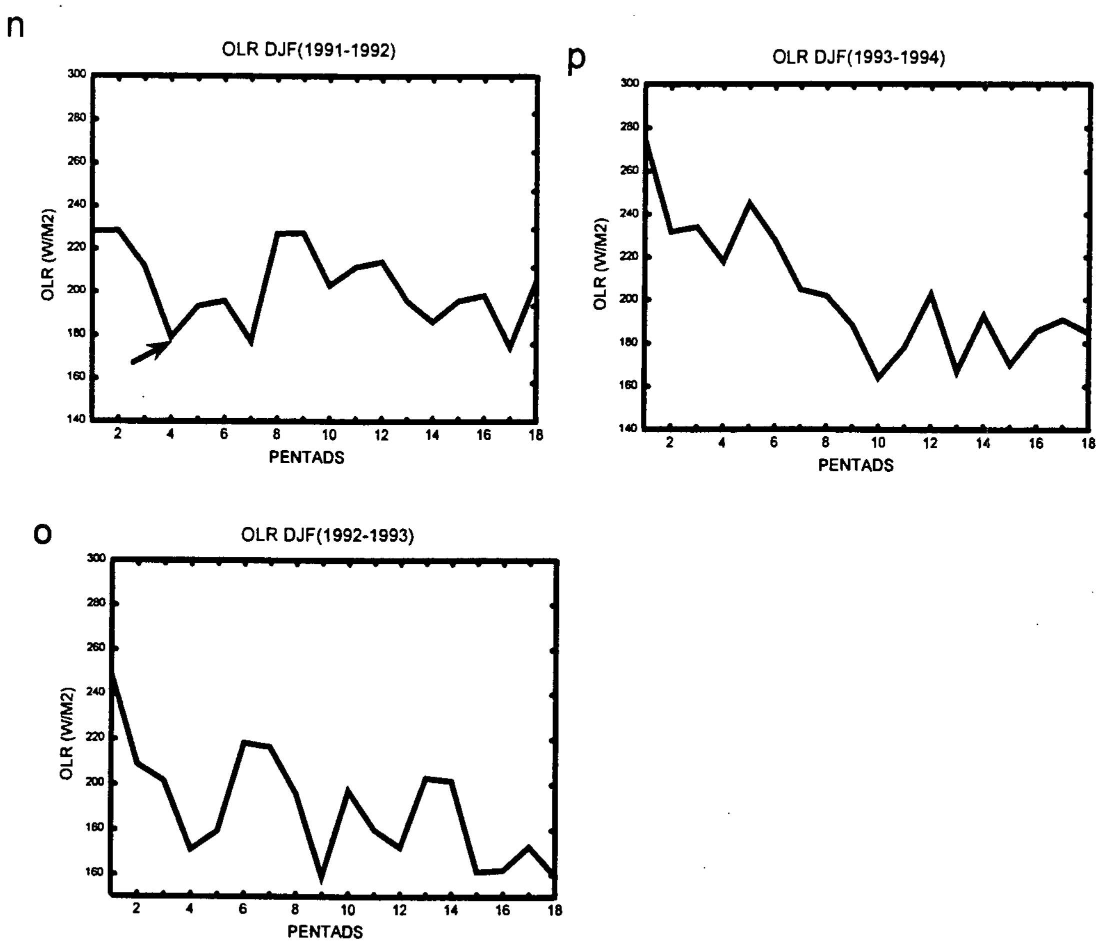

Figure 3.1: Continued

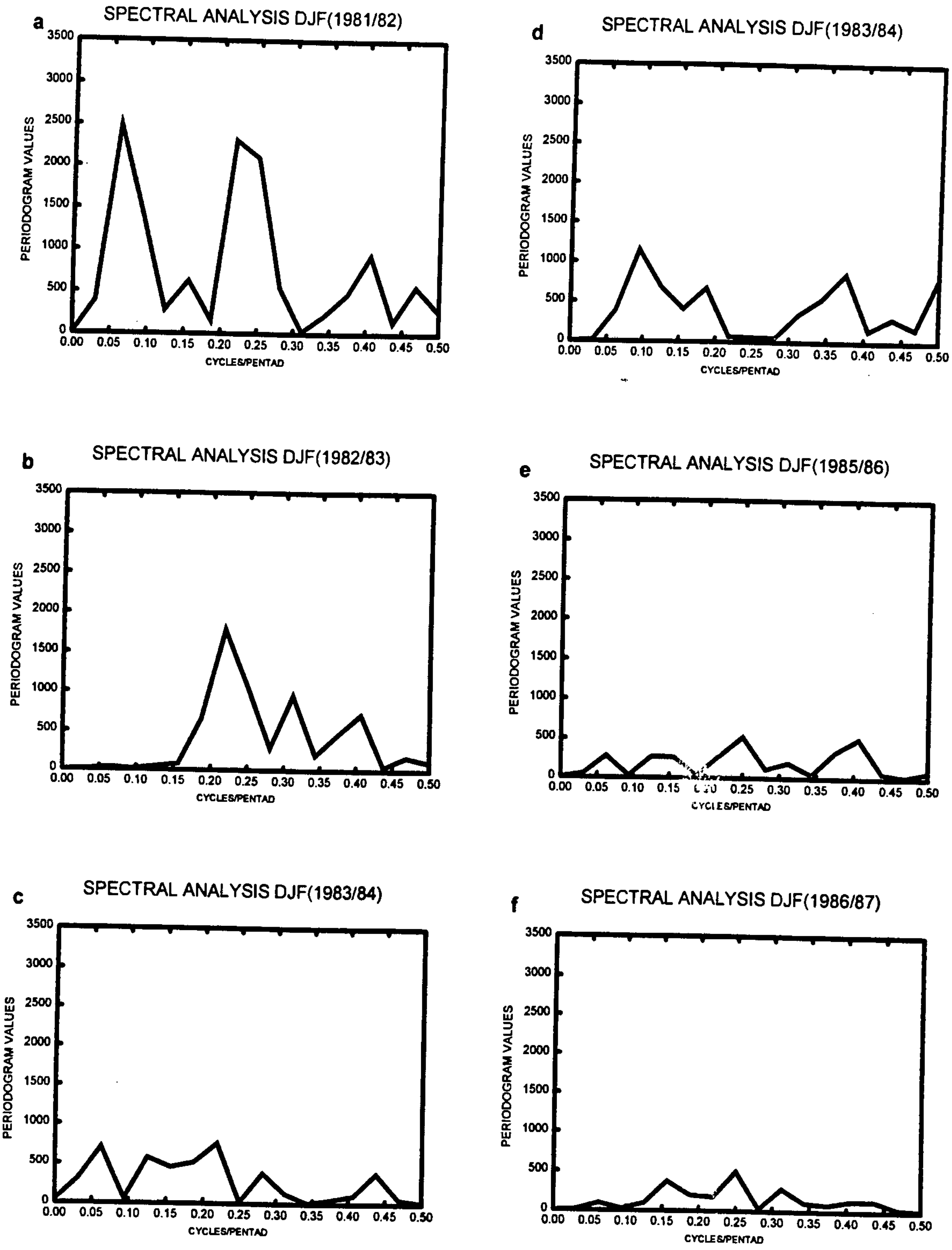

Figure 3.2: Periodogram Analysis of pentad OLR index over southwestern Tanzania for DJF seasons (18pentads) from 1981/82 to 1993/94 (1980/81season not included

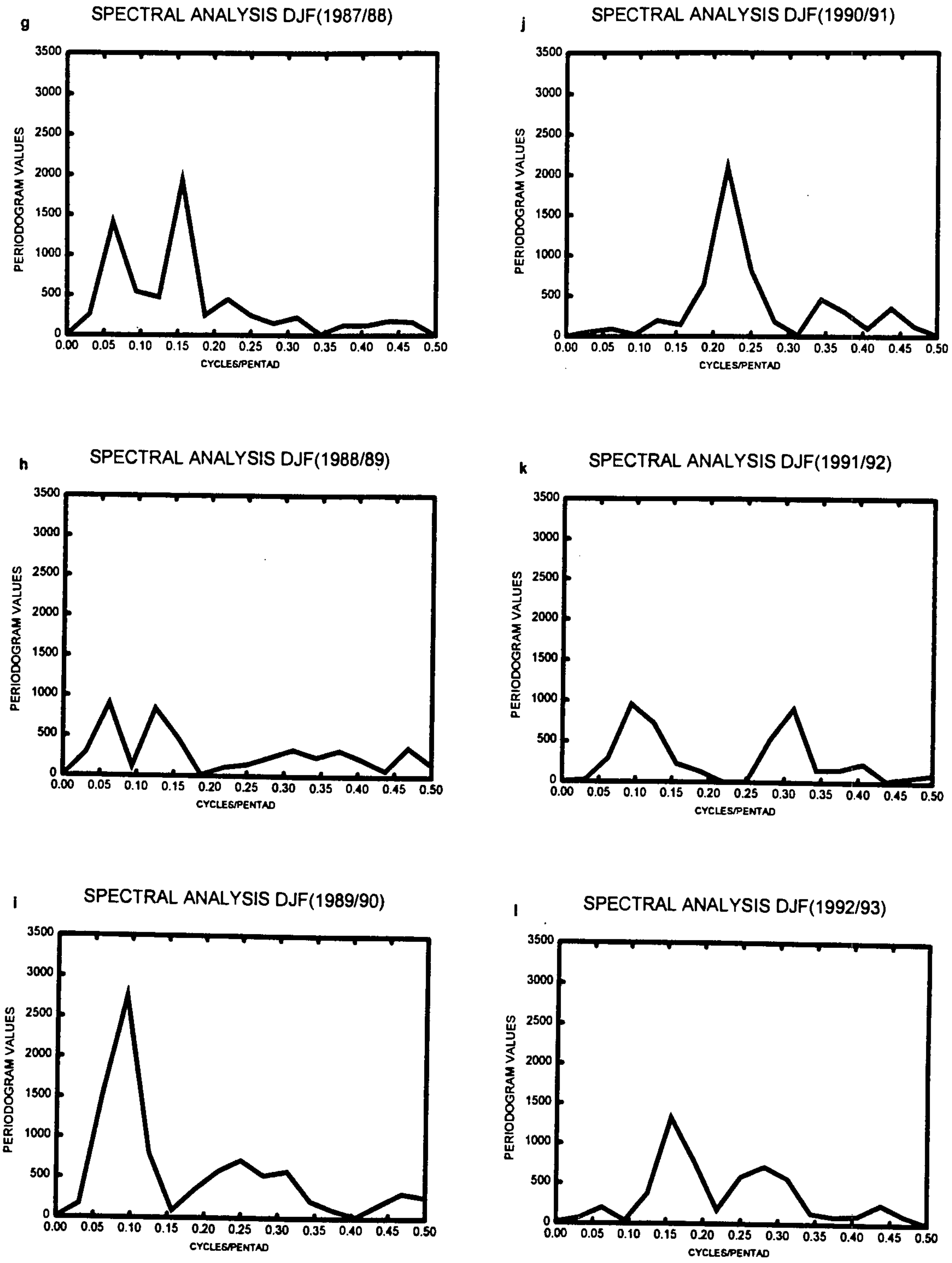

Figure 3.2 Continued: because of missing pentad 4 and 5 of 1981)

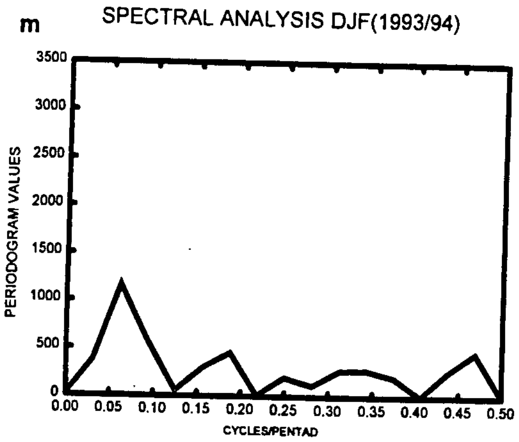

Figure 3.2 Continued:

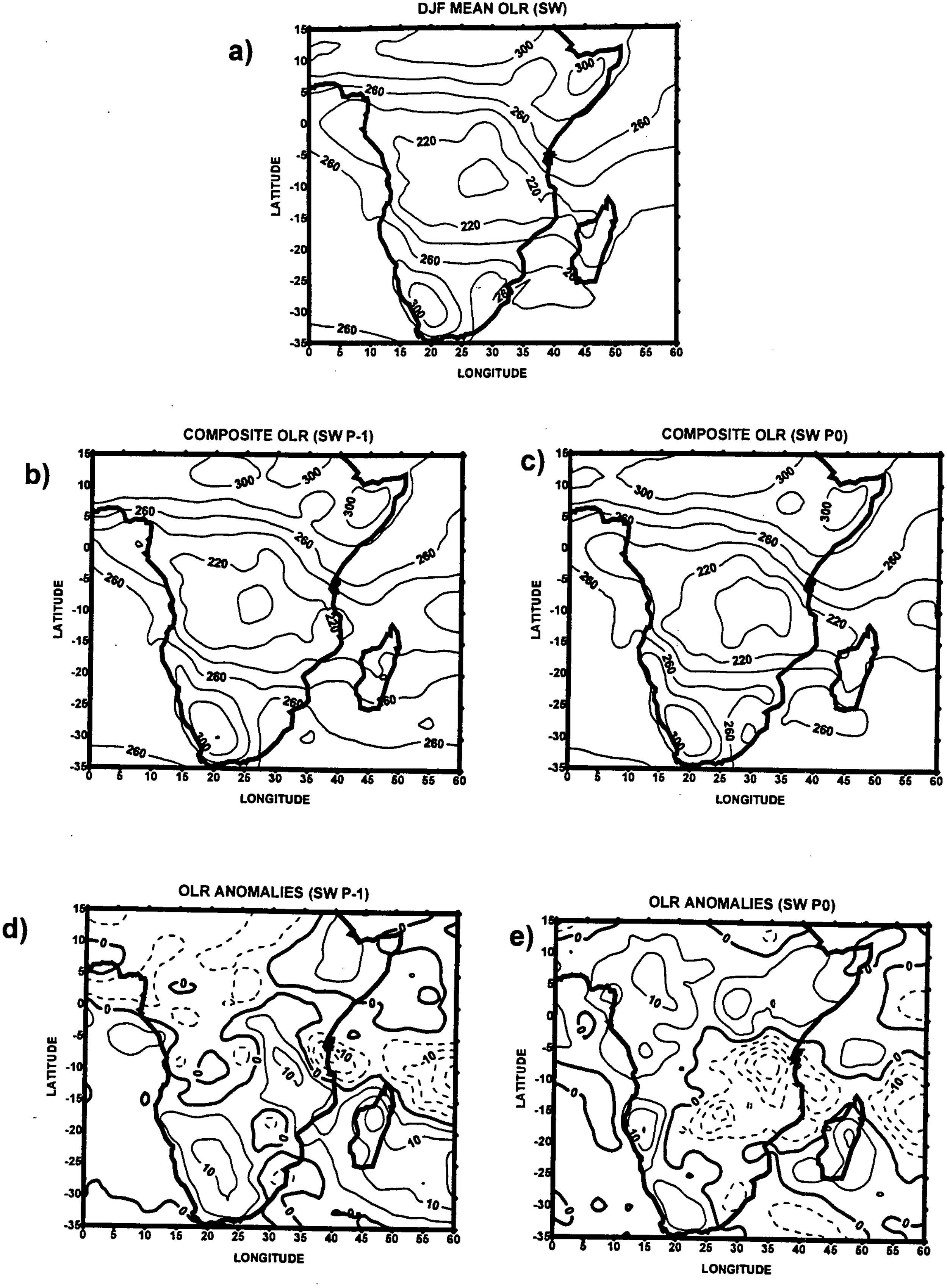

Figure 3.3: (a) DJF OLR mean; (b and c) mean composite OLR values for P-1 and P0 contour interval 20 W m^{-2}.; (d and e) OLR composite anomaly contour interval 10 W m^{-2}

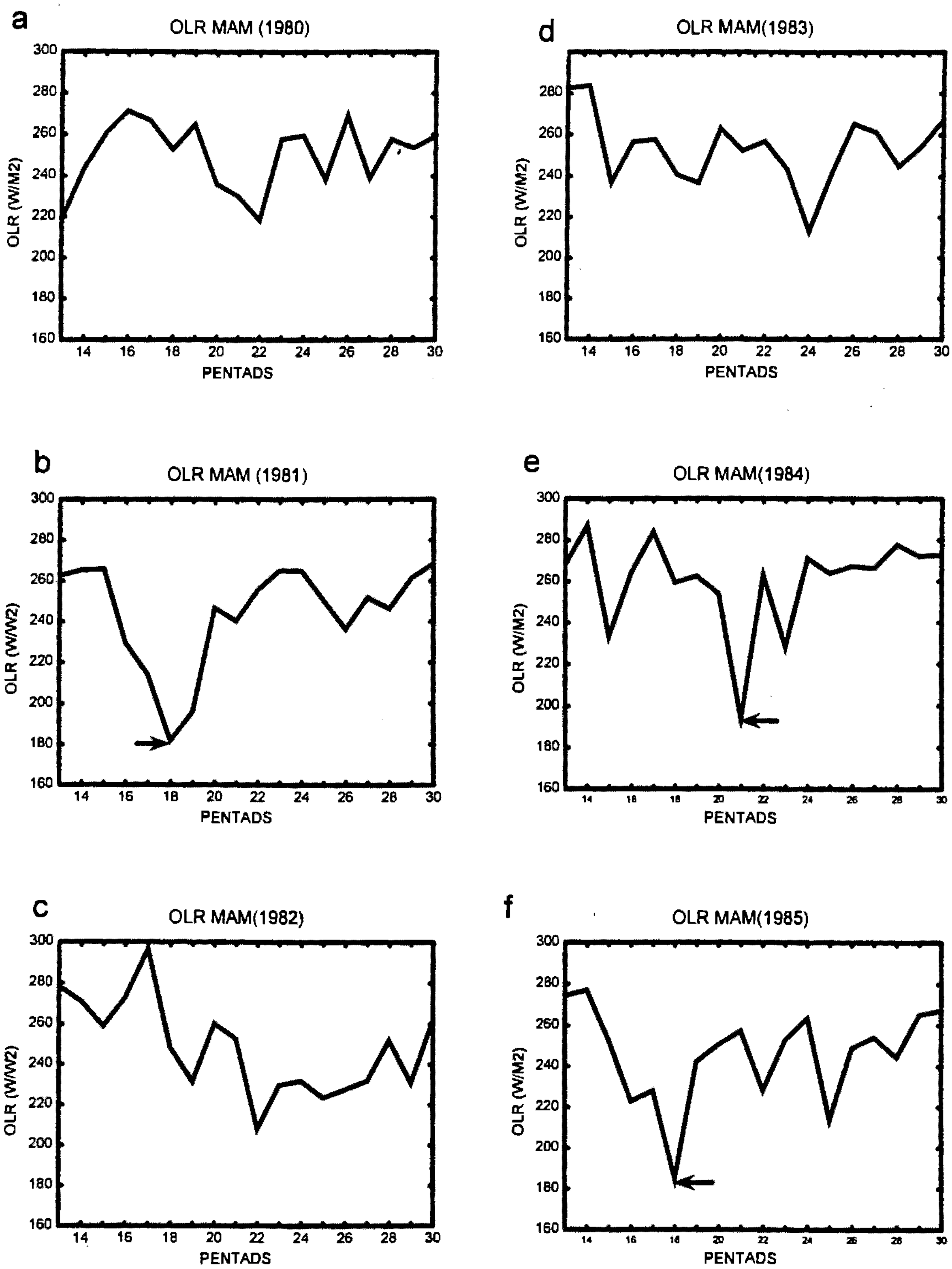

Figure 3.4: Time series of pentad OLR (W m $^{-2}$) for Mar-May for 1980-1994. selected P0 (Active convection) cases for compositing are indicated by arrows.

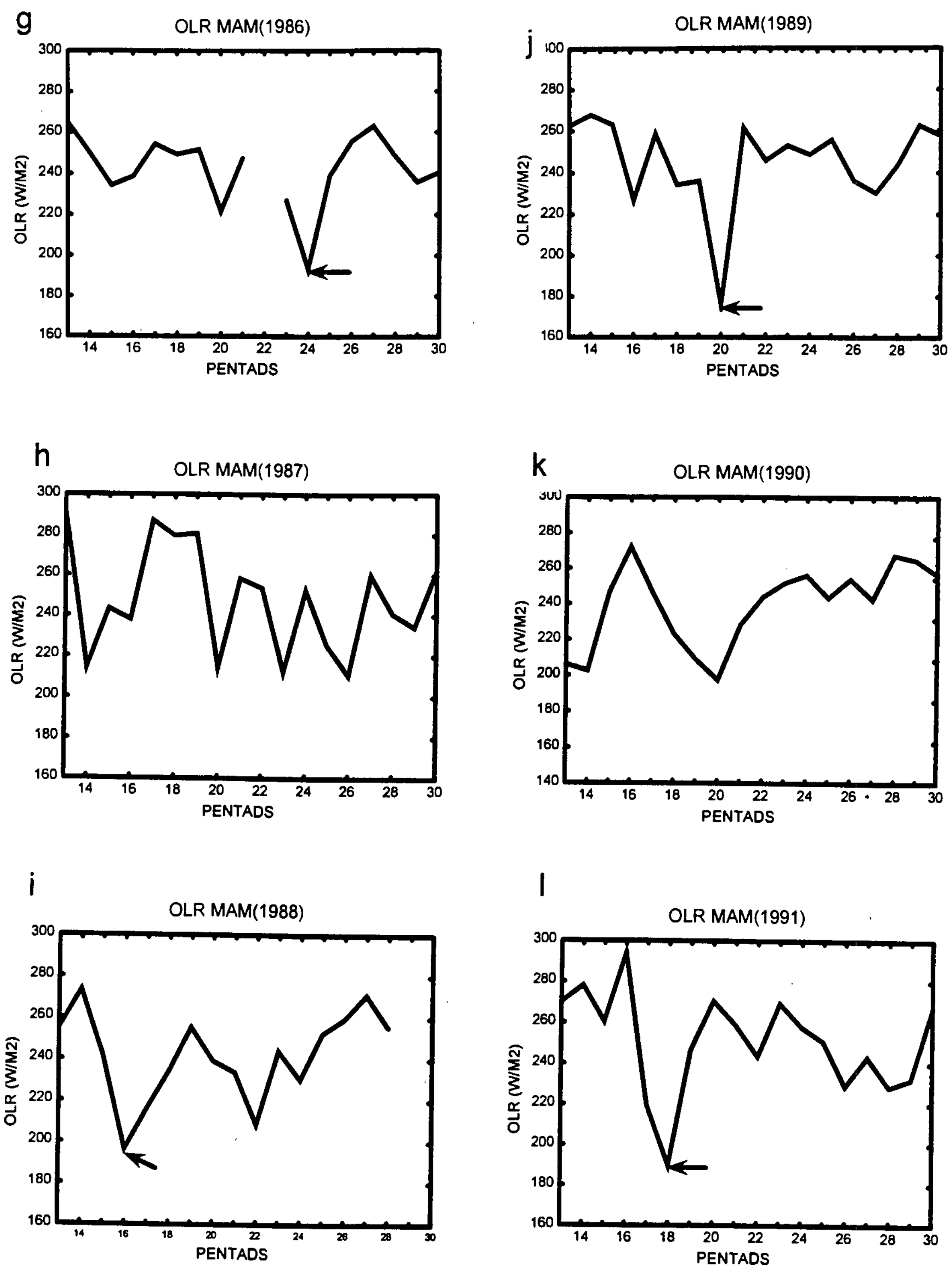

Figure 3.4 Contd:

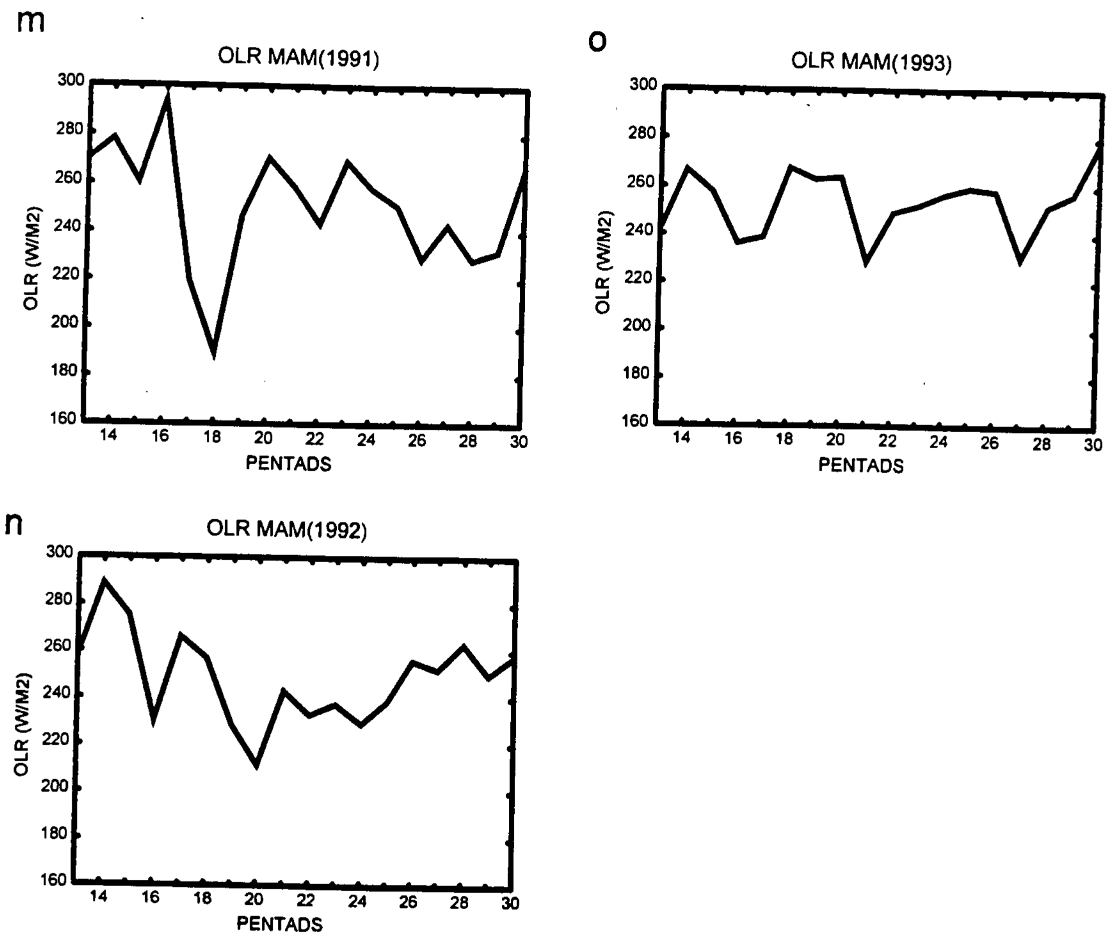

Figure 3.4 Continued:

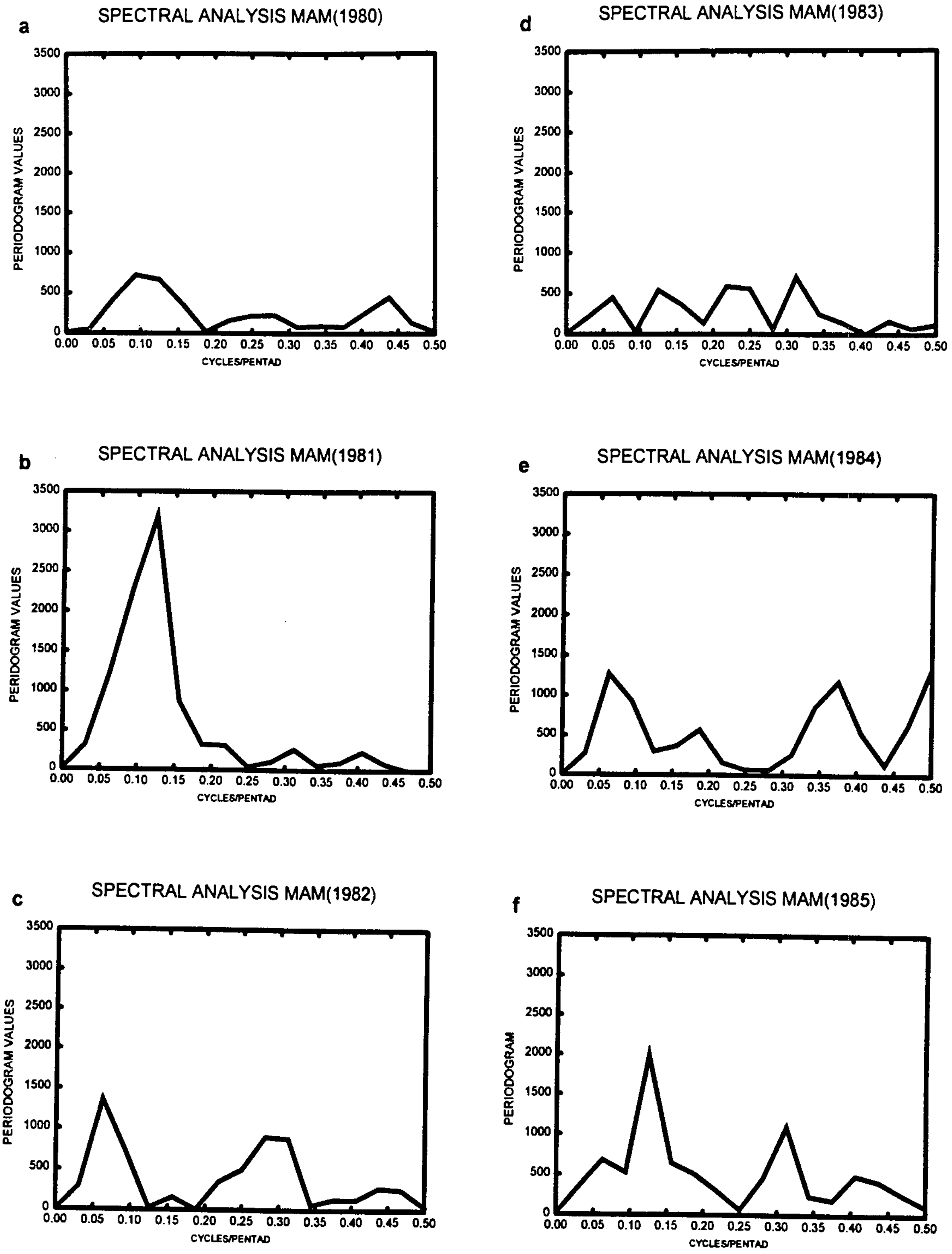

Figure 3.5: Periodogram Analysis of pentad OLR index over Northeastern Tanzania for MAM seasons for 1980 to 1993 (1986 and 1988 not included because of missing data)

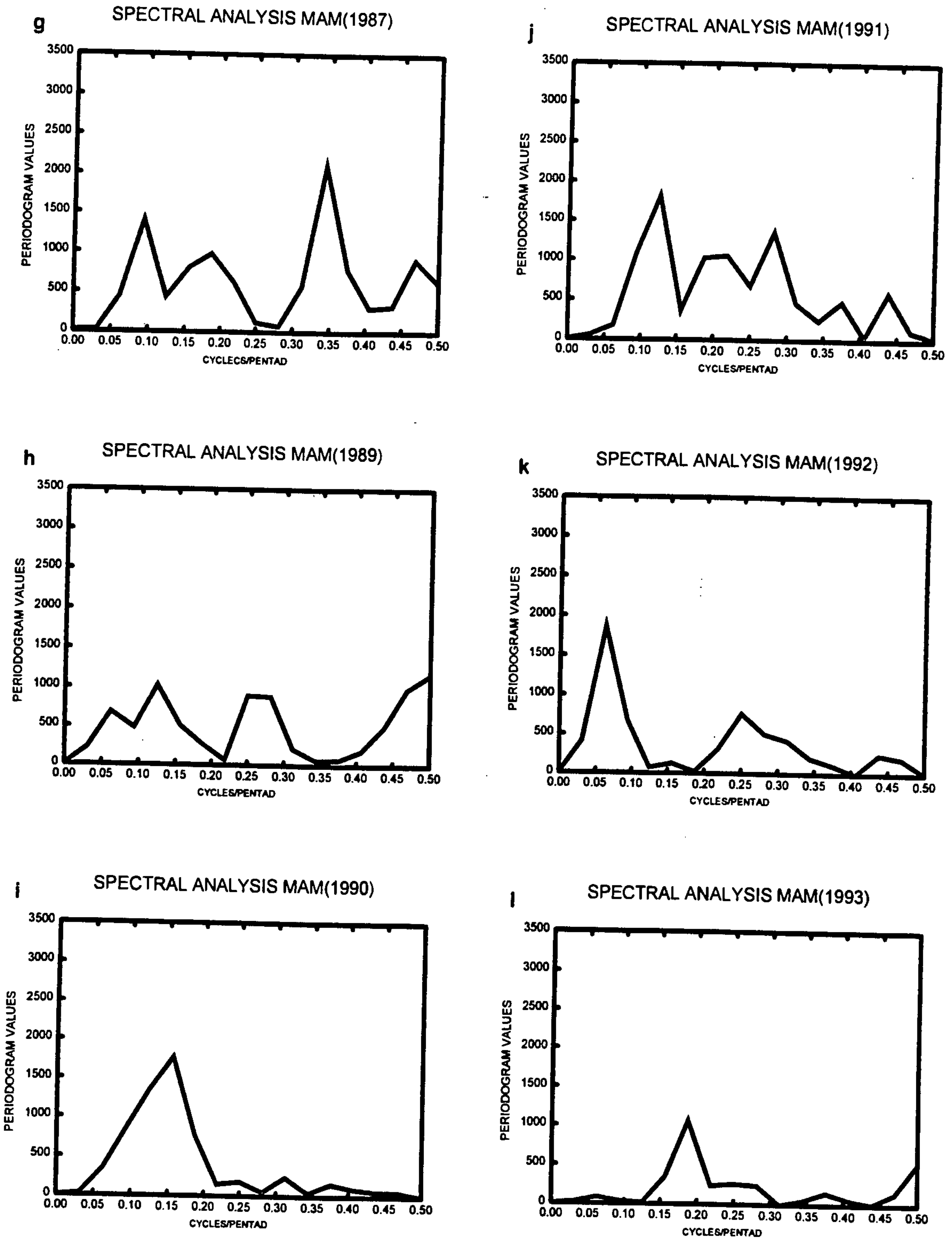

Figure 3.5 Continued:

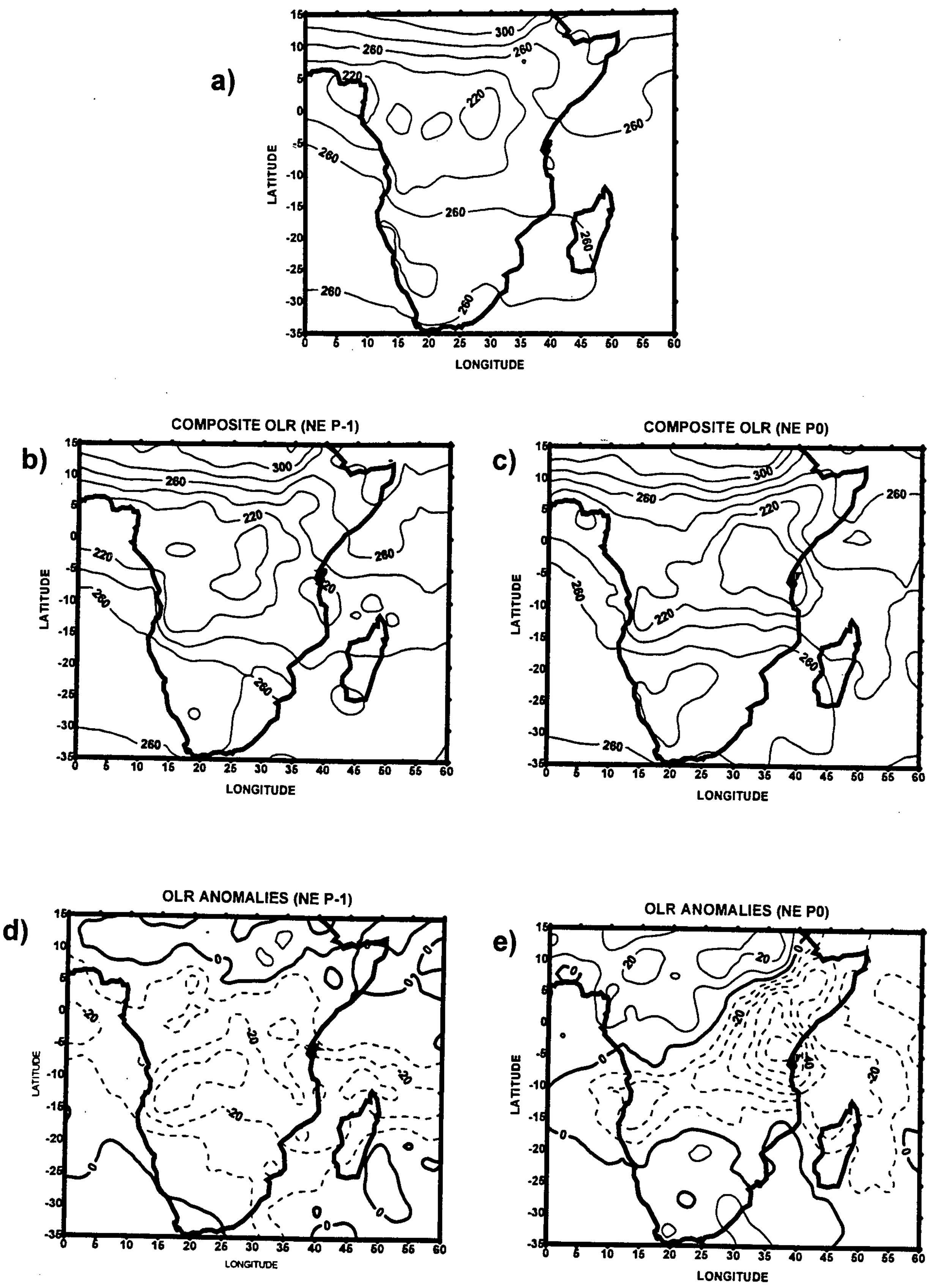

Fig. 3.6: (a) MAM OLR mean (b and c) mean composite OLR for P-1 and P0 contour interval 20 W m^{-2} (d and e) OLR composite anomaly for P-1 and P0, contour interval 10 W m^{-2}

CHAPTER 4

DYNAMICS OF THE PENTAD CONVECTIVE SEQUENCE: SOUTHWESTERN AREA

4.0 Introduction

Chapter 3 demonstrated convective variability, inferred from the selected OLR indices for southwestern and northeastern areas. It was revealed that there were dominant spectral peaks in the 2-8 pentad range. The purpose of this chapter is to analyse and the underlying kinematics and thermodynamic features associated with the convective oscillations, over the southwestern area of Tanzania. Comparisons of with those observed elsewhere will be discussed.

4.1 Seasonal mean analysis for DJF

In this section seasonal mean structures for various fields are analysed and used as a background in understanding evolution of composite anomalies of wet spells. The seasonal means are calculated for the period December-February, (DJF), 1980-1994 in the domain 15°N-35°S, 0°-60°E. The mean is based on 126 pentads.

4.1.1 Geopotential Heights at 850 hPa and 200 hPa

Geopotential heights at 850 hPa level in figure 4.0a reveal the mean position of the ITCZ in austral summer. Relatively low geopotential heights over southern Africa separate the Atlantic and the Indian Ocean anticyclones. The Indian

Ocean anticyclone is farther to the East and extends a weak ridge towards southern Africa. Over the central part of the continent a low pressure system is revealed oriented in the northeast-southwest direction; the meridional part of the ITCZ commonly known as ZAB (Zaire Air Boundary, Mason, 1993). A low pressure cell over the Indian Ocean and Madagascar indicates the mean position of the ITCZ over the Indian Ocean, similar to results obtained by Jury et al., (1994); Nassor, (1994) and others. The northeastern part of eastern Africa is dominated by the Arabian ridge, a common feature during the northern winter season. At 200 hPa, figure 4.0b, an anticyclone lies over southern Africa with its zonal ridge axis along about 15°S.

4.1.2 Water Vapour Flux and Wind Flow pattern at 200 hPa

The DJF mean integrated WVF between the surface and 500 hPa, figure 4.1a, indicates the source of water vapour during the season. The parameter is used because it can show the horizontal wind flow at low levels as well as the amount of water vapour contained in the wind flow. During DJF moisture supply over Africa seems to be mainly from the southern and northern Indian Ocean. The shallow Angola low draws water vapour from both the easterly winds, in the 22°-30°S latitude band, over the southern Indian Ocean and the northeasterly monsoon from the northern Indian Ocean. The ITCZ is indicated by the converging northeasterlies and southeasterlies over southern Africa, and northwesterlies and easterlies over Madagascar. Very little water vapour is contributed from the Atlantic Ocean.

At 200 hPa level (figure 4.1b) an anticyclone with its shear line along about 17°S is revealed. South of 20°S the flow is mainly westerly with a slight troughing along 45°E while over the continent North of 10°S there is a cross-equatorial flow. An anticyclone is revealed in the North centred at about 40°E, 7.5°N.

Figure 4.1c show the north-south vertical cross-section of u-components, along 32.5°E. The tropical belt between 7°N and 15°S is dominated by easterly winds with speed increasing with height. Easterly winds with speed above 8 m s^{-1} are indicated at 200-100 hPa levels. Easterlies are also revealed below 800 hPa between 18°-32°S. In the North, westerlies are revealed starting at 800 hPa increasing in wind speed and expanding northward with height. Maximum speeds of about 16 m s^{-1} are located at about 200 hPa and then decreasing above it. In the South, westerlies are revealed starting at about 700 hPa level. The westerly wind belt expands northwards and increasing in wind speed with height reaching maximum speed of above 26 m s^{-1} at about 200 hPa. This is the mean position of the sub-tropical jet stream in summer. Figure 4.1d presents the north-south vertical cross-section of the meridional wind components along 32.5°E. Between 15°N and 12°S a baroclinic pattern is revealed while between

12°S and 27°S a barotropic pattern is indicated. The line which separates northerlies and southerlies at the 1000 hPa level suggests the mean position of the ITCZ during the DJF period.

Mean east-west vertical cross-section of u- and v-components along 7.5°S are presented in figure 4.1e and 4.1f respectively. Figure 4.1e reveals positive values of u-component (westerly) below 800 hPa, from 10°E to 25°E; and below 600 hPa, from 50°E to 60°E. The rest of the troposphere is occupied by negative values (easterly) with maximum speed of about 9 m s^{-1} at 200 hPa level. It is noteworthy that between 10°E and 25°E there is a strong easterly component at higher levels and westerly component at lower levels suggesting a baroclinic atmosphere there. This is the average latitude band where there is normally strong convection. Below 800 hPa level from 0° to 20°E, figure 4.1f reveals positive values (southerly) with maximum values over the Atlantic Ocean and above this section up to 100 hPa there are negative v-component values with maximum values of about 1.5 m s^{-1} and 2 m s^{-1} at 700 hPa and 200 hPa levels respectively. From 20° to 50°E, below 400 hPa level there are negative values up to -3 m s^{-1} at about 850 hPa level. Positive v-components are also located East of 50°E between 400 hPa and 850 hPa level with a core of high v-component values of about 1.5 m s^{-1} at 700 hPa. High positive v-component values of about 3 m s-1 at 200 hPa level, between 400 hPa and 100 hPa.

4.1.3 Divergence at 850 and 200 hPa

Figure 4.2 show the mean divergence pattern at 850 hPa and 200 hPa during DJF. At 850 hPa level negative values of about $-16\times10^{-6}\ s^{-1}$, $-8\times10^{-6}\ s^{-1}$ and $-12\times10^{-6}s^{-1}$ are located over Madagascar, East of South Africa, and Ethiopia respectively. Also over East Africa can be seen some negative divergence values. These partly reflect orographic effects. A band of negative (convergence) in the South, i.e. over Madagascar, North Mozambique, Malawi, Zambia, Zimbabwe, Angola and central Africa indicates the position of the ITCZ during southern summer and fits well with the converging winds in figure 4.1a. Positive values are shown over eastern and southern Africa and refers to diverging northeasterly flow over Eastern Africa and diverging southeasterly flow over southern Africa. At 200 hPa (figure 4.2b) the mean divergence pattern is the opposite to that at the 850 hPa level. Areas which were negative/positive at 850 hPa level are replaced with positive/negative values aloft. It is interesting to note that the ITCZ is well reflected at this level, all the way from the Indian Ocean to over the continent. High positive values of about $7\times10^{-6}s^{-1}$ are revealed over Madagascar.

4.1.4 Vorticity at 850 and 200 hPa

In the southern hemisphere negative values (cyclonic vorticity) are located over southern Madagascar and the Mozambique Channel, Angola and over the West coast of southern Africa, (figure 4.3a). Positive values (anticyclonic vorticity), in the southern hemisphere, matches areas covered by southern hemisphere anticyclones. In the northern hemisphere negative values (anticyclonic vorticity) are revealed over eastern Africa, and Libya. Positive values (cyclonic vorticity) are located over Ethiopia, Sudan, central and West Africa, areas which are covered by the low pressure system at 850 hPa level (figure 4.0a). The 200 hPa level vorticity pattern (figure 4.3b) shows positive values (anticyclonic vorticity) over southern Africa with maximum values of about $2x10^{-6}s^{-1}$ at about 15°S, 20E. Negative values (anticyclonic vorticity) are observed North of 5°S

4.1.5 Vertical Motion at 500 hPa

Figure 4.4a shows the mean DJF vertical motion pattern at 500 hPa. Negative values (indicating upward motion) covers most of the continent and Madagascar except the northwestern area, the horn of African and the adjacent northwestern Indian Ocean, the Arabian sea and central southern Africa. Positive values are also revealed over the Atlantic Ocean and the southern Indian Ocean. Large negative values over Madagascar, Ethiopia, East of southern Africa, Cameroon and East Africa are partly due to orographic influence and also to diurnal effects (15UT).

4.1.6 Precipitable water

Figure 4.4b shows precipitable water integrated from the surface to 300 hPa. The map shows high precipitable water, above 55 mm, mainly over the southern tropics. Lowest values of precipitable water are over the Sahara desert. Low values are also revealed over the area covered by the Arabian ridge over the horn of Africa.

4.1.7 Equivalent potential temperature:

Figure 4.5a and 4.5b presents the DJF mean EPT field at 850 hPa and 500 hPa levels respectively. High EPT value are located over Africa centred at about 25°E, 15°S at 850 hPa and at about 25°E, 10°S, at 500 hPa indicating a warm moist unstable area over the Congo basin. The mean position of the ITCZ over the Indian Ocean is revealed by the area bound by the 340°K and 336°K isoline at the 850 hPa and 500 hPa levels respectively. Similar results were obtained by Nassor, (1994). The meridional arm of the ITCZ is indicated by the northeastward penetration of high EPT values to northeastern Africa. Over West Africa high EPT values are confined to the North of equator because of cooler Atlantic Ocean surface waters which are partly due to Benguela upwelling.

The north-south vertical cross section, of equivalent potential temperature, figure 4.5d, along 32.5°E reveals warm moist unstable air between about 7°S and 15°S, which is the expected mean position of the ITCZ during southern summer season. Between 0° and about 20°S, EPT values decrease with height from 1000 hPa to about 700 hPa, indicating instability. From about 350 hPa to 100 hPa EPT values increase with height. Figure 4.5c presents the west-east vertical cross-section, along 7.5°S, of EPT. Low EPT values over the Atlantic Ocean in comparison with Indian Ocean are expected from sea surface temperatures. This shows that the Indian Ocean is more convectively mixed than the Atlantic Ocean along the latitude band. Between 12°E and 32°E it is revealed that there is warm moist unstable air. This does not come as a surprise as the zone is within the Congo basin which is often under deep convection. Equivalent potential temperature decreases with height starting at about 350 hPa level.

4.2 Composite and Anomaly Analysis

4.2.1 Geopotential Heights at 850 hPa and 200 hPa

Low geopotential height (compared to other locations at the same latitude) indicates the presence of a trough, normally associated with convection depending on moisture availability, while relatively high geopotential height indicates a ridge. The 850 hPa geopotential composites, figure 4.6a and 4.6b, reveals a low pressure system across Africa in a north-south orientation and two subtropical pressure centres, i.e. the Atlantic anticyclone or St. Helena high, and the Southwest Indian Ocean anticyclone, the Mascarene high. Also revealed is a low pressure system to the northeast of Madagascar with a trough axis along the 10°S latitude. It can be noted that the St Helena anticyclone intensifies in situ and shows little movement from P-1 to P0 while the Mascarene anticyclone shifts to the East thus relaxing the ridge over southern Africa. The area covered by the low pressure system over the continent of Africa is larger at P0 than at P-1 and has extended to the East with the 1500 gpm isoline shifting to the coast of East Africa at P0. Also at P0 the low over the Indian Ocean seem to have deepened and enlarged together with the trough over Madagascar.

Geopotential anomalies at 850 hPa level for P-1 and P0 are shown in figures 4.6c and 4.6d respectively. Figure 4.6c shows positive gpm anomaly values over the Atlantic Ocean and over the southern Indian Ocean with largest positive anomaly values of 16 gpm at about 30°S and 55°E. Negative anomaly values can be seen over the southern parts of South Africa and the South Atlantic Ocean, and to the northeast of Madagascar. At P0 (figure 4.6d), negative anomaly values can be seen over the Indian Ocean, East Africa, Central and southern Africa. A zero line can be seen across the continent in a southwest-northeast orientation.

At P-1 there is an upper anticyclone over southern Africa with its west-east axis ridge along about 12°S figure 4.6e-h. The area covered by the anticyclone shows a decrease in area to P0, as inferred by the area enclosed by the 12430 isoline in the two situations. There is an indication of a trough over the Mozambique Channel. The geopotential anomalies at 200 hPa for P-1 and P0 are shown in figures 4.6g and 4.6h respectively. The two maps shows negative gpm over the South of the continent and Madagascar but with more negative values covering Madagascar at P0. Positive gpm values occupy the Mozambique Channel and the eastern parts of the continent.

4.2.2 Water Vapour Flux and Wind Flow Pattern at 200 hPa

With sufficient moisture in the atmosphere, one mechanism which can initiate convection is wind convergence at low levels and wind divergence at upper levels. As suggested by Steiner, (1989); Chen and Tzeng, (1990) and many, others the combination of the dynamics and moisture fields results in a closer relationship to convection than either the wind convergence or moisture alone. We have analysed the WVF and 200 hPa level wind flow patterns to see whether converging and diverging circulations can be traced. The WVF represents lower levels and the 200 hPa represents upper flow.

Water vapour flux patterns are similar with the wind flow patterns at 850 hPa level (not shown). From figure 4.7a we see that water vapour from the Atlantic Ocean is not advected into the African continent. At pentad P-1 moisture is advected from the Indian Ocean towards Madagascar and into southern Africa. At this time water vapour is advected from the Arabian Sea and Indian Ocean to Eastern Africa by the Northeast Monsoon. Figure 4.7b shows some interesting features. During P0 we observe a well-organised cyclonic circulation over Angola which draws water vapour from the Indian and Atlantic Oceans. Also we observe a linear convergence of the North-east Monsoon to western Tanzania. In figure 4.7c we observe a strong anticyclonic water vapour flux anomaly over the Indian Ocean. Figure 4.7c shows us that water vapour anomaly is advected from North Madagascar across the continent in the 5°S-15°S latitude band to a cyclonic vortex over southern Africa. Figure 4.7d reveals westerly water vapour anomalies between 5°S and 15°S over central Africa and Tanzania. Over the Indian Ocean there is a cyclonic water vapour flux circulation anomaly East of Madagascar and a well organised anticyclonic circulation just North of Madagascar. In between, a strong westerly water vapour flux anomaly denies some moisture to the coast of Kenya and northern Tanzania. Over the Mozambique Channel we observe a cyclonic water vapour anomaly.

The composite flow pattern at 200 hPa level is basically the same for both P-1 and P0. The flow, within the tropics, over East Africa at P-1 is mainly easterly with an anticyclone to the South centred at about 15°S and 25°E, while during P0 the flow is more cross-equatorial, with stronger winds than at P-1. The anticyclone is centred at almost the same position at both P-1 and P0. The anomaly flow pattern at 200 hPa reveals a divergent flow during P0. At P-1 there is a trough covering southern Africa and an anticyclonic anomaly South of Madagascar. North of 20°S the flow anomalies are westerly. During P0 we find a cyclonic anomaly over Madagascar replacing an anticyclonic anomaly at P-1. Over Kenya and Uganda strong southeasterly anomalies are established. Also of interest during P0 is a ridge anomaly along 31°E, South of 2.5°S. This anomaly pattern suggests a diffluent flow at upper levels over the area of interest.

4.2.3 Divergence at 850 hPa and 200 hPa

At 850 hPa for both P-1 and P0, figure 4.8a and 4.8b, high negative values of divergence can be seen centred over northeastern Africa, eastern South Africa and Madagascar. The features can be associated with orography. But it is interesting to note that there are no big changes in the divergence patterns at P-1 and P0. A closer look at P0 reveals negative divergence values over southwestern Tanzania with a value $-2\text{x}10^{-6}$ s^{-1} not seen at P-1. The composite divergence field at 200 hPa level, for P-1 and P0 (figures 4.8c and 4.8f) shows some interesting patterns. Waves of negative and positive divergence values can be seen North of 5°N at P-1. Negative values over the Mozambique Channel at P-1 seem to have slightly fallen at P0 where central values of about $-4\text{x}10^{-6}$ s^{-1} can be seen at about 27°S and 40°E while high positive values seen over southeastern Africa have decreased in value and area coverage at P0. Generally it can be observed that at P-1 the area over southwestern Tanzania upper level convergence which suppresses convection. At P0 we see that the area is under positive divergence values, which induces convergence at low levels and hence upward motion leading to convection.

The divergence anomaly fields at 850 hPa, figures 4.8c and 4.8d, are unexpected. At both P-1 and P0 over the area of interest we see that positive divergence values dominate. It can be noted that positive values over Angola at P-1 shift northeastwards at P0 while positive divergence anomaly centres in the North increase in area coverage and value from P-1 to P0. Also it can be seen that positive divergence anomaly values over Madagascar shifts to the South and values become less positive. The divergence anomaly at 200 hPa, figures 4.8g and 4.8h, shows some interesting results. The positive/negative divergence wave pattern observed in the composite analysis can still be seen in the anomaly divergence field North of 5°N. Also in the South can be observed a similar wave pattern whereby the positive/negative wave pattern are northwest-southeast oriented. Negative divergence anomalies over Madagascar at P-1 penetrate into the continent covering northern Mozambique and some parts of Zimbabwe, while negative divergence anomalies covers South Africa and positive divergence anomalies occur to the North of it. At P-1 southwestern Tanzania area is covered with negative divergence anomalies while at P0 the same area is covered with positive divergence anomalies. This augurs well with what is happening at 850 hPa during the same period; upper level divergence is supported with low level convergence and hence convection.

4.2.4 Vorticity at 850 and 200 hPa

Figures 4.9a and b illustrate composite vorticity at 850 hPa for P-1 and P0 respectively. At P-1 relative cyclonic vorticity (negative values in the southern hemisphere) is located over southwestern Africa, Madagascar and to the northeast of Madagascar. Positive vorticity values are located over southern Atlantic and Indian Oceans and southeastern Africa. Also negative vorticity is observed over East Africa while positive vorticity is located over the Indian Ocean off the coast of East Africa. At P0 a similar pattern is revealed but more cyclonic vorticity is indicated over eastern Africa between 0° and 20°S. At 200 hPa level, (figures 4.9e and 4.9f), anticyclonic vorticity (negative in the northern hemisphere) is shown North of 5°S at both P-1 and P0 while in the South larger positive vorticity values, $2.5\text{x}10^{-6}\text{s}^{-1}$ are observed more so at P0 than P-1.

The vorticity anomaly at 850 hPa is illustrated in figures 4.9c and d, for P-1 and P0, respectively. More negative values are revealed, over southern Tanzania, Malawi, Zambia, and northern Mozambique, at P0 than P-1. Also stronger anticyclonc vorticity is seen at P0, over the Indian Ocean off the coast of East Africa than at P-1. Composite anomaly vorticity patterns at 200 hPa level for P-1 and P0 are presented in figures 4.9g and 4.9h. Figure 4.9g shows positive vorticity in the 5°-12° S latitude band and negative vorticity anomaly in the 15°-22°S latitude band. Large positive anomaly values, $1.2\text{x}10^{-6}\text{s}^{-1}$, are revealed over the southern Indian Ocean centred at about 45°E, 30°S. Figure 4.9h shows a northwest-southeast positive vorticity anomaly band from central Africa to the Indian Ocean. Large cyclonic vorticity is located over Madagascar while large positive vorticity are seen over southeastern Africa

4.2.5 Vertical wind motion at 500 hPa

Vertical motion was considered at 500 hPa level as this is the level where it is expected to be maximum. It can be observed that the vertical motion pattern, for the composites at P-1 and P0, figure 4.10a and 4.10b, takes the shape of the continent. The explanation behind this is that the values used are those at 12UT and as it should be expected vertical motion over land during this time is highest due to the solar heating of the atmosphere from below. Large negative values (upward motion) can be seen to be associated with high ground e.g. over northeastern Africa, southeastern Africa and northern Tanzania. These features are removed when seasonal mean values are subtracted from the composited values. Composite maps at P-1 and P0 show that Africa has negative values except over northwest areas i.e. the Sahara desert, where downward motion or subsidence dominates. At P-1 rising motion centres can be found over central Africa, Ethiopian and Eritrea, Coastal areas of East Africa and to the East of North Madagascar. At P0 the whole of East Africa is under upward motion. With upward motion as indicated, at P0, convective activity can be expected depending on the availability of moisture. The vertical motion anomaly patterns at 500 hPa are shown in figures 4.10c and d for P-1 and P0. At P-1 negative anomalies are revealed over the Congo basin, the coast of East Africa and to the northeast of Madagascar. At P0 negative anomalies cover some parts of Tanzania (the target area is also under vertical motion) and the southwest Indian Ocean.

4.2.6 Precipitable Water

Precipitable water is maximum within the tropics at both pentads P-1 and P0 as shown in figure 4.11a and 4.11b. At both pentads precipitable water decreases toward the Sahara desert. At P-1 we find maximum values centred at about 10°S and 25°E. Central values are greater than 60 mm, while at P0 the area of maximum precipitable water has shifted eastward, centred at about 12.5°S and 27.5°E with central values above 65 mm. Also we observe that at P0 there is also we observe that at P0 there is an area of maximum precipitable water above 55 mm in the Indian Ocean just northeast of Madagascar. High values of precipitable water are found within the ITCZ, as expected for this time of the year. Figures 4.11c and 4.11d shows precipitable water anomalies for P-1 and P0 respectively. Precipitable water anomaly analysis reveals that there is positive values extending from the Indian Ocean to the target region by P0, and negative precipitable water anomalies over Zaire, Angola, Namibia, South Africa and central South Indian Ocean at both P-1 and P0.

4.2.7 Equivalent Potential Temperature

EPT can be used to monitor atmospheric moisture content, mixing depth, and atmospheric stability as it is a quasi-conservative parameter. At 850 hPa, figures 4.12a and 4.12b, composite Equivalent Potential Temperature (EPT) pattern are similar at P-1 and P0 in which we find high values are basically in the southern tropics over the African continent (figures 412a and b). The significant EPT isoline is 350°K in both cases, centred approximately at about 12°S and 30°E. At 500 hPa, figures 4.12e and 4.12f, EPT patterns are slightly different from those at 850 hPa level. At this level we find two centres: one centre over the African continent and the other over the Indian Ocean along 10°S during pentad P-1 and about 12.5°S during pentad P0. An interesting observation at this level is that the area covered by the 338°K EPT isoline at P0 is more than that at pentad P-1. This indicates that there is more heat and moisture injected into the middle atmosphere and one possible mechanism which can bring this about is convection. Figure 4.12(c, d) and 4.12(g, h) reveals the horizontal equivalent potential temperature anomaly fields at 850 hPa and 500 hPa levels respectively at pentad P-1 and P0. At 850 hPa level, at P-1 (figure 4.12c) negative EPT anomaly values are located over the central South Indian Ocean, South Africa, Angola, Namibia and southern Zaire. Also negative anomaly values can be found over Ethiopia and Cameroon. Positive EPT anomaly values are located the over Atlantic Ocean North of 30°S, off the coast of Tanzania, Southeast southern and central Africa and the Mozambique

Channel. At P0 (figure 4.12d) the pattern has changed. An increase in EPT is revealed the over southwestern Indian Ocean, the Mozambique Channel, and southeastern Africa. Positive EPT anomalies are in the 10-15°S latitude band over the Atlantic Ocean. In the North, negative anomaly values can be found within the 5-10°N latitude band over Africa. More negative anomaly values are found over central Africa at P0 than at P-1, which indicates cooling there. Negative EPT anomalies can also be found over the eastern part of Madagascar. At 500 hPa level (figure 4.12g and 4.12h) interesting features are revealed. At P-1 negative EPT anomaly values are revealed over the whole southern hemisphere South of 10°S except the southern part of the Atlantic Ocean. Positive EPT anomaly values are found over the Indian Ocean North of 10°S, the horn of Africa and across Africa in the 5°N-5°S latitude band. At P0 positive EPT anomalies are found over Eastern Africa, Zambia, Malawi northern Zimbabwe and Mozambique the Indian Ocean North of 15°S and the horn of Africa. More negative EPT anomaly values are located over the Atlantic Ocean South of 7.5°S and Madagascar. This indicates a warming up of the mid-troposphere at P0 when compared to P-1. It can be suggested that the warming of the mid troposphere is brought about by the release of latent heat in cloud development during convection.

4.3 North-South vertical Sections

4.3.1 Zonal and Meridional components

The North-South vertical cross-section along 32.5°E from 15°N to 35°S shows that the zonal wind pattern is similar during pentad P-1 and P0 with few differences. During pentad P-1 (figure 4.13a) the zero line separating westerlies from easterlies is located at about 34°S, at the surface, and tilts towards the tropics with height as expected, while the zero line separating westerlies from easterlies during P0 is South of 35°S. The zone covered by easterlies is bigger during pentad P-1 than pentad P0. The core of strong westerlies seems to have pushed farther South at P0. The results are similar to the observation made by Hendon and Liebmann, (1990). The above patterns shows that the subtropics ridge-line shifts to the South, at the surface during P0. It is also observed that easterlies at 200 hPa strengthens during the same pentad. Figures 4.13e and 4.13f illustrate the composite vertical cross-sections along 32.5°E for P-1 and P0 respectively. One point to note is the northward shift of a convergence point between the northerlies and southerlies at the 1000 hPa level. The zero line which is at about 16°S at P-1 shifts to about 8°S at P0. Stronger southerlies are indicated at P0, in the south, than at P-1 at lower levels. Anomalies of v-components in the north-south vertical cross-sections are presented in figures 4.13g and 4.13h for P-1 and P0 respectively. The two figures do not show clear patterns. However relatively strong northerly anomalies are revealed over 30°S at the 200 hPa level at P-1 while relatively strong southerly anomalies are revealed over 5°N at 200 hPa level.

Figure 4.13c and 4.13d presents the north-south vertical section of u-component wind anomalies along longitude 32.5°E, the longitude dividing the target area. At P-1 (figure 4.13c) easterlies can be found between 850 hPa and 400 hPa and 15°N-20°S. South of 20°S from 850 hPa to 100 hPa and above 400 hPa between 10°N and 20°S westerly wind anomalies are found. At P0, figure 4.13d two interesting features are revealed. Easterly anomalies are established at 200 hPa over 2.5°N and 15°S while in the lower troposphere easterly anomalies are located below the 600 hPa level North of 10°S and also between 15°S and 25°S. The mid-troposphere between 15°N and 12.5°S which was occupied by easterly anomalies at P-1 is covered by westerly anomalies. Westerly anomalies aloft are less intense compared to P-1.

4.3.2 Equivalent Potential Temperature

The composite north-south vertical cross section along 32.5°E from 15°S to 35°S between 1000 hPa and 100 hPa indicates high values at about 11°S, at the surface (figures 4.14a and 4.14b). This is the expected position of the ITCZ during this time of the year. In the mid-troposphere, between 450 hPa and 650 hPa levels EPT increases towards 11°S from both North and south. Above 400 hPa the pattern is the same both during P-1 and P0 as EPT increases with height. It is important to note that during P-1 the EPT isoline goes up to 700 hPa, above 10°S while at P0 the isoline rises to about 700 hPa over the latitude. Anomaly analysis of the EPT vertical cross sections along 32° during P-1 and P0, figures 4.14c and 4.14d respectively, reveal some interesting results. At P-1, between 1000 hPa and 900 hPa levels there are negative EPT anomalies, between about 900 hPa and 600 hPa positive anomalies are located between 15°S and 30°S, while between 550 hPa and 300 hPa there are negative anomalies and positive anomalies aloft. During P0 higher positive EPT anomalies between 5°S and 15°S occupy the layer 850 hPa to about 400 hPa. This shows that there is high instability during P0, over the study area. High convection injects warm moist air into higher levels, whilst cooling occurs at low levels from precipitation.

4.4 East-West Cross Section

4.4.1 Zonal and Meridional Components along 7.5°S

The East-west vertical cross-section of zonal wind composites and anomalies are presented in figures 4.13(i-l). Figures 4.13i and 4.13l shows that easterlies dominates the upper levels at P-1 and P0 with relatively stronger easterlies at P0. At low levels westerly winds are located between 10° and 20°E, from 1000 hPa to 800 hPa level, and between 50°E and 60°E from 1000 hPa to 400 hPa level at P-1. An interesting feature at P0 is the expansion of westerlies which occurs between 10°E and 30°E and decrease in easterlies between 30°E and

50°E. Figure 4.13k and 4.13l reveals the vertical cross-sections of zonal wind anomalies. Westerly anomalies are depicted at upper levels and easterly anomalies at lower levels between 0° and 30° while westerlies are revealed between 40° and 60°E, at P-1. At P0 we see an expansion of westerlies at lower and middle levels with a decrease of westerlies and emergence of easterly wind anomalies at upper levels. Figures 4.13(m-p) represents the east-west vertical cross-section of meridional wind components. Figure 4.13m and 4.13n shows the composite east-west vertical cross-sections of the v-component at pentad P-1 and P0 respectively. At P-1 northerly wind components cover the whole troposphere above 850 hPa between longitude 0° and 20°E and below the 850 hPa level northerlies are revealed. Between 20°E and about 50°E northerlies are found from 850 hPa to 500 hPa, above which southerlies occur up to 100 hPa (Hadley overturning). Over the Indian Ocean between longitude 50°E and 60°E southerlies dominate from 850 hPa to 100 hPa. An interesting feature at P-1 is the westward tilt of southerlies with height. A core of maximum southerlies at 700 hPa and 200 hPa. Though, the same pattern is maintained at P0, wind speed changes are revealed. At 200 hPa stronger southerlies are noted while at 700 hPa there is a decrease in southerlies over the Indian Ocean, and an increase in northerlies at about 850 hPa along 40°E. The northerlies above 40°E are associated with the northwesterly monsoon wind at this time of the year.

East-west vertical sections of meridional wind component anomalies along 7.5°S are revealed in figures 4.13o and 4.13p at pentad P-1 and P0 respectively. At P-1 southerly anomalies prevail between 850 hPa and 780 hPa. Northerly anomalies dominate in the upper troposphere with the core of maximum at 200 hPa above 15°E. Southerly anomalies are found between 50°E and 60°E and they tilt to West with height up to about 300 hPa. Northerly anomalies are observed between 750 hPa and 500 hPa within longitude 0° and 30°E. At P0 northerly anomalies are established over the Indian Ocean between 1000 hPa and 650 hPa. At 200 hPa are revealed northerly anomalies between 0° and 35°E. The mid-troposphere is dominated by wind flow from the south.

4.4.2 Equivalent Potential Temperature along 7.5°S

Figure 4.14 reveals the east-west vertical sections of equivalent potential temperature along 7.5°S. Figure 4.14e and 4.14f which represent pentad P-1 and P0 show that that patterns are basically similar with high values below 700 hPa revealed between 20°E and 30°E. Also revealed are high equivalent potential temperature over the Indian Ocean in comparison with the Atlantic Ocean at both P-1 and P0; indicating that the lower troposphere over the Indian Ocean is warmer/moister than that over the Atlantic Ocean as expected. It is also noted that there is an eastward shift of the 335°K isoline at P0 when compared with the pattern at P-1. The anomaly east-west vertical section, figures 4.14g and 4.14h reveals an eastward shift of positive EPT anomalies and at the same time positive EPT anomalies penetrates into the upper troposphere up to about 350 hPa. Negative EPT anomalies are revealed at 200 hPa. The warming up of the mid-troposphere could be due to deep convection and the release of latent heat into the atmosphere.

4.5 Summary

The objective of this chapter was to identify the time evolution of kinematic and thermodynamic structures associated with deep convection and its precursor phase over the southwestern areas during the DJF season. This was achieved by analysing some meteorological parameters. The mean structures reveal similarities of the characteristics of rainfall over Tanzania during the season. Some interesting results are revealed in the time evolution composite analyses. Major findings are summarised as follows:

- With general geopotential height falls, at the 850 hPa level, over western Indian Ocean a west-east pressure gradient is created. It has also been revealed that low geopotential heights over the equatorial central Africa shift eastwards accompanied with low geopotential heights in mid-latitudes corresponding with OLR patterns observed in figure 3.3 (c and e). With this set-up moist warm unstable air, as indicated by high equivalent potential temperatures, from the Congo basin blows towards southwestern Tanzania during deep convection;
- Weakening of northeasterly WVF over the western Indian Ocean is accompanied by the establishment of a westerly WVF over the Congo basin

thus forming a convergence zone over the target region and surrounding areas. A westerly WVF anomaly is clearly indicated similar to westerly wind anomalies, at 850 hPa, observed by Rui and Wang, (1990) during a deep convection event;

- A baroclinic structure in the zonal winds is indicated in the east-west vertical cross-sections over the Congo basin in both composites and the DJF mean patterns;
- Though there is no indication of strong convergence at the 850 hPa level at P0 over the target area, it is clearly shown that there is strong divergence at the 200 hPa level suggesting convergence at low levels. This is also supported by well established vertical motion over southwesten areas;
- The EPT at 850 hPa and 500 hPa levels, and integrated preciptable water spatial patterns indicate an eastward shift of warm moist unstable air and precipitable water respectively from P-1 to P0.
- The north-south and west-east vertical sections reveals the expansion and strengthening of easterlies at 200 hPa level within the tropics at P0. The northward shift of the 0 isoline of the meridional wind component at low levels, in the north-south vertical cross-section from P-1 to P0 suggest that convective activities are also a contribution from the ITCZ. At low levels weak westerly winds are established over the target area, at P0. The N-S and W-E vertical cross section show that there is an increase of EPT values of about 1.5°K in the mid-levels and some EPT falls in the lower levels.

Kinematics and thermodynamic parameters analysed above have shown consistence in the coupling with convection shown in chapter 3. The analyses in this chapter have also shown that dynamic as well as the thermodynamic processes support cumulus convection. It has also been shown that the kinematics and thermodynamic features have supported cumulus convection as suggested by

Similar analyses will be performed in chapter 5 for the northeastern areas in order to identify kinematic and thermodynamic structures associated with deep convection during the MAM season

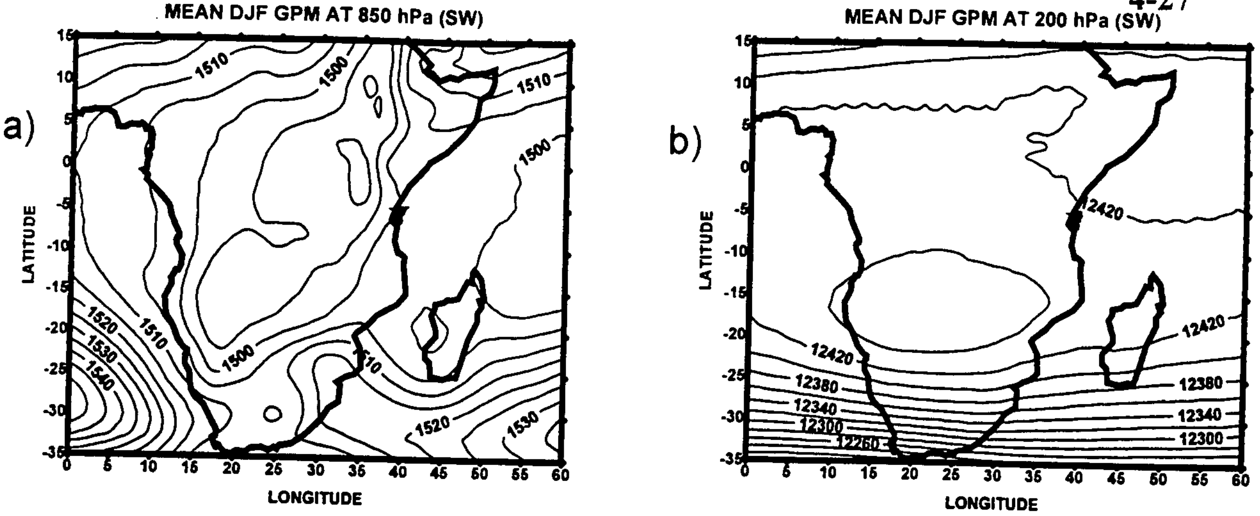

Fig. 4.0: (a) DJF mean geopotential height at 850 hPa, contour interval 5 gpm, (b) DJF mean geopotential height at 200 hPa, contour interval 20 gpm.

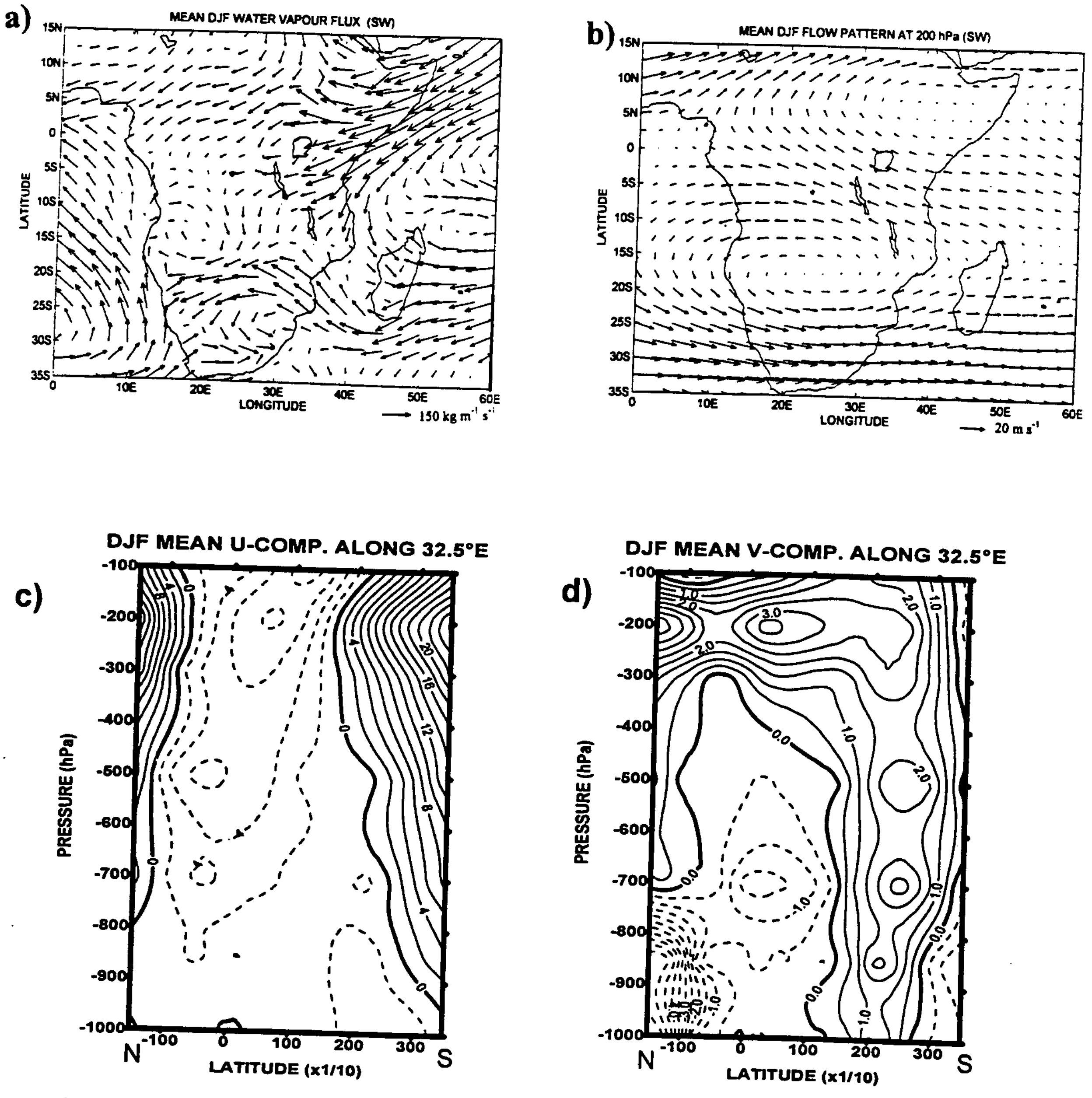

Figure 4.1: Mean DJF . a) WVF; b) wind flow pattern at 200 hPa; c) vertical section of u-comp along 32.5°E ; d) vertical section of v-component along 32.5°E

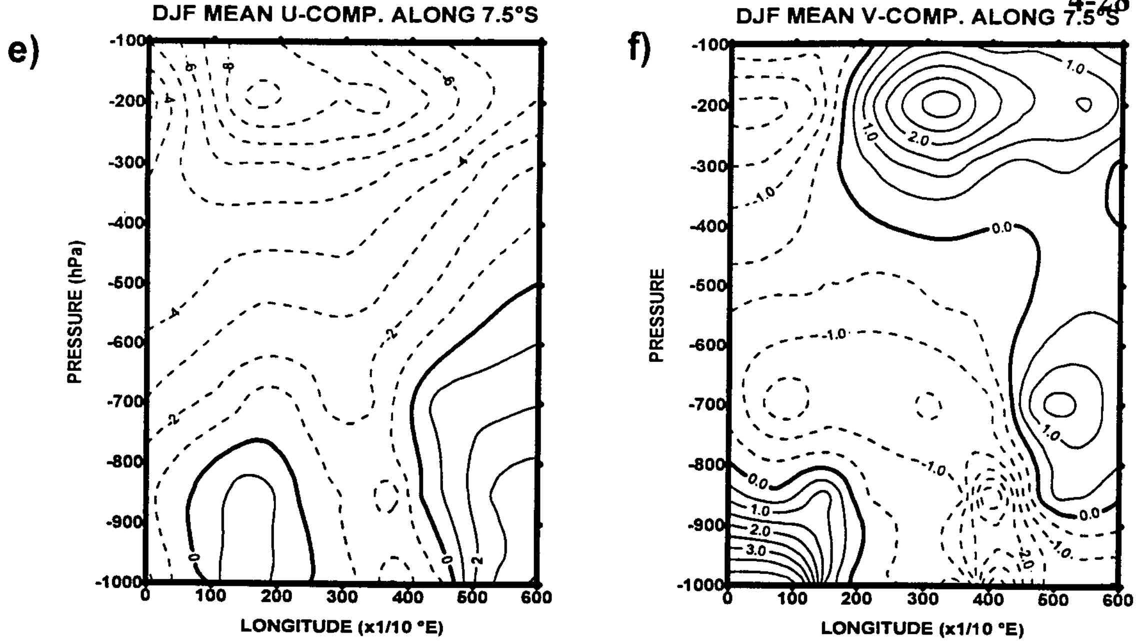

Figure 4.1 Continued: (e and f) vertical section of u-component along 7.5°S., contour interval 2 m/s; vertcal section of v-component along 7.5°S, contour interval .5 m/s

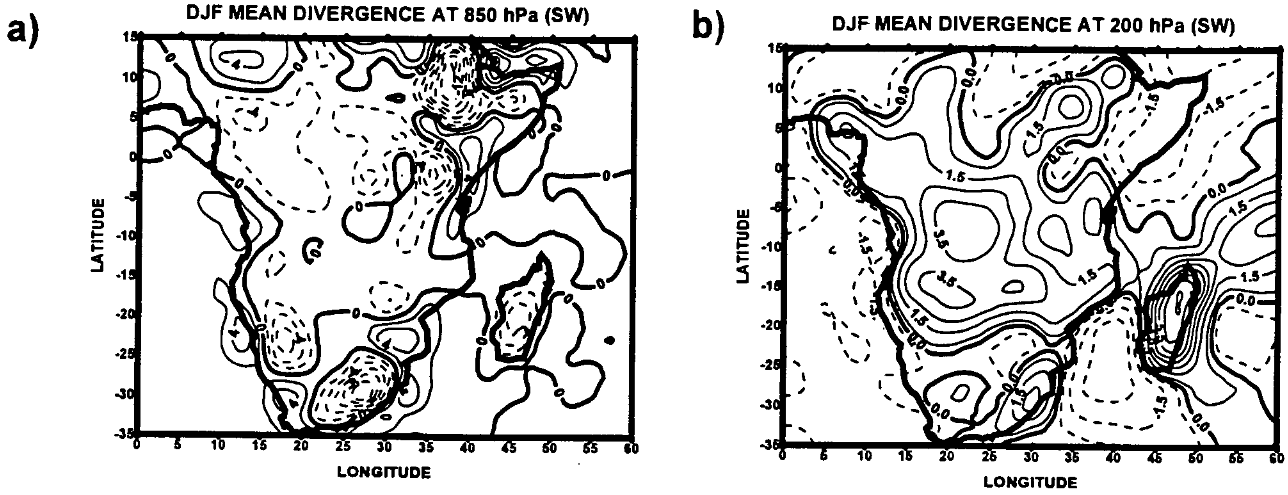

Figure 4.2 DJF mean divergence. a) at 850 hPa, conour interval 2 x 10-6 s-1; b) at 200 hPa, contour interval 1 x 10-6 s-1.

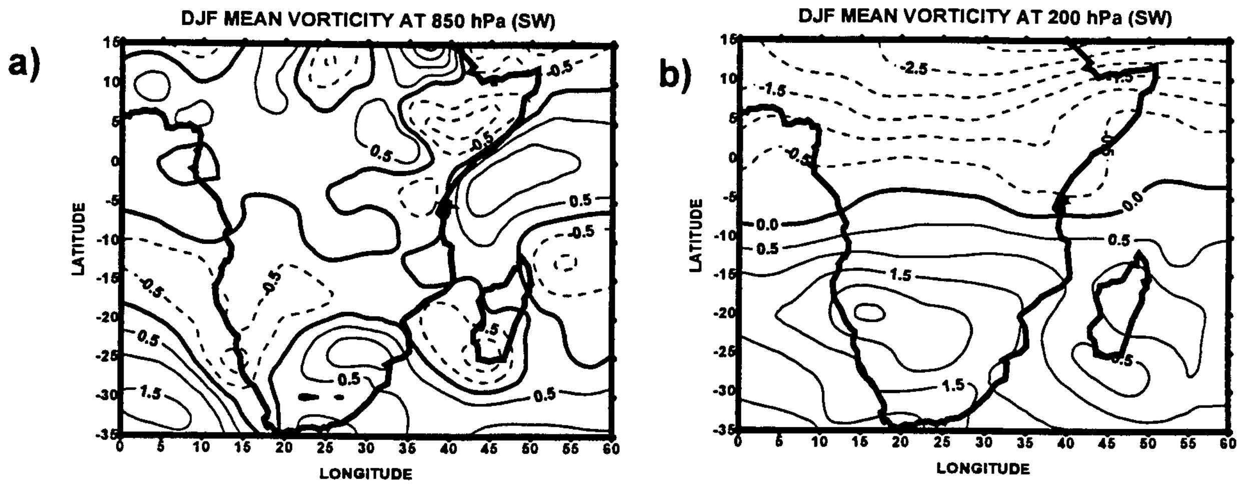

Figure 4.3: DJF mean vorticity. a) at 850 hPa; b) DJF mean vorticity at 200 hPa; contour interval $.5 \times 10^{-6}\ s^{-1}$

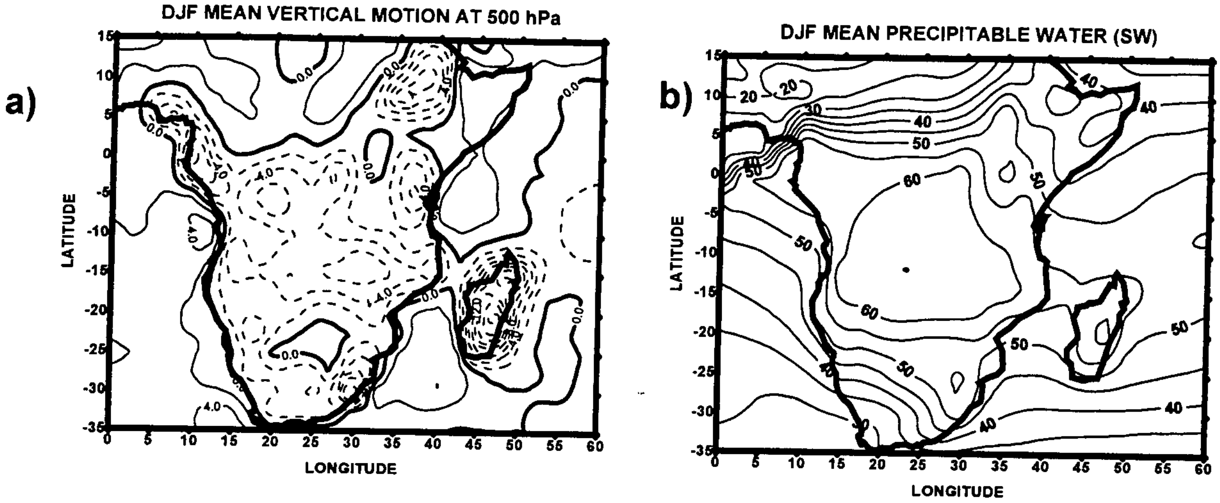

Fig. 4.4: DJF mean. a) vertical motion at 500 hPa, contour interval 2x1C^{-2}Pa/s; b) precipitable water integrated from the 1000 to 300 hPa, contour interval 5 mm.

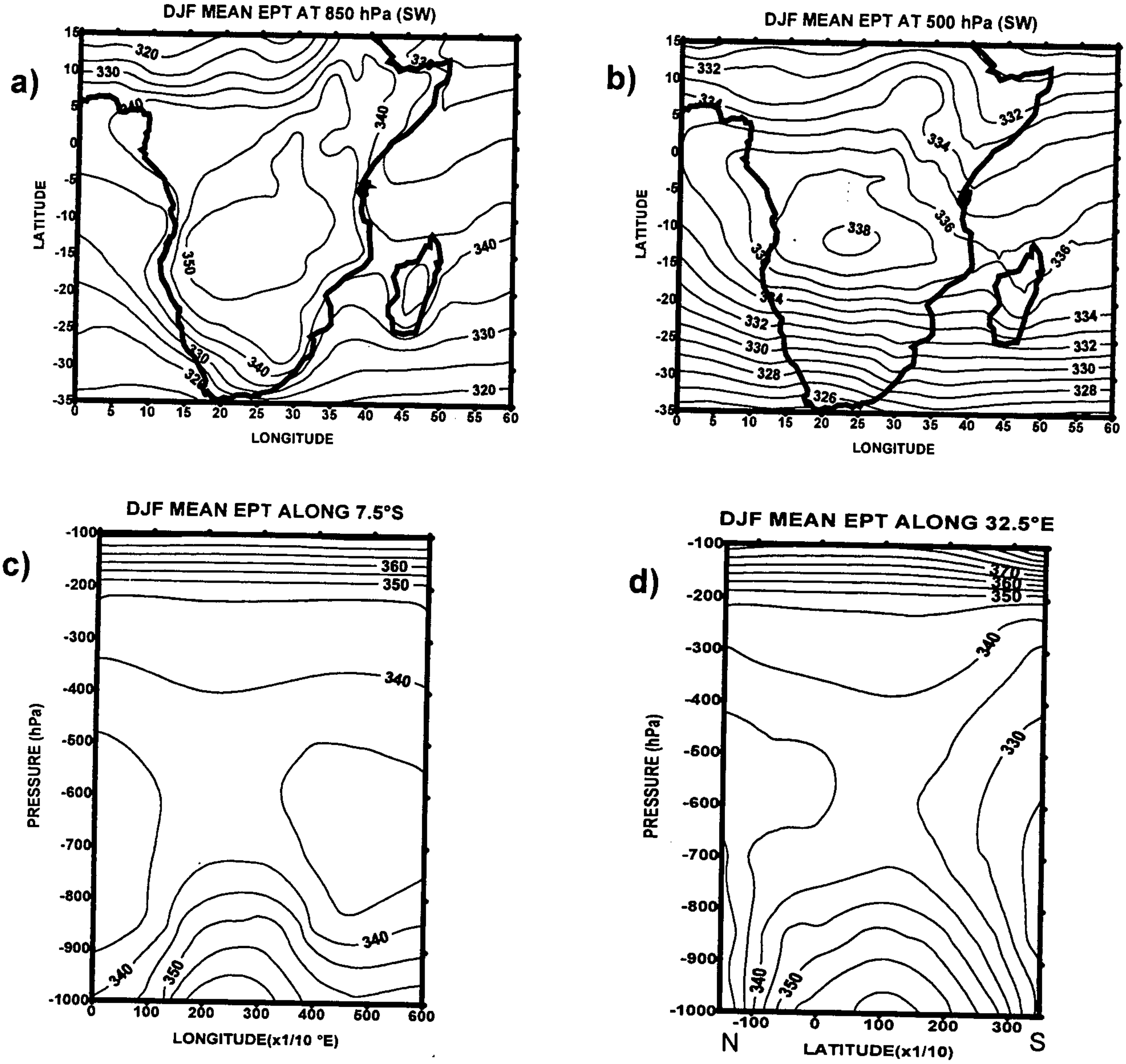

Fig. 4.5: a) DJF mean EPT at 850 hPa, contour interval 5°K; b) DJF mean EPT at 500 hPa, contour interval at 1°K; c) DJF mean EPT E-W vertical cross-section along 7.5°S; (d) DJF mean EPT N-S vertical cross-section along 32.5°E, contour interval 5°K.

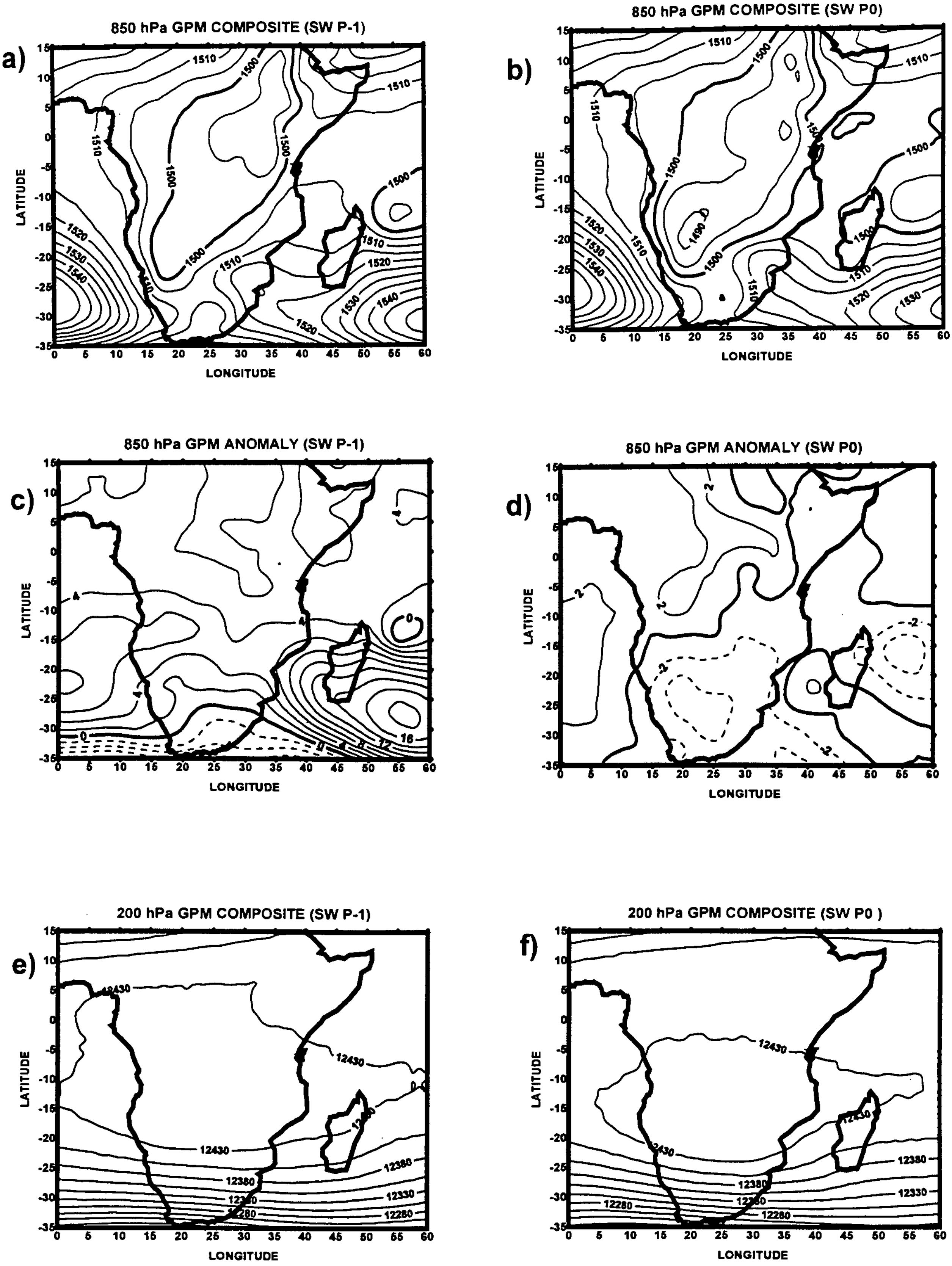

a) 850 hPa GPM COMPOSITE (SW P-1)

b) 850 hPa GPM COMPOSITE (SW P0)

c) 850 hPa GPM ANOMALY (SW P-1)

d) 850 hPa GPM ANOMALY (SW P0)

e) 200 hPa GPM COMPOSITE (SW P-1)

f) 200 hPa GPM COMPOSITE (SW P0)

Figure 4.6: Geopotential heights for P-1 to P0. (a and b) composites at 850 hPa, contour interval 5 gpm; (c and d) anomalies at 850 hPa, contour interval 2 gpm; (e and f) composites at 200 hPa level, contour interval 25 gpm; (g and h) gpm anomalies at 200 hPa level, contour interval 5 gpm.

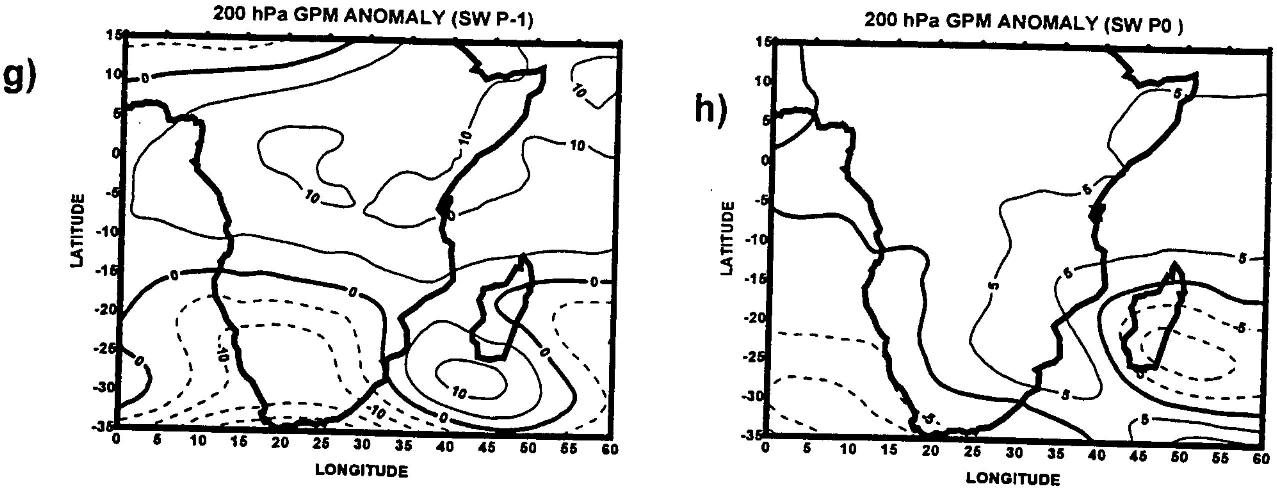

Figure 4.6 continued:

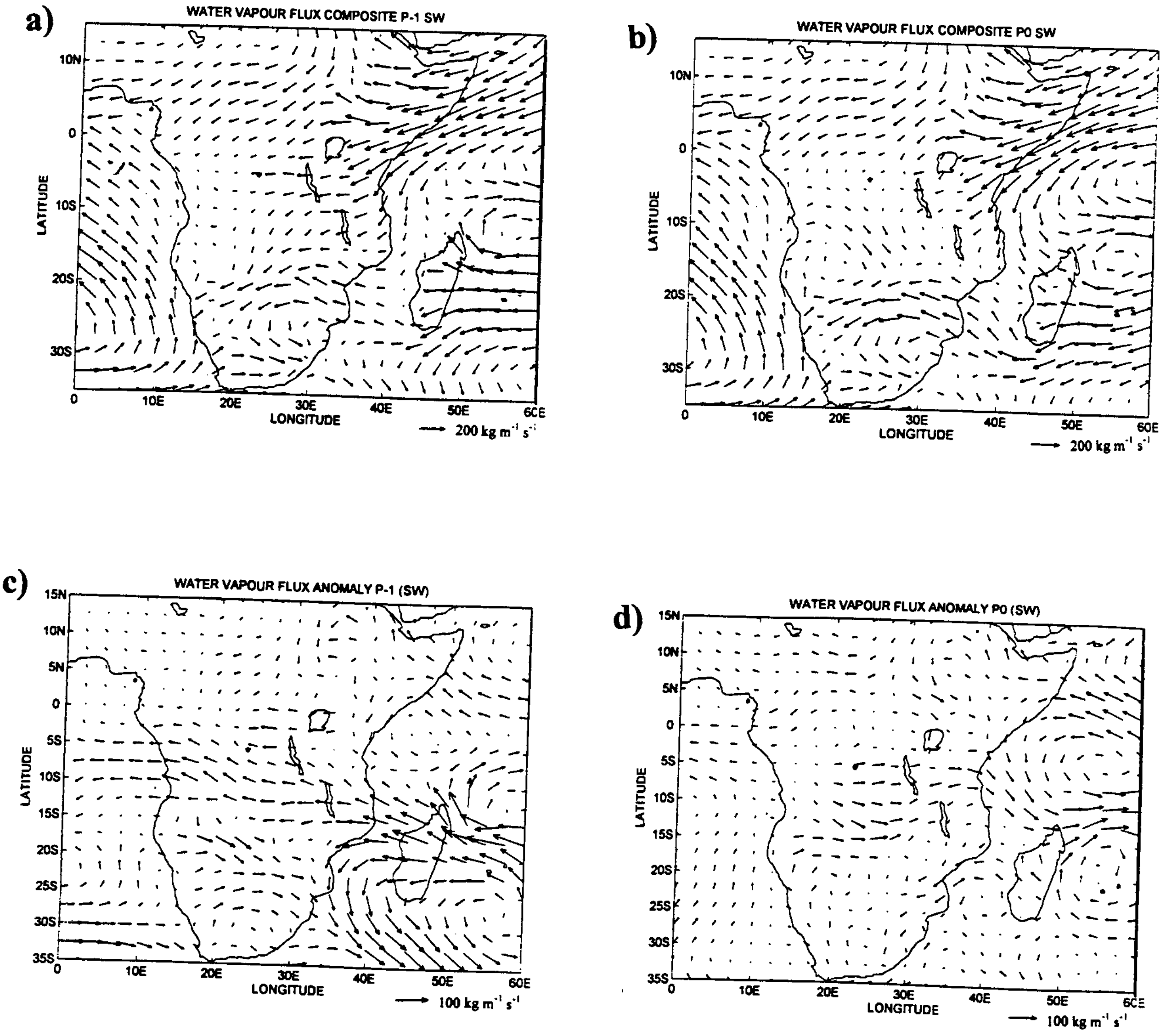

Figure 4.7: WVF and Horizontal wind flow pattern at 200 for P-1 to P0. (a and b) composite WVF integrated from 1000 hPa to 500 hPa; (c and d) WVF anomalies; (e and f) Composite flow pattern at 200 hPa; (g and h) anomaly flow pattern at 200 hPa.

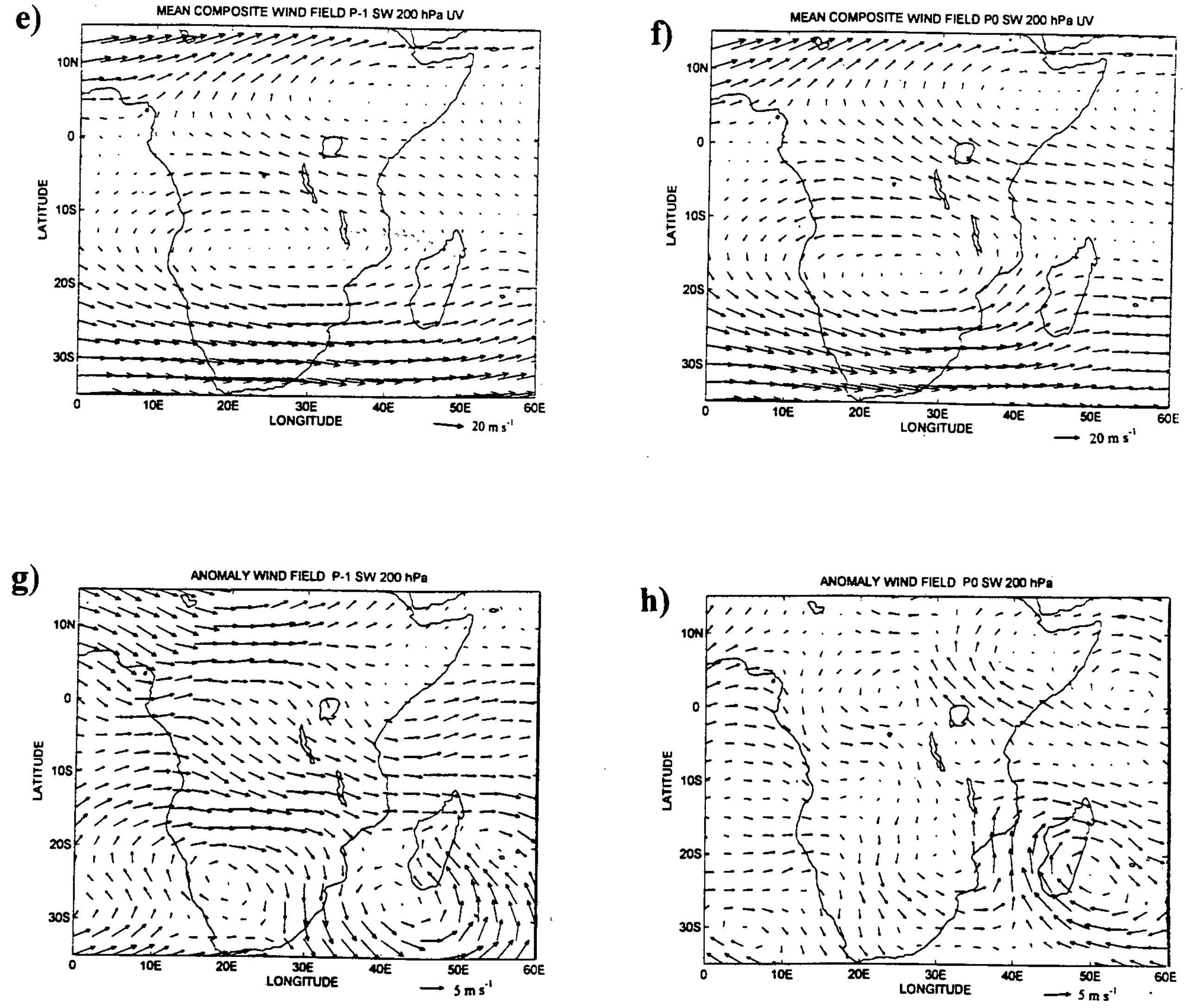
MEAN COMPOSITE WIND FIELD P-1 SW 200 hPa UV

MEAN COMPOSITE WIND FIELD P0 SW 200 hPa UV

ANOMALY WIND FIELD P-1 SW 200 hPa

ANOMALY WIND FIELD P0 SW 200 hPa

Figure 4.7 continued:

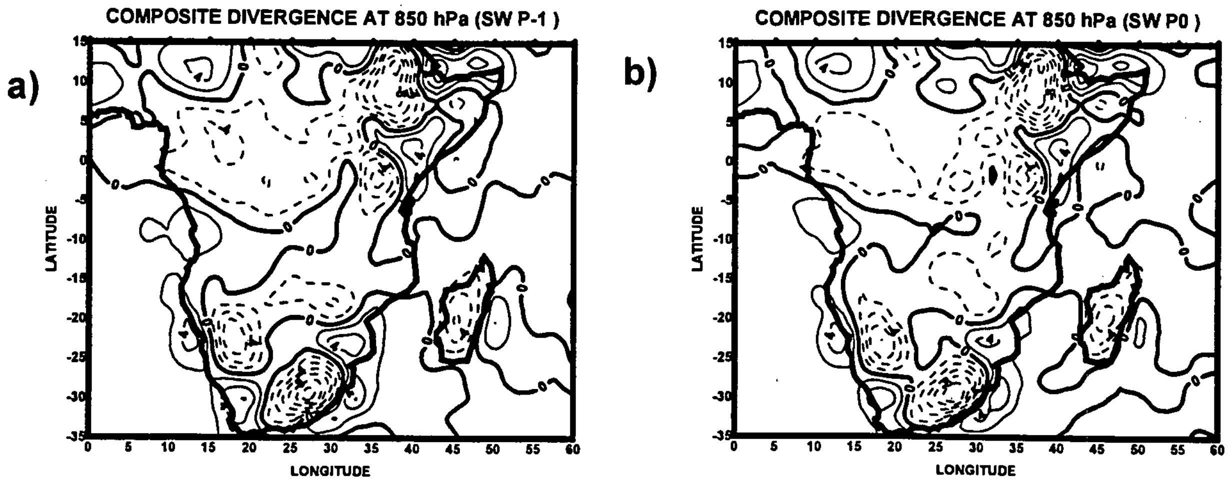
COMPOSITE DIVERGENCE AT 850 hPa (SW P-1)

COMPOSITE DIVERGENCE AT 850 hPa (SW P0)

Figure 4.8: Divergence for P-1 to P0. (a and b) composite divergence at 850 hPa level, contour interval $2 \times 10^{-6}\ s^{-1}$ (c and d) composite anomalies at 850 hPa, contour interval $.5 \times 10^{-6}\ s^{-1}$

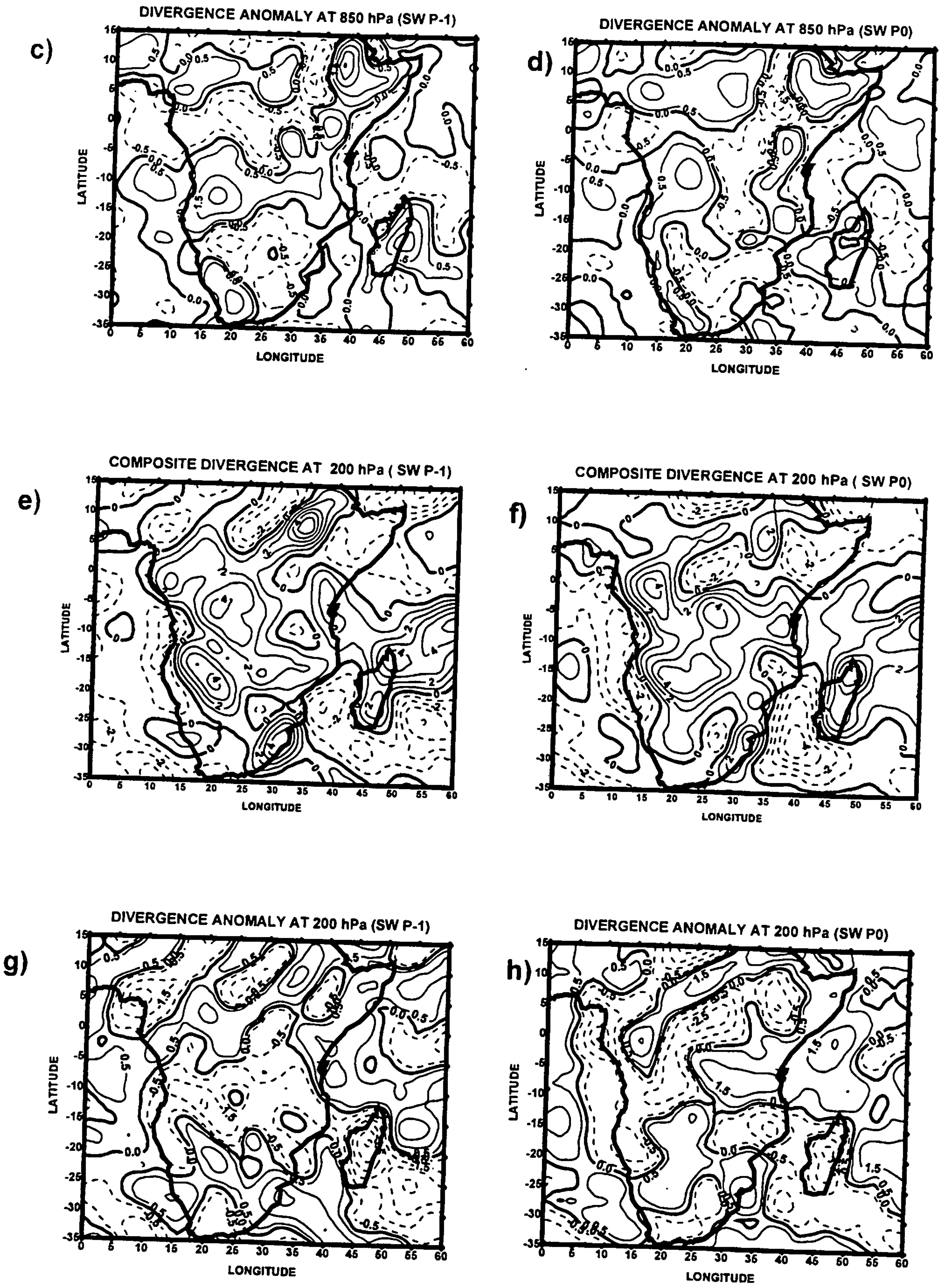

c) DIVERGENCE ANOMALY AT 850 hPa (SW P-1)

d) DIVERGENCE ANOMALY AT 850 hPa (SW P0)

e) COMPOSITE DIVERGENCE AT 200 hPa (SW P-1)

f) COMPOSITE DIVERGENCE AT 200 hPa (SW P0)

g) DIVERGENCE ANOMALY AT 200 hPa (SW P-1)

h) DIVERGENCE ANOMALY AT 200 hPa (SW P0)

Figure 4.8 Continued: (e and f) composite divergence at 200 hPa level, contour interval 1×10^{-6} s^{-1} (g and h) composite divergence anomalies at 200 hPa, contour interval 1×10^{-6} s^{-1}

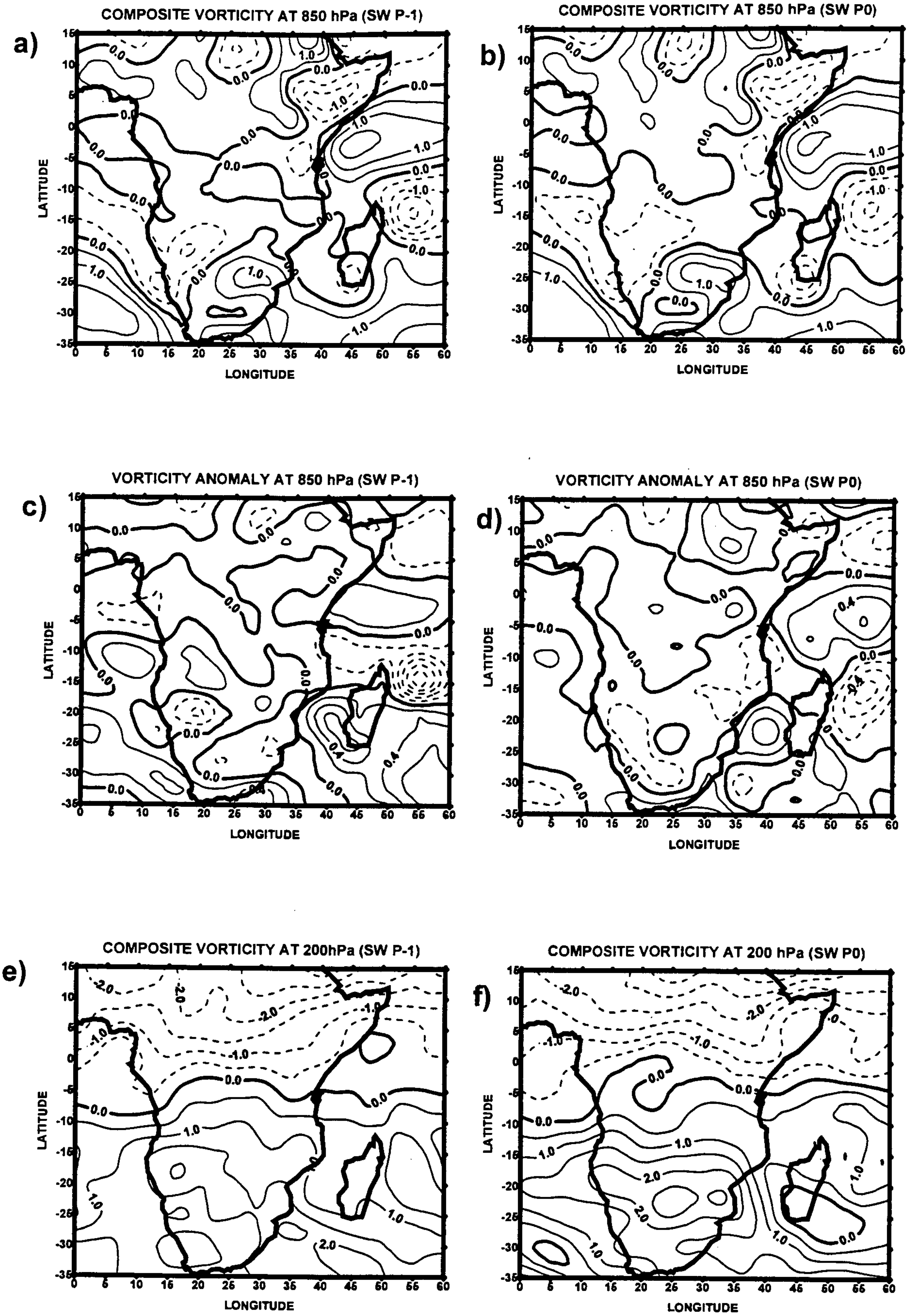

Figure 4.9: Vorticity for P-1 to P0. (a and b) composite vorticity at 850 hPa level, contour interval 1x10 $^{-6}$ s^{-1}, (c and d) vorticity anomaly at 850 hpa, contour interval .2x10 $^{-6}$ s^{-1}, (e and f) composite vorticity at 200 hPa level, contour interval .2x10 $^{-6}$ s^{-1}

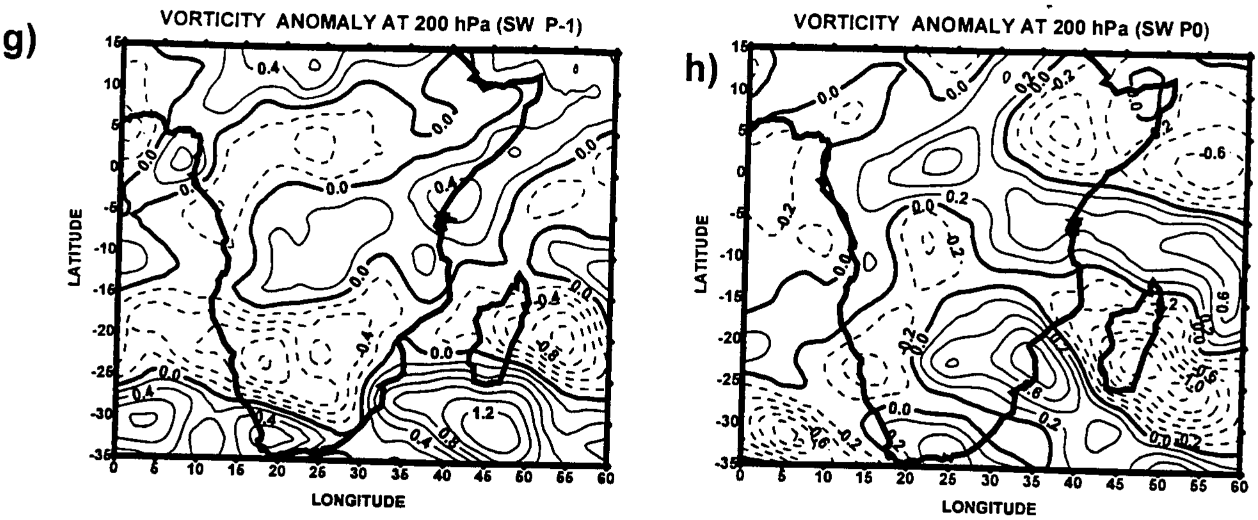

Figure 4.9 Continued: (g and h) vorticity anomalies at 200 hPa, contour interval .2x10 $^{-6}$ s^{-1}

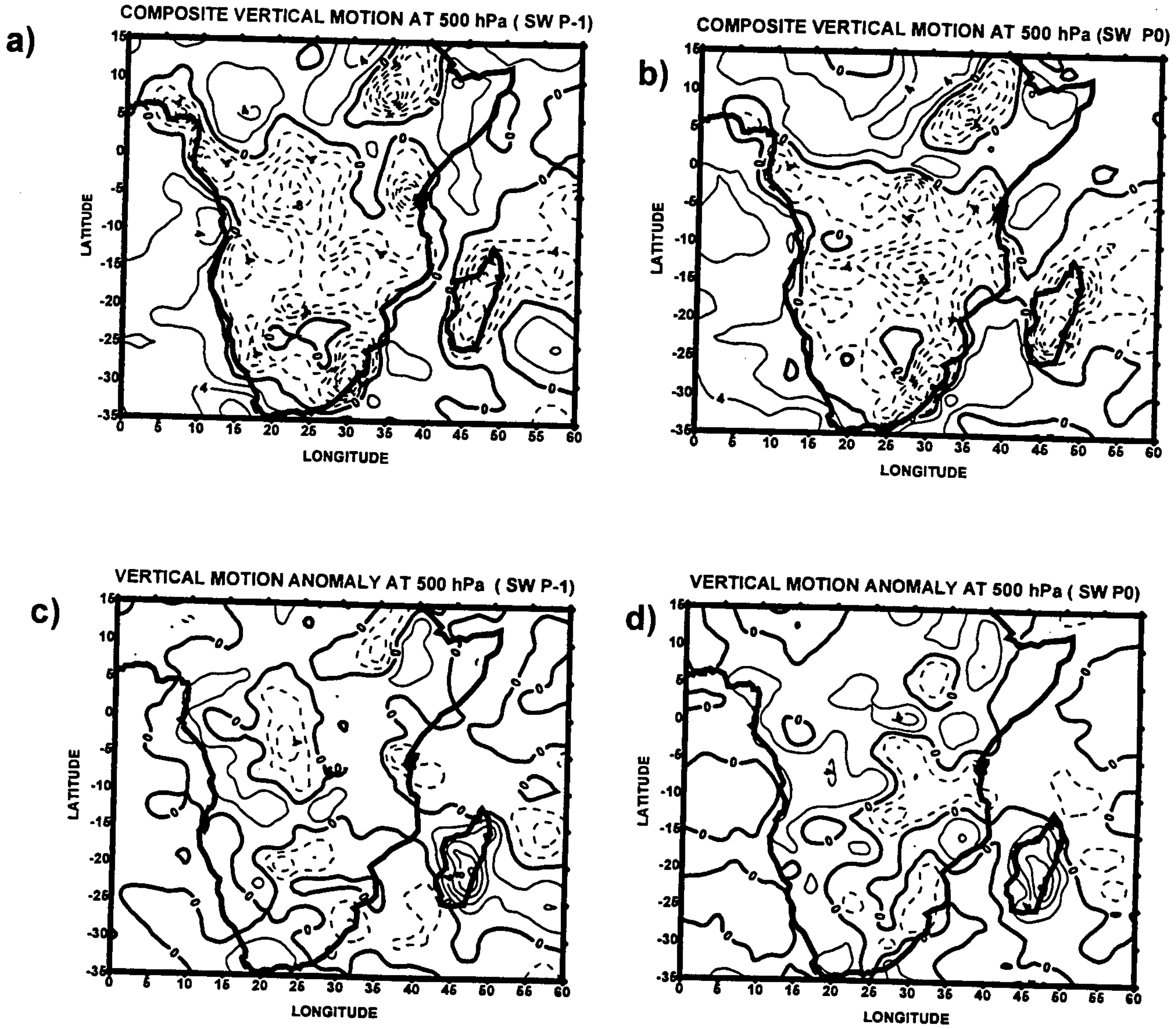

Figure 4.10: Vertical wind motion at 500 hPa for P-1 to P0. (a-b) composite vertical wind motion; vertical wind analysis; (c and d) anomaly vertical wind motion at 500 hPa, contour interval 2x10 $^{-2}$ Pa/s.

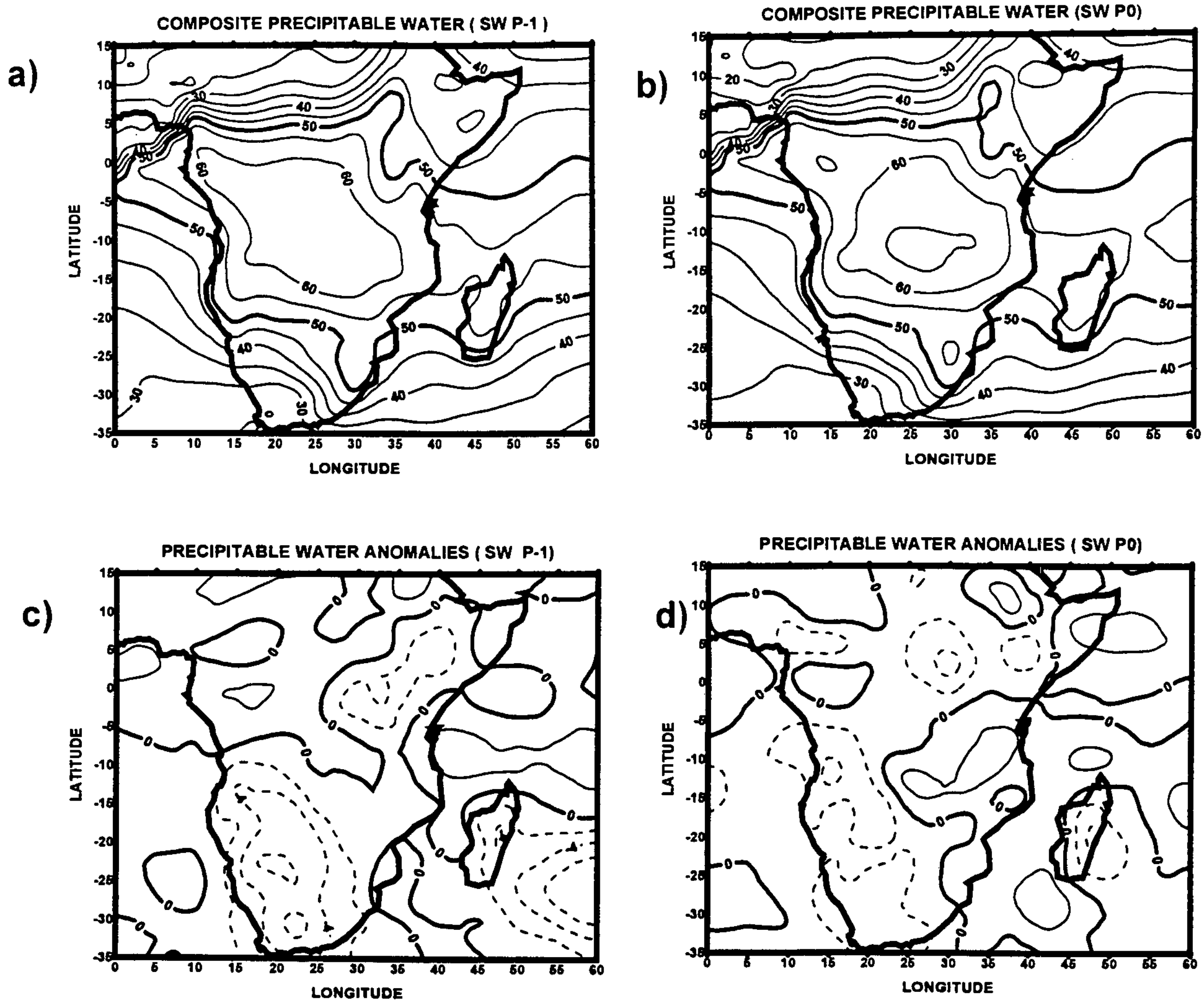

Figure 4.11: Precipitable water integrated from 1000 hPa to 500 hPa for P-1 to P0. (a and b) composite analyses, contour interval 5 mm; (c and d) anomaly analysses contour interval 1 mm.

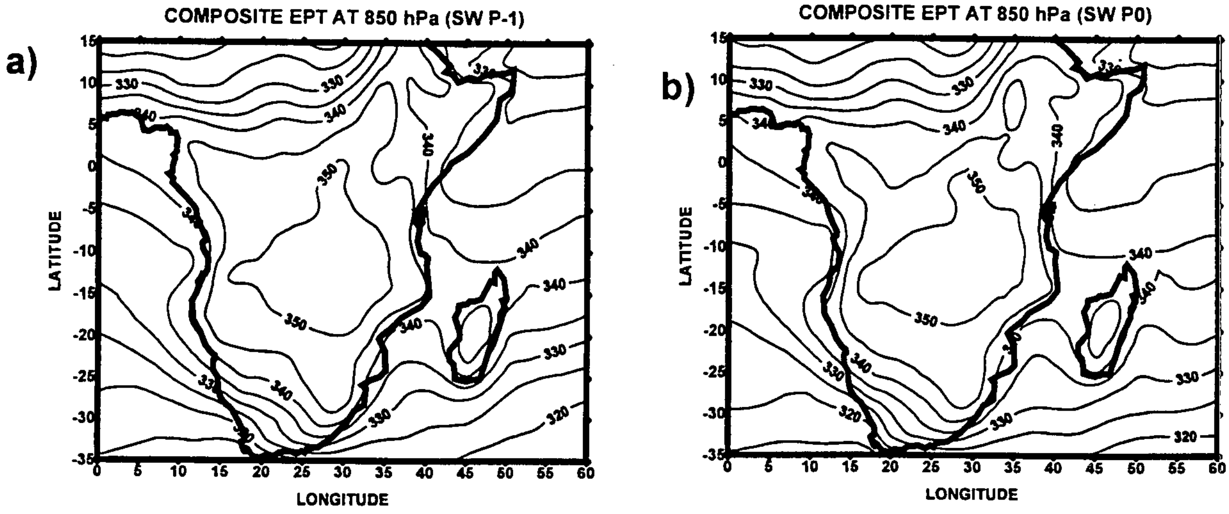

Figure4.12: Equivalent Potential Temperature. (a and b) composite EPT at 850 hPa level, contour interval 5 °K; (c abd d) EPT anomaly at 850 hPa level, contour interval 1°K; (e and f) composite EPT at 500 hPa level, contour interval 1°K; (g and h) EPT anomaly at 500 hPa,

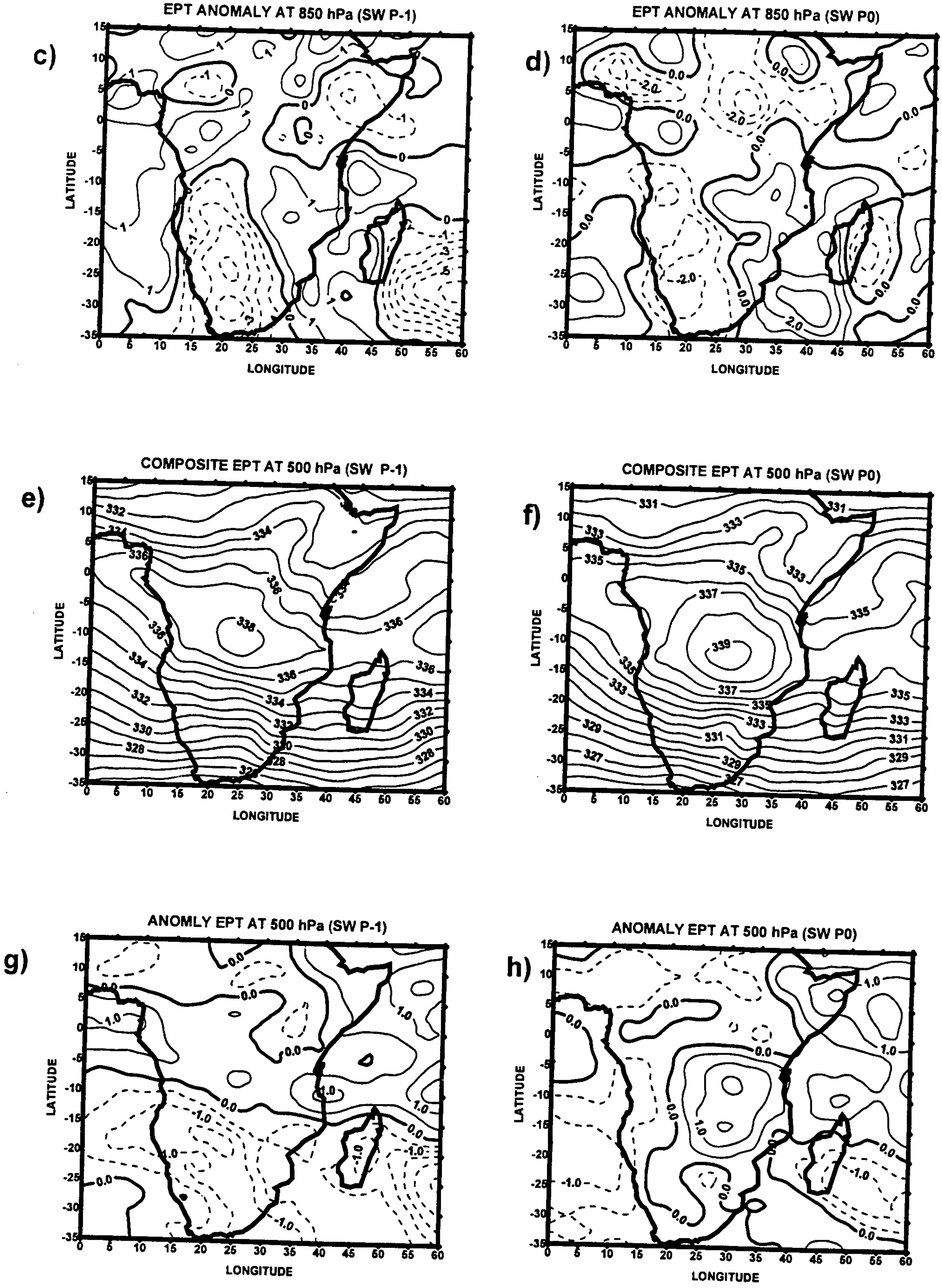

Figure 4.12 Continued: contour interval 5°K.

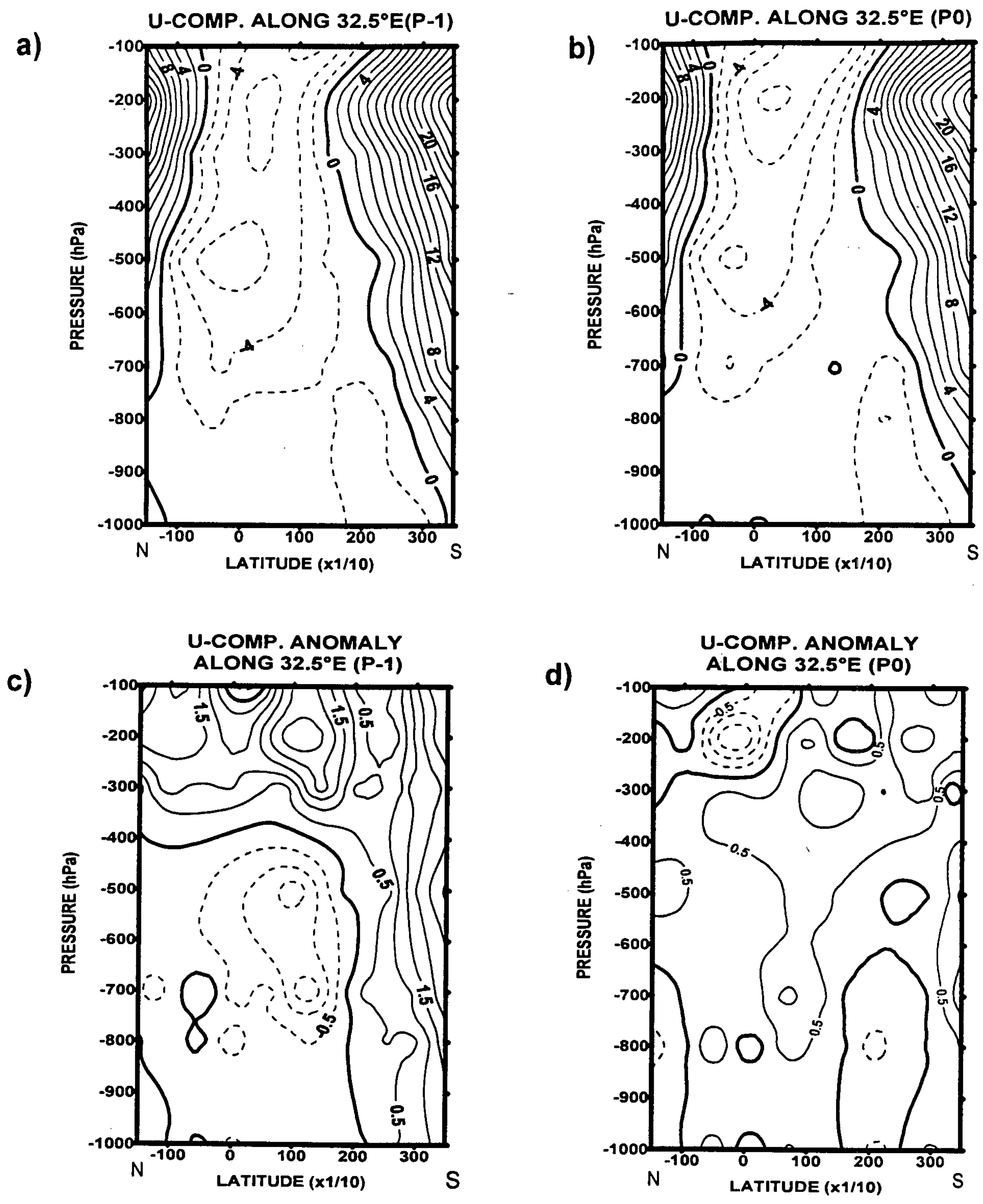

Figure 4.13: Vertical cross-sections of zonal and meridional wind components along 32.5°E for P-1 to P0 . (a and b) zonal wind component composites, contour interval 2 m/s; (c and d) zonal component anomaly along 32.5°E, contour interval .5 m/s

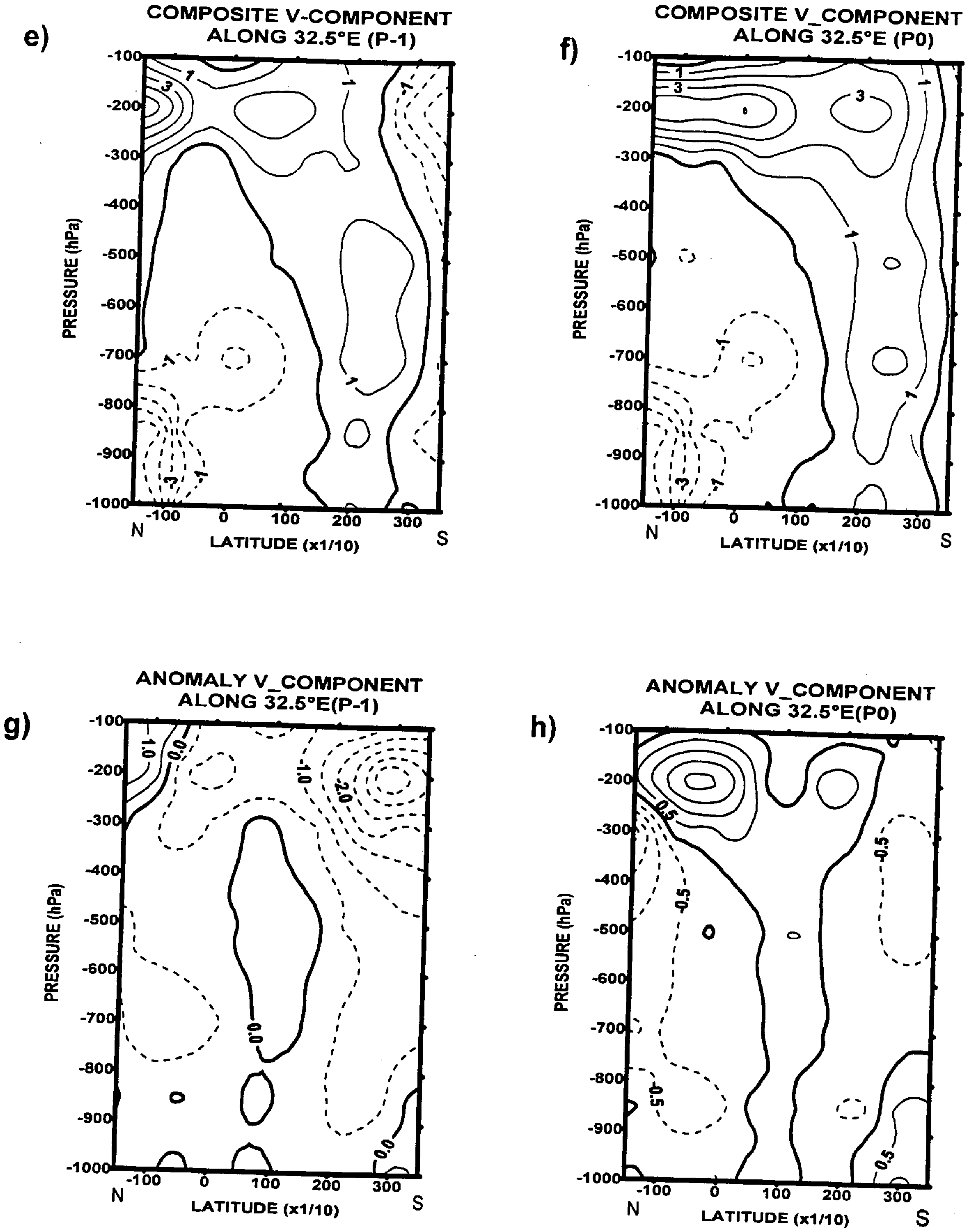

Figure 4.13 Continued: (e and f) meridional wind component, contour interval 1 m/s; (g and h) meridional wind component anomaly, contour interval .5 m/s;

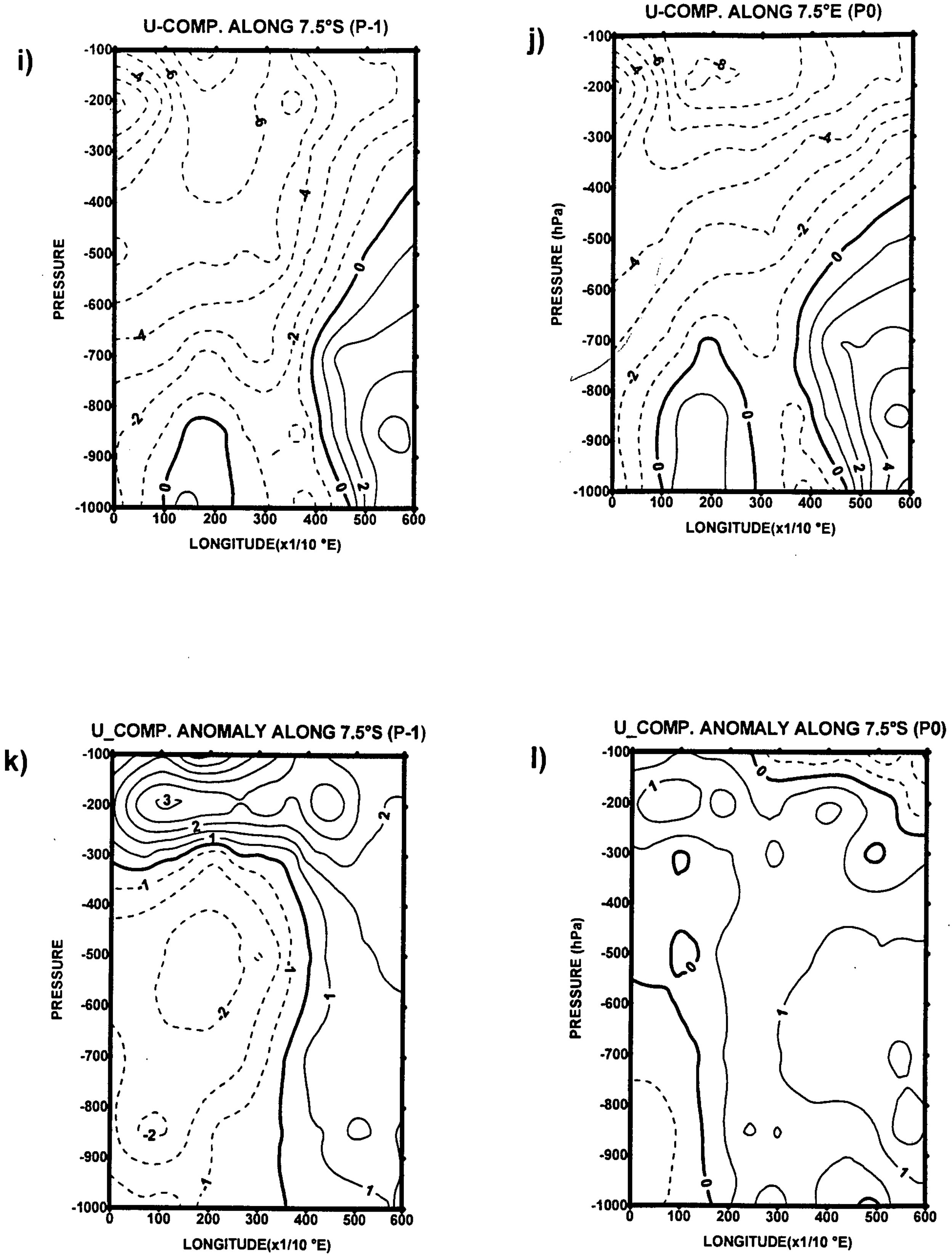

Figure 4.13 Continued: (i andj) u-component along 7.5°S, contour interval 2 m/s; (k and l) u-component anomaly along 7.5°S, contour interval .5 m/s.

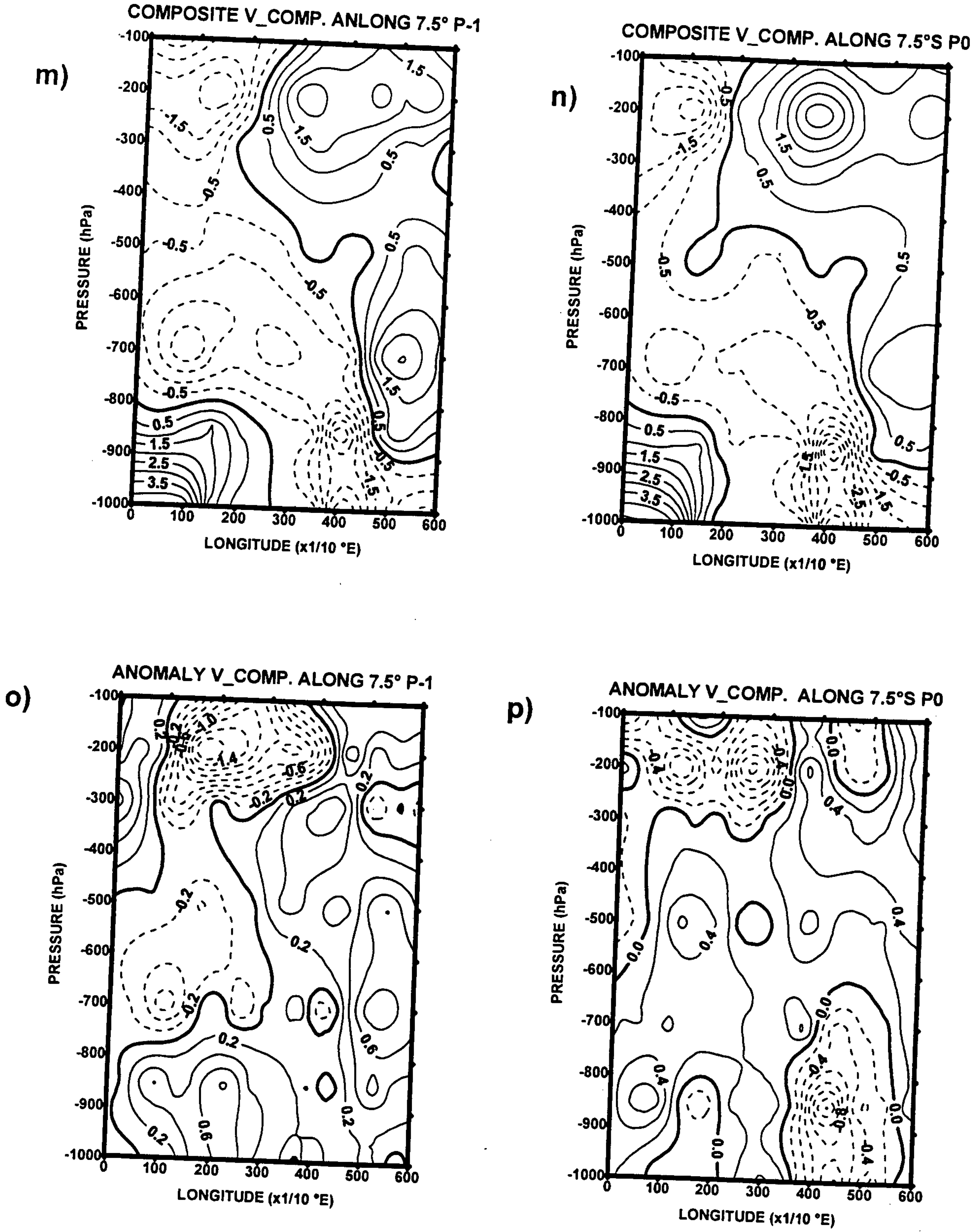

Figure 4.13 Continued: (m and n) v-component composite along 7.5°S; (o and p) v-componet anomaly along 7.5°S, contour interval .5 m/s

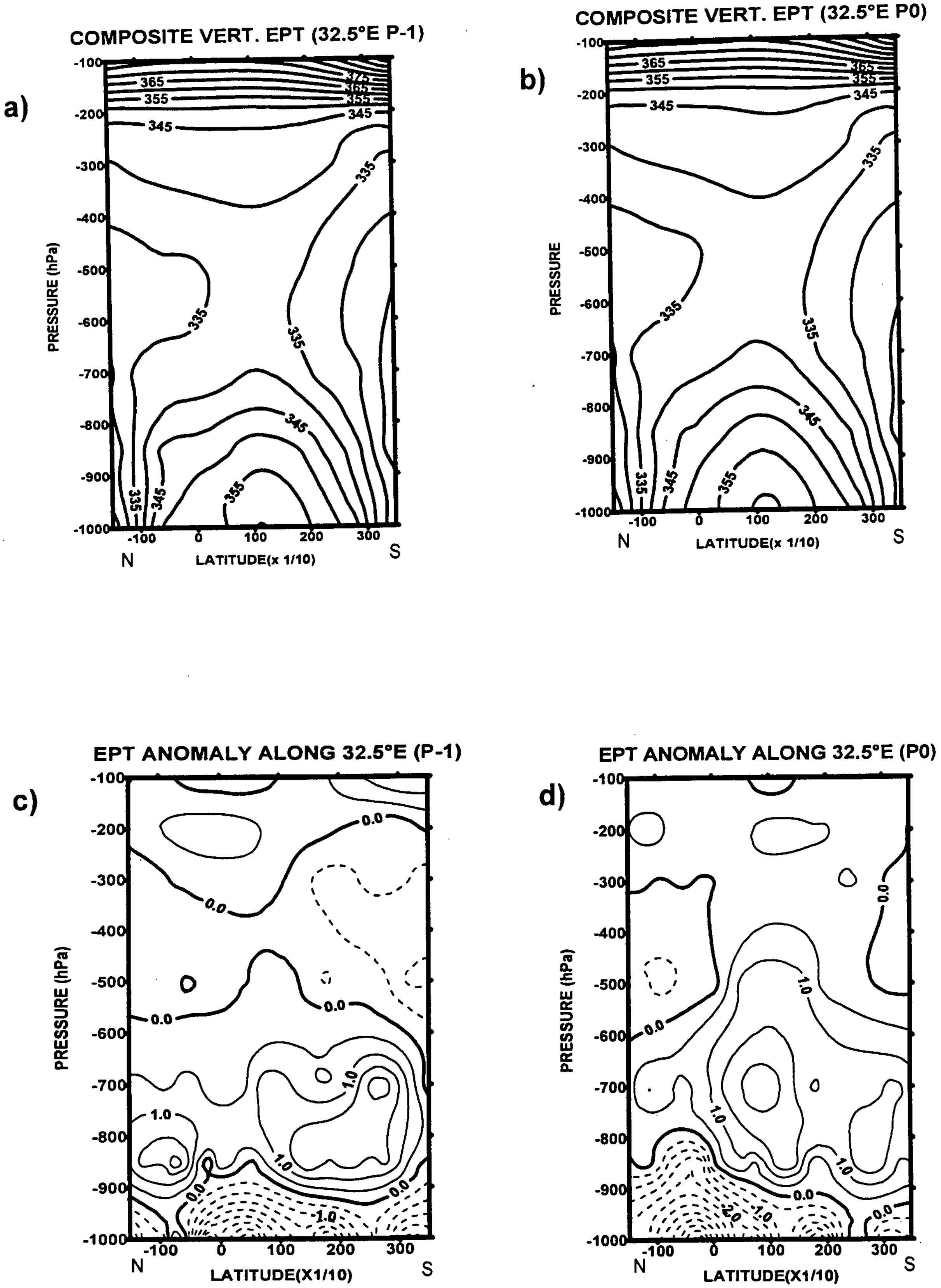

Figure 4.14: Vertical cross-section of EPT along 32.5°E for P-1 to P0. (a and b) composite EPT, contour interval 5°K; (c and d) composite EPT anomaly, contour interval .5°K.

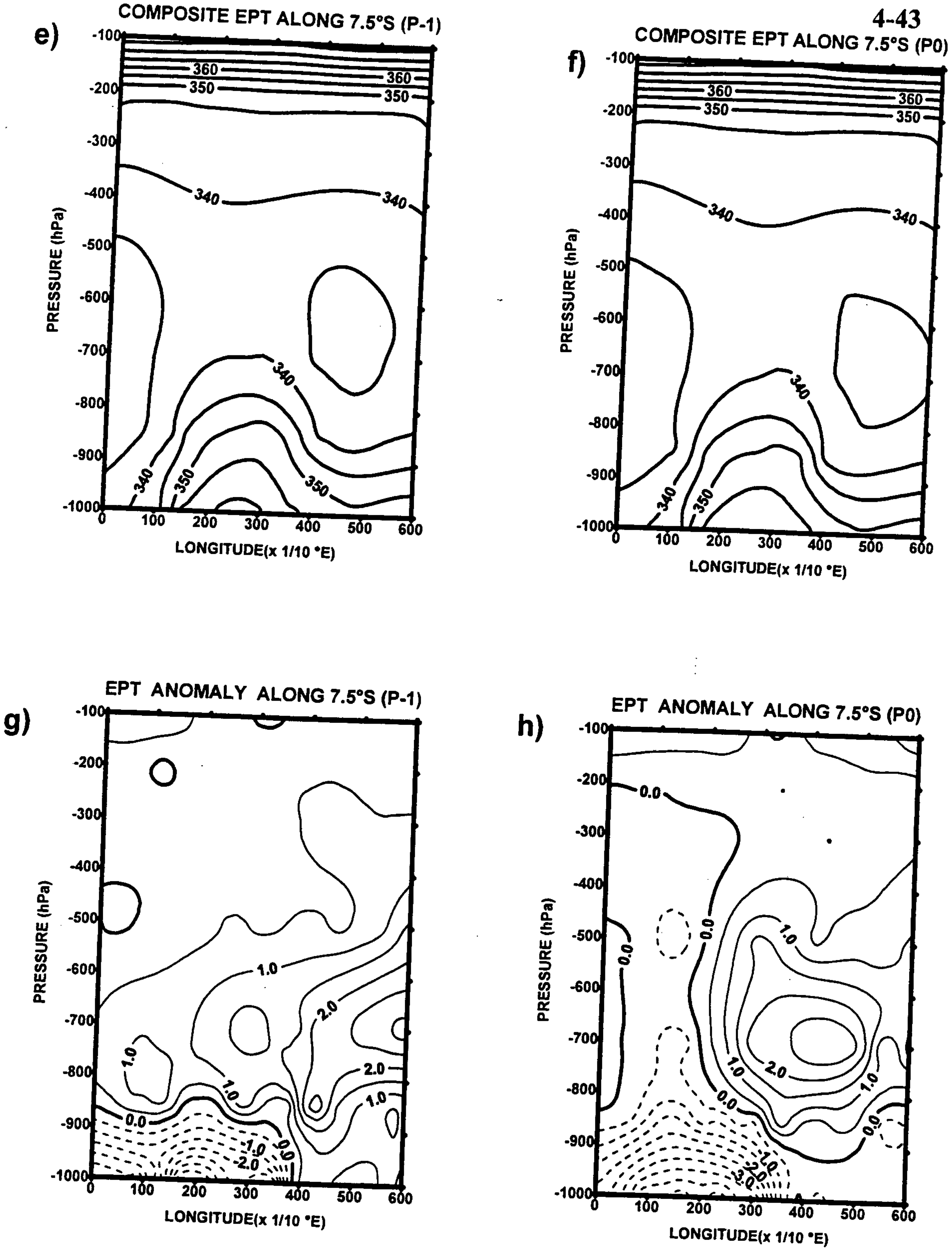

Figure 4.14: Vertical cross-section of EPT along 7.5°S for P-1 to P0. (e and f) composite EPT, contour interval 5°K; (g and h) composite EPT anomaly, contour interval .5°K.

CHAPTER 5

DYNAMICS OF THE PENTAD CONVECTIVE SEQUENCE: NORTHEASTERN AREA

5.0 Introduction

Chapter 3 demonstrated convective variability, inferred from the area-averaged pentad OLR index, for the northeastern area during the MAM season. It was revealed that there were dominant spectral peaks in the 2 to 4 and 4 to 6 pentad period bands and periods greater than 6 pentads. The intention of this chapter is to identify and describe the structure of kinematic and thermodynamic features associated with deep convection by analysing the time evolution of various atmospheric fields.

5.1 Seasonal Mean Analysis for MAM

In this section seasonal mean structures for various fields are analysed and used as a background in understanding evolution of composite anomalies. The seasonal means are calculated for the period March-May 1981-1994 in the domain 15°N-35°S, 0°-60°E. The mean is based on 135 pentads.

5.1.1 Geopotential Heights at 850 hPa and 200 hPa

The mean MAM geopotential height map at 850 hPa level (figure 5.0a) reveals a high pressure over southern Africa with its ridge extending to East Africa thus inducing diffluence over eastern parts of southern Africa. The Atlantic and the Southwest Indian anticyclones dominate the southern hemisphere sub-tropics. Over Sudan and Ethiopia lies a low pressure system with its associated trough extending southwestward to Angola. Another low pressure is located over the Indian Ocean. It is also important to note that the Arabian ridge is rather weak or almost non-existent. At the 200 hPa level (figure 5.0b) the high pressure ridge axis is along about 7.5°S. Slight troughing is indicated along 42°E. The tight contour lines suggests a westerly flow over the southern sub-tropics to about 15°S.

5.1.2 Water Vapour Flux and Wind Flow pattern at 200 hPa

The water vapour flux field figure 5.1a shows that the Indian Ocean is the main contributor of water vapour to the continent during MAM. A slight troughing along 28°E and wind convergence over central Africa is revealed. Over north-eastern Africa a convergence of north-westerly and south-easterly water vapour flux is found.

At the 200 hPa level (figure 5.1b) westerly wind flow dominates the southern hemisphere south of 12°S with a slight troughing indicated along 42°E. Two anticyclones are revealed, one in the southern hemisphere with its centre at about 25°E, 8°S and another in the northern hemisphere with its centre at about 35°E, 7°N. Easterly winds are located between 5°N and 5°S with relatively strong wind speeds west of 30°E. The north-south vertical cross-section of the mean zonal wind along 37.5°E (figure 5.1c) shows the existence of easterlies between about 5°N and 10°S, from 1000 hPa to 100 hPa level. North of 8°N the troposphere is mainly dominated by westerly winds with large values of about 10 m s^{-1} indicated at about 200 hPa level. In the southern hemisphere westerlies start featuring at 1000 hPa, at about 35°S, extending northward and increasing speed with height reaching a maximum of about 20 m s^{-1} and northward extent at about 200 hPa level. Figure 5.1d illustrate the MAM mean pattern of the meridional wind component in the north-south vertical cross-section along 37.5°E. Southerly wind components dominate the troposphere between 5°S and 30°S while northerlies between 15°N and 10°N tilts southwards with height up to 100 hPa. The pattern is not consistent at low levels because of land interactions.

Figures 5.1e and 5.1f present the mean MAM east-west vertical cross-sections of u-component and v-component respectively along 5°S. Figure 5.1e reveals negative u-component (easterlies) throughout the troposphere with values of about 4.5 m s^{-1} at about 700 hPa level. Figure 5.1f reveals that below the 800 hPa level the v-component values are positive (southerly) with large values over the Atlantic Ocean. Between 800 hPa and 400 hPa level the v-component values are negative (northerly) from 0° to 50°E with large values at 700 hPa. At upper levels, i.e. between 350 hPa and 100 hPa, the v-component values are negative from 0° to about 20°E with positive values occurring at about 200 hPa level. It can be said that below 800 hPa level the flow is basically south-easterly. However, care should be taken when interpreting wind values over the continent due to land interaction with lower pressure surfaces.

5.1.3 Divergence at 850 and 200 hPa

The divergence field at 850 hPa level (figure 5.2a) reveals large negative values (convergence) over Ethiopia and Somalia $-14\mathrm{x}10^{-6}\mathrm{S}^{-1}$. North of 5°S, the continent is covered by negative divergence values except over northeastern Kenya and Somalia which are covered by positive divergence values. South of 5°S positive values are dominant, except over Madagascar, eastern South Africa and Namibia. Large negative values over these areas could partly be due to orographic influence. At 200 hPa level (figure 5.2b) positive divergence values predominate over the Congo basin, west Africa, Sudan, Ethiopia, the coast of Kenya and Tanzania, Uganda and Madagascar. This may partly explain less active convection during this period over the inland areas of Tanzania while coastal and northeastern areas are normally more convectively active. Upper level convergence (negative values) is located over the Atlantic Ocean, Central and western Tanzania, and the rest of southern Africa except the southwestern tip of which is under positive divergence. Negative divergence also covers the coast of Somalia and adjacent Ocean areas.

5.1.4 Vorticity at 850 and 200 hPa

At 850 hPa level, (figure 5.3a), over the southern hemisphere, negative vorticity (cyclonic) is located over the coast of Namibia, southern Madagascar and Mozambique Channel and central Indian Ocean. The lee trough on the western side of Madagascar, which is partly due to an easterly current crossing the mountain range, can partly explain the cyclonic vorticity there (Holton, 1973). Positive vorticity (anticyclonic) areas are located over the southern Atlantic and Indian Oceans, southern Africa and northern Madagascar. In the northern hemisphere positive vorticity (cyclonic) is located over Libya and Chad, Sudan, Uganda and Kenya, while negative vorticity (anticyclonic) is located over the eastern part of Somalia and Ethiopia. At 200 hPa level (figure 5.3b), large positive vorticity values of about $2x10^{-6}s^{-1}$ are confined along 15°S, indicating the zonal ridge axis of the southern hemisphere subtropical anticyclones. Negative values over 5°E, 25°E and 45°E, 27°S indicate the position of troughs at the 200 hPa level. North of the equator negative values dominate (anticyclonic).

5.1.5 Vertical motion at 500 hPa

The vertical motion at 500 hPa, the mid-troposphere level at which maximum vertical motion is located, (figure 5.4a), shows negative values (upward motion) over Madagascar, Ethiopia, the eastern part of South Africa, and Cameroon. The enhanced vertical motion is partly influenced by orography and insolation (data is for 12UT). Positive values (indicating subsidence) are located over the Atlantic and southern Indian Oceans, and Botswana coinciding with anticyclonic features. Positive values are also located over the horn Africa.

5.1.6 Precipitable water

Centred at about 25°E and 0° latitude is the maximum mean precipitable water above 65 mm, (figure 5.4b). Lower values of less than 35 mm are located over the Sahara desert, southern Atlantic and Indian Oceans and southern parts of Africa. The areas covered by high precipitable water coincides with the position of the geopotential trough at the 850 hPa level (figure 5.0a).

5.1.7 Equivalent potential temperature

Areas with warm moist air as shown by 340°K isoline at 850 hPa level (figure 5.5a) are over central Africa, west and northeastern Africa and Madagascar. Dry and stable areas are located over the Indian and Atlantic Oceans and Sahara desert. At 500 hPa level (figure 5.5b) warm moist air is confined between 5°S and 5°N over the continent, and between 10°S and 5°N over the

Indian Ocean. The east-west vertical section, (figure 5.5c) along 5°S suggests an unstable area between 5°E and 45°E, however, more instability is suggested to be between 5° and 40°E where there are high EPT values of about 355°K at the surface. At upper levels, from 400 hPa, EPT values start increasing with height with tight gradients between 200 hPa and 100 hPa. The north-south vertical section of EPT (figure 5.5d), suggests an unstable area between 15°S and 7°N which tilts with height up to the 700 hPa level. The section between 15°N and 7°N is under stable configuration up to 800 hPa. At upper levels, there is a tight gradient of EPT and values increase with height from about 250 hPa to 100 hPa level.

5.2 Composite and Anomaly Results.

5.2.1 Geopotential Heights at 850 hPa and 200 hPa

At pentad P-1, geopotential height anomalies at 850 hPa (figure 5.6a), reveal two low pressure areas, one over Africa and another over the Indian Ocean. Farther south two subtropical anticyclones are dominant, the St. Helena and the Mascarene over the Atlantic and the Indian Oceans respectively. At P0, figure 5.6b, geopotential height rises are indicated over southern Africa while at the same time geopotential height falls are observed over the Mozambique Channel, Madagascar and Indian Ocean. The tightening of contours to the East of southern Africa suggests an increase of southeasterlies towards East Africa.

Geopotential height anomalies at 850 hPa level show some eastward shift of negative gpm anomalies and falls over the Indian Ocean. At P-1 (figure 5.6c) negative geopotential heights dominate over Africa with large negative values over Namibia and central eastern Africa. At P0, figure 5.6d, we observe a large area covered by negative gpm over the Indian Ocean and over eastern Africa, while positive geopotential height anomalies are located over the Atlantic Ocean and southern and southwestern Africa. This pattern acts to strengthen south-easterly flow towards northeastern Tanzania and adjacent areas.

The geopotential composite maps at 200 hPa level, shows that there are high pressure cells with ridge axes along 12.5°S at both pentads P-1 and P0, figure 5.6e and 5.6f, respectively. At P0 a trough is observed over the Mozambique Channel. The troughing pattern over the Mozambique Channel supports anticyclonic development at low levels over southern Africa and cyclonic development to the East of Madagascar. Figure 5.6g and 5.6h presents geopotential height anomalies for P-1 and P0 respectively at the 200 hPa level. Negative geopotential height anomalies are observed within the tropical belt and positive geopotential height anomalies occur in the southern hemisphere south of 10°S at both P-1 and P0.

5.2.2 Water Vapour Flux and Wind Flow pattern at 200 hPa

The WVF flow patterns are similar to those observed in the winds at 850 hPa (not shown). The composite WVF patterns for P-1 and P0 are illustrated in figures 5.7a and 5.7b. At both P-1 and P0 we observe an easterly water vapour flux between the 15°S-27°S latitude band. At P-1 water vapour flux is southeasterly as it approaches the eastern coast of Africa becoming easterly over the continent between 5°S and 22°S latitude band. Over the Arabian Sea water vapour flux is mainly from northeasterly. At P0 water vapour flux over the eastern coast of southern Africa is southeasterly with a strong southerly component and over the continent the flux is southeasterly in the 20-27°S latitude band. Also at P0 we observe a cyclonic water vapour flux to the North of Madagascar (figure 5.7b) which was not there at P-1. This augurs well with the presence of a low pressure over the same area in the 850 hPa geopotential height map at P0. Water vapour convergence is stronger at P0 than at P-1 over the target area.

The water vapour flux anomalies (figures 5.7c and 5.7d) at P-1 and P0 reveals some interesting patterns. At P-1 relatively strong westerly anomalies of water vapour flux are indicated between 5°N-5°S latitude band west of Lake Tanganyika. At P0 relatively strong westerly water vapour flux anomaly is revealed just North of Madagascar in the 5°S-10°S latitude band. An anomaly water vapour flux convergence over the coast of East Africa (northern coast of

Tanzania and the southern coast of Kenya) is also indicated. At P0 we observe strong southeasterly water vapour flux anomaly over the Mozambique Channel. The flow continues northward to Tanzania where it converges with westerly WVF from the Congo basin and north-easterly WVF from the Arabian Sea and northern Indian Ocean. The equatorward penetration of WVF is from 35°S to 5°S over the Southeast coast of Africa, along 35°E.

The mean composite wind circulation pattern at 200 hPa level (figures 5.7e and 5.7f), reveals an anticyclone at about 15°S, 25°E with its shear line along 15°S, at P-1. In the North an anticyclone is located at about 9°N, 51°E. At P0 the mean composite circulation pattern shows an anticyclone at about 15°S, 50°E. At P0 a trough is revealed in the South with its axis lying along about 45°E. The anomaly wind field at pentad P-1, figure 5.1g) reveals an anticyclonic anomaly flow centred at 9°N, 50°E and another anticyclonic anomaly in the southern hemisphere at 30°S, 36°E. The flow over the Mozambique Channel is northeasterly and that over Ethiopia and Sudan is southeasterly thus inducing an anomalous upper divergent flow over the target region, promoting convergence below it.

5.2.3 Divergence at 850 hPa and 200 hPa

The mean composite divergence field at 850 hPa level, at both P-1 and P0 (figures 5.8a and 5.8b) reveals negative divergence values over the east of southern Africa, Southwest Africa, Madagascar, northern Africa with maximum negative values over Ethiopia and over Uganda and Kenya. At P0 the area covered by negative values expands when compared with that at P-1. Positive divergence values are revealed at P-1 over Zambia, Zaire, northeastern Kenya and Somalia. At P0 the area covered by positive divergence increases over Zaire. At this time the whole of Mozambique, Zimbabwe and Zambia area is under positive divergence. Also at P0 positive divergence over Somalia shrinks in size giving way to the negative divergence shifting to the East. Apart from a slight shift of negative divergence from P-1 to P0, over East Africa, the pattern remains basically the same.

At 200 hPa level the mean composite divergence at P-1 shows positive divergence over a bigger part of Africa. The feature of interest to note in figure 5.8e is the tongue of negative divergence over Kenya and northern Tanzania and Uganda. At P0 this area is replaced with positive divergence values and thus enhancing convergence at low level as depicted at the 850 hPa level. Figure 5.8f further reveals positive divergence over Ethiopia and Sudan, over the whole central and East Africa and Madagascar. Over South Africa we note mainly negative upper divergence. Figures 5.8c and 5.8d represent the divergence anomaly field at 850 hPa level for P-1 and P0 respectively, and figures 5.8g and 5.8h shows divergence anomaly field at 200 hPa levels at P-1 and P0 respectively. Figure 5.8g reveals convergence anomalies over the target area while figure 5.8h shows the same area replaced by an upper positive divergence anomaly. It is not clear whether the divergence is a response or causal mechanism.

5.2.4 Vorticity at 850 and 200 hPa

Figure 5.9a shows negative (cyclonic) vorticity over southwest Africa and its coast, southern Madagascar, and to the north-east of Madagascar. Positive vorticity is revealed over the south Atlantic Ocean, southern Africa and southern Indian Ocean coinciding with anticyclonic centres. At P0, (figure 5.9b), negative mean composite vorticity develops to the East of Madagascar. The positive vorticity field over Africa pushes northwards and that over the Atlantic Ocean shifts eastwards. The vorticity anomaly field at 850 hPa level figure 5.9c looks similar to the mean composite vorticity at the same level. An interesting feature at P0 is the massive negative vorticity anomaly to the west and east of Madagascar. At 200 hPa level the composite vorticity field, (figures 5.9 and 5.9f), reveals negative vorticity in the North and positive vorticity from 5°S-26°S in the southern hemisphere. Farther south we observe northwest-southeast tilting alternating negative and positive vorticity fields indicative of a wave train. At P0 a broad band of negative vorticity is revealed over South Africa and south of Madagascar.

At 200 hPa level wave-trains of negative and positive vorticity anomaly are found (figures 5.9g and 5.9h). In the 5°S-17°S latitude band over Africa there are negative vorticity anomalies at P-1 while at P0 we see positive vorticity anomalies. Furthermore, negative vorticity anomalies observed at P-1 over the target region are replaced with positive anomalies at P0, suggesting anticyclonic vorticity there.

5.2.5 Vertical wind motion at 500 hPa

At P-1, (figure 5.10a), negative vertical motion is revealed over almost the whole continent and over Madagascar except over the Sahara desert, off the coast of Somalia and Kenya, the Mozambique Channel and over the Atlantic Ocean. At P0, figure 5.10b negative values of vertical motion can be found over Madagascar, northeastern Africa, Central Africa and East Africa, while positive values are found over southern Africa and the Sahara desert. Widespread positive values over southern Africa are noteworthy. High negative values occur over the northeastern part of Africa.

Vertical motion anomaly at 500 hPa level, figures 5.10c and 5.10d reveals a shift to the East of upward motions with values becoming more intense. A positive vertical motion anomaly field is established over Namibia and Zimbabwe around 20°S at P0.

5.2.6 Precipitable Water

Figures 5.11a and 5.11b show the vertically integrated precipitable water field composites at P-1 and P0 respectively. Maximum precipitable water is over central Africa, where central values are enclosed by a 70 mm isoline. From the two figures we observe that precipitable water shifts northeastwards from P-1 to P0.

The precipitable water anomalies (figures 5.11c and 5.11d) at P-1 and P0 reveal some interesting results. At P-1 we observe a centre of above 16 mm precipitable water anomaly over southern Africa, and in northwest Africa negative precipitable water anomalies occur. At P0 (figure 5.11d) we observe a shift of positive precipitable water anomaly north-eastwards.

5.2.7 Equivalent Potential Temperature

A noticeable change is seen in the composite equivalent temperature at both 850 hPa and 500 hPa level. At 850 hPa level, (figures 5.12a and 5.12b), both composites reveal centres of high equivalent potential temperatures at 5°N, 15°E; 0°, 27°E; 12.5°S, 20°E and over Madagascar. It is also noted that there is a general shift of high equivalent potential temperature northeastwards over the continent, with a slight decrease in values from P-1 to P0. We also observe a northward increase of equivalent potential temperature over the eastern coast of southern Africa from P-1 to P0. At 500 hPa level, (figures 5.12e and 5.12f), at P-1 we observe the centre of high equivalent potential temperature is over 12.5°S, 35°E. At P0 we see the area enclosed by a 338°K isoline expanding and shifting eastward. We also notice a northward shift of the equivalent potential temperature high value centre, from P-1 to P0.

Figures 5.12e and 5.12f show equivalent potential temperature anomalies at P-1 and P0 respectively. Highest EPT anomaly values are located at about 21°S, 24°E with values of about 12°K, followed by another centre at about 22°S, 44°E with a central value of about 10°K. Negative anomaly values are located in the North. At P0, figure 5.12d, there is a general shift of the pattern to the East. This is shown by the eastward shift of the 4°K isoline at P0 when compared with its position at P-1. Figures 5.12g and 5.12h presents EPT anomaly fields at 500 hPa for P-1 and P0. Higher anomaly EPT values are observed to be in the southern hemisphere. At P-1, figure 5.12g, high EPT are indicated about 20°S, 35°E with values of over 5.5°K while at P0, figure 5.12h the centre is at 22°S, 55°E, an eastward shift of about 20° of longitude in about five days. Another positive anomaly moves to 7.5°S, 35°E, a northward shift of about 13° latitude in 5 days. The target area shows an increase of EPT of about 1.5° to 2.0° at 500 hPa from P-1 to P0.

5.3 North-South Vertical Sections

5.3.1 Zonal and Meridional Wind Components

The north-south vertical cross-section of the zonal wind component along 37.5°E between 15°N and 35°S and 1000 hPa and 100 hPa are illustrated in figure 5.13. At P-1, figure 5.13a, maximum westerly winds are revealed at about 200 hPa, at 35°S with values above 26 m s^{-1}. A core of easterlies with values above 6 m s^{-1} is located at 5°S, at the same level. The zero line in the south tilts equatorward with height as expected; as it represents the ridge of the southern subtropical anticyclone. In the North there is a narrow band of westerlies between 15°N and 8°N in the upper and lower troposphere. At P0, figure 5.13b, we observe an increase in strength of easterlies at about 200 hPa level, while at the same time westerlies decrease in strength at the same level. Easterlies dominate over the target area from 1000 hPa to 100 hPa, suggesting a barotropic pattern.

Figures 5.13c and 5.13d show u-component anomalies for pentad P-1 and P0. At P-1, figure 5.13c, we observe a core of easterly zonal wind anomaly at about 200 hPa above 20°S while figure 5.13d, reveal two easterly wind anomaly cores, one at 100 hPa, above 10°S, with a wind speed above 5 m s^{-1} and the second at about 200 hPa, above 30°S, with a wind speed above 6 m s^{-1}. Easterly wind anomalies expand southwards and northwards. Wind speed anomalies increases, between 2.5°N and 5°S at the 200 hPa level, are noted in figure 5.13d when compared with figure 5.13c.

Figures 5.13e and 5.13f illustrate the vertical cross-sections of meridional wind components for P-1 and P0 respectively along 37.5°E. at P-1 a barotropic feature is revealed between 10°S and 30°S, in which southerly components are depicted. At P0 a column of northerly components from 1000 hPa to 100 hPa level and between 15°N and 10°N tilts southwards reaching 25°S at 100 hPa level. Southerlies dominate at P0 with largest values of about 6 m s^{-1} at about 900 hPa. Anomalies of meridional winds in the north-south vertical cross-sections for P-1 and P0 are shown in figures 5.14g and 5.13h respectively. At P-1 southerlies are revealed above 300 hPa level and mostly northerlies below 500 hPa. At P0 we see that northerlies and southerlies converge at about 6°S. A column of northerlies between 15°N and 6°S tilts southwards up to 100 hPa with southerlies to the south of it.

5.3.2 Equivalent Potential Temperature

Figure 5.14 reveals the vertical cross-section of EPT, along 37.5°, from 1000 hPa to 100 hPa between 15°N and 35°S. Figures 5.14a and 5.14b show that high values of EPT are located between 5°N and 20°S at the surface and then tilt equatorward up to about 600 hPa. Tight EPT gradients are found at upper levels between 200 hPa and 100 hPa. EPT anomaly analyses reveal interesting features. At P-1, figure 5.14c we observe high EPT anomaly values of above 8°K between 900 hPa and 700 hPa above 20°S. The pattern changes at P0, figure 5.14d. At P0 we observe that the system shifts northward by about 15° latitude, in the mid-troposphere. This suggests the northward shift of warm moist air associated with the ITCZ. An increase of about 1-1.5°K is seen above the target region between 900-300 hPa.

5.4 East-West Cross Section

5.4.1 Zonal and Meridional Wind Components along 5°S

Figures 5.13(i-l) presents the east-west vertical cross-sections of zonal wind composites and anomalies along 5°S for P-1 and P0. The composite sections at P-1 and P0 reveals easterly winds at 200 hPa level with relatively stronger force at P0, at about 10°E. Between about 20°E and 50°E there exists easterly winds all the way from 1000 hPa to 100 hPa level. Weakening of easterlies between 20° and 50°E from 1000 hPa to about 400 hPa level is noted. Figure 5.13j shows clear increase in easterly wind anomalies in upper levels east of 30°E and increase in westerly anomaly winds at lower levels. It is noted that anomaly winds pushes aloft from P-1 to P0 giving way to westerly wind anomalies. Figure 5.13(m-p) illustrates the sequence of vertical cross-section along 5°S of meridional wind composites and anomalies from P-1 to P0. A southerly wind component is revealed between about 800 hPa and 1000 hPa in both figure 5.13m and 5.13n west of 50°E and northerly wind components to the East. The mid-troposphere is mainly occupied by northerly wind component. A shift of southerly wind components occur from pentad P-1 to P0 at about 200 hPa level. Vertical cross-section anomalies of meridional components show a strengthening of northerlies to 1.6 m s^{-1} at P0, at about 700 hPa level above 40°E (figure 5.13p), from about 0.8 m s^{-1} at P-1, (figure 5.13k). Wind anomaly strength is less at P0 than at P-1 at 200 hPa. An eastward shift of southerlies in the mid-troposphere is also indicated.

5.4.2 Equivalent Potential Temperature along 5°S

Figure 5.14e and 5.14f reveal that high values of EPT are over the continent. The two figures show that lower values of EPT are over the Atlantic Ocean than the Indian Ocean. From the surface, between 20°-30°E, the axis of higher values of EPT tilt towards the West at both pentads P-1 and P0. The pattern is the same at both pentads above 400 hPa.

Figure 5.14g and 5.14h reveal the vertical cross-section of EPT anomalies. Negative EPT anomalies are indicated at the 200 hPa level and west of 20°E between 600 hPa and 1000 hPa levels at P0 (figure 5.14h). A 1.5°K increase of EPT in the mid-troposphere, between 700 hPa and 350 hPa is indicated above 38°E. There is an eastward shift of the warm moist layer by 15° of longitude in 5 days.

5.5 Summary

The aim of this chapter was to investigate the time evolution of kinematic and thermodynamic features associated with the deep convection (P0) phase and its precursor over northeastern Tanzania during the MAM season. In order to achieve this pentad composite kinematic and thermodynamic parameters were analysed for the two phases. Main findings in this chapter are summarised as follows:

- The general eastward shift of convection is supported by geopotential rises over Northwest Africa and falls over the western Indian Ocean. The tightening of geopotential height contours over the Mozambique Channel is indicative of the strengthening of southeasterly wind which in turn advects moist unstable air from the Indian Ocean to the north-eastern areas at P0;

- Convergent northeasterly and southeasterly water vapour flux is clearly shown at P0. The northeastward shift of the convergent area is well depicted in the anomaly WVF pattern which is associated with the ITCZ. WVF anomaly convergence is over western Tanzania at P-1 and at P0 is over the northern coast of Tanzania and southern coast of Kenya. This suggests that convection development is supported by dynamic as well as the availability of moist air. The main source of moisture is shown to be the Indian Ocean. The anomaly wind pattern at the 200 hPa level shows that there is an expansion in area and slight increase in wind speed of diffluent easterly anomaly winds over the northern part of Africa during deep convection.
- Divergence and vorticity at 200 hPa and vertical motion at 500 hPa support convection over the target area;
- Integrated precipitable water anomaly shifts northeastwards to the target region from pentad P-1 to P0;
- Eastward shift of warm moist air is revealed at 850 hPa and 500 hPa levels. The relatively strong southeasterly winds over the Mozambique Channel and Madagascar observed, in figures 5.7a and b, advects warm moist air from the Indian Ocean to the coast of East Africa;

- The North-South and East-West cross-sections of composite u-component indicates a strengthening of upper level easterlies above the target region and weakening of easterlies or establishment of westerlies at low level at P0. A barotropic structure in zonal wind is revealed during this season. The zonal and meridional wind component anomalies exhibits baroclinic patterns similar. The north-south and east-west vertical cross-section of EPT show that there is an increase of EPT values in the mid-troposphere and EPT falls in the low levels over the target area at P0.

-deep convection is accompanied with the warming up of the mid-troposphere by about 1.5°K. The northward and eastward shift of this warming suggest that the ITCZ is associated with the increase in the convective activity over the target area.

The analyses in this chapter have identified the mean structure of some of the atmospheric parameters during the MAM season. The patterns revealed are similar to previous studies. Based on the compositing procedure of the pentad ECMWF data, used in this study, the analyses have identified the time evolution of kinematic and thermodynamic features associated with deep convection and its precursor during the MAM season. Spatial characteristics of convective systems will be investigated in chapter 6 by analysing time-longitude diagrams of pentad OLR, zonal winds at 850 hPa and 200 hPa, and precipitable water integrated from surface to 300 hPa anomalies.

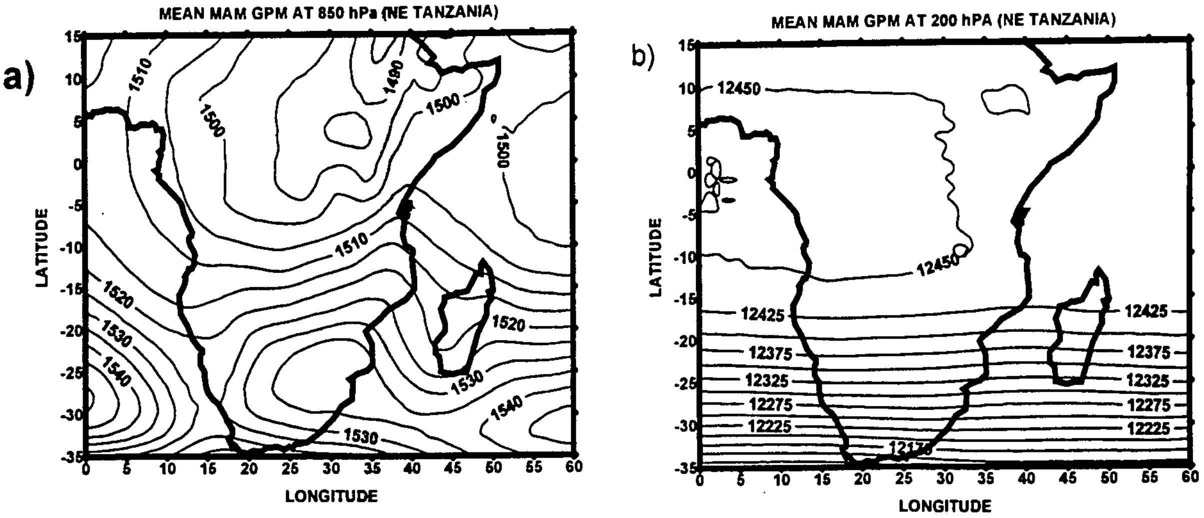

Figure 5.0: a) MAM mean geopotential heights at 850 hPa, contour interval 5 gpm; b) MAM mean geopotential heights at 200 hPa, contour interval 20 gpm.

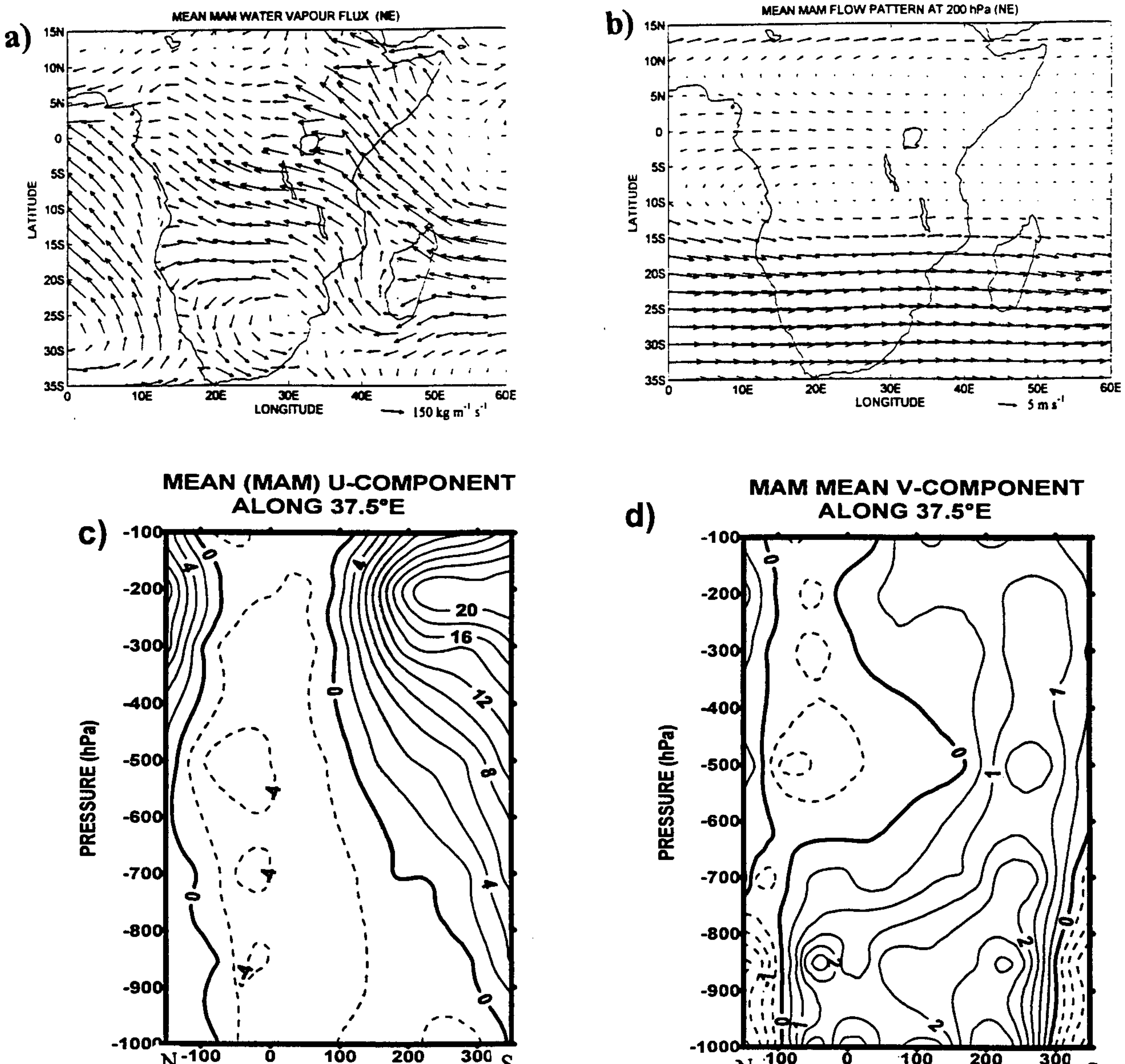

Figure 5.1: MAM mean. a) WVF integrated from 1000 to 500 hPa; b) wind flow pattern at 200 hPa level; c)vertical cross-section of zonal wind component along 37.5°E, contour interval 2 m s^{-1}; d) vertical

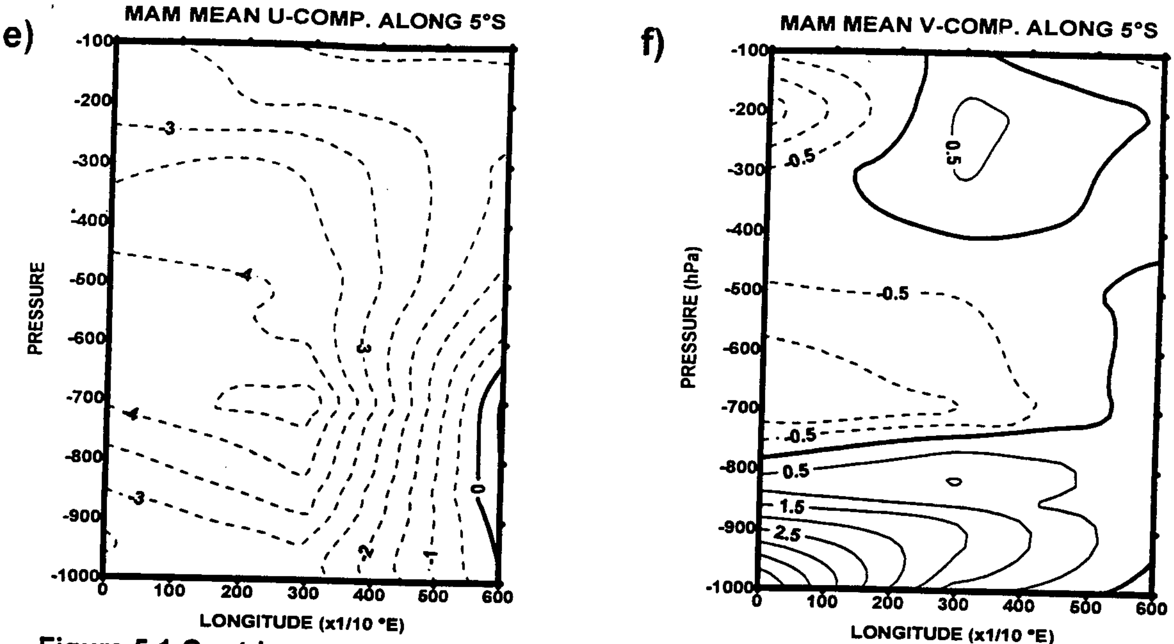

Figure 5.1 Contd: cross-section of meridional wind component along 37.5°E,contour interval .5 m/s; e) vertical cross-section of zonal wind component along 5°S; f) vertical section of meridional wind component along 5°S, contour interval .5 m/s.

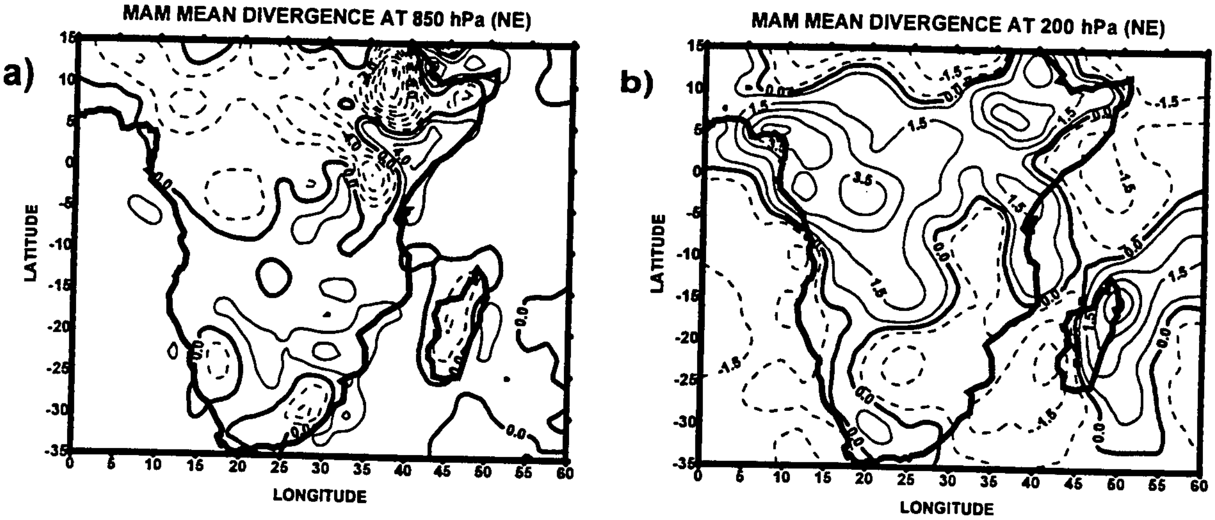

Figure 5.2: MAM mean divergence. a) at 850 hPa, contour interval 2x10 $^{-2}$ s^{-1} b) at 200 hPa, contour interval 1x10 $^{-6}$ s^{-1}

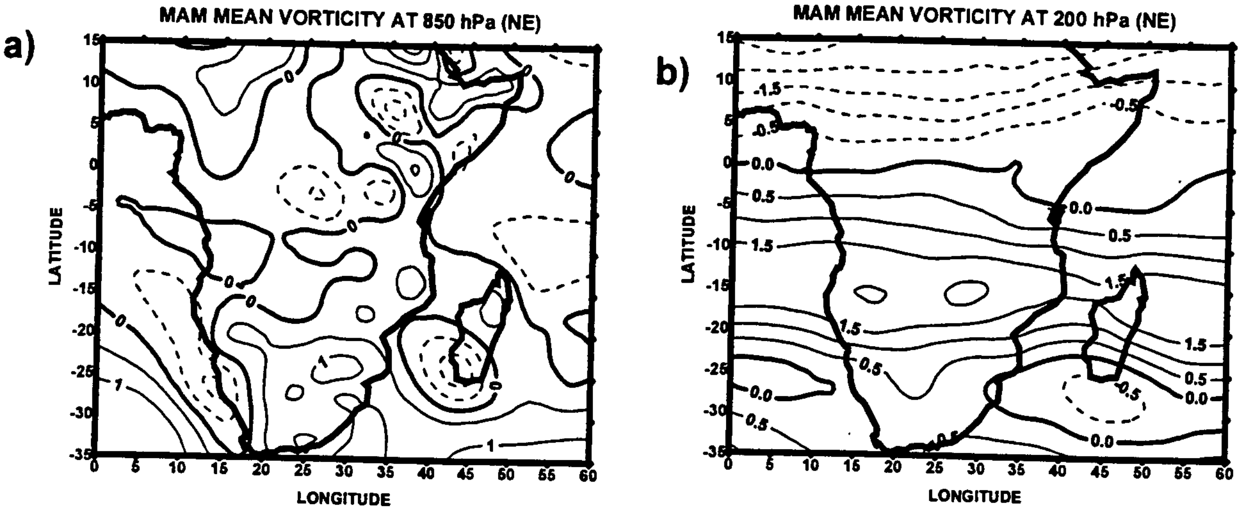

Figure 5.3: MAM mean vorticity a) at 850 hPa; b) at 200 hPa, contour interval .5 x 10 $^{-6}$ s^{-1}

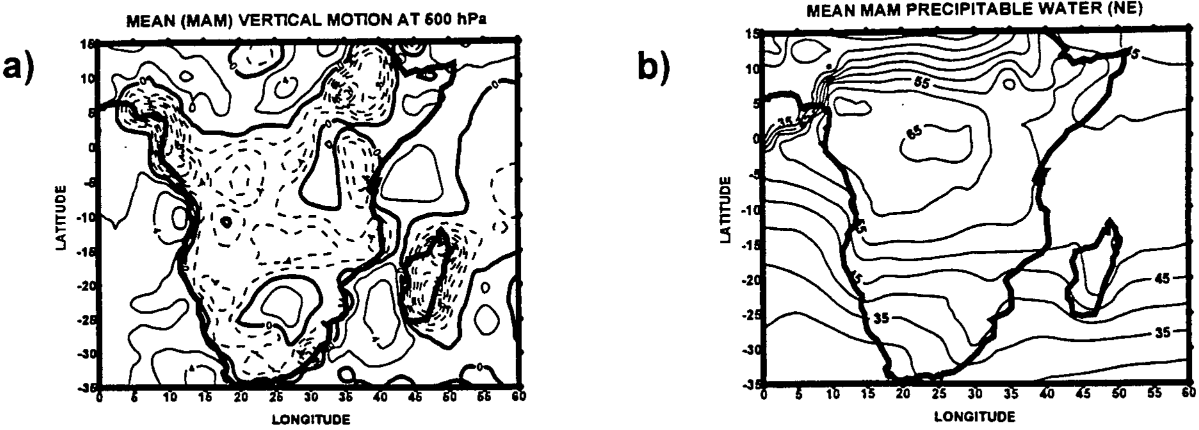

Figure 5.4: MAM mean. a) Vertical motion at 500 hPa, contour interval 2x 10^{-2} Pa /s ; b) precipitable water integrated from the 1000 hPa to 300 hPa level, contour interval 5 mm

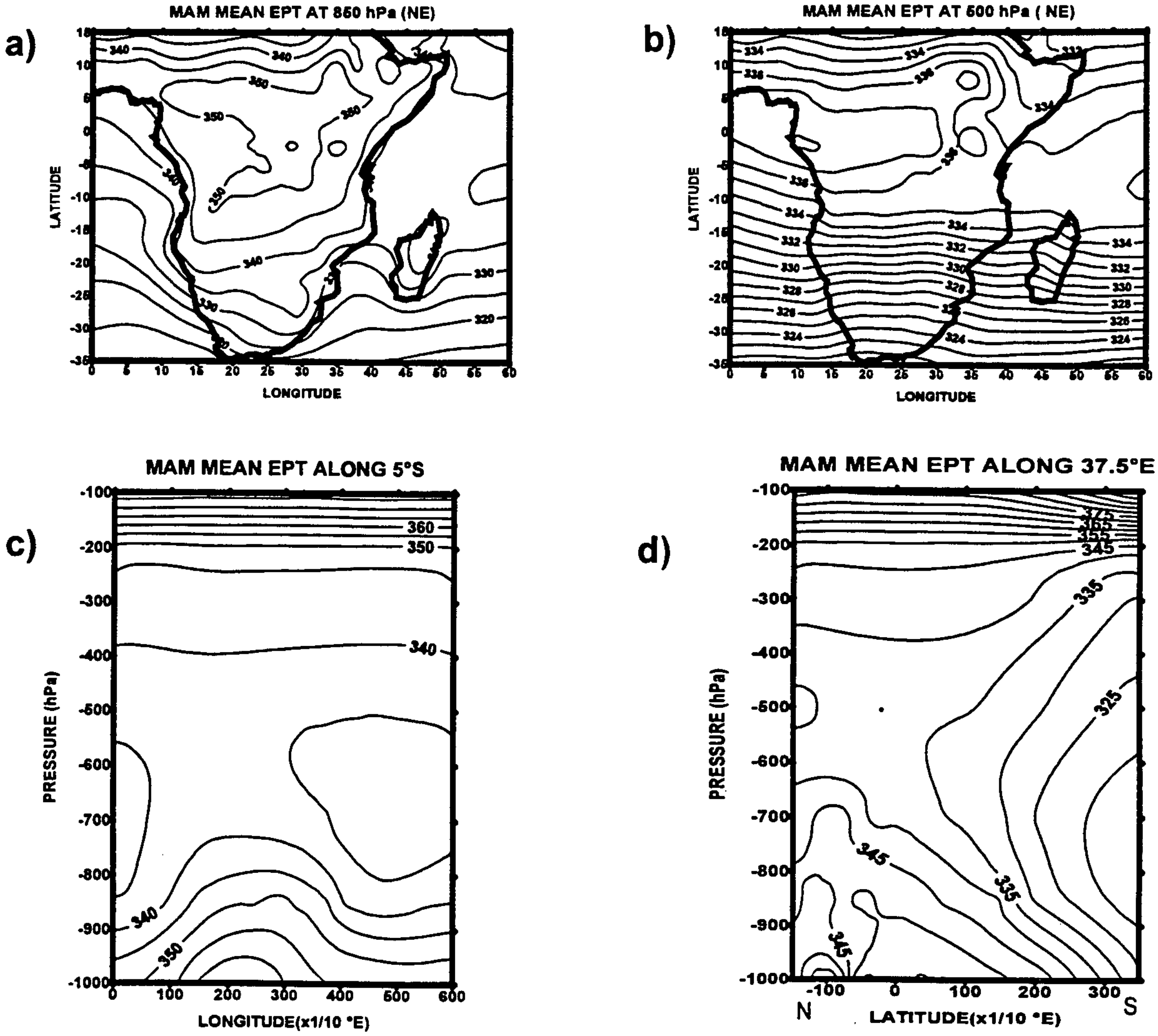

Figure 5.5: a) MAM mean EPT at 850 hPa, contour interval 5°K ; b) MAM mean EPT at 500 hPa, contour interval 1°K; c) MAM mean EPT East-West vertical section along 5°S; d) MAM mean EPT N-S vertcal section along 37.5°E, contour interval 5°K.

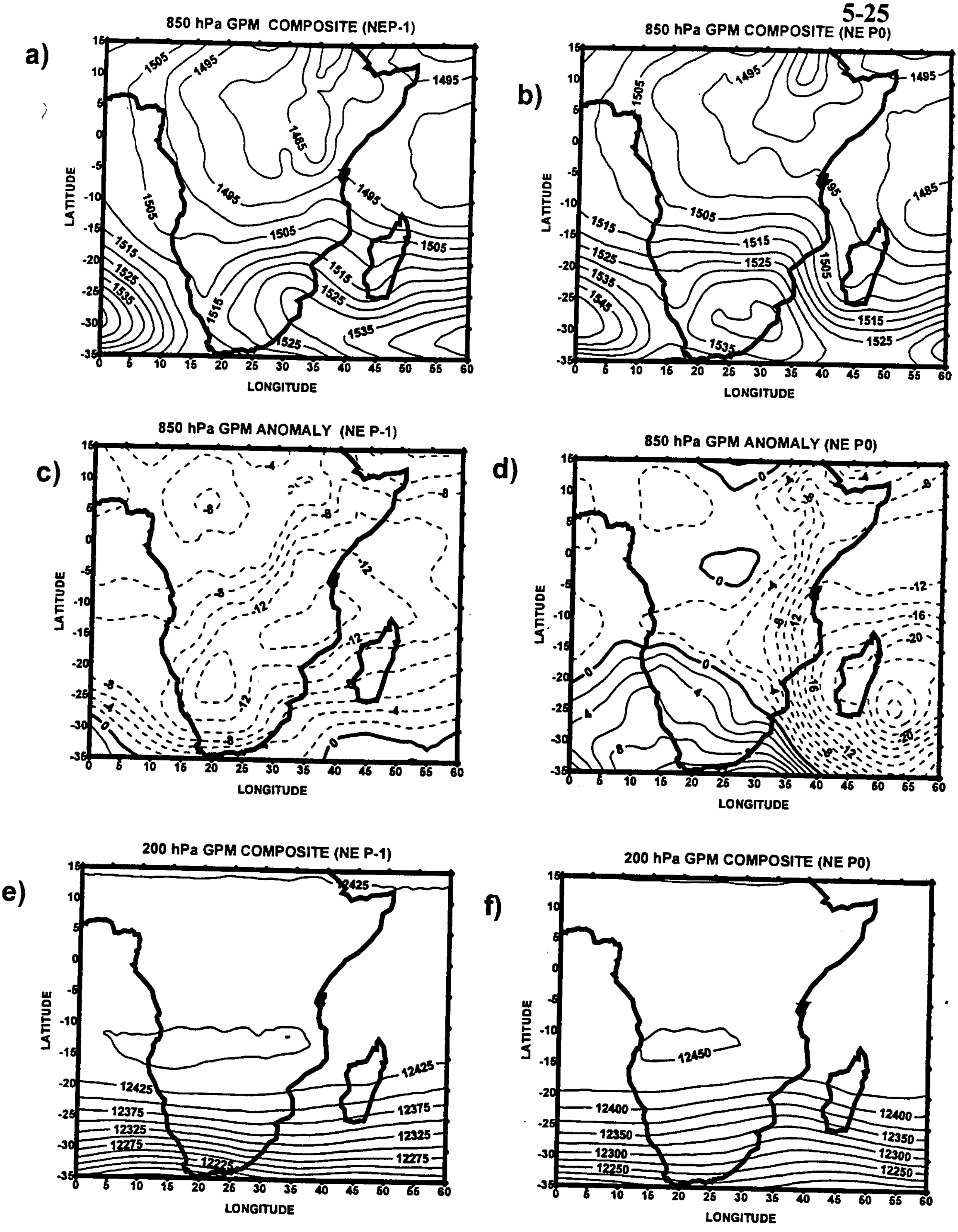

Figure 5.6: Geopotential heights for P-1 to P0. (a and b) composites at 850 hPa, contour interval 5 gpm; (c and d) anomalies at 850 hPa level, contour interval 2 gpm; (e and f) composites at 200 hPa level contour interval 25 gpm; (g and h) gpm anomalies at 200 hPa, contour interval 5 gpm

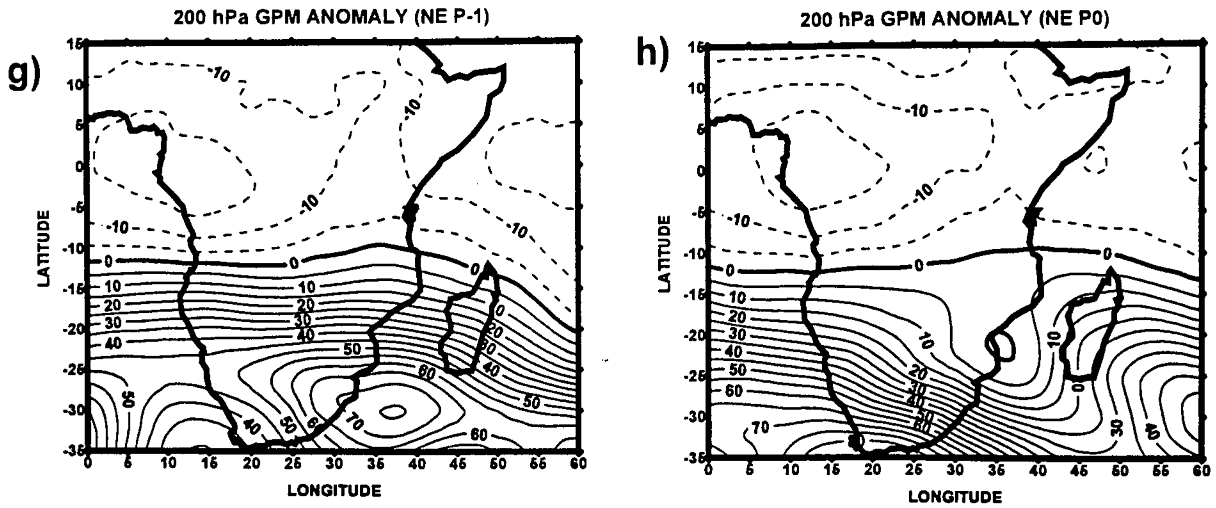

Figure 5.6 continued:

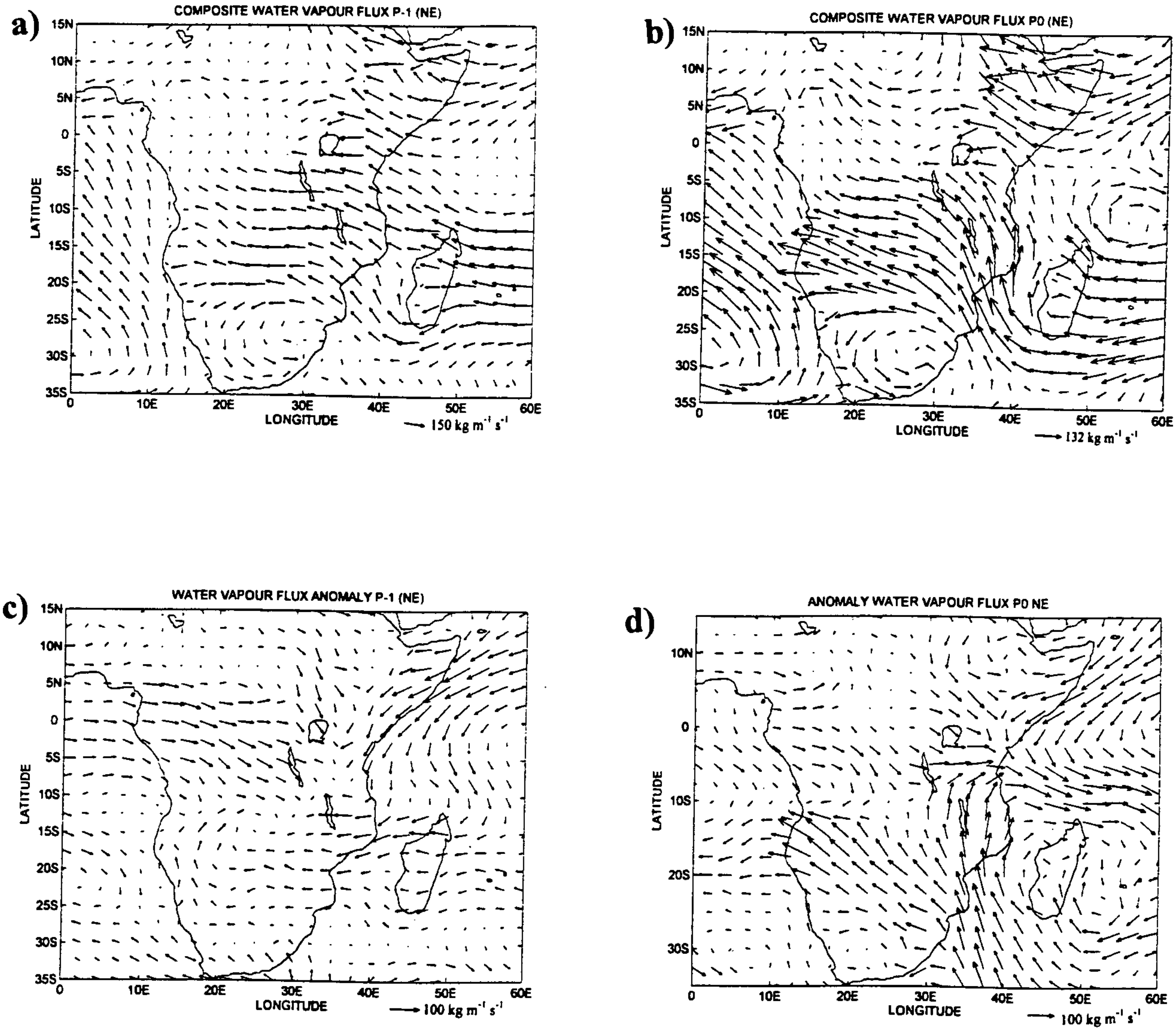

Figure 5.7: WVF and horizontal wind flow pattern at 200 hPa level for P-1 to P0. (a and b) composite WVF integrated from surface to 500 hPa; (c and d) WVF anomalies;

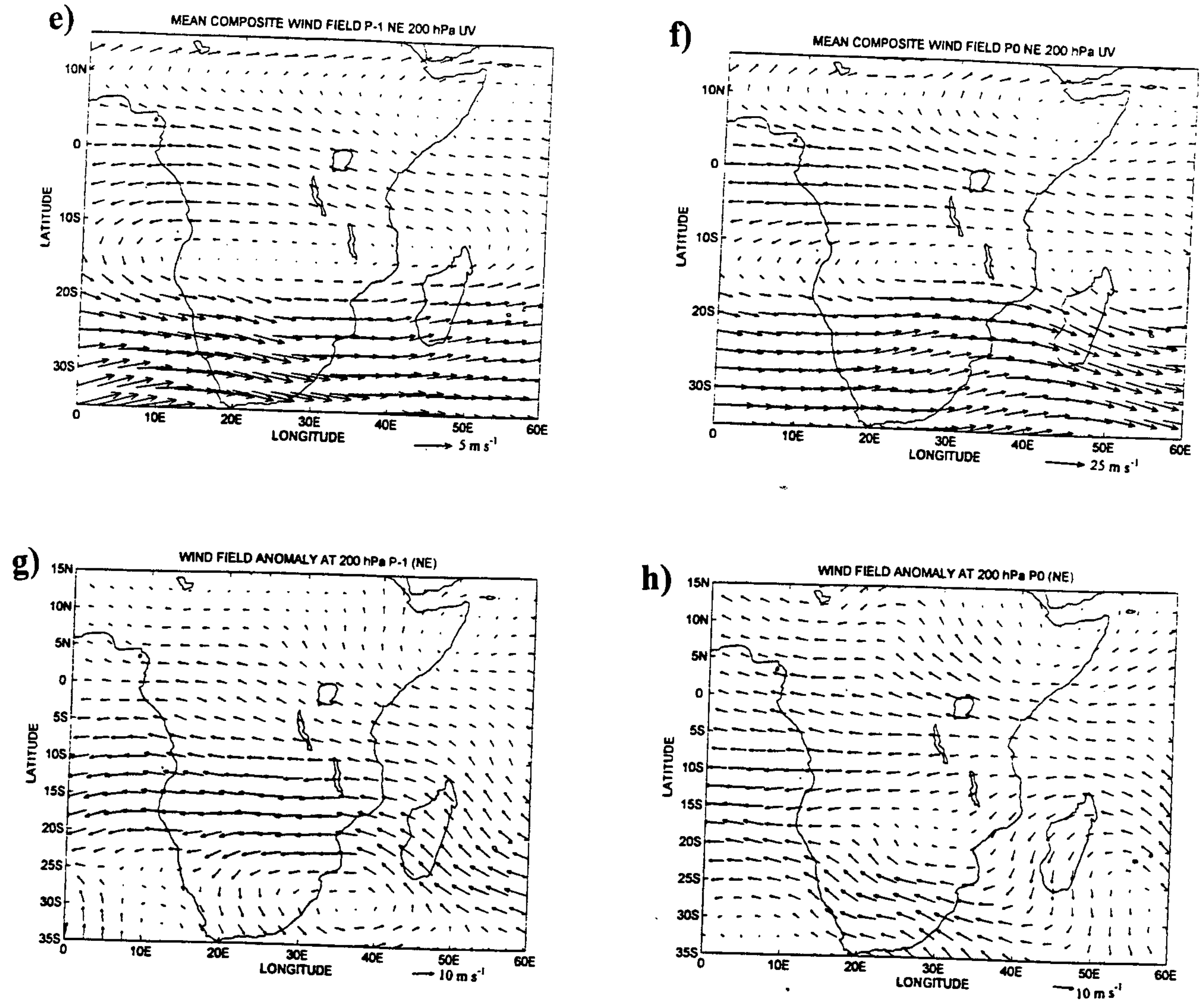

Figure 5.7 Continued: (e and f) composite flow pattern at 200 hPa; (g and h) anomaly flow pattern at 200 hPa.

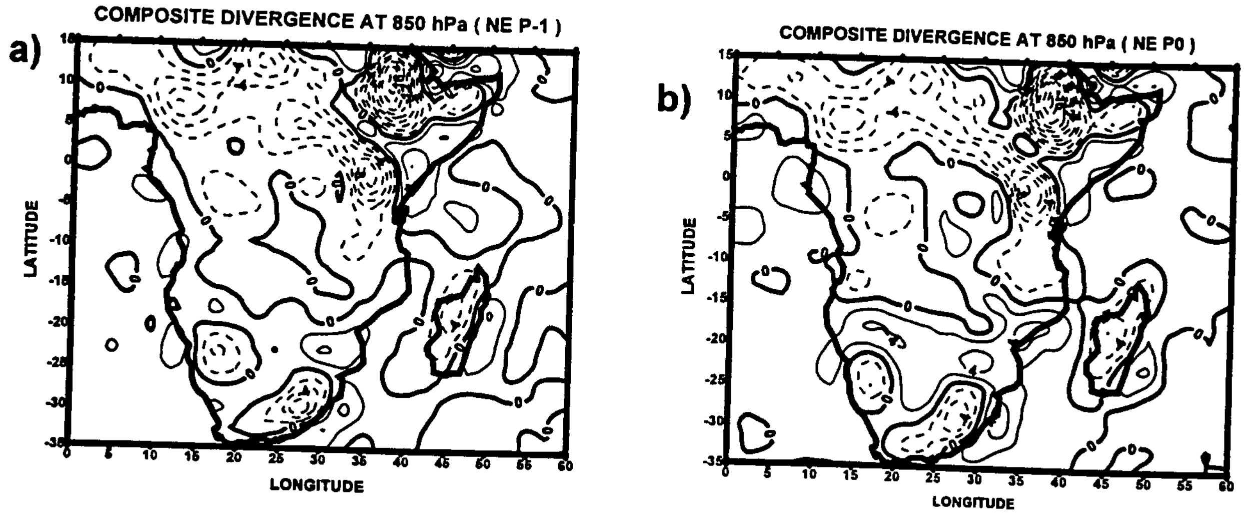

Figure 5.8: Divergence for P-1 to P0. (a and b) Composite divergence at 850 hPa; contour interval 2x10 $^{-6}$ s^{-1}; (c and d) composite anomalies at 850 hPa, contour interval .5x 10 $^{-6}$ s^{-1};

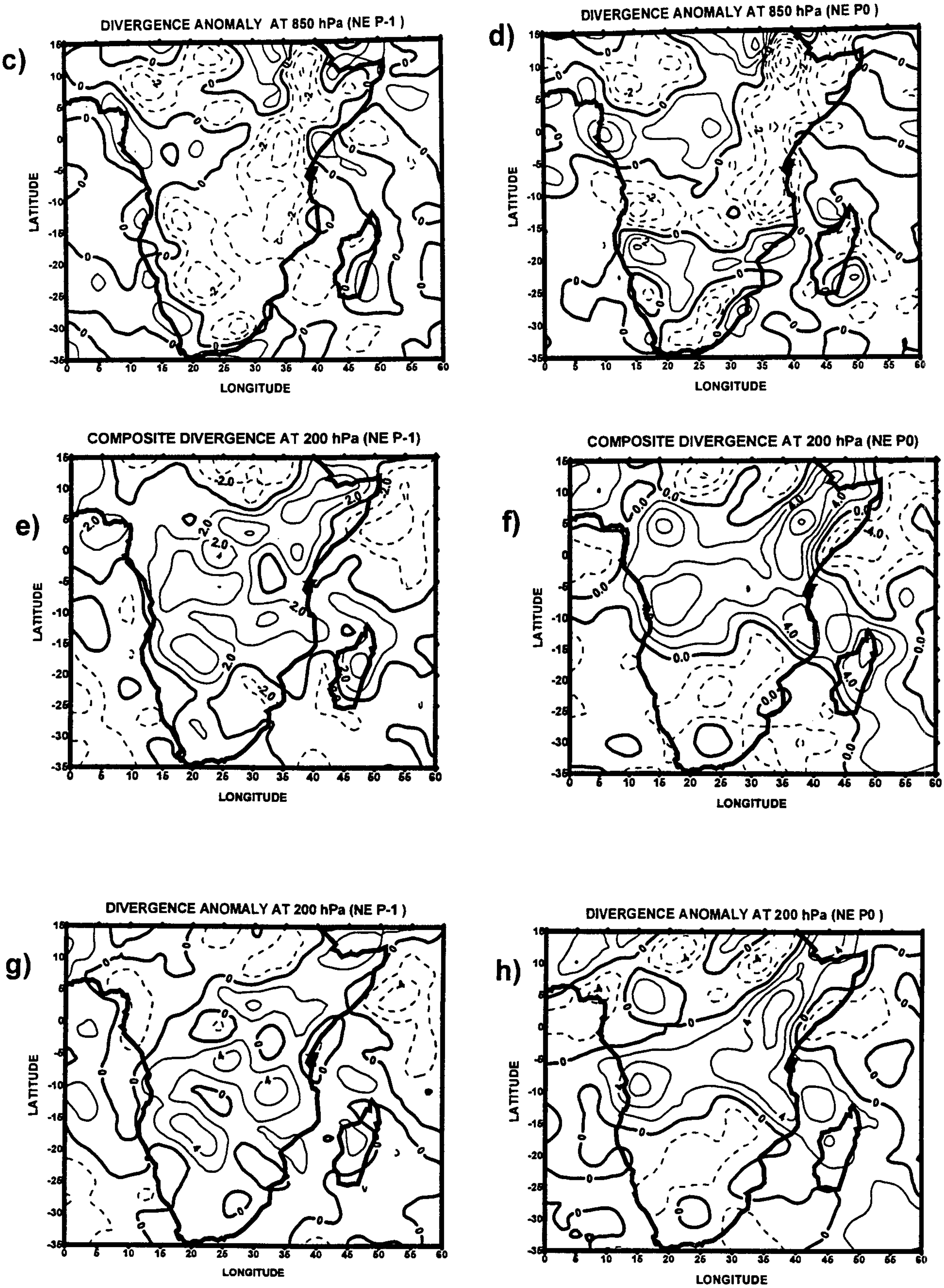

Figure 5.8 Contd: (e and f) composite divergence at 200 hPa, contour interval 2x10 $^{-6}$ s^{-1}; (g and h) composite divergence anomalies at 200 hPa, contour interval 2 x 10 $^{-6}$ s^{-1}

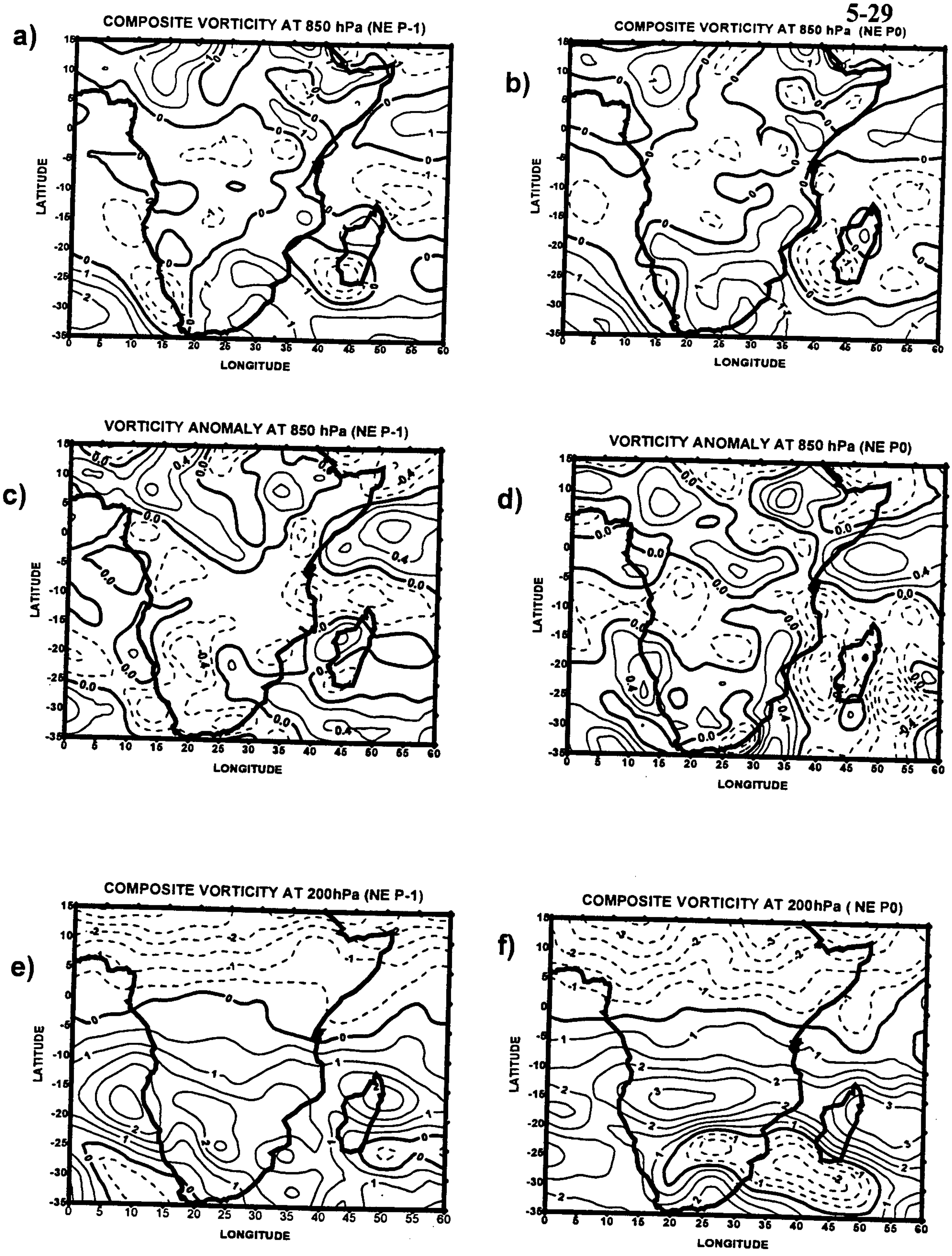

Figure 5.9: Vorticity for P-1 to P0. (a and b) Composite vorticity at 850 hPa, contour interval $1\times10^{-6}\ s^{-1}$; (c and d) vorticity anomaly at 850 hPa, contour interval $.2\times10^{-6}\ s^{-1}$; (e and f) composite vorticity at 200 hPa level, contour interval $.5\times10^{-6}\ s^{-1}$

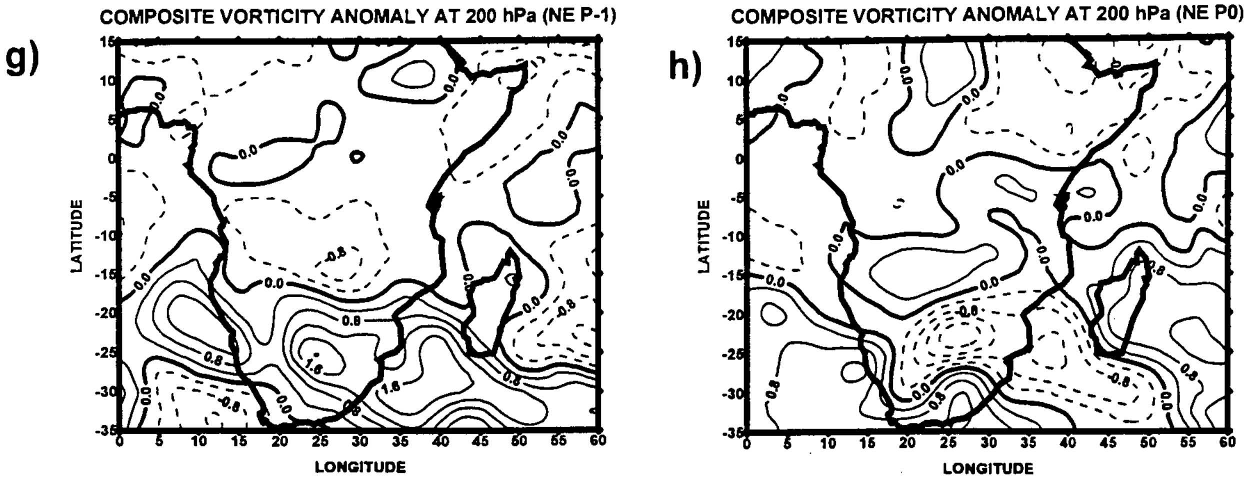
COMPOSITE VORTICITY ANOMALY AT 200 hPa (NE P-1)

COMPOSITE VORTICITY ANOMALY AT 200 hPa (NE P0)

Figure 5.9 Contd: (g and h) vorticity anomalies at 200 hPa, contour interval .2x10-6 s-1

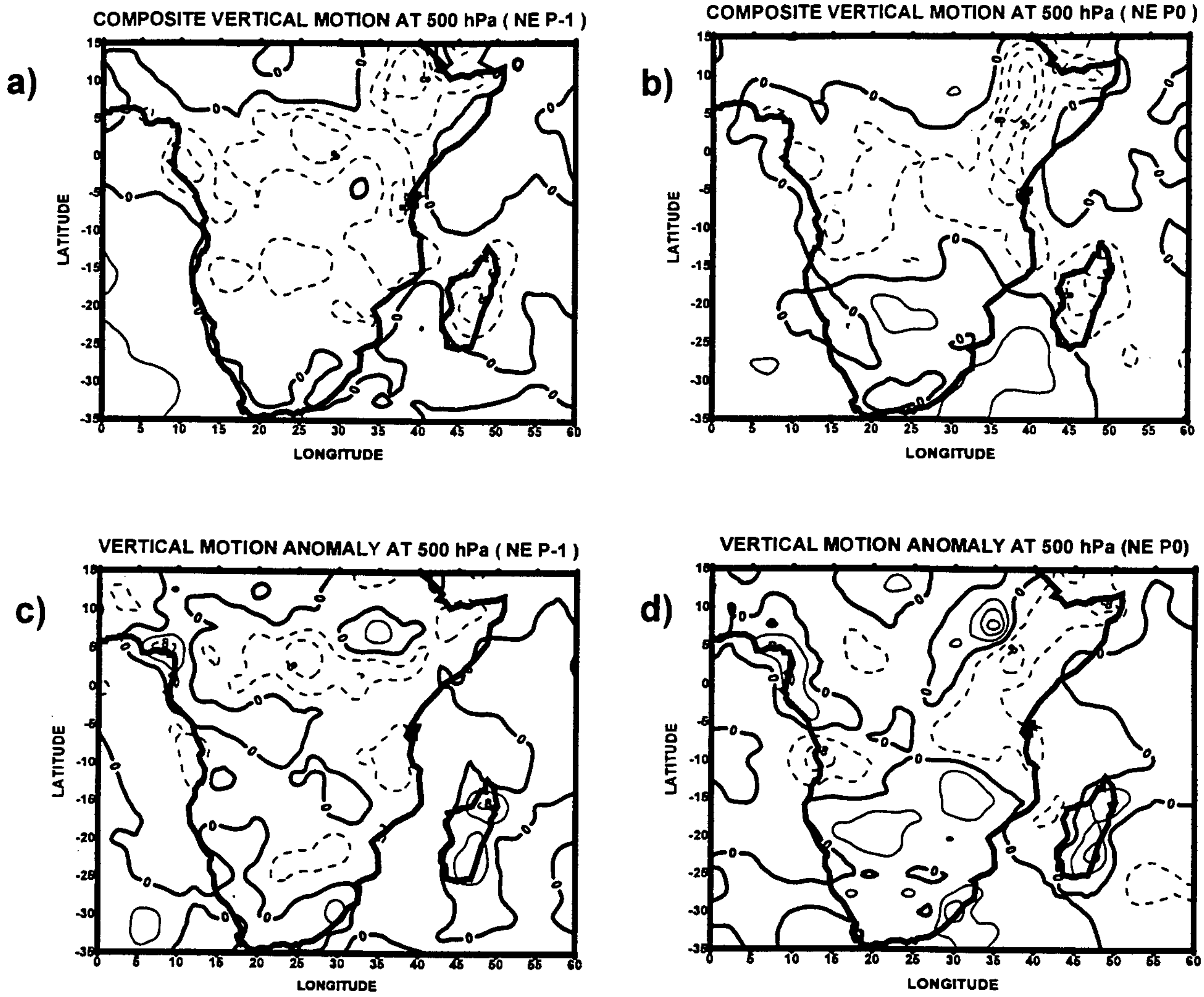
COMPOSITE VERTICAL MOTION AT 500 hPa (NE P-1)

COMPOSITE VERTICAL MOTION AT 500 hPa (NE P0)

VERTICAL MOTION ANOMALY AT 500 hPa (NE P-1)

VERTICAL MOTION ANOMALY AT 500 hPa (NE P0)

Figure 5.10: Vertical motion at 500 hPa for P-1 to P0; (a and b) Composite vertical motion; (c and d) anomaly vertical motion, contour interval 4 x10 $^{-2}$Pa/s

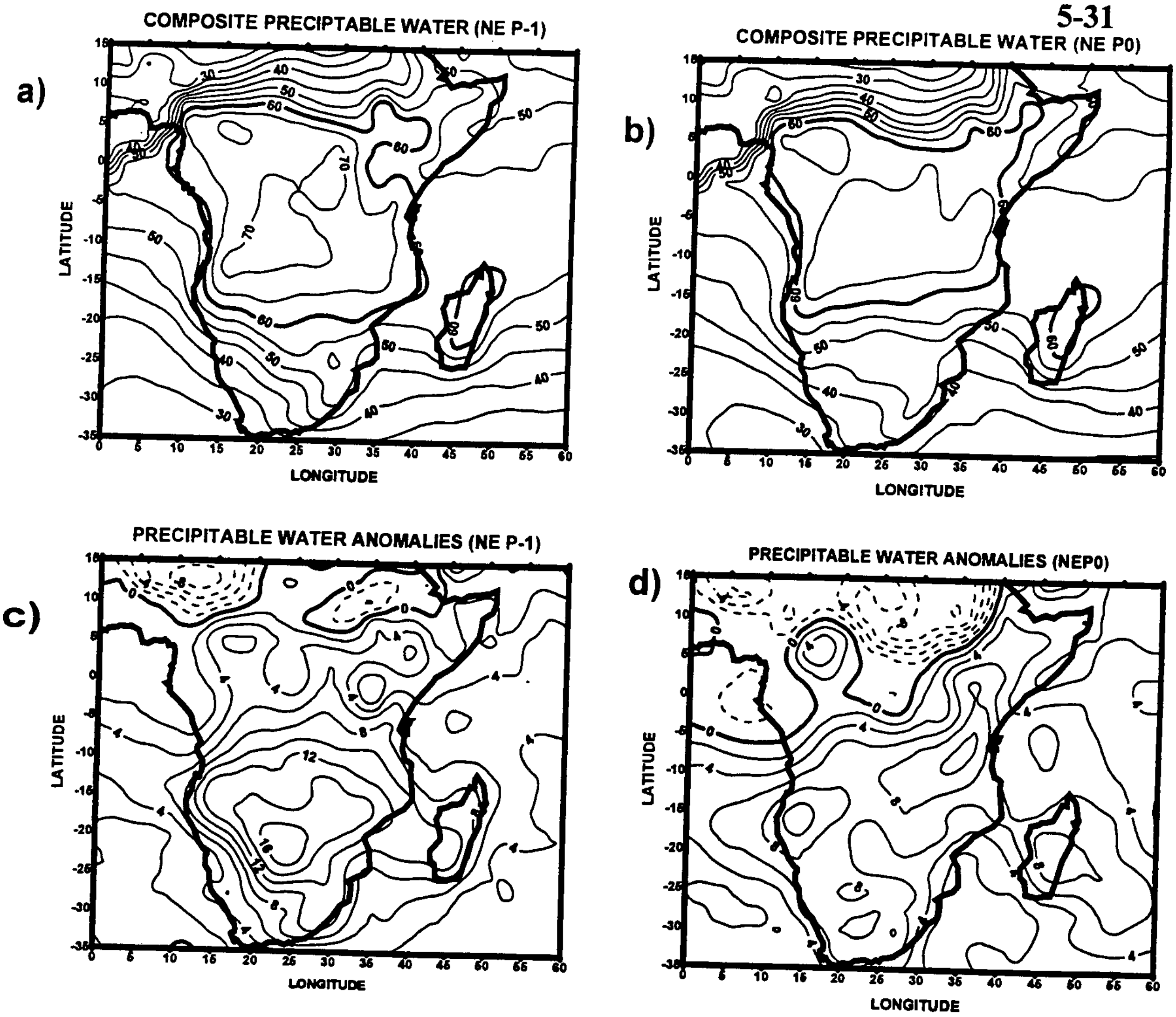

Figure 5.11: Precipitable water integrated from 1000 hPa to 300 hPa for P-1 to P0 . (a and b) Composite analyses, contour interval 5 mm; (c and d) anomaly analyses, contour interval 2 mm.

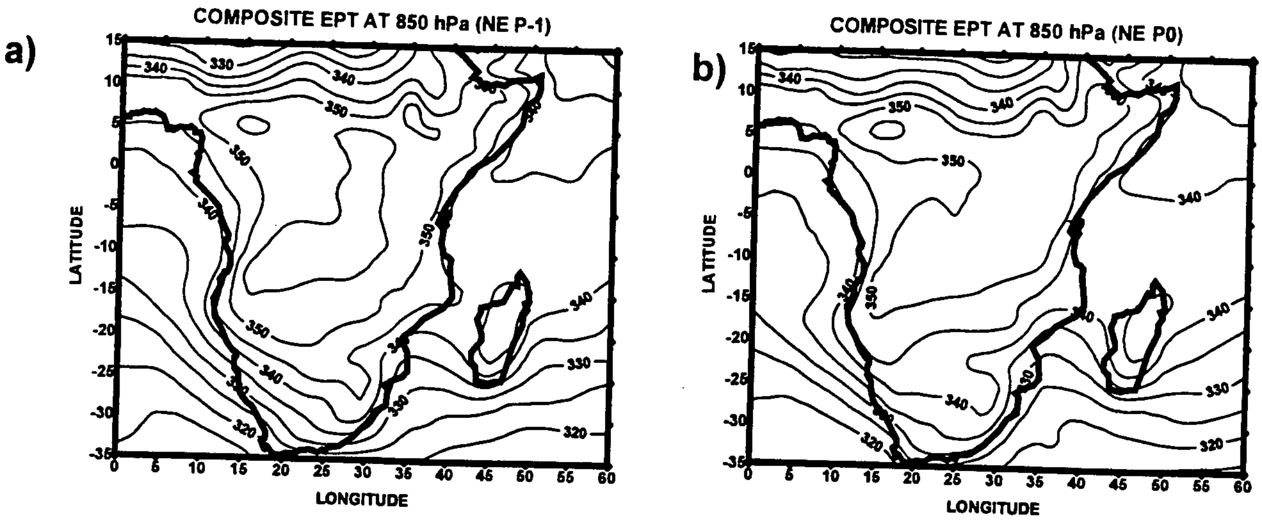

Figure 5.12: Equivalent Potential temperature. (a and b) Composite EPT at 850 hPa level, contour interval 5°K; (c and d) EPT anomaly at 850 hPa level, contour interval 1°K; (e and f) Composite EPT at 500 hPa level, contour interval 1°K; (g and h) anomaly EPT at 500 hPa, contour interval .5°K

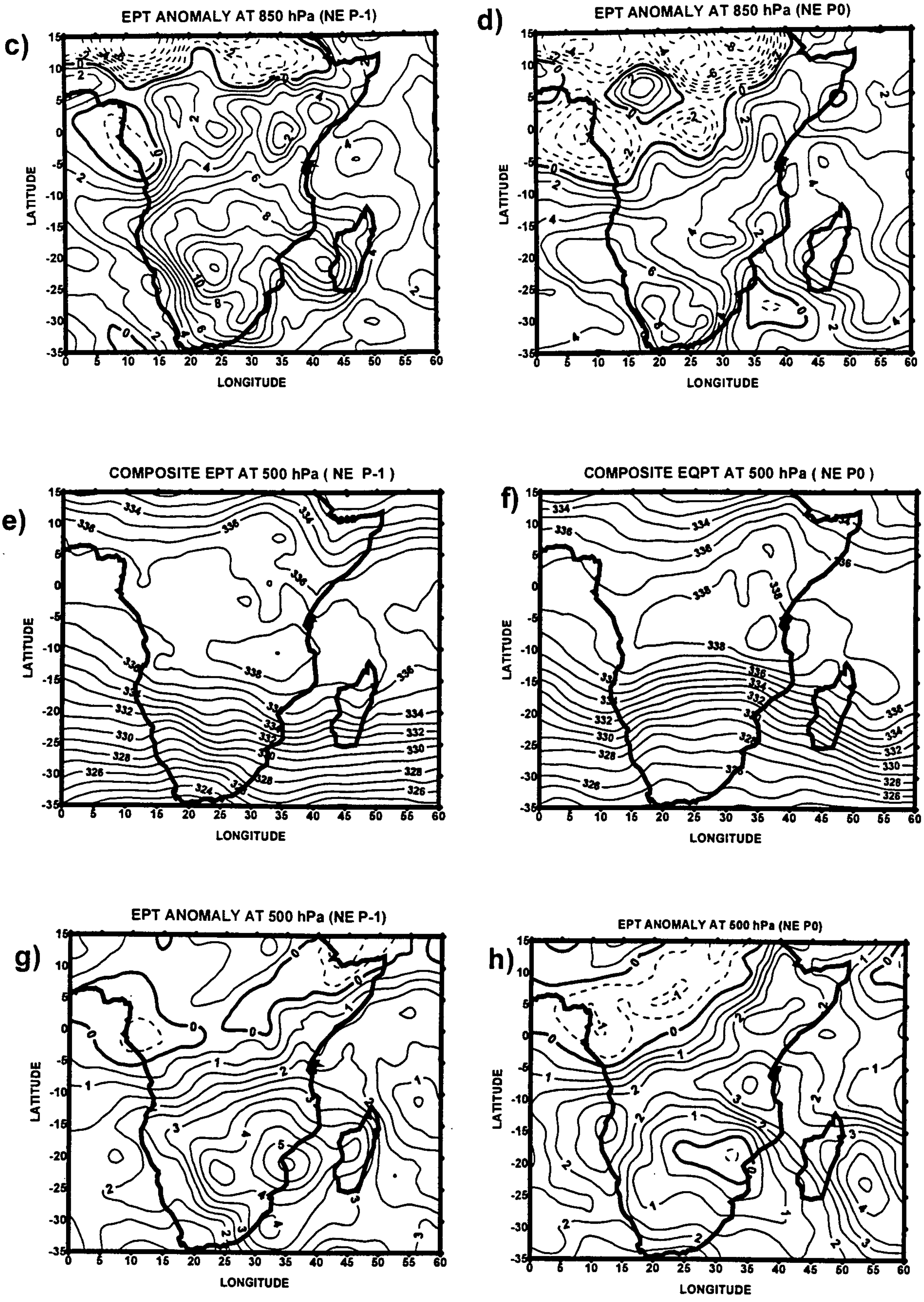

c) EPT ANOMALY AT 850 hPa (NE P-1)

d) EPT ANOMALY AT 850 hPa (NE P0)

e) COMPOSITE EPT AT 500 hPa (NE P-1)

f) COMPOSITE EQPT AT 500 hPa (NE P0)

g) EPT ANOMALY AT 500 hPa (NE P-1)

h) EPT ANOMALY AT 500 hPa (NE P0)

Figure 5.12 continued:

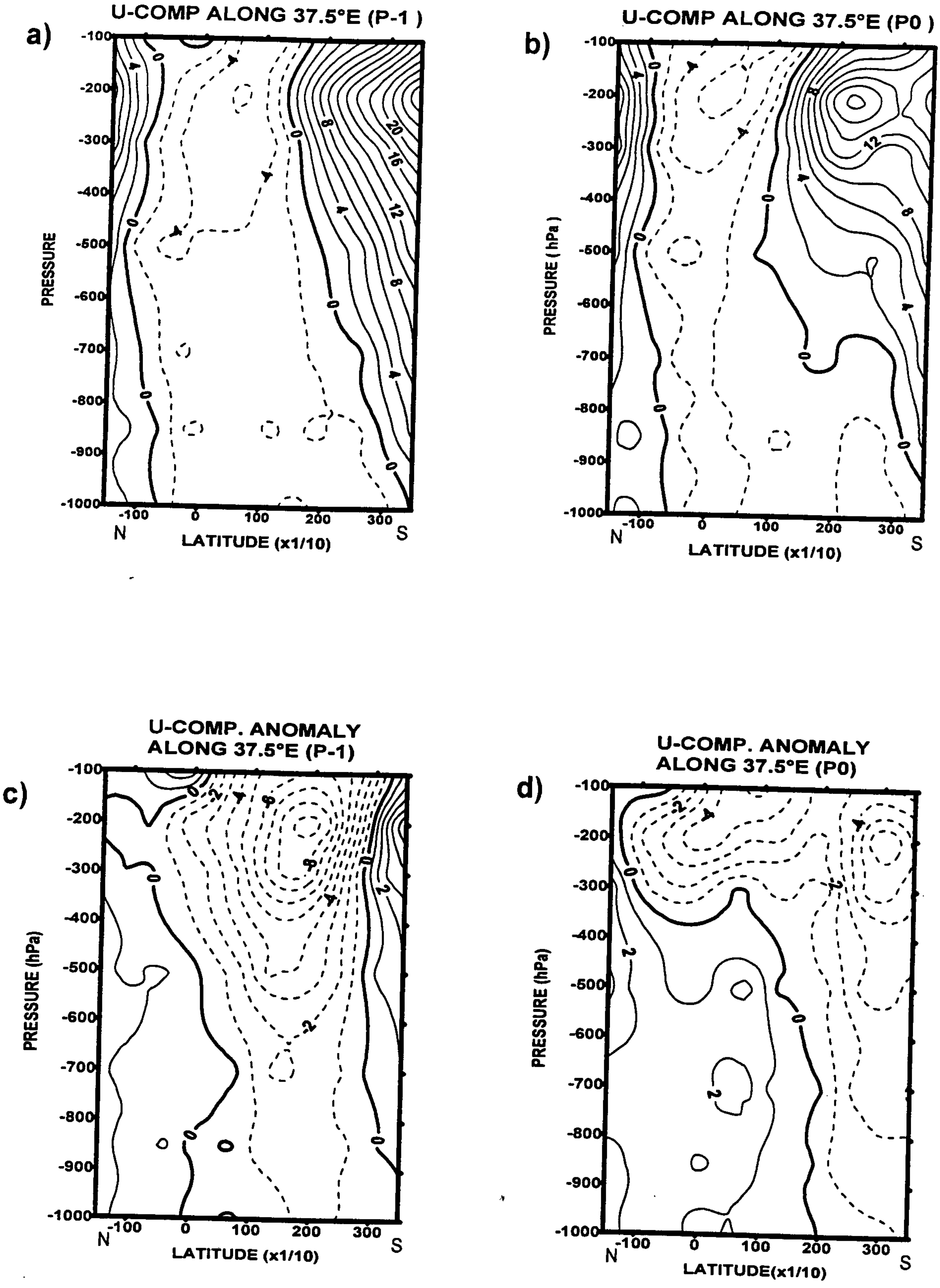

Figure 5.13:Vertical cross-section of zonal and meridional wind compnents for P-1 to P0 along 37.5°E. (a and b) zonal wind component composites, contour interval 2 m/s; (c and d) zonal wind component anomaly, contour interval 1 m/s

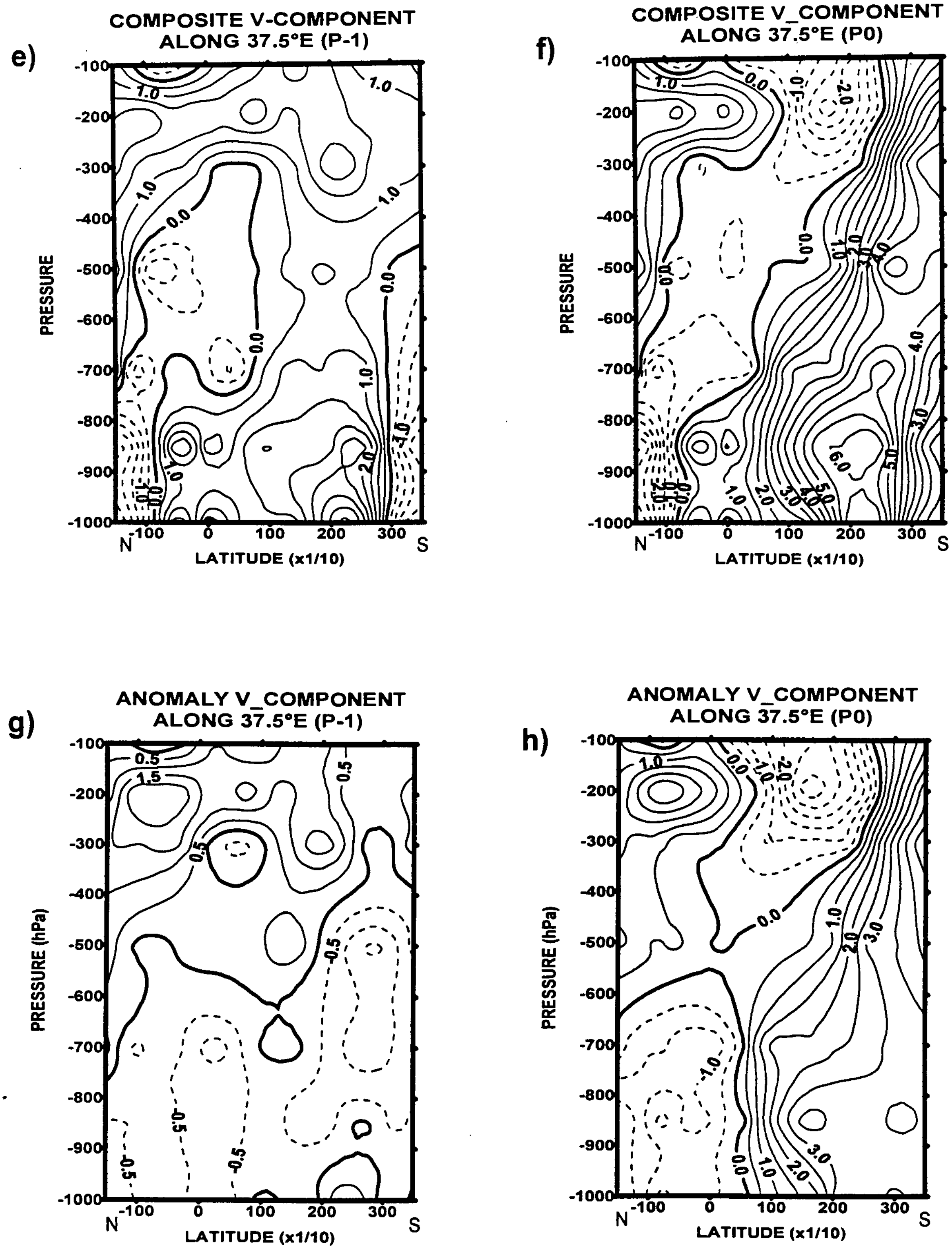

Figure 5.13 Continued: (e and f) v-component along 37.5°E, contour interval .5 m/s; (g abd h) v-component anomaly along 37.5°E, contour interval .5 m/s.

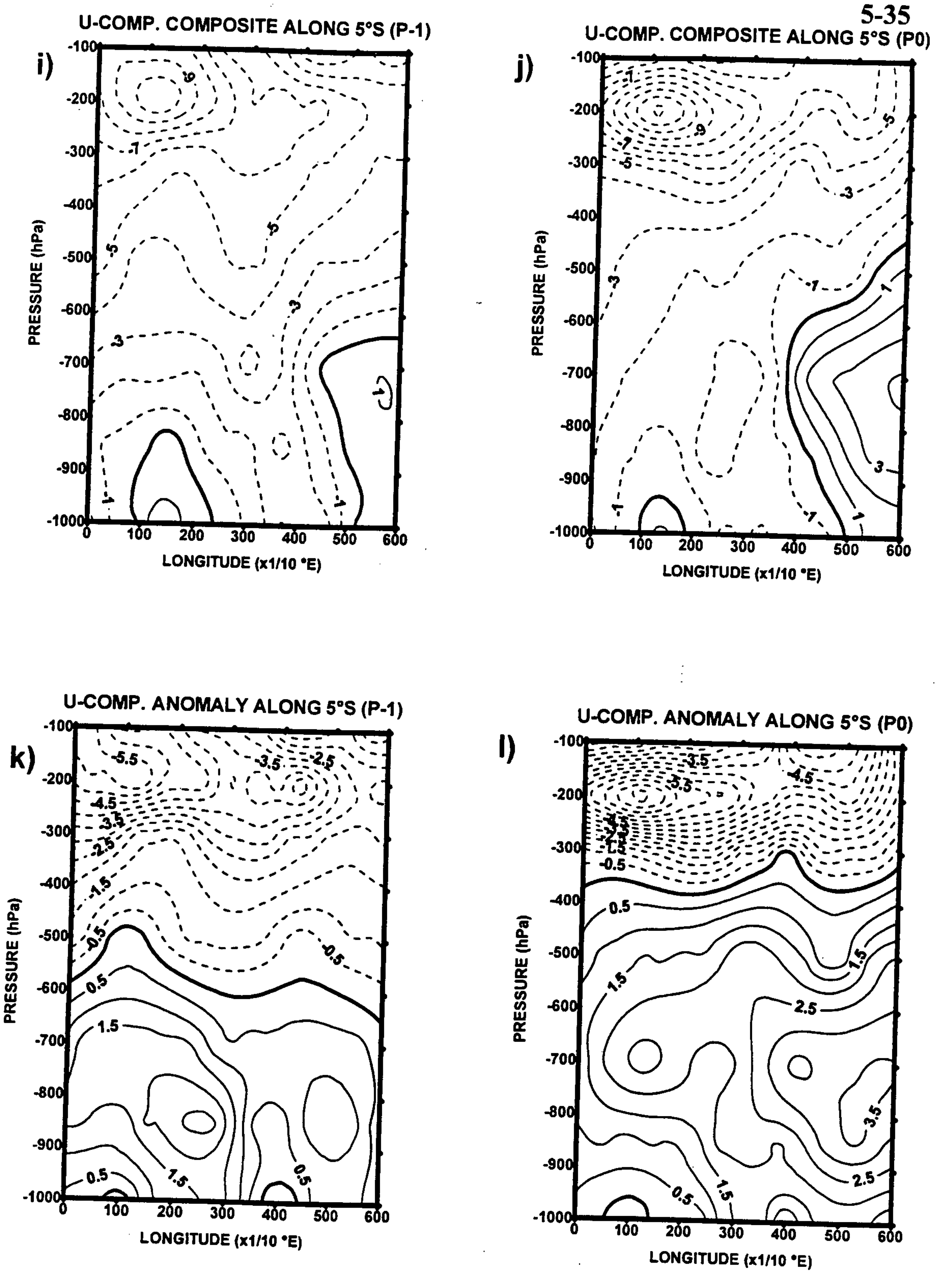

Figure 5.13 Contd: (i and j) zonal wind component along 5°S, contour interval 2 m/s; (k and l) zonal wind anomaly along 5°S, contour interval .5 m/s

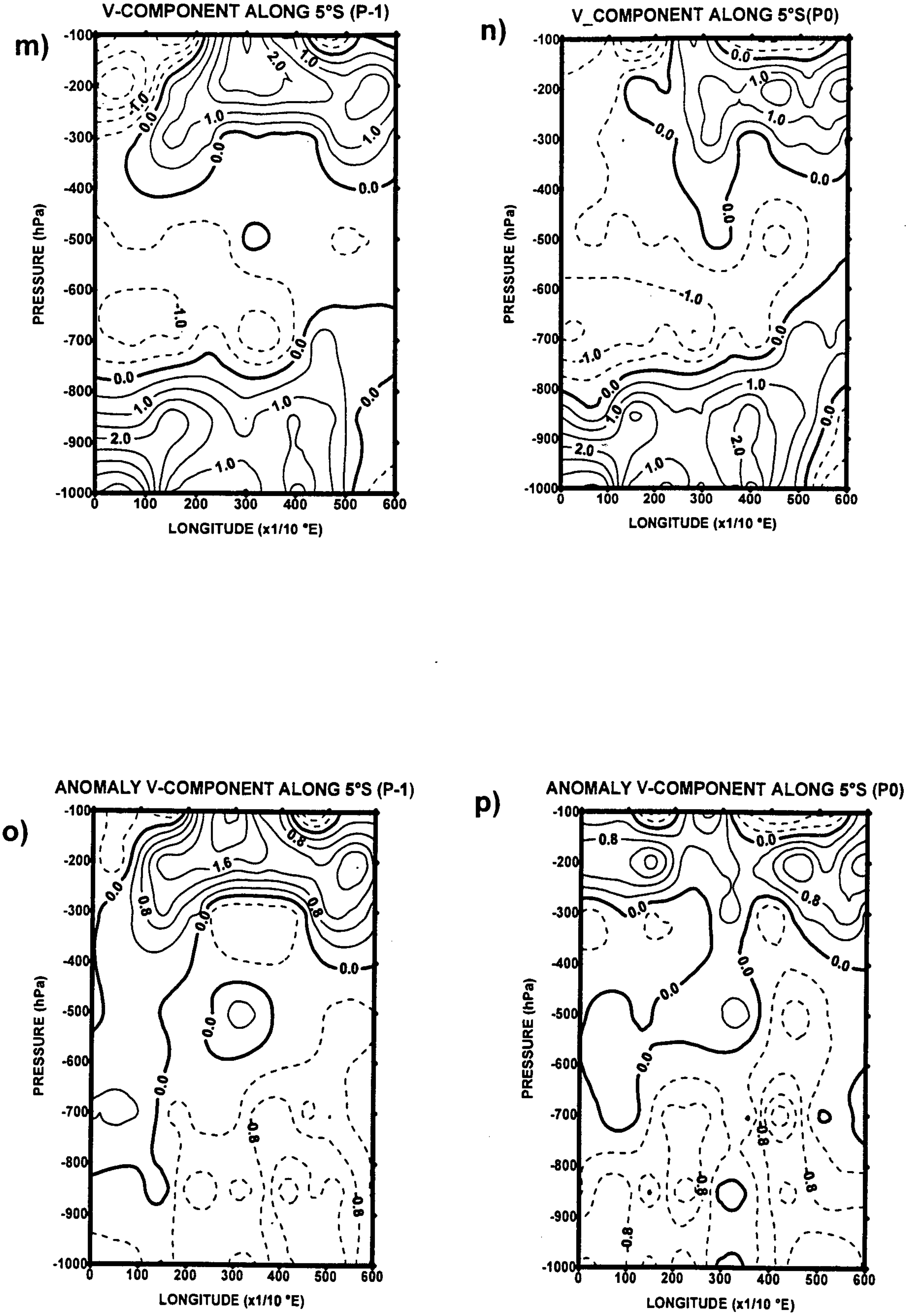

Figure 5.13 Contiuned: (m and n) v-component composite along 5°S, contour interval .5 m/s; (o and p) v-component anomaly along 5°S, contour interval 0.4 m/s.

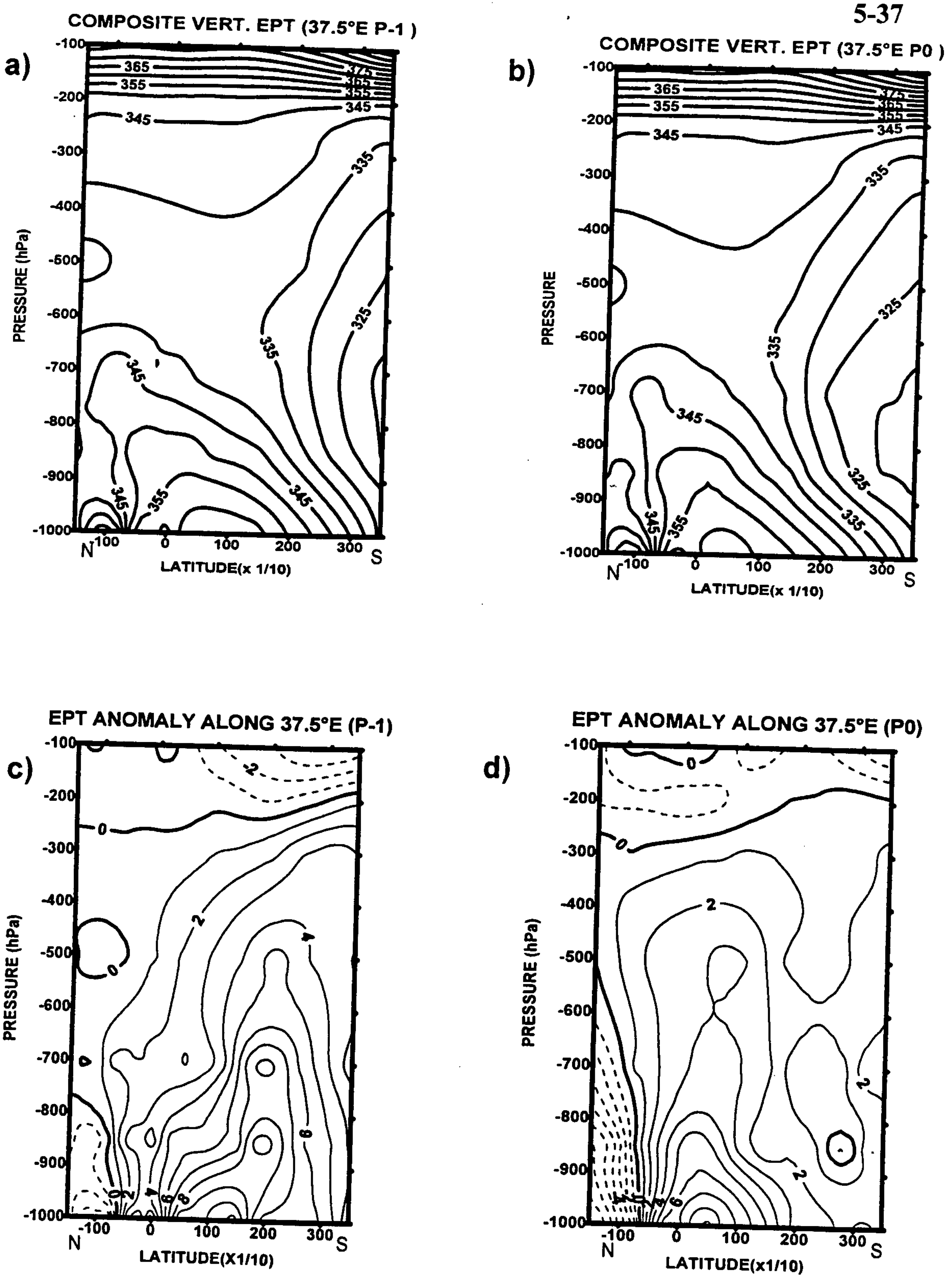

Figure 5.14:North- south vertical cross-section of EPT for P-1 to P0. (a and b) EPT composite along 37.5°, contour interval 5°K; EPT anomaly along 37.5°K, contour interval .1°K.

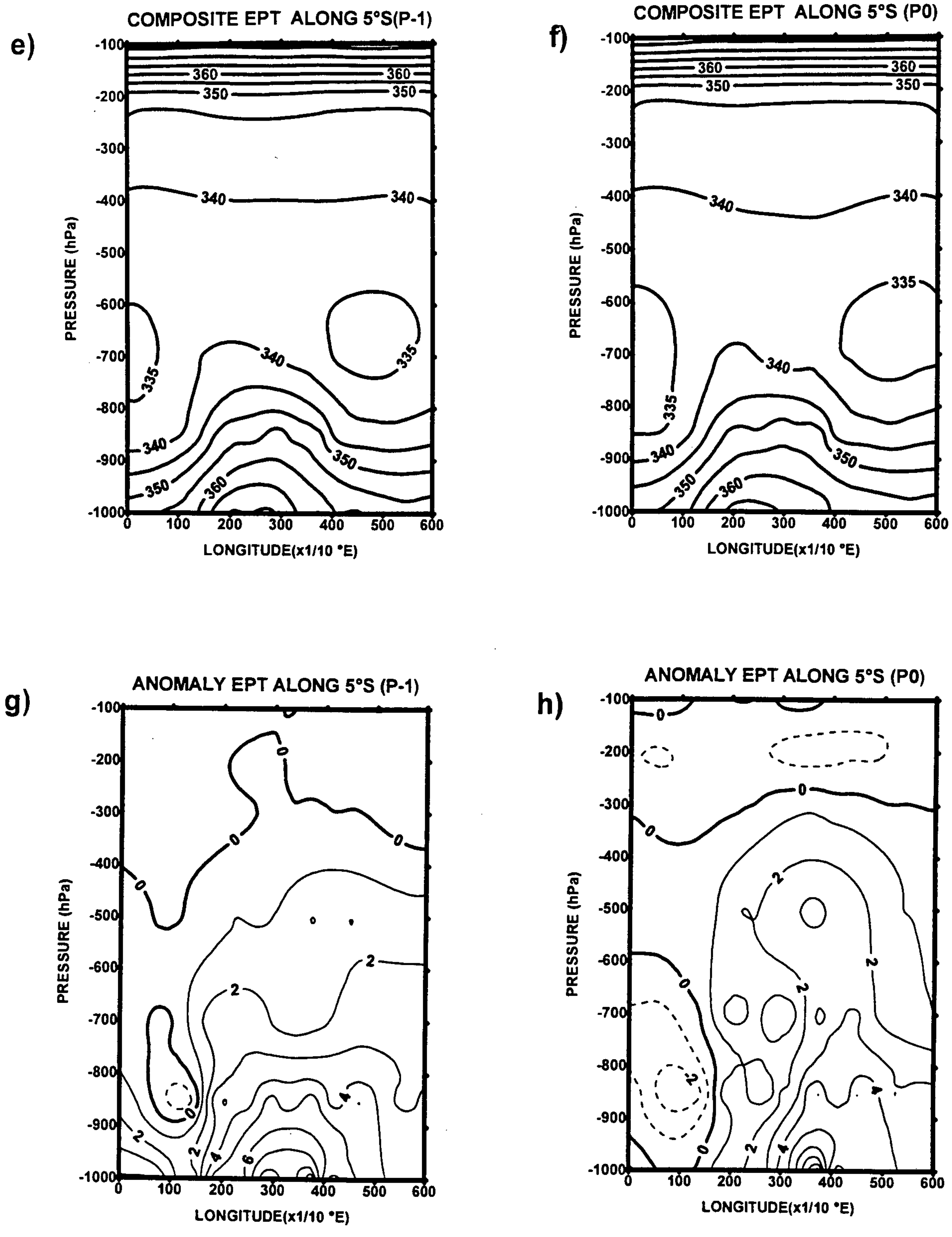

Figure 5.14: Continued: (e and d) EPT composite along 5°S, contour interval 5°K; (g and h) EPT anomaly along 5°S, contour interval .1°K

CHAPTER 6

ANALYSIS OF SYSTEM PROPAGATION

6.1 Hovmoller Analysis

6.1.1 Introduction

The analysis in this section aims at identifying the characteristics of propagating convective systems. Hovmoller or longitude-time plots are used in identifying or detecting zonally propagating systems. Parameters used in longitude-time plots are anomalies of OLR, zonal wind component at 850 and 200 hPa, and precipitable water for 1980 to 1994. The plots were for 42 pentads, i.e. from November to May. Longitude-time plots revealed some eastward and westward propagating convection and in-situ developing convection, inferred from OLR anomaly patterns. The in-situ developing convective feature is deduced from the OLR anomaly pattern which has the same sign in a latitude band such that it shows no apparent propagation. We shall refer to such patterns as non-propagating or quasi-stationary. However, many stationary features were observed to the west of 40°E and these were suspected to be due to high frequency and small weather systems over land. To suppress the high frequency (5-15 day) oscillations a Fast Fourier Transform (FFT) technique was applied using NAG subroutine. The anomalies were subjected to a 4-12 pentad (20-60 day) band filter. First a Fourier transformation was performed on the series and the real and imaginary parts of the series were made zero for periods between 1-3 pentad (5-15 day) and above 12 pentads (60 day), and finally re-computing the series via the inverse Fourier transform. Longitude-time analysis was done for the filtered OLR, zonal wind component at 850 hPa and 200 hPa, and precipitable water (mm) integrated between the 1000 hPa and 300 hPa anomalies for southwestern and northeastern regions. For southwestern areas values have been averaged over the latitude belt, 7.5°-10°S and for northeastern areas values have been averaged over the latitude belt 2.5°-5°S. Eastward and non-propagating convective systems will be selected for north-eastern and south-western areas for MAM and DJF seasons respectively. To understand the behaviour of the convective evolution associated with the two convective systems, 4 pentad phases shall be selected for analysis. Considering that the deep convection phase is P0 then two pentads P-2 and P-1 prior to deep convection and one pentad after deep convection P-1 shall be analysed for the two types of systems.

6.1.2 South-western (7.5°-10°E)

6.1.2.1 OLR anomalies

The OLR anomaly data averaged between 7.5°-10°S was filtered as described in section 6.1.1 above. Figures 6.1(a-m) illustrate longitude-time plots of filtered OLR anomalies between November-May periods for 1980/81-1992/93. In this section features in the DJF season will be discussed. The plots reveals eastward propagating negative and positive OLR anomalies as well as the westward propagating features. It is shown that most large negative anomaly values (less than -40 W m^{-2}) are to the east of 40°E while west of 40°E both negative and positive anomaly values are not large. This indicates that more active convection is over the Indian Ocean as found by other researchers like Rui and Wang, (1990). The non-propagating pattern of negative/positive OLR could be associated with the ITCZ. These patterns are more clearly seen over the Indian Ocean than over Africa. This is true for both eastward propagating features as well as non-propagating anomalies. Eastward propagating OLR anomalies are shown to occur in most years. Westward propagating features were observed in Jan81-Mar82, and Apr83-May83, while non-propagating negative anomalies are observed in Jan, 1993. Some of the propagating OLR anomalies are seen to originate west of 0° and continue east to 100°E while others seem to originate between 20°-40°E and continue beyond 100°E. This seems to confirm with the results obtained by other researchers like Levey, 1993 and others. Eastward propagating features were found to have different phase speeds in different years and over different areas. Sometimes the features move slowly then became stationary and resume propagating in the same direction. Examples of such features are in 1989. Eastward propagating features generally propagate between 2-8 m s^{-1}. Alternating negative and positive OLR anomalies are a common feature east of 40°E while west of 40°E there are a disorganised patterns. Strong meridional circulations along the East African coast likely inhibit propagation.

6.1.2.2 Zonal wind component anomalies at 850 hPa

Figures 6.2(a-m) shows longitude-time plots of filtered zonal wind component anomalies at 850 hPa between 7.5 to 10°S. Clear alternating positive and negative zonal wind anomalies and propagating features are readily identified. Eastward propagating systems are revealed in most years while westward propagating features are indicated in 1981 and 1982. The period of oscillation of positive u-component anomalies was found to be between 6 to 10 pentads. Large u-component anomaly values greater than 4 m s^{-1}, with well defined patterns are revealed east of 40°E longitude. The interaction of land surface and the 850 hPa flow may interfere with system propagation. Hovmoller plots of zonal wind at 850 hPa level may be compared with respective OLR anomaly hovmoller plots (figures 6.1a-m). It is found that the areas of large negative (strong convection) anomalies couple well with areas of strong westerly anomalies. Such an association have been revealed by Rui and Wang, (1990); Knutson and Weickmann, (1987); Hendon and Liebmann, (1991) and many others. On the average it is found that the u-component at 850 hPa and the OLR anomalies are negatively correlated, though the correlation coefficient is small.

6.1.2.3 Zonal wind component anomalies at 200 hPa

Figures 6.3(a-m) show hovmoller plots of u-component anomalies at 200 hPa. Positive and negative zonal wind components are shown to propagate eastwards as well as westwards. Westward propagating negative anomalies are shown to propagate in 1982, 1983, 1984 and 1986. Some years like, 1983/84 and 93/94, are dominated by easterlies at the 200 hPa level. Eastward propagating negative/positive anomalies are revealed in most years. On comparing eastward propagating OLR anomaly and u-component anomaly at 200 hPa in the hovmoller plots it is found that large negative OLR values (deep convection) are coupled with negative zonal wind (easterly) anomalies. It is also observed that the zonal wind at the 200 hPa level is out of phase with winds at the 850 hPa level, typical of convectively driven regimes, similar to observations made by Hendon and Liebmann, (1990).

6.1.2.4 Precipitable Water anomalies

Figures 6.4(a-m) presents longitude-time plots of precipitable water anomalies averaged between 7.5°S and 10°S latitude. The plots do not reveal propagating features clearly. However, alternating positive and negative precipitable water anomalies are revealed and indicate aperiodic oscillations. 1992/93 and 1993/94 are dominated with negative precipitable water anomalies. Eastward and westward propagating positive/negative precipitable water anomalies correspond with strong eastward and westward propagating negative/positive OLR anomalies respectively.

6.1.3 Northeastern (2.5°-5°S)

6.1.3.1 OLR anomalies

Figures 6.5(a-m) reveal hovmoller plots of filtered OLR anomalies averaged between 2.5°S and 5°S. The filtering was done as described in section 6.1.1. More defined alternating negative and positive OLR anomaly patterns are revealed to the east of 40°E with eastward propagating features indicated in most years. To the west of 40°E negative/positive anomaly pairs are rather disorganised partly due to orographic influence. It is found that about 1 to 2 negative OLR anomalies transit the latitude band during MAM with an average period of about 6 to 7 pentads. Some of these propagating features seem to be originating within 20°-30°E while few of them seem to emerge west of the 0° longitude. Areas with large negative values, i.e. with values less than -40 W m^{-2} are located to the east of 40°E, over the Indian Ocean. It is noted that eastward propagating patterns are more frequent than westward propagating ones. Westward propagating OLR anomalies can be observed in March-April, 1992 and April-May, 1983. The phase speed of eastward propagating patterns is found to be between 1.7-6.4 m s^{-1}. An interesting situation is observed in March-April, 1992, when an eastward propagating negative anomaly interacts with a westward propagating system between pentad 31 and 34, within longitude 40°-50°E. The two systems seem to continue with their opposing propagation, undeterred, thereafter.

6.1.3.2 Zonal wind component anomalies at 850 hPa

Hovmoller plots of zonal wind anomalies are shown in figures 6.6(a-m). The plots reveal alternating positive and negative zonal wind anomalies. More eastward propagating cells occur in comparison to westward ones. When plots of figure 6.5(a-m) are compared with respective plots of figure 6.6(a-m) it is noted that large negative/positive OLR anomalies are coupled with westerly/easterly wind anomalies. Over land, i.e. between 15°E and 40°E the zonal wind anomalies are weak and do not show any definite pattern. As explained above this could be attributed to orography.

6.1.3.3 Zonal wind component anomalies at 200 hPa

Figures 6.7(a-m) present longitude-time plots of zonal wind component anomalies. The plots reveal alternating positive and negative cells with an average oscillation period between 6 to 7 pentads. Some years are dominated by negative (easterly) anomalies e.g. 88/89 and some years are dominated by positive (westerlies) e.g. 81/82. It is also observed that most propagating features moves all the way from 0° to 100°E. When compared with respective OLR anomaly plots (figures 6.5(a-m)) it is found that areas of large negative OLR anomalies (deep convection) are coupled with strong negative (easterly) anomalies, a good example is figure 6.5h, and figure 6.7h, between March-April, 1988. Strong u-component anomalies are revealed east of 40°E.

6.1.3.4 Precipitable Water

Figures 6.8(a-m) shows longitude-time plots of precipitable water anomalies. Alternating positive/negative precipitable water anomaly patterns are revealed. Eastward and westward propagating precipitable water anomalies correspond with large OLR anomalies. While westward propagating precipitable water anomalies are short lived, some eastward propagating cells consistently move from 0° to 100°E. This shows that areas of high precipitable water are areas with deep convection. Also precipitable water anomalies are in phase with large positive zonal wind anomalies at 850 hPa and out of phase with negative zonal wind anomalies at 200 hPa during intense or deep convection.

6.2 Spatial temporal sequence analysis

6.2.1 Introduction

Longitude-time analysis of OLR, u-component winds at 850 hPa and 200 hPa and precipitable water anomalies have revealed a number of characteristics: eastward and westward moving and quasi-stationary convective features. In this section the kinematics and thermodynamic spatial patterns associated with the observed features are studied. Eastward and non-propagating or quasi-stationary convective systems will be selected over the northeastern and southwestern areas for MAM (March-April-May) and DJF (December-January-February) seasons respectively. To understand the behaviour of the convective evolution, 4 pentad phases are selected. Considering that the deep convection phase is P0 then two pentads, P-2 and P-1 prior to deep convection and one pentad after deep convection (P+1) are considered. OLR, geopotential heights at 850 hPa, horizontal winds, at 850 hPa and 200 hPa level, precipitable water, and divergence at 200 hPa shall be analysed.

SOUTHWESTERN AREAS				
YEARS	P-2	P-1	P0	P+1
S-1993	P01	P02	P03	P04
P-1981	P66	P67	P68	P69
NORTHEASTERN AREAS				
	P-2	P-1	P0	P+1
S-1990	P09	P10	P11	P12
P-1988	P14	P15	P16	P17

Table 6.1: Selected pentads for case study. P01 = pentad 1, S- Stationary, P-Propagating.

6.2.2 Southwestern area

6.2.2.1 Outgoing Longwave Radiation

Figures 6.9(a-d) show the spatial pattern and temporal progression from P-2 to P+1 associated with non-propagating OLR anomalies. The anomalies were obtained by subtracting the 1980-94 January mean from pentad OLR values. The left penal figure 6.9(a-d) shows the time evolution of OLR anomalies from pentad 1 to pentad 4 of 1993. At P-2 negative OLR anomalies are located over the continent between 10° and 20°S and positive OLR anomalies are found over Tanzania. At P-1 large negative OLR anomalies are shown off the coast of Tanzania and between 10° and 20°S. A steady eastward push of negative OLR anomalies is indicated from pentad P-1 to P+1 as positive OLR anomalies develop over southern and north-western Africa. Spatial evolution of OLR phases from pentad 66 to pentad 69 of 1981 for the eastward propagating case is shown in the right hand panel of figure 6.9 (e-h). The anomalies were obtained by subtracting the 1980-93 November-December mean from pentad OLR values. At P-2 positive OLR anomalies are depicted over East Africa while at the same time a northwest-southeast oriented OLR anomaly band from the gulf of Guinea to the southern Indian Ocean is observed. Eastward propagation of the negative OLR anomaly band is seen from pentad P-1 to P0.

6.2.2.2 Geopotential Heights at 850 hPa

The left panel of figure 6.10 show geopotential heights contours at 850 hPa level associated with the negative OLR non-propagating (convective) features between 7.5° and 10°S, for pentad 1 to pentad 4 of 1993. At P-2 a trough is depicted over central Africa and a ridge over eastern Africa south of the equator. With the collapse of the ridge over Eastern Africa and intensification of the Atlantic anticyclone and pressure rise over Northwest Africa, the trough over Africa moves eastwards from pentad P-1 to P+1 similar to Lyons, (1991). The trough over Africa seems to move eastward in sympathy with an extra-tropical trough from pentad P-1 to P+1. The Arabian ridge is relaxed from P-2 to P0. Figures 6.10(e-h) reveals the spatial sequence of geopotential heights from pentad 14 to pentad 17, at 850 hPa, associated with an eastward propagating convective system between 7.5° and 10°S. At P-2 low geopotential heights are located over Madagascar and over Angola and Namibia with generally low geopotential heights over central Africa. Geopotential falls are observed from pentad P-1 to P+1 with simultaneous geopotential rises to the west thus 'pushing' convective activity to the east. The ridge axis of the southern hemisphere anticyclones are more zonal from pentad P-1 to P+1, figures 6.10 (f-h).

6.2.2.3 WVF and Wind Flow Pattern at 200 hPa

Water vapour flux field for a non-propagating negative OLR depicted between 7.5° and 10°S (convective) case for P-2 to P+1 are presented in figure 6.11(a-d), left panel. At P-2 moisture supply to the continent is mainly from the northeasterly monsoon and south-easterly trade winds from the Indian Ocean. Water vapour flux confluence is revealed over the continent along 17°S and over Madagascar. At P-1 a northwest-southeast convergence zone is observed over the western part of the continent. At P0 a convergence zone is revealed from the gulf of Guinea to Madagascar, across Africa. This convergence zone shifts northeastward from P-2 to P+1. Westerly wind flow, between 0° and 10°S starts appearing at P-1 over the west coast of Africa. The spatial temporal sequence of WVF for pentad 66 to 69 in 1981 are presented in the right panel of figure 6.11(e-h). These patterns are associated with a propagating convective feature in the 7.5-10°S latitude band. At P-2 there is a northeasterly WVF flow across East Africa and a cyclonic flow over Namibia and Angola. Southeasterly and northeasterly WVF converges over northern Mozambique, Malawi and western Tanzania at P-1. Figure 6.11g reveals a northwest-southeast WVF confluence zone over western Tanzania and northern Mozambique. The confluence zone shows a steady northeastward shift from P-1 to P+1.

The evolution of wind flow patterns from pentad 1 to 4 of 1993, at 200 hPa level, are shown in the left panel of figure 6.12(a-d). Diffluent flow is located over the Congo basin at both P-2 and P-1. Slightly stronger easterly winds are located over the coast of Angola and Zaire. A cyclonic flow centred over northwest Tanzania could be associated with mountain waves as suggested by Semazzi, (1980). A cross equatorial flow is dominant at P0 and easterly winds are weak over the central west coast of Africa. At P+1 relatively strong southeasterlies are observed over the coast of East Africa. A steady eastward shift of the southern anticyclone is noted from P-2 to P+1. This is accompanied with the meridional expansion of easterly winds. The time evolution of horizontal wind flow patterns at 200 hPa level are presented in 6.12(e-h) right panel. At P-2, an anticyclonic flow is located over southern Africa with its centre at 27°E, 20S with a trough to the East of Madagascar along 55°E. In the northern hemisphere two anticyclonic systems are indicated, one centred over Kenya and another at 12°E, 6°N. Easterly winds between 0° and 15°S are observed over the continent. At P-1, the anticyclone shifts northeastwards to 32°E,15°S. A northeasterly cross-equtorial flow is revealed over central Africa. A weak anticyclonic circulation is noted over Tanzania at P0. Eastward shift of features is noted within the tropics

6.2.2.4 Divergence at 200 hPa

Spatial temporal progression of divergence field patterns at 200 hPa level, from pentad 1 to pentad 4 of 1993, associated with a non-propagating negative OLR (convective) case between 7.5 to 10°S are presented in figures 6.13(a-d), left panel. At P-2 positive divergence values are indicated over west-central Africa and negative divergence over East Africa. Between 5° and 15°S an eastward push of positive divergence (suggesting low level convergence which can be associated with convection) is revealed from pentad P-1 to pentad P+1. Divergence field patterns associated with an eastward propagating case from pentad 14 to pentad 17 of 1981 are shown in figure 6.13(e-h), right panel. At P-2, positive divergence at 200 hPa is observed over Zaire and Angola. At P-1 positive divergence is seen to spread eastwards. Movement of positive divergence values between 0° and 15°S is fast between pentad P0 and P+1. At P+1 positive divergence values, above $8x10^{-6}s^{-1}$ are located over East Africa.

6.2.2.5 Precipitable Water

Spatial temporal evolution patterns of precipitable water associated with non-propagating OLR anomalies are presented in figures 6.14(a-d) from pentad P-2 to pentad P+1. High precipitable water, roughly trace the average position of ITCZ as shown at pentads P-2 to P+1. Low precipitable water values are revealed over the Sahara desert, Arabian ridge, southwestern Africa and East of southern Africa. A sequence from P-2 to P+1 of precipitable water associated with the eastward propagating OLR anomalies (convective) case as depicted between 7.5° and 10°S are illustrated in figures 6.14(e-h). At P-2 high precipitable water is located over the continent, Madagascar and central Indian Ocean with highest values of about 90 mm over the Congo basin At P-1, P0 and P+1 values steadily increase eastwards while they decrease to the west. However, eastward propagation is not easily discernible.

6.2.3 North-eastern

6.2.3.1 Outgoing Longwave Radiation

Temporal progression of OLR anomaly patterns from pentad 9 to 12 of 1990, associated with a non-propagating convective feature in the 2.5°S-5°S band are presented in figures 6.15(a-d), left panel. The anomalies were obtained by subtracting the 1980-94 February mean from pentad OLR values. At P-2 positive OLR anomalies are revealed over southwest Africa and eastern Africa with negative OLR anomalies to the East of southern Africa and northern

Madagascar. A general north-eastward shift of negative OLR anomalies is observed from P-1 to P+1. Positive OLR anomalies are established over southern Africa from pentad P-1 to P+1. The spatial temporal progression of OLR anomalies from pentad 14 to pentad 17, associated with an eastward propagating convective feature in the MAM season, is shown in figure 6.15(e-h), right panel. The anomalies were obtained by subtracting the 1980-94 March mean from pentad OLR values. At P-2 negative OLR anomalies are observed over central Africa and positive OLR anomalies over East Africa. Eastward shift of negative OLR anomalies between 0° and 15°S is observed from pentad P-2 to pentad P+1.

6.2.3.2 Geopotential Heights at 850 hPa

The map sequence of geopotential heights at 850 hPa level for pentad 9 to 12 of 1990, associated with a non-propagating convective feature shown in figure 6.16(a-d), left panel. At P-2 there are relatively high geopotential heights over the Atlantic Ocean and eastern parts of southern Africa. With low geopotential heights located over East Africa, western southern Africa and the southern Indian Ocean. At P-1 the trough over southern Africa moves eastwards thus weakening the high pressure over southeastern Africa. Simultaneous pressure rises over southern Africa and northwestern Africa 'push' the low pressure system north-eastwards and at the same time strengthening convergence over the Congo basin and northeastern Africa. Figure 6.16(e-h), right panel, presents geopotential height fields at 850 hPa level, associated with a propagating convective feature in the latitudes 2.5°-5°S. At P-2 low geopotential heights are observed over north-eastern Africa, the southern Atlantic Ocean and over Angola, Zimbabwe and Botswana. From P-2 to P-1 the pressure systems in the south shift eastwards. Simultaneous geopotential height rises to the west with geopotential height falls to the east are observed from pentad P-1 to P+1. Throughout the case evolution, the Arabian ridge is relaxed or non-existent.

6.2.3.3 WVF and Wind Flow Pattern at 200 hPa

The spatial temporal sequence from P-2 to P+1 of water vapour flux patterns for a non-propagating OLR anomaly feature in the latitudes of northern Tanzania are presented in figures 6.17(a-d), left panel. Water vapour confluence is depicted in P-2 and P-1 over the continent and Indian Ocean along latitude 15°S. The flow over central Africa is northerly at P-2 becoming north-westerly at P-1. A weak confluence is also revealed over East Africa. At P0 a similar pattern as at P-1 is observed. Southerly water vapour flux converges with northerly water vapour flux over the northern coast of Tanzania and the southern coast of Kenya while over the western part of the continent northeasterlies converge with southeasterlies over Angola and Namibia. The right panel of figure 6.17(e-h) shows the sequence of WVF pattern for a propagating negative OLR feature between 2.5° and 5°S. At P-2 easterly water vapour flux converges with westerly water vapour flux along about 25°E.

Convergence of WVF is also depicted along 20°S over southeastern Africa and the Mozambique Channel. The convergence zone moves northeastwards and is located west of the East African Lakes at P-1. At P+1 it is located over northern Tanzania and the central Indian Ocean.

Figure 6.18(a-d) shows the flow pattern for pentad 9 to pentad 12 (MAM season) at 200 hPa level. At P-2 easterlies are confined between 3°N and 10°S with anticyclonic centres located at 45°E, 6°N and 30°E, 14°S. Diverging winds are located over west Africa and East of Madagascar. At P-1 the wind flow in the southern hemisphere suggest a northwest-southeast tilting trough and an outflow axis along about 11°S. In the northern hemisphere there is mainly a cross-equatorial flow east of 15°E. The flow pattern at P0 is similar to that at P-1 but with a better organised anticyclonic flow centred at about 28°E, 15°S and more diffluent winds over the Congo basin and northeastern Africa. A trough is established over the Mozambique Channel separating two anticyclones with cross-equatorial flow over northeastern Africa. The sequence of wind flow patterns from pentad 14 to 17 at 200 hPa level, are shown in figure 6.18(e-h), right panel. At P-2 there is a band of relatively strong easterly winds between 10°N and 10°S, west of 45°E. Cross-equatorial flow is observed at P0. At pentad P-1, wind speeds to the west. Between latitude 5°N and 10°S, at pentad P+1 relatively strong easterlies lie to the east of 45°E, with strong easterlies west of 12°E.

6.2.3.4 Divergence at 200 hPa

The map progression from pentad 9 to pentad 12 of 1990, of divergence patterns at 200 hPa level associated with a non-propagating convective feature in the 2.5°-5°S latitude band, is shown in figures 6.19(a-d), left panel. At P-2 a positive divergence zone indicates the position of the ITCZ. It is observed that positive divergence over the continent shifts northwards from pentad P-2 to pentad P+1. However, negative upper divergence exists over Somalia at all pentads, suggesting low level divergence there. The map progression from pentad 14 to 17 of 1988, of divergence patterns associated with an eastward propagating convective case is shown in the right panel of figure 6.19(e-h). Eastward movement of positive upper divergence is clearly observed between 5°N and 10°S from P-2 to P+1.

6.2.3.5 Precipitable water

Progression from P-2 to P+1 of precipitable water patterns associated with a non-propagating convective feature between 2.5°S and 5°S are presented in figures 6.20(a-d). At P-2 high precipitable water, is located over central Africa centred at about 30°E, 10°S, and over Cameroon, Ethiopia, Sudan, and to the northeast of Madagascar. The centre of high precipitable water is maintained at the same position at P-1 and P0, as at P-2 while precipitable water increases to the northeast and decreases over southwestern Africa. At P0 and P+1 high precipitable water is over East Africa. Figure 6.20(e-h) show the evolution of precipitable water patterns associated with an eastward propagating convective feature between 2.5°S and 5°S. Eastward propagation of precipitable water is observed from pentad P-2 to pentad P+1.

6.3 Summary

The main purpose in this chapter was to reveal the propagation of convection features in the 2.5-5°S and 7.5°-10°S latitude bands for northeastern and southwestern areas respectively. The goal was to understand the kinematics and thermodynamic patterns associated with these propagating and stationary convective oscillations. The main results of this chapter are summarised as follows:

It has been demonstrated that there are eastward stationary and westward propagating convective features, inferred from OLR anomalies. A good example is the convective system of 1981, which started over central Africa and western Indian Ocean and off the coast of East Africa Few cases seem to start west of 0° longitude where they are weak and seem to gain strength over the Indian Ocean. Similar analyses with the using u-component at 850 hPa and 200 hPa levels and integrated precipitable water revealed that strong convective systems couple with positive (negative) u-component at 850 hPa, (u-component at 200 hPa) and positive integrated precipitable water. Weaker features do not show much coupling. The eastward phase speed of the systems was found to be between 2 to about 8 m s^{-1}. The period of oscillation was in the range 4 to 11 pentad (systems with period between 2 to 3 pentad were filtered. The second part was a case study of propagating convective systems with associated geopotential heights at 850 hPa, horizontal flow patterns at 850 hPa and 200 hPa, divergence at 200 hPa, and integrated precipitable water. Four events were selected, two for each area within the same season. One event was for west-east propagating convective system and the other for stationary convective system. The second system was picked when convection occurred simultaneously at all longitudes in the respective latitude bands. Evolution from pentad p-2 to pentad P+1 was examined. A date was selected when convection was high between longitudes 30° and 35°E and 35°-40°E for south-western and northeastern respectively. Dates for two pentads before P0 date and the pentad thereafter was selected. Based on the above selection, spatial analysis of OLR, gpm at 850 hPa, horizontal wind flow at 850 hPa and 200 hPa levels, divergence at 200 hPa, and integrated precipitable water were done in order to understand the features associated with the systems and also to see whether the feature was similar to those found elsewhere by other researchers of intraseasonal oscillations.

Generally we observe that there is an association between large negative OLR anomaly (deep convection) and westerly (positive u-component anomaly) wind anomaly flow at low level. It is interesting to note that wind flow over the northern Indian Ocean is more in the stationary cases. Tropical westerly wind over the continent, associated with two cyclonic features which are asymmetrical about the equator do not propagate eastward across Tanzania.

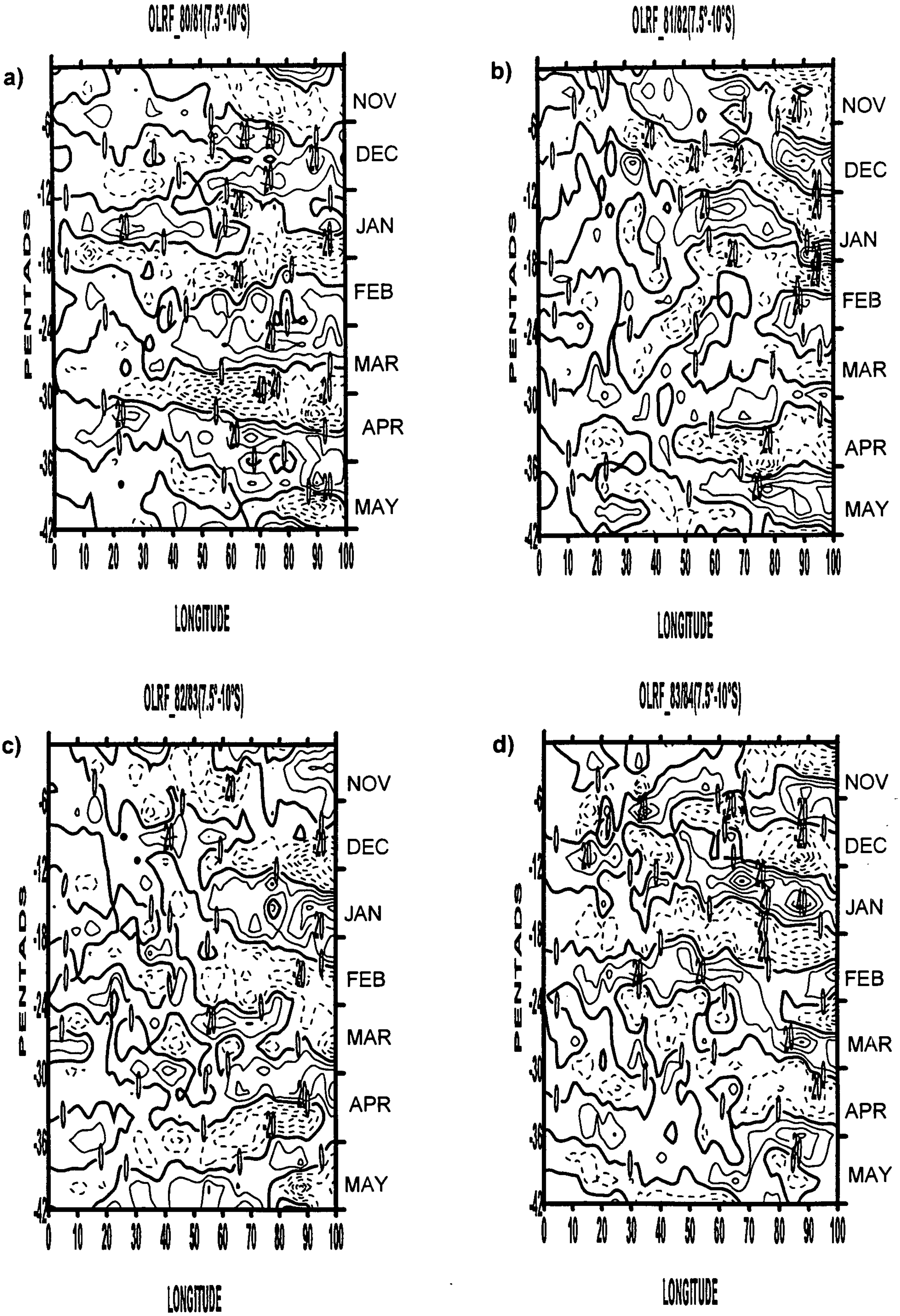

Figure 6.1: Hovmoller diagrams of 20-60 day band filter applied to OLR anomalies averaged between 7.5°S and 10°S from 0° to 100°E for pentad 62 to pentad 30

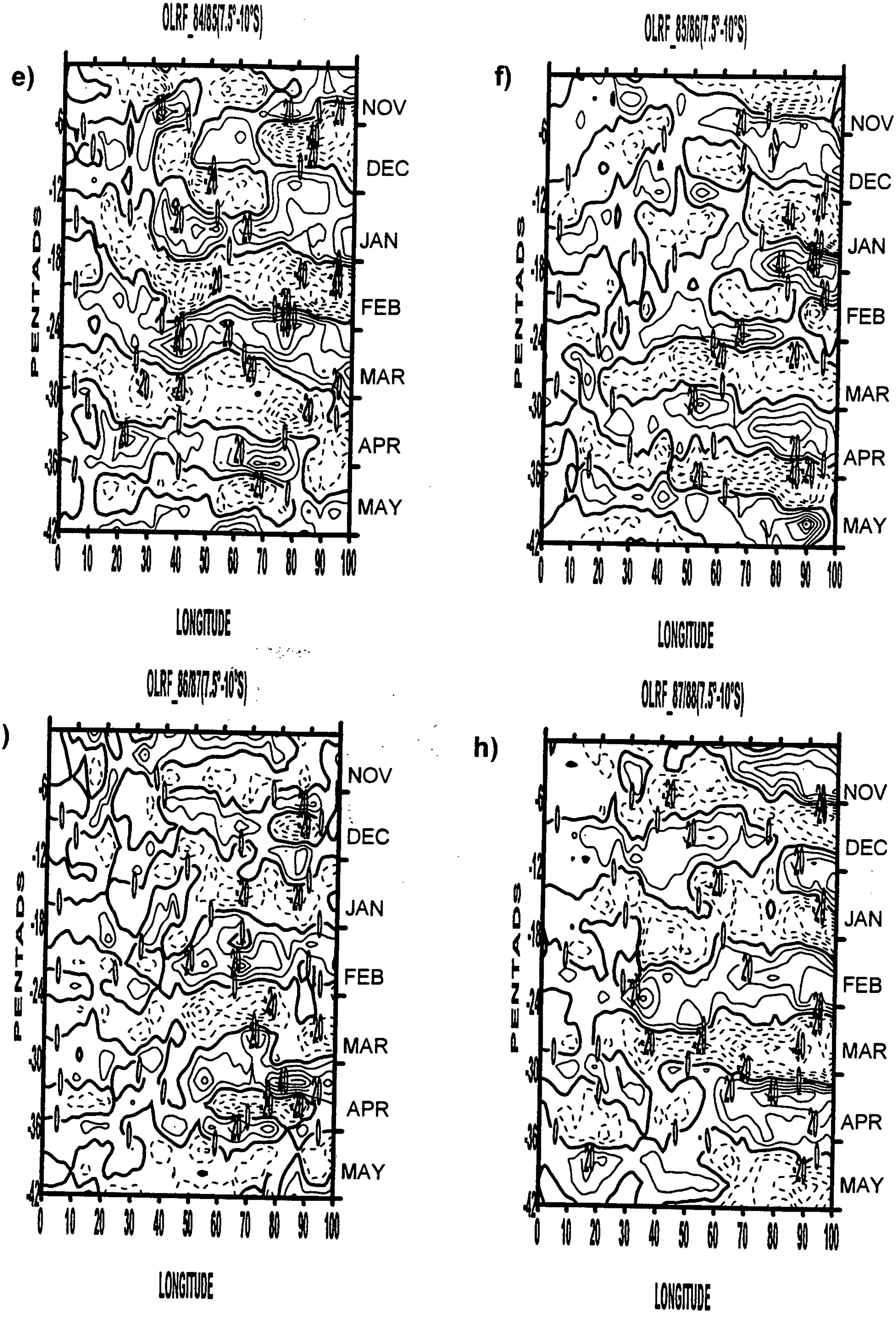

Figure 6.1 continued: (i.e. Nov-May (1980-1981 to 1992-93) with time mean removed. Solid (dashed contours indicate positive (negative) anomalies, contour interval 20 $W\ m^{-2}$

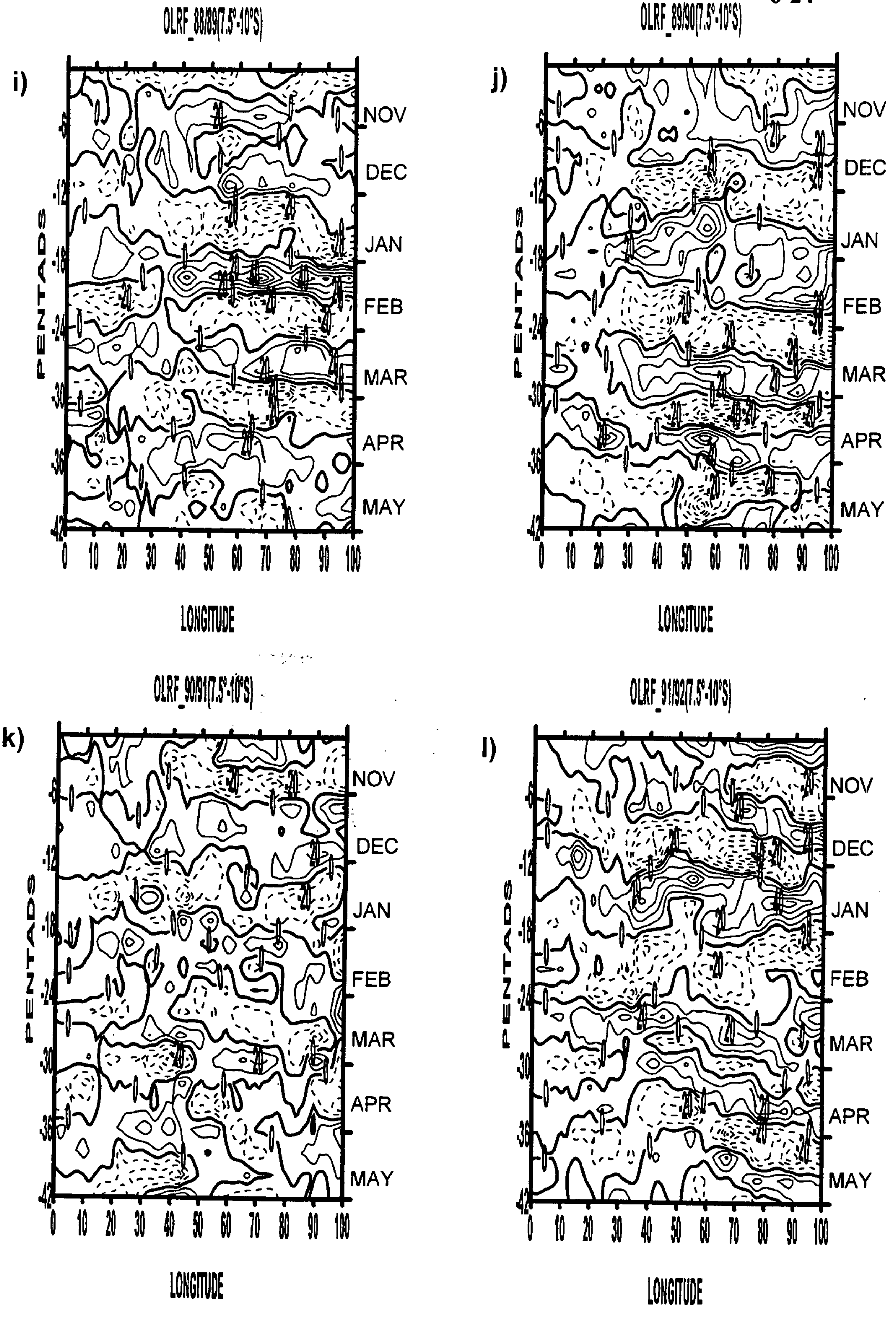

Fig. 6.1 Continued:

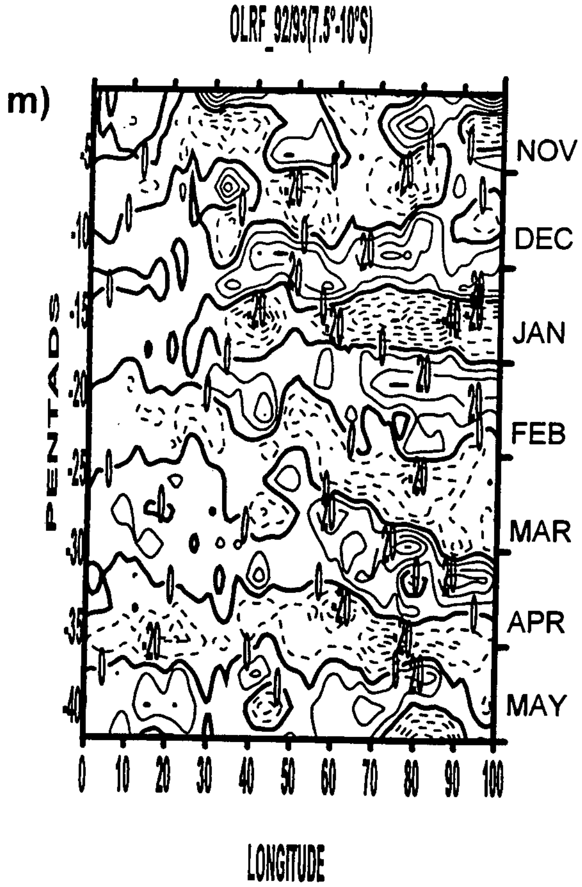

Fig. 6.1 Continued:

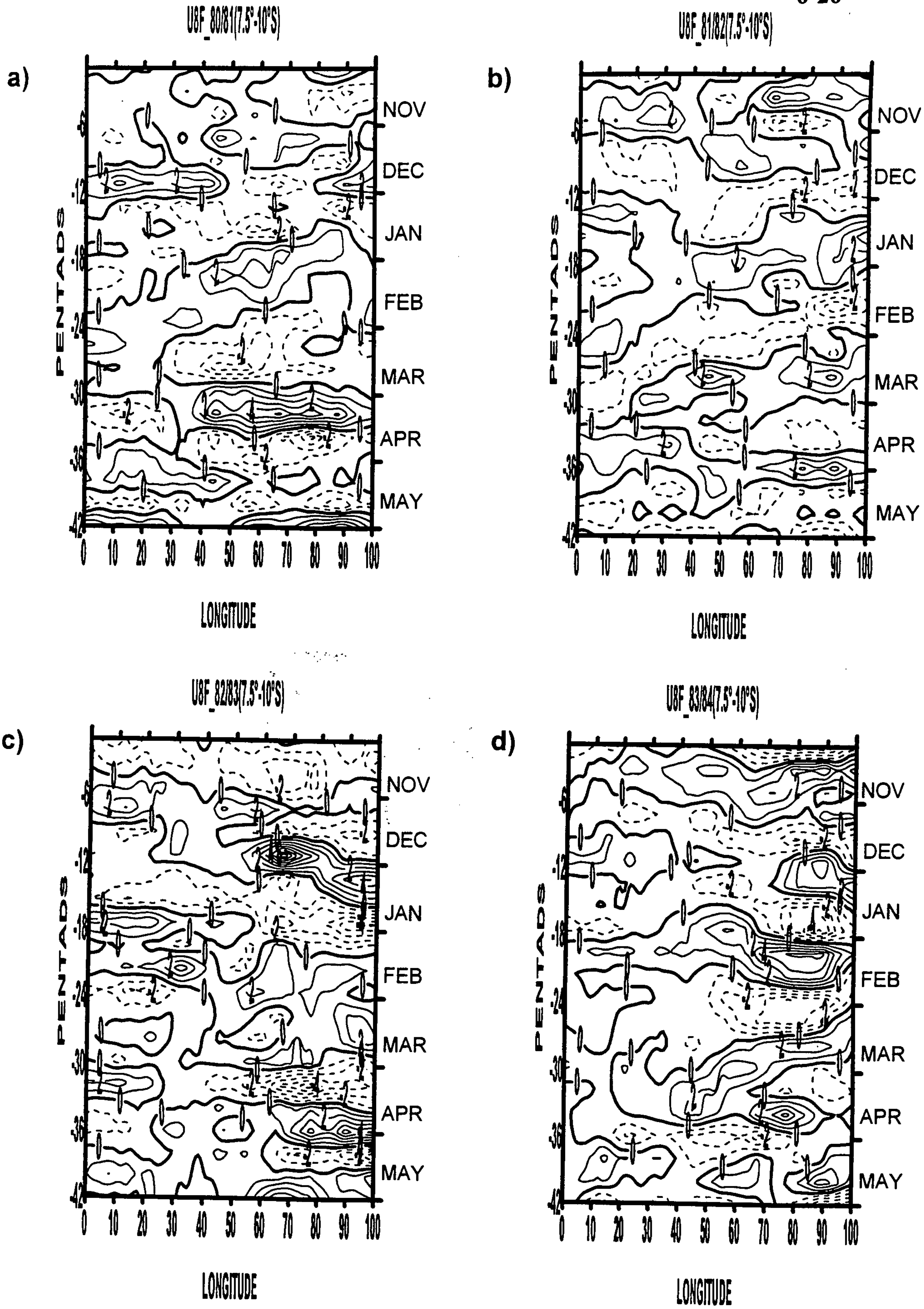

Figure 6.2: Hovmoller diagrams of (4-12 pentad) 20-60 day band filtered applied to zonal wind speed anomalies at 850 hPa averaged between 7.5°S and 10°S from 0° to 100°E for pentad 62 to pentad 30 (i.e Nov-May 1980/81-1993/94)

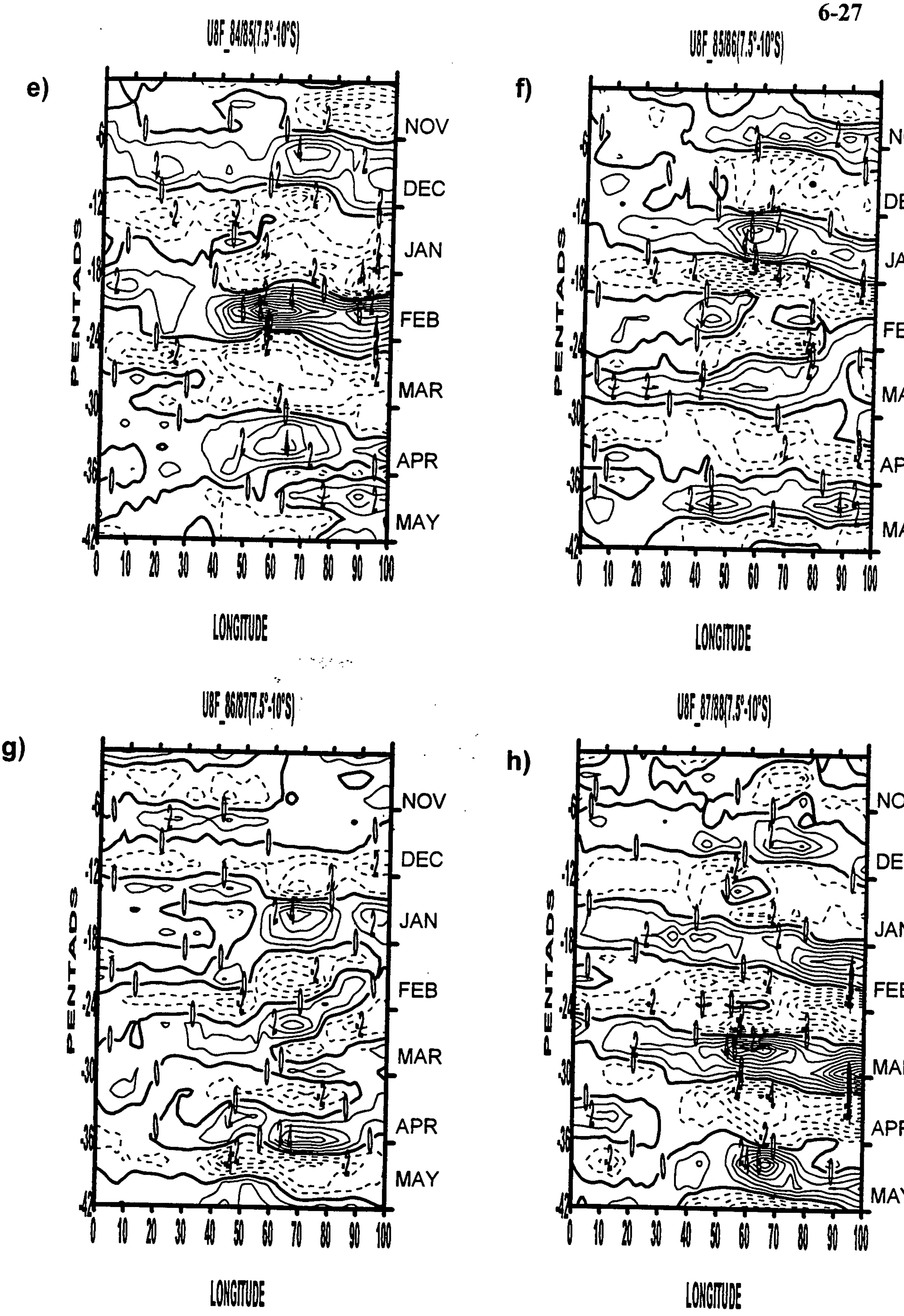

Figure 6.2 Continued: with mean removed. Solid (dashed) contours indicate westerlies (easterlies), contour intervals 1 m/s

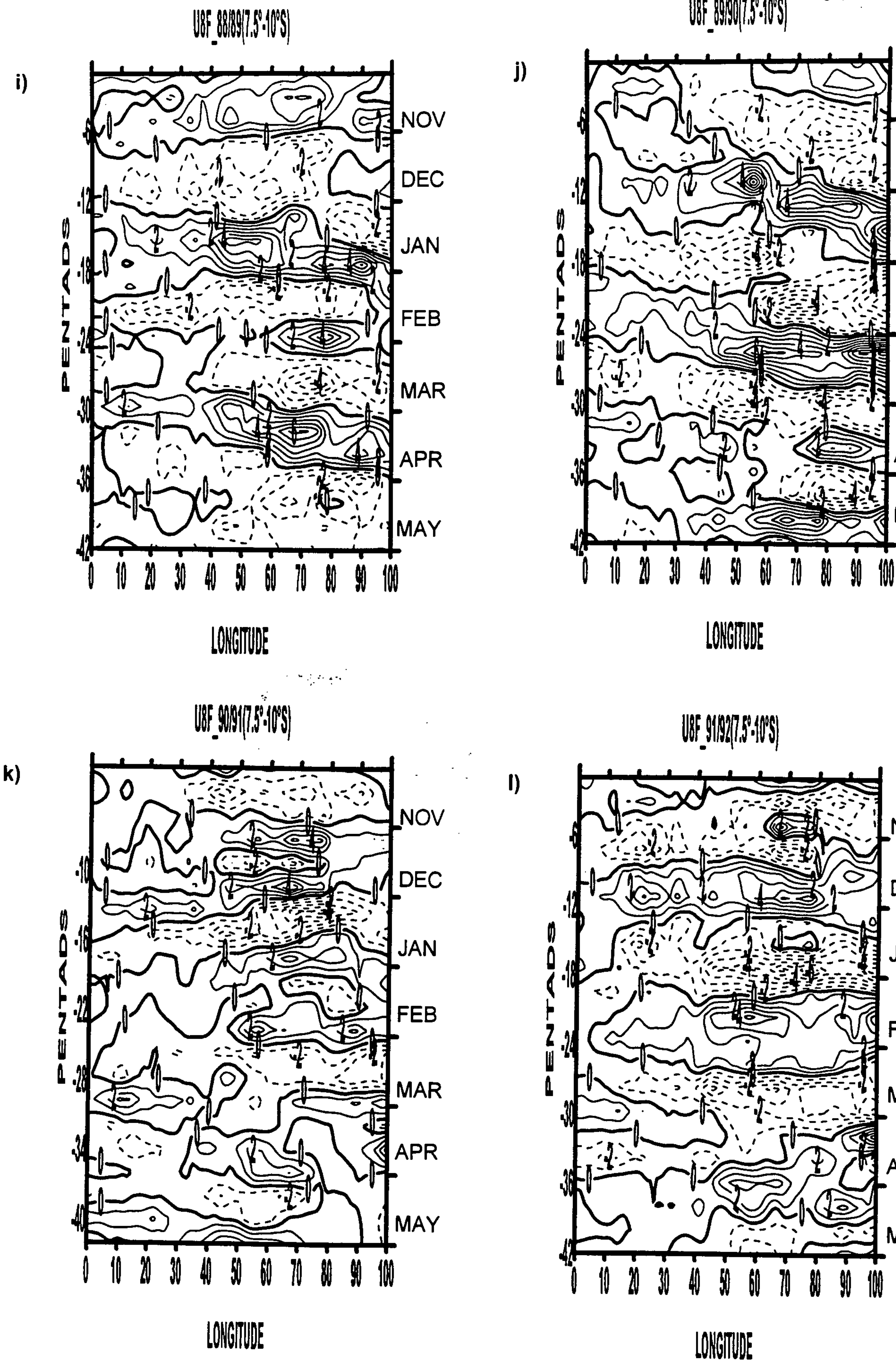

Figure 6.2 Continued:

m)

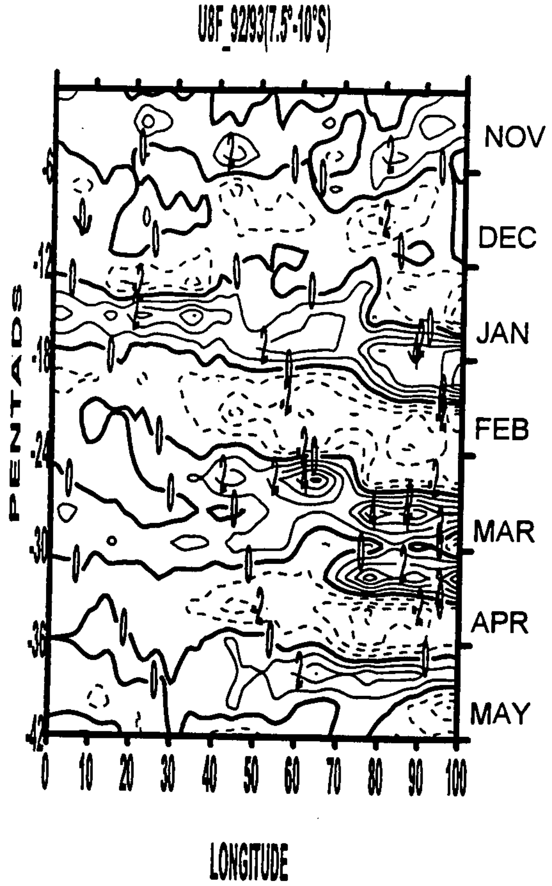

Figure 6.2 Continued:

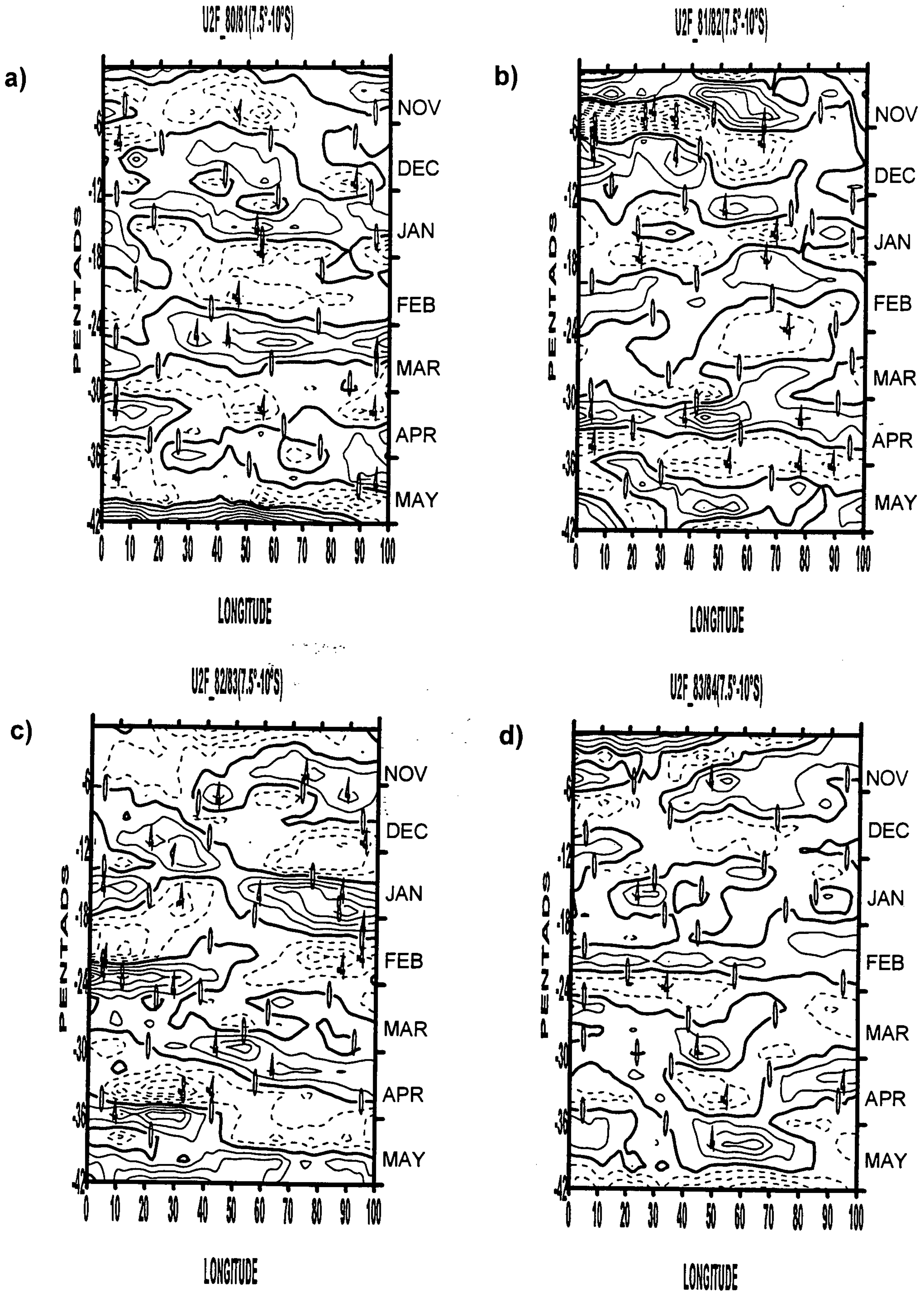

Figure 6.3: Hovmoller diagrams of (4-12 pentad) 20-60 day band filter applied to zonal wind component anomalies at 200 hPa averaged between 7.5°S and 10°S from 0° to 100°E for pentad 62 to pentad 30 i.e. Nov-May (1980/81-1993/94)

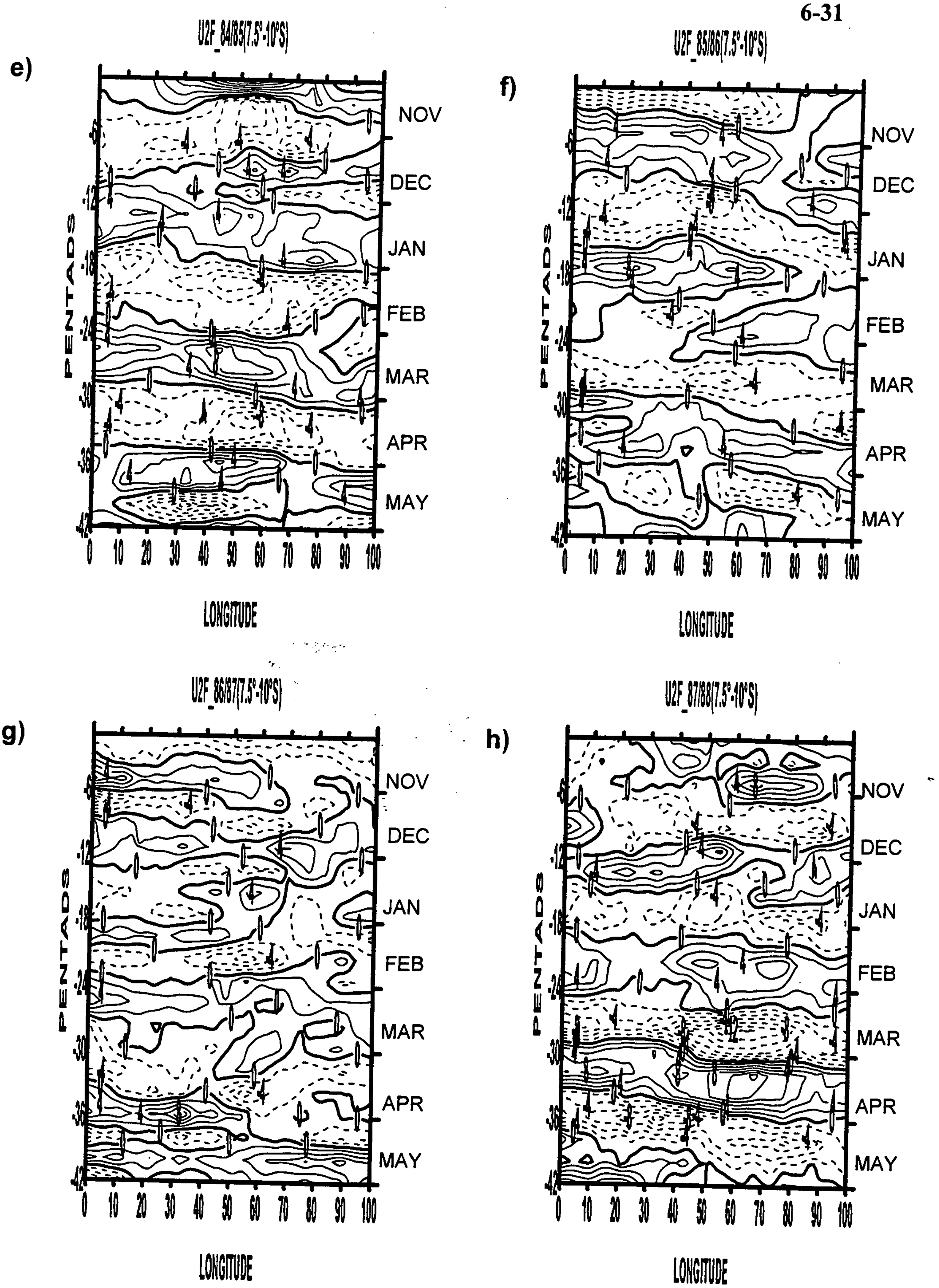

Figure 6.3 Continued: with time mean removed. Solid (dashed) contours indicate westerlies (easterlies) Contour interval 2 m/s

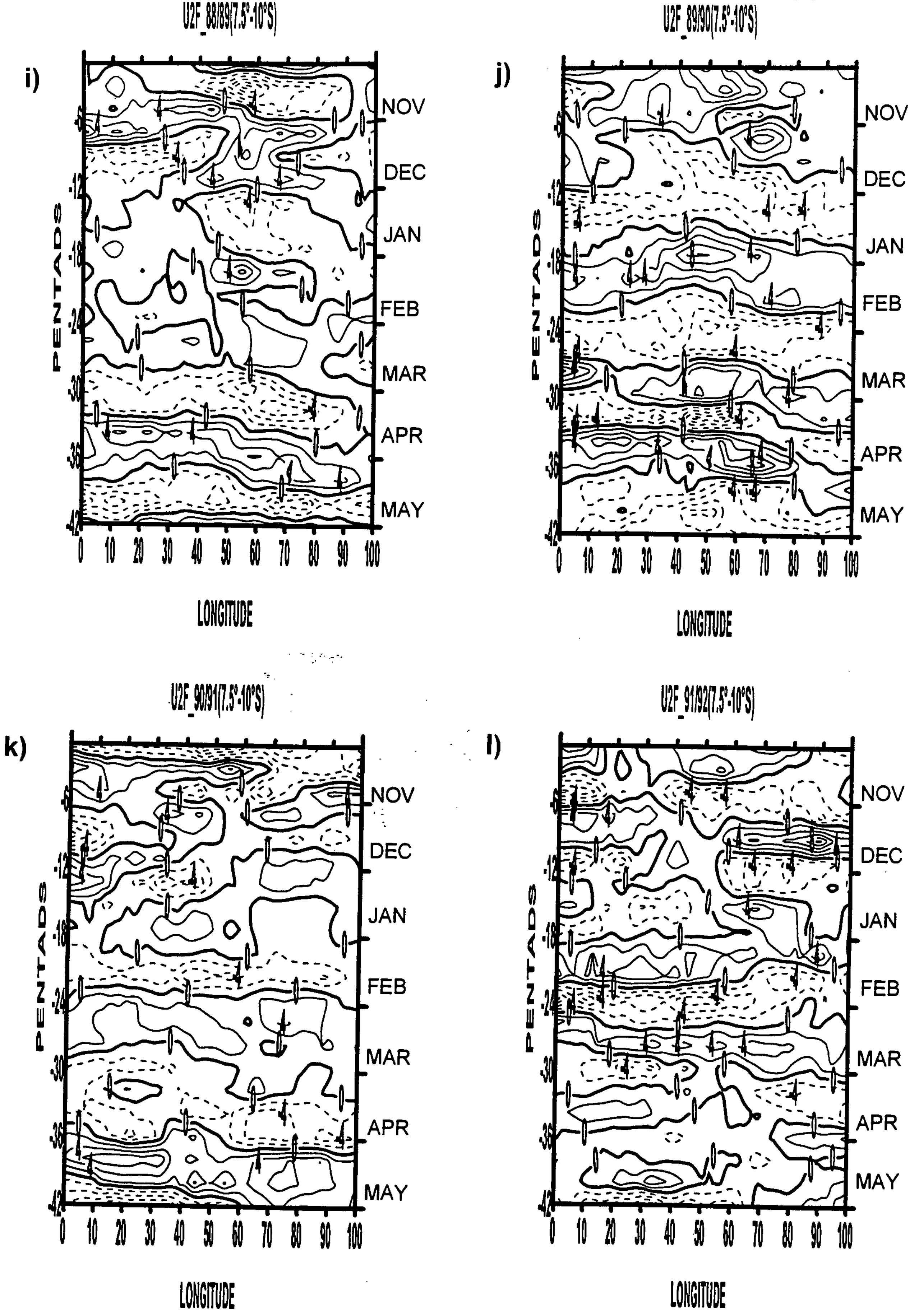

Figure 6.3 Continued:

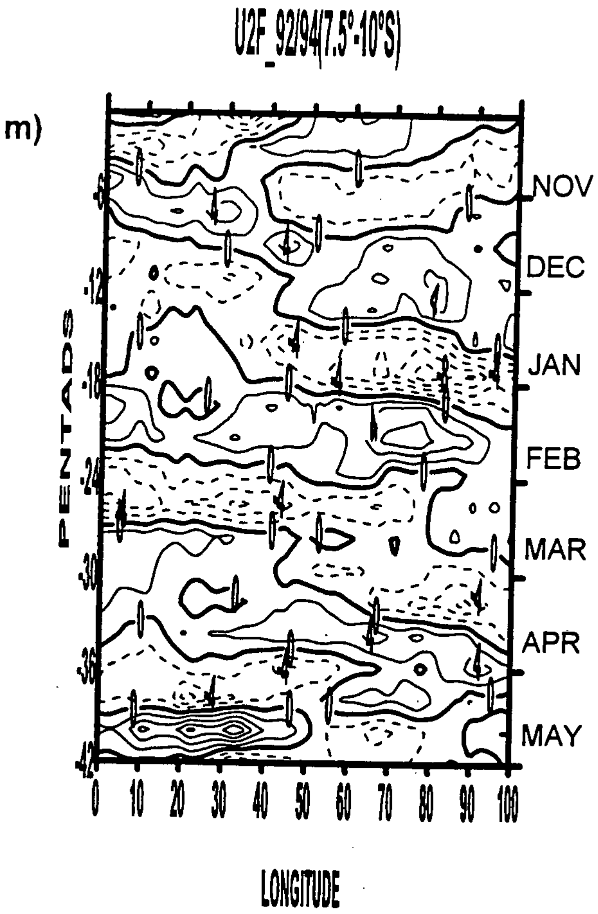

Figure 6.3: Continued:

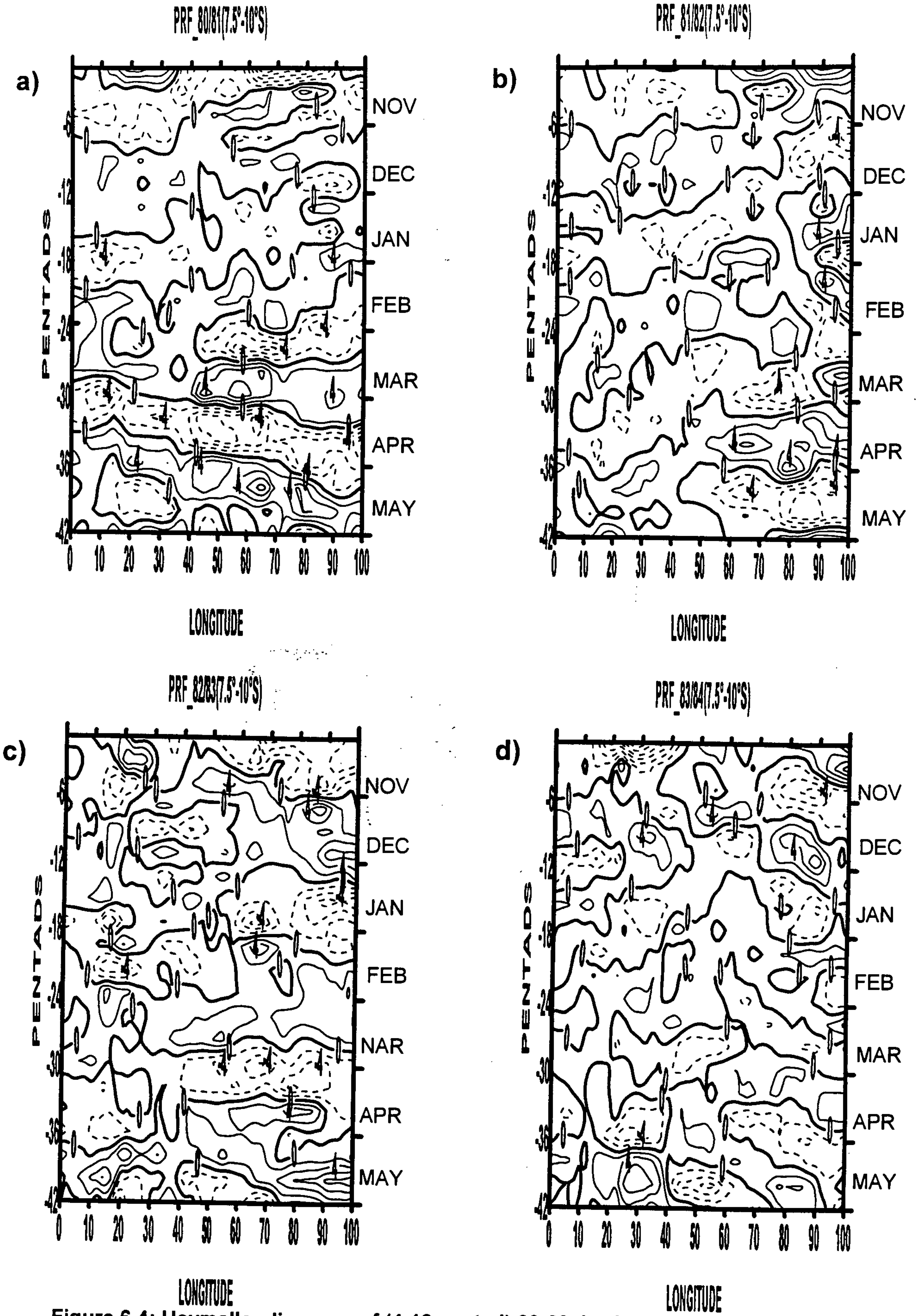

Figure 6.4: Hovmoller diagrams of (4-12 pentad) 20-60 day band filter applied to precipitable water anomalies integrated from surface to 300 hPa level averaged between 7.5°S and 10°S from 0 °to 100°E for pentad 62 to pentad 30,

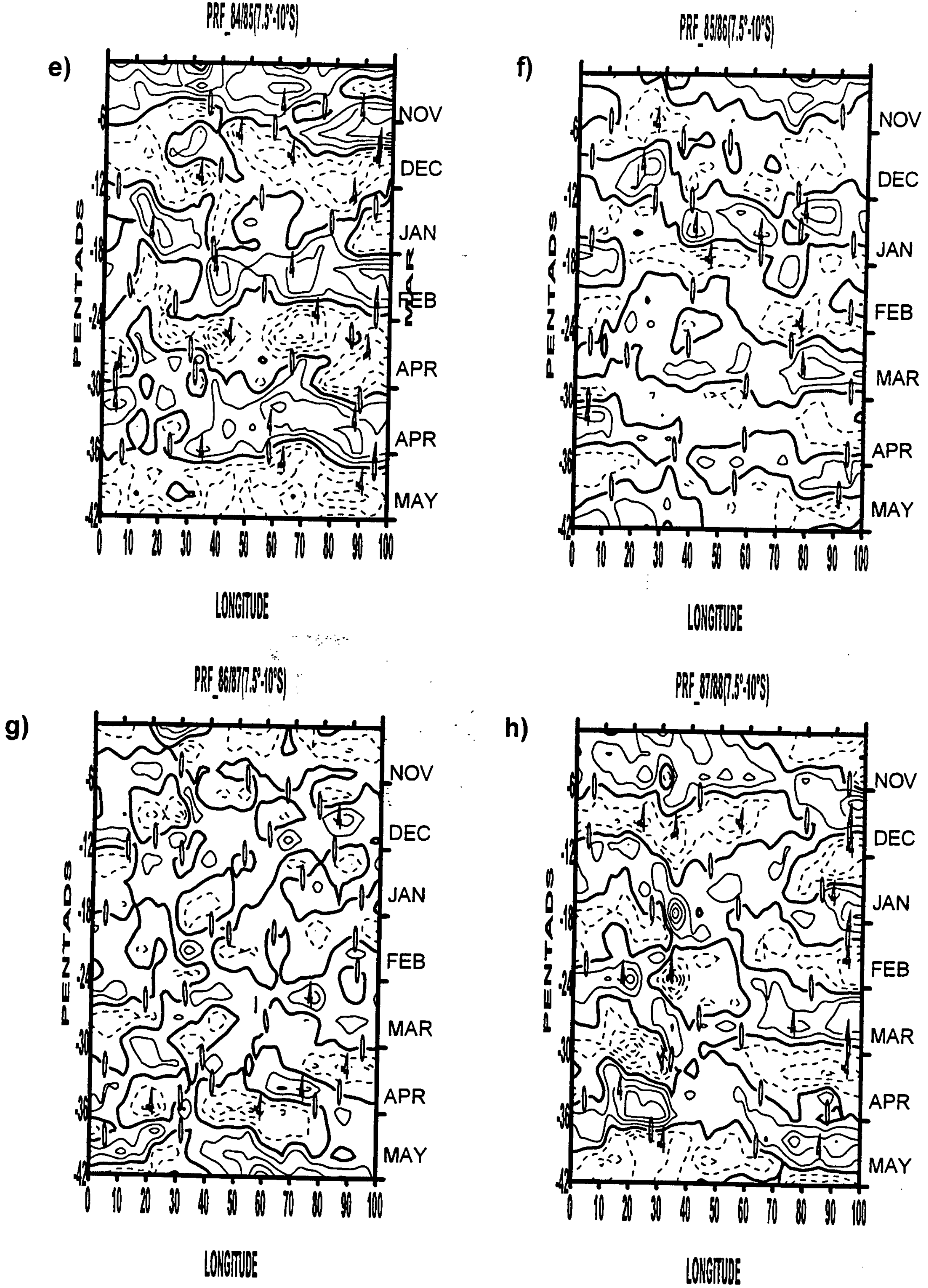

Figure 6.4 Continued: (i.e. Nov-May 1980-1992/93) with time mean removed. Solid (dashed) contours indicate positive (negative) anomalies, contour interval 2 mm

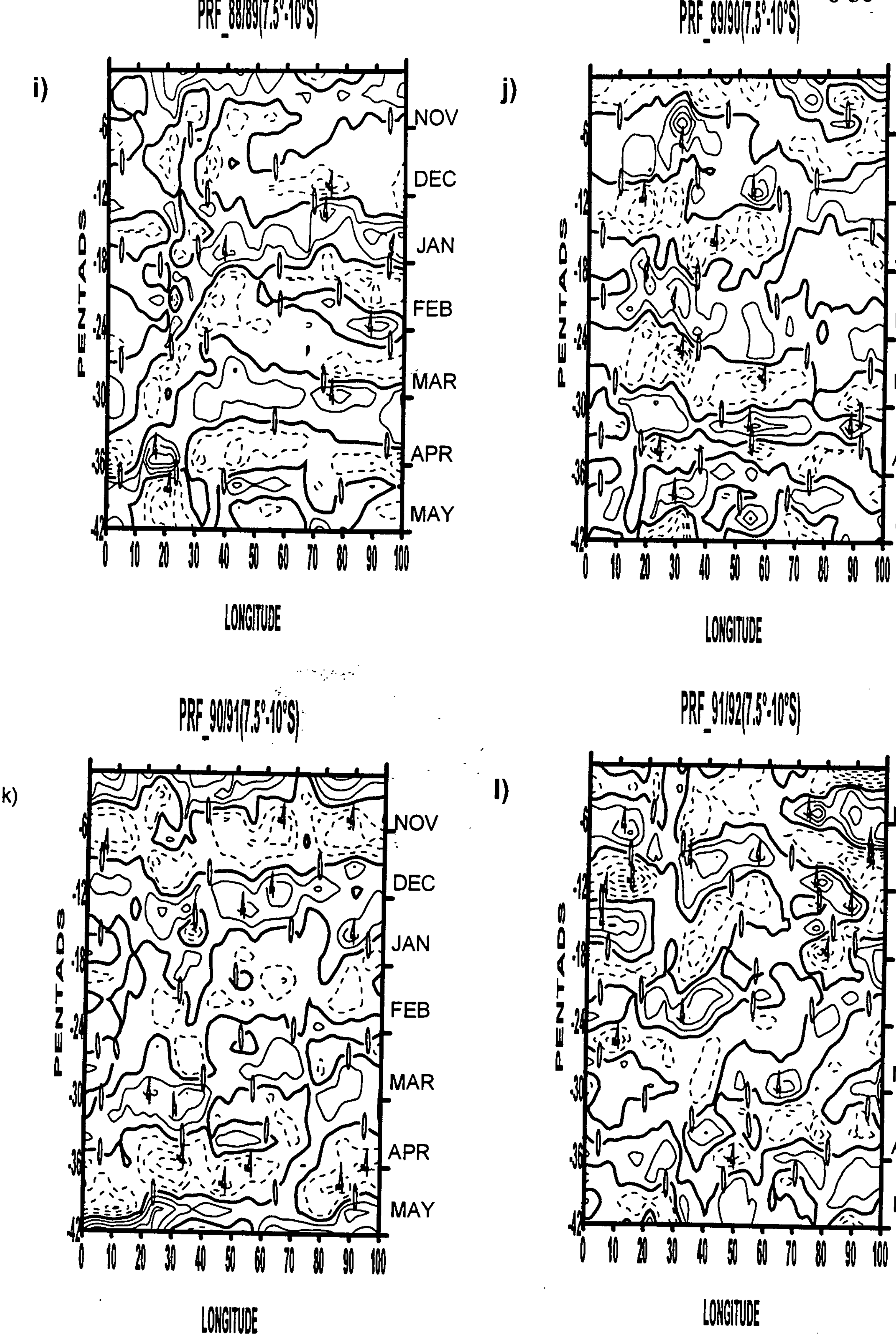

Figure 6.4 Continued:

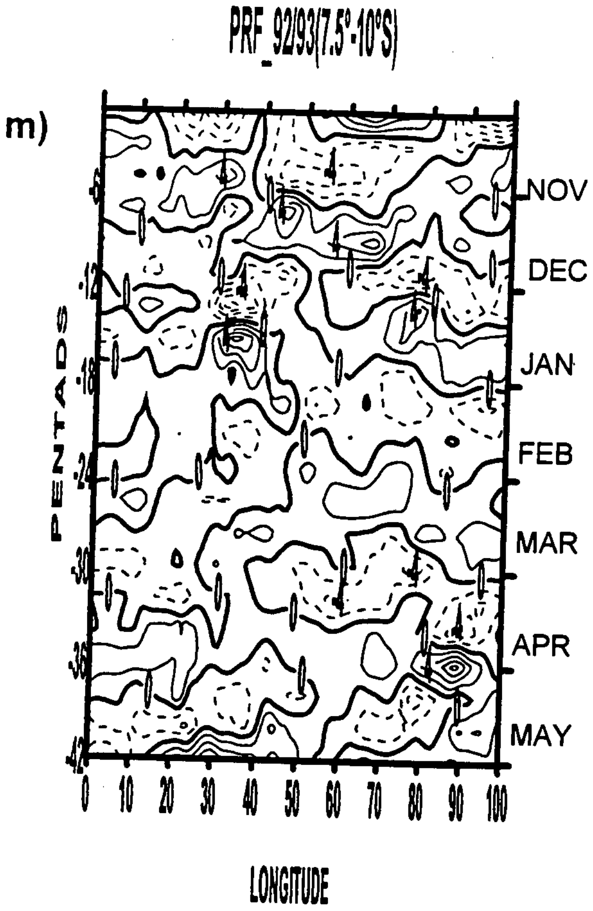
PRF 92/93(7.5°-10°S)

Figure 6.4 Continued:

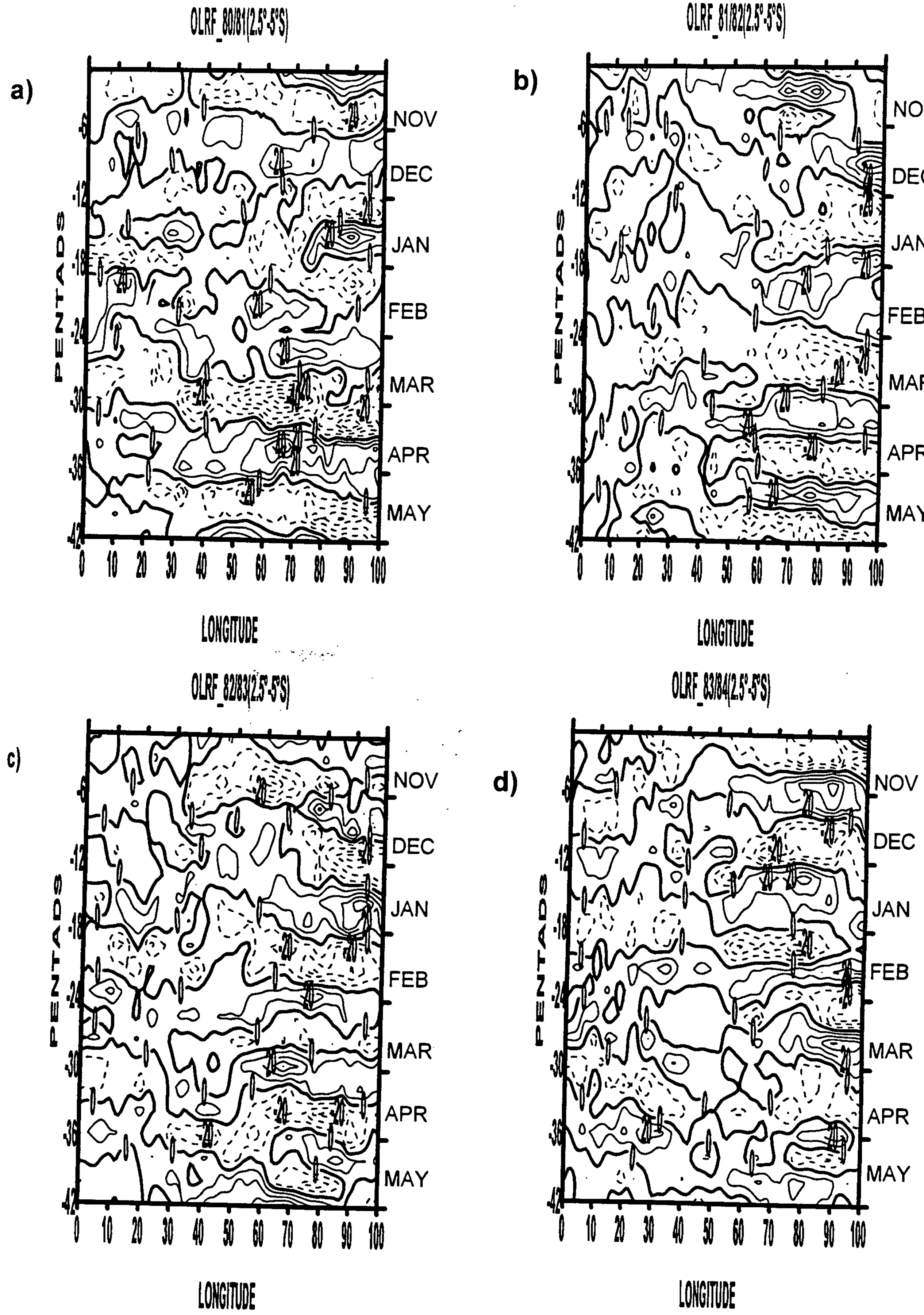

Figure 6.5: Hovmoller diagrams of (4-12 pentad) 20-60 day band filter applied to OLR anomalies averaged between 7.5°S and 10°S from 0 to 100°E for pentad 62 to pentad 30

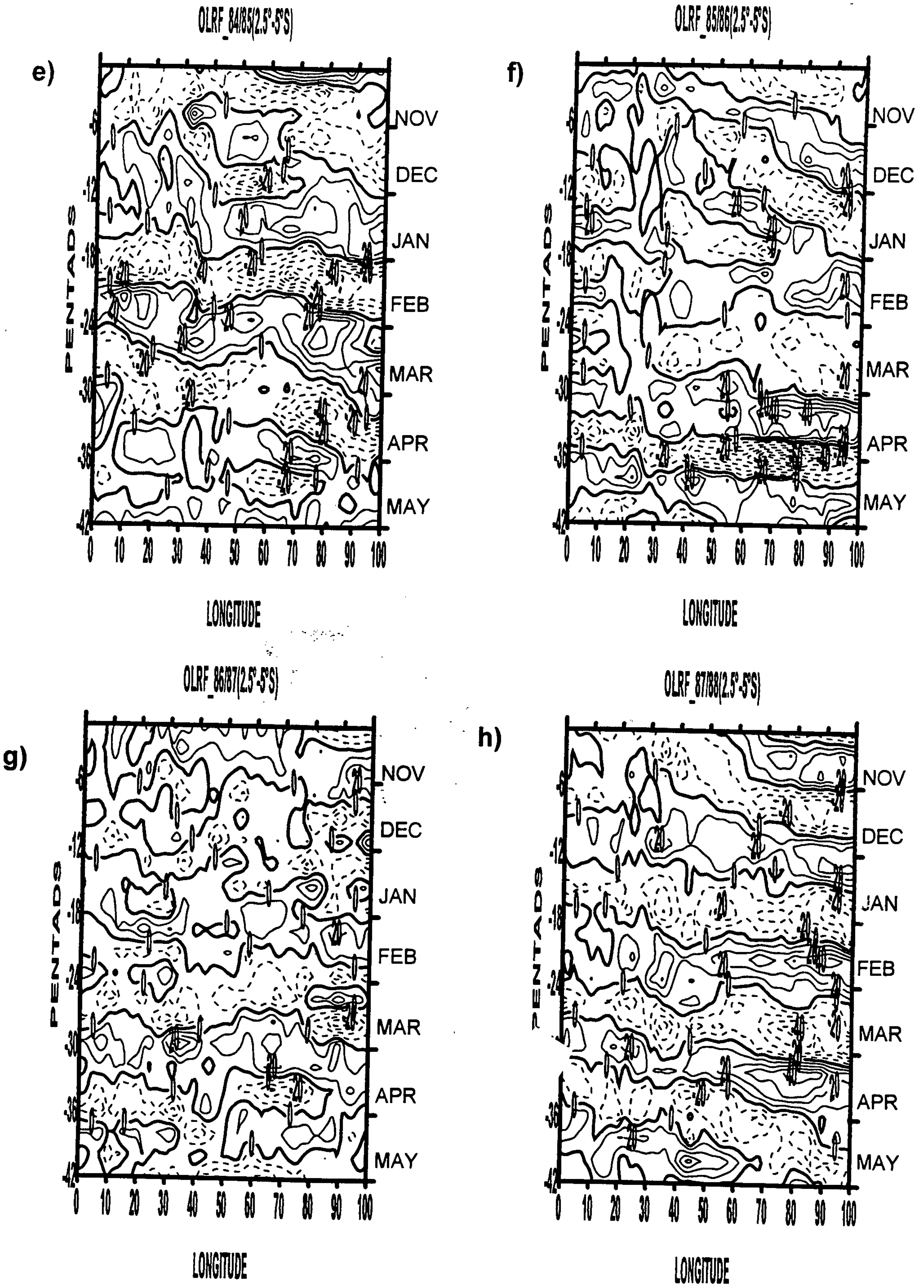

Figure 6.5 Continued: (i.e. Nov-May 1980/81 to 1992/93) with time mean removed. Solid (dashed) contours indicate positive (negative) anomlies, contour interval20 W m^{-2}

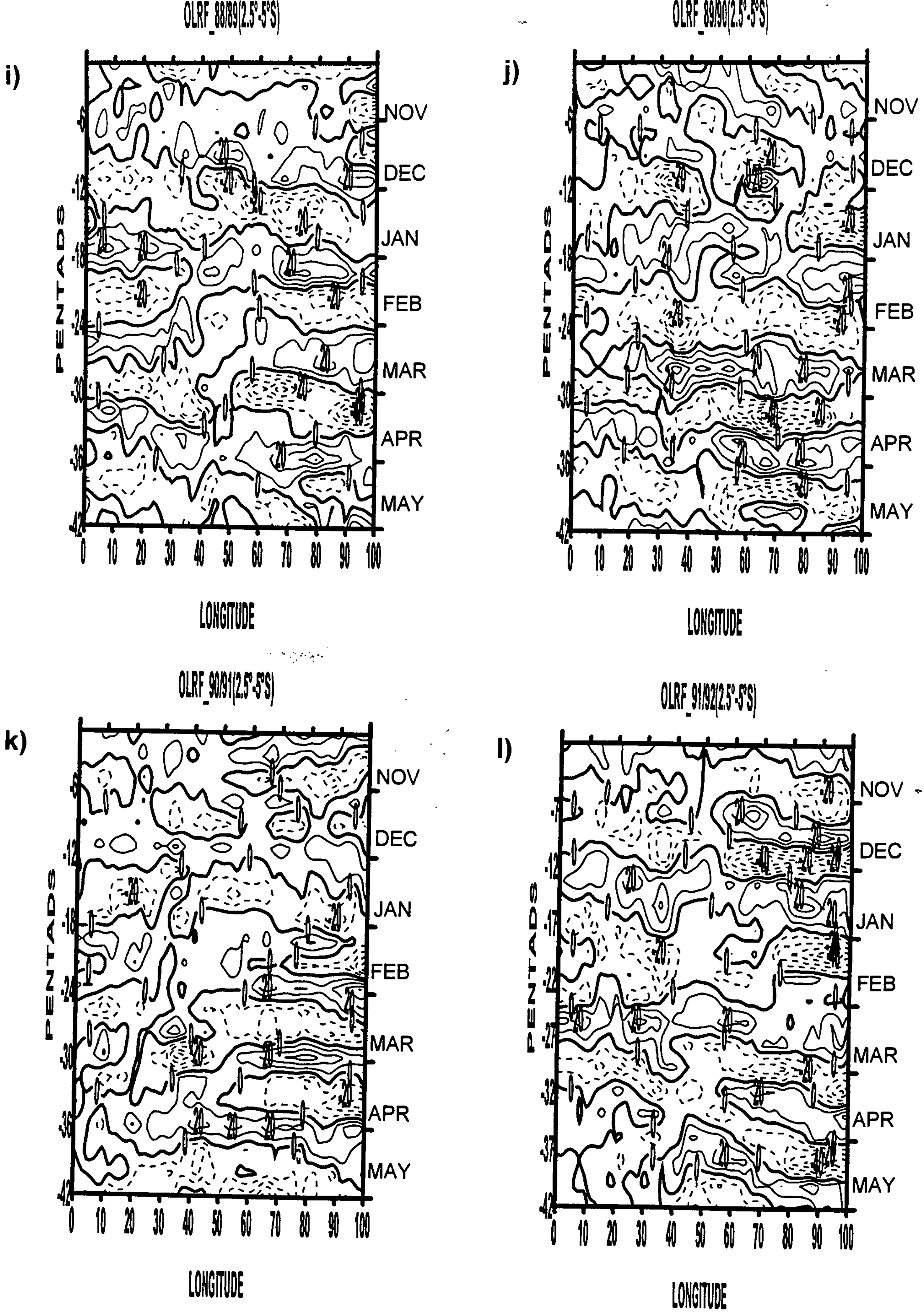

Figure 6.5 Continued:

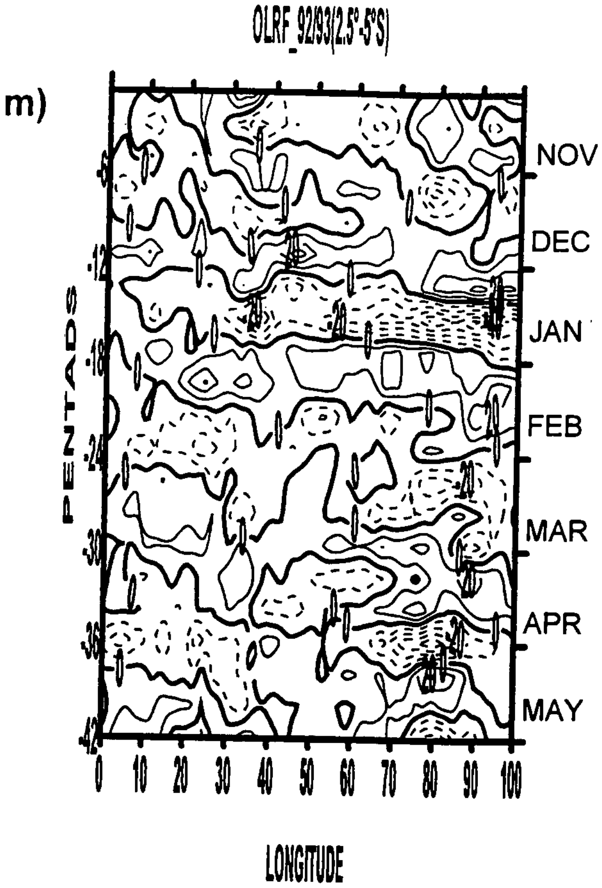

Figure 6.5 Continued:

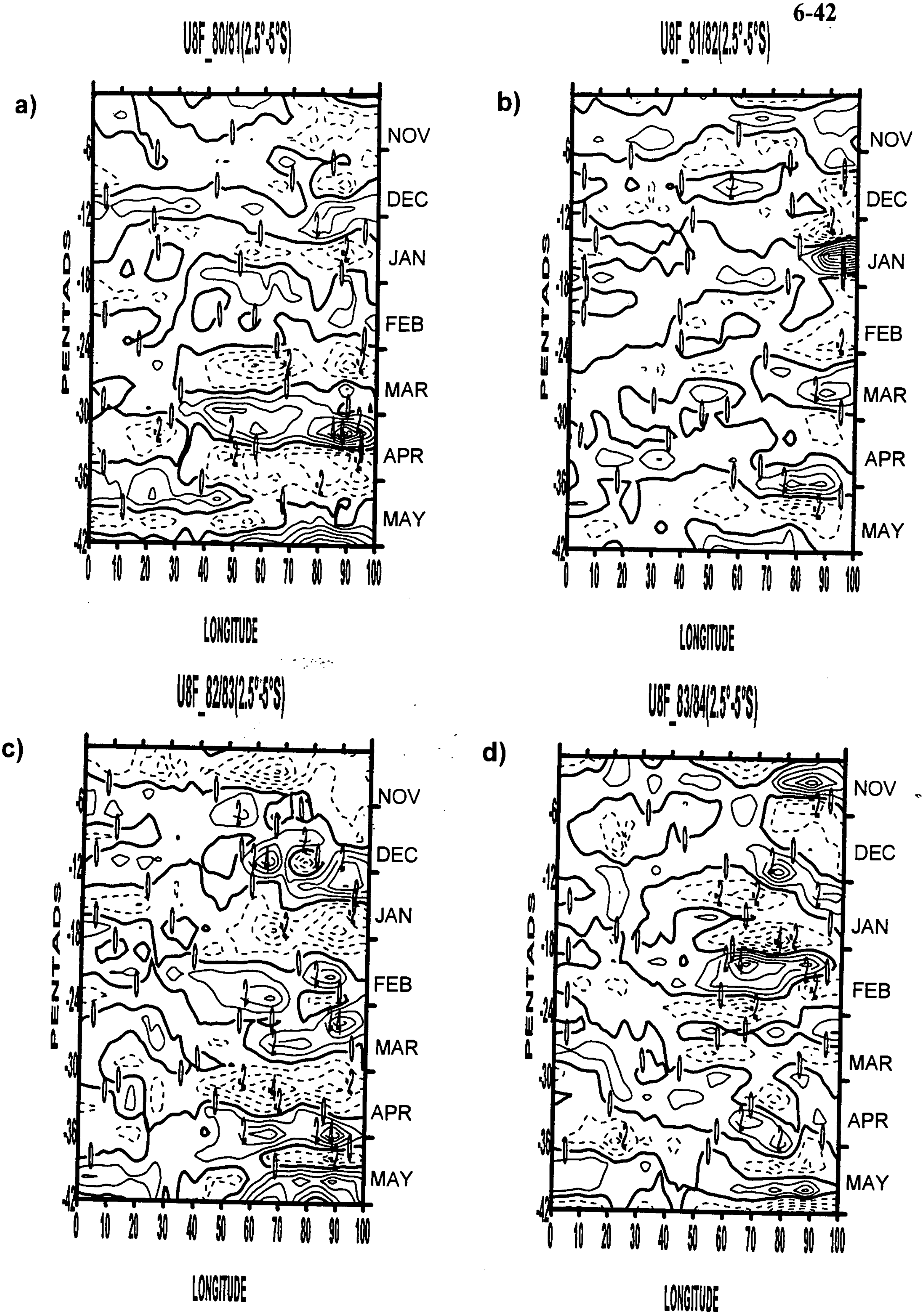

Figure 6.6: Hovmoller diagrams of (4-12 pentad) 20-60 day band filter applied to zonal wind component anomalies at 850 hPa averaged between 2.5° and 5°S from 0° to 100°E for pentad 62 to pentad 30 (i.e. Nov-May 1980/81-1994)

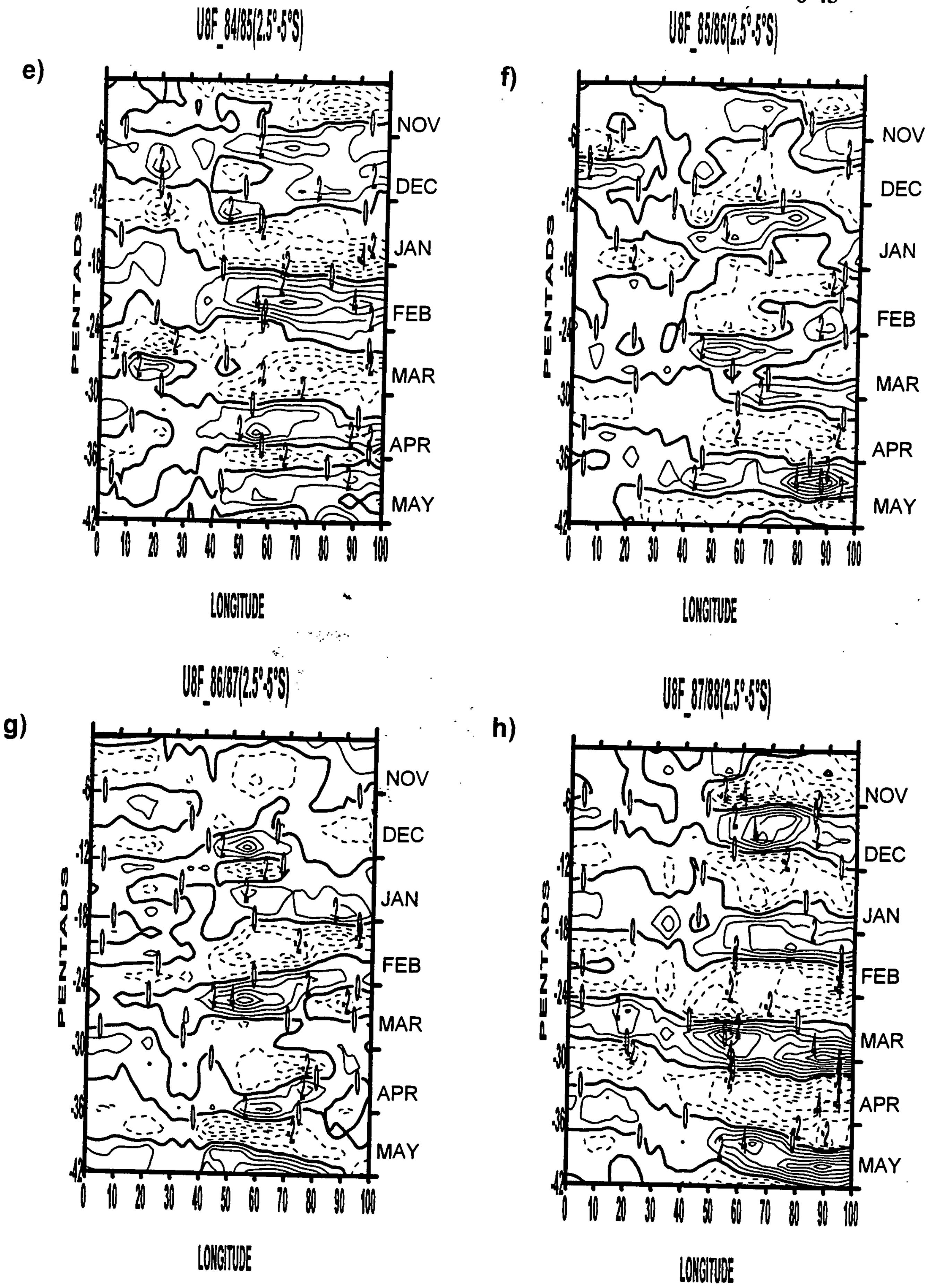

Figure 6.6 Continued: with time mean removed. Solid (dashed) contours indicate westerlies(easterlies), contour interval 1 m/s

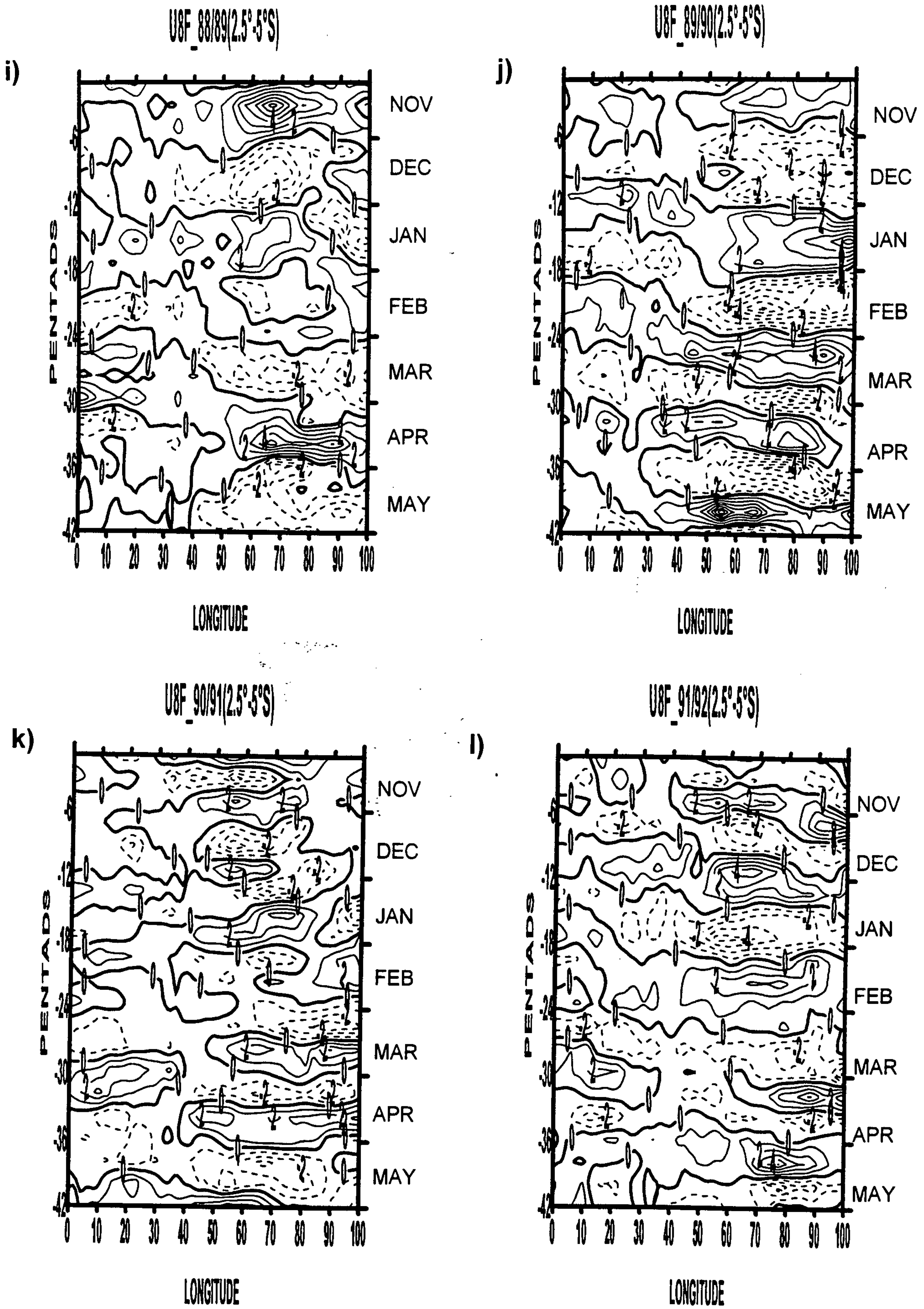

Figure 6.6 Continued:

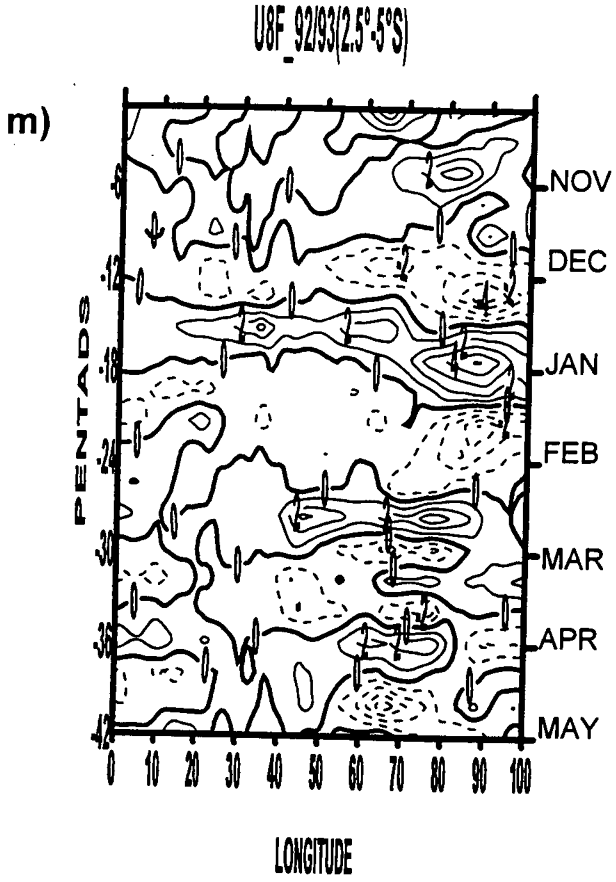

Figure 6.6 Continued:

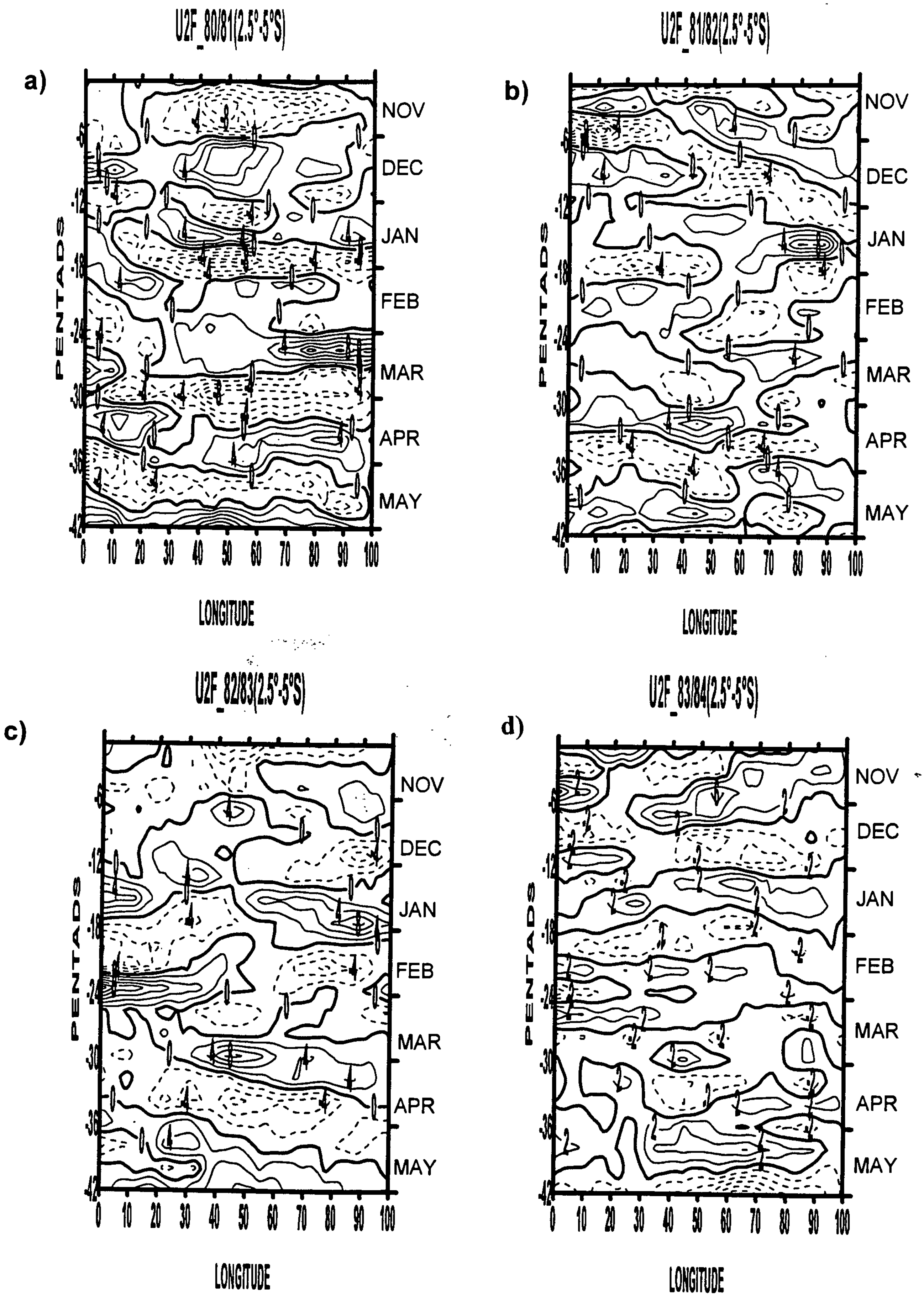

Figure 6.7: Hovmoller diagrams of (4-12 pentad) 20-30 day band filter applied to pentad zonal wind anomalies at 200 hPa level averaged between 2.5°S and 5°S from 0° to 100°E for pentad 62 to pentad 30 (i.e. Nov-May 1980/81-1993/94)

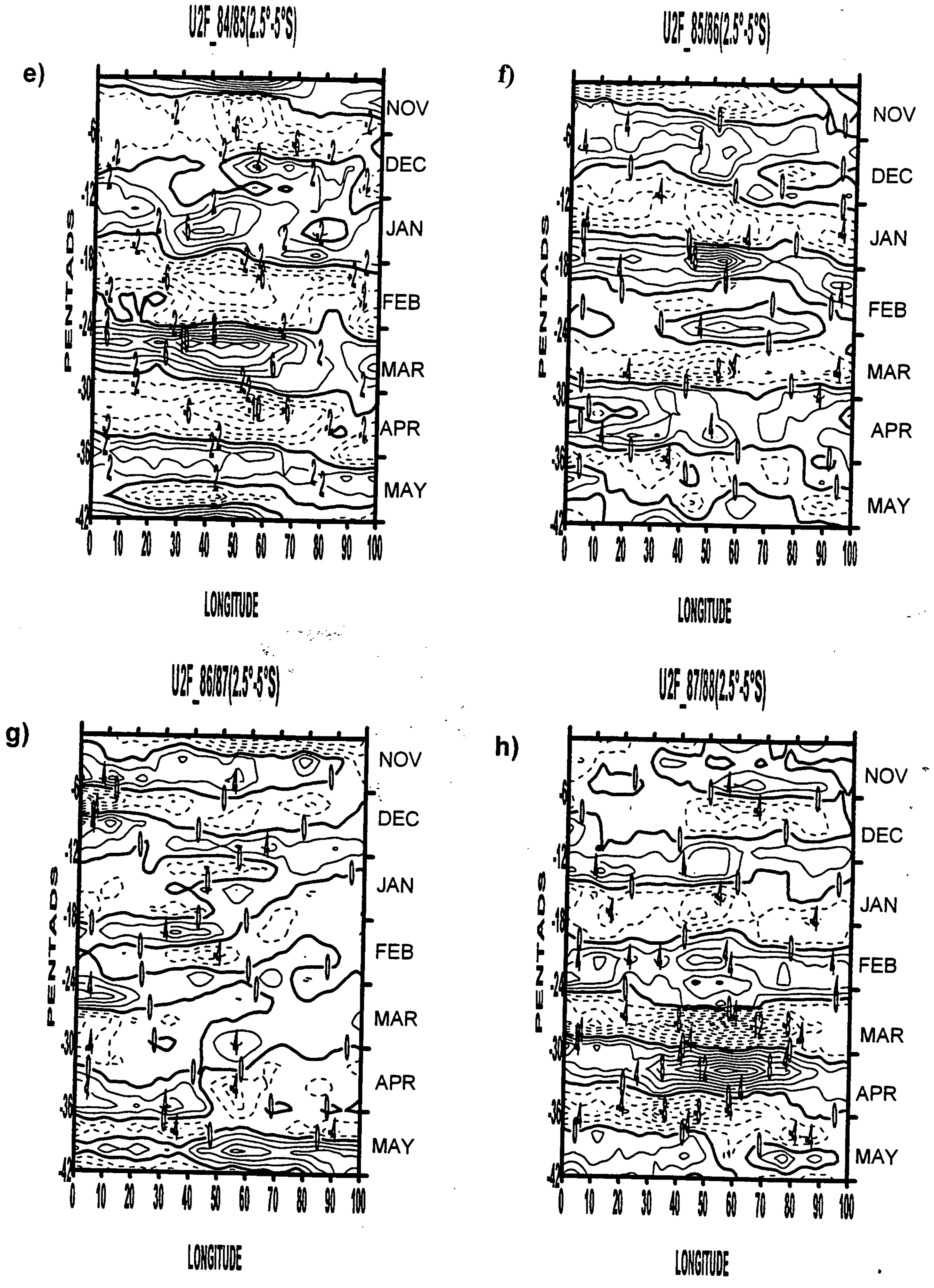

Figure 6.7 Continued: with time mean removed. Solid (dashed) contours indicate westerlies (easterlies), contour intervals 2 m/s.

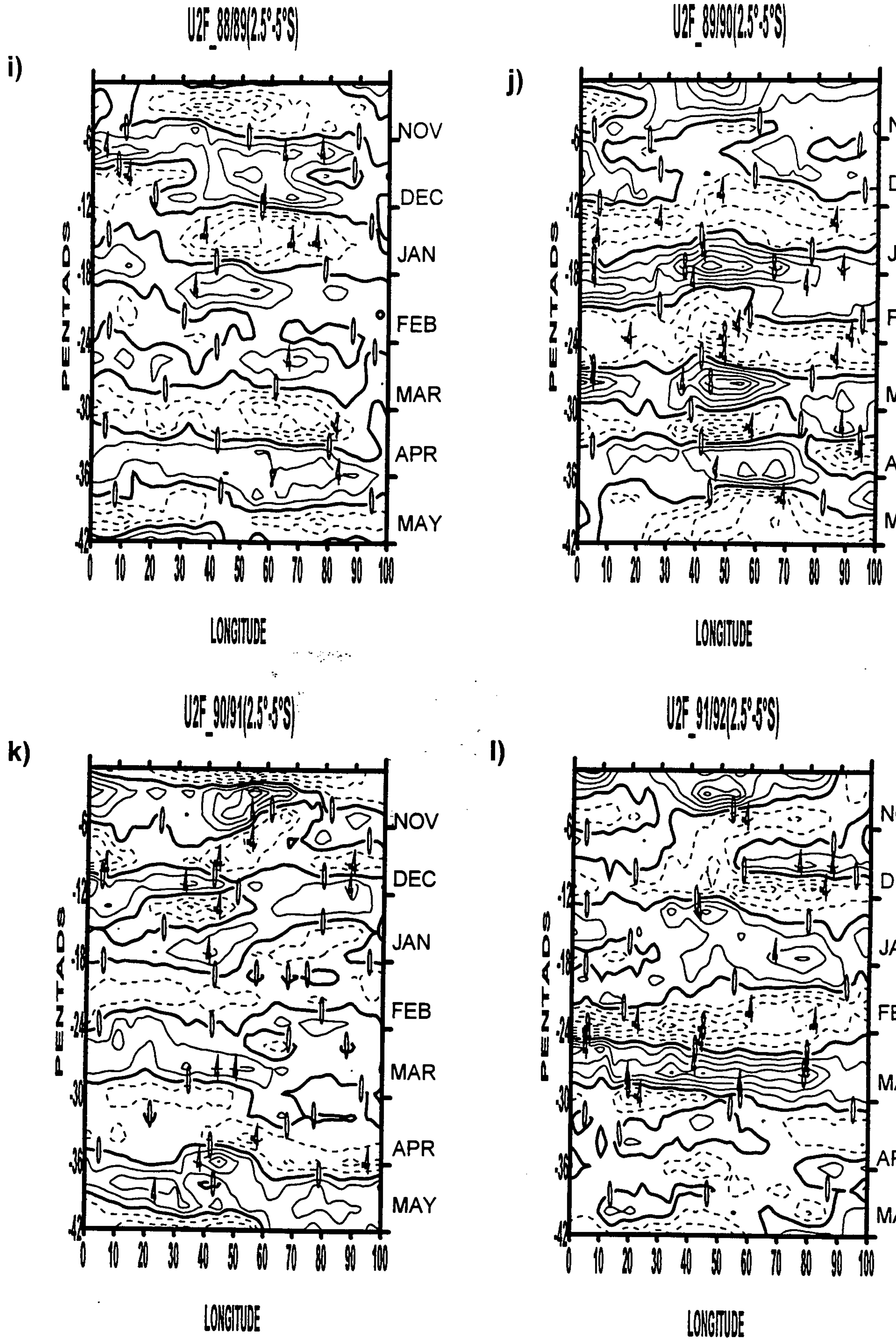

Figure 6.7 Continued:

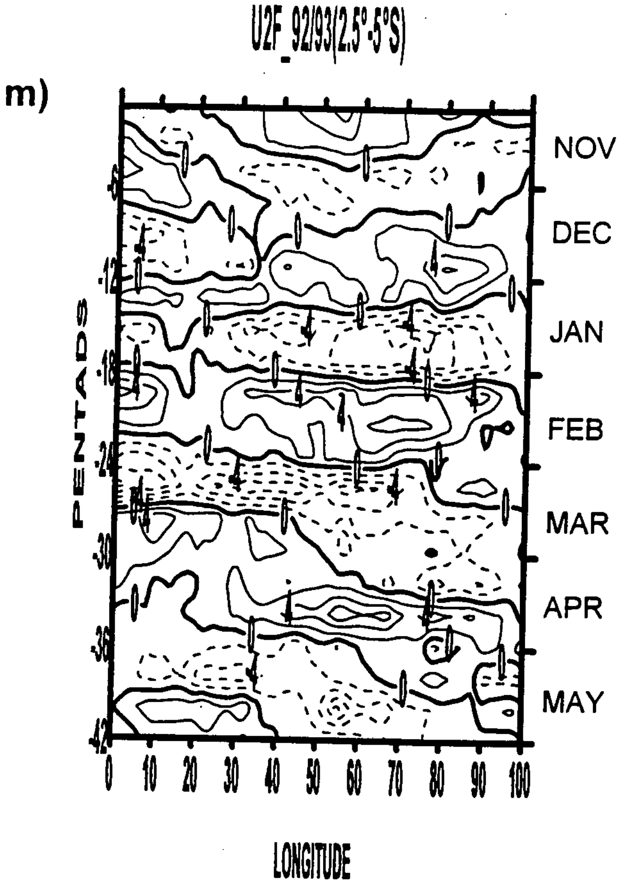

Figure 6.7 Continued:

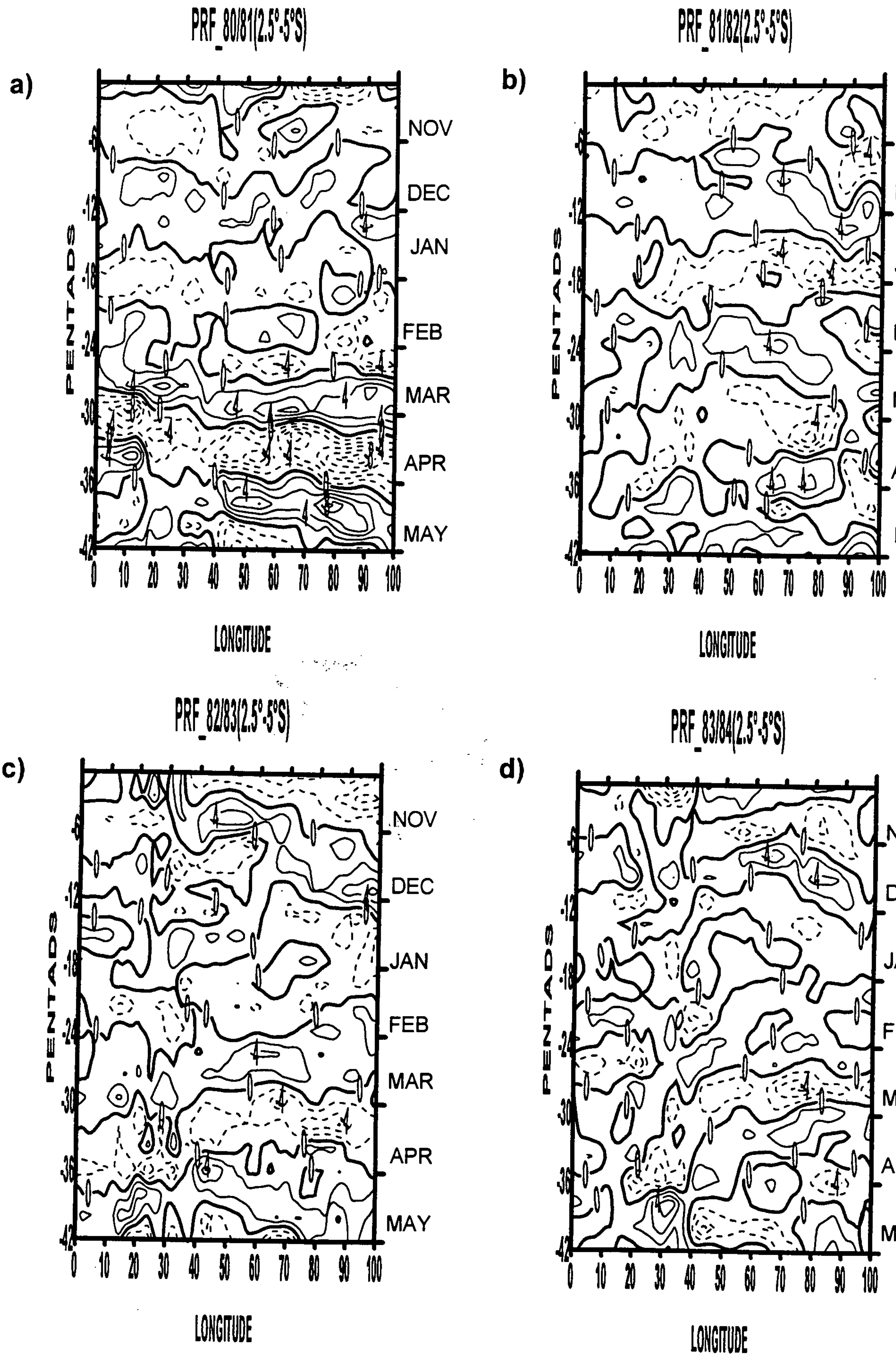

Figure 6.8: Hovmoller diagrams of (4-12 penated) 20-60 day band filter applied to pentad precipitable water anomalies integrated from 1000 hPa to 300 hPa level averaged between 2.5 to 5°E from 0° to 100°E for pentad 62 to

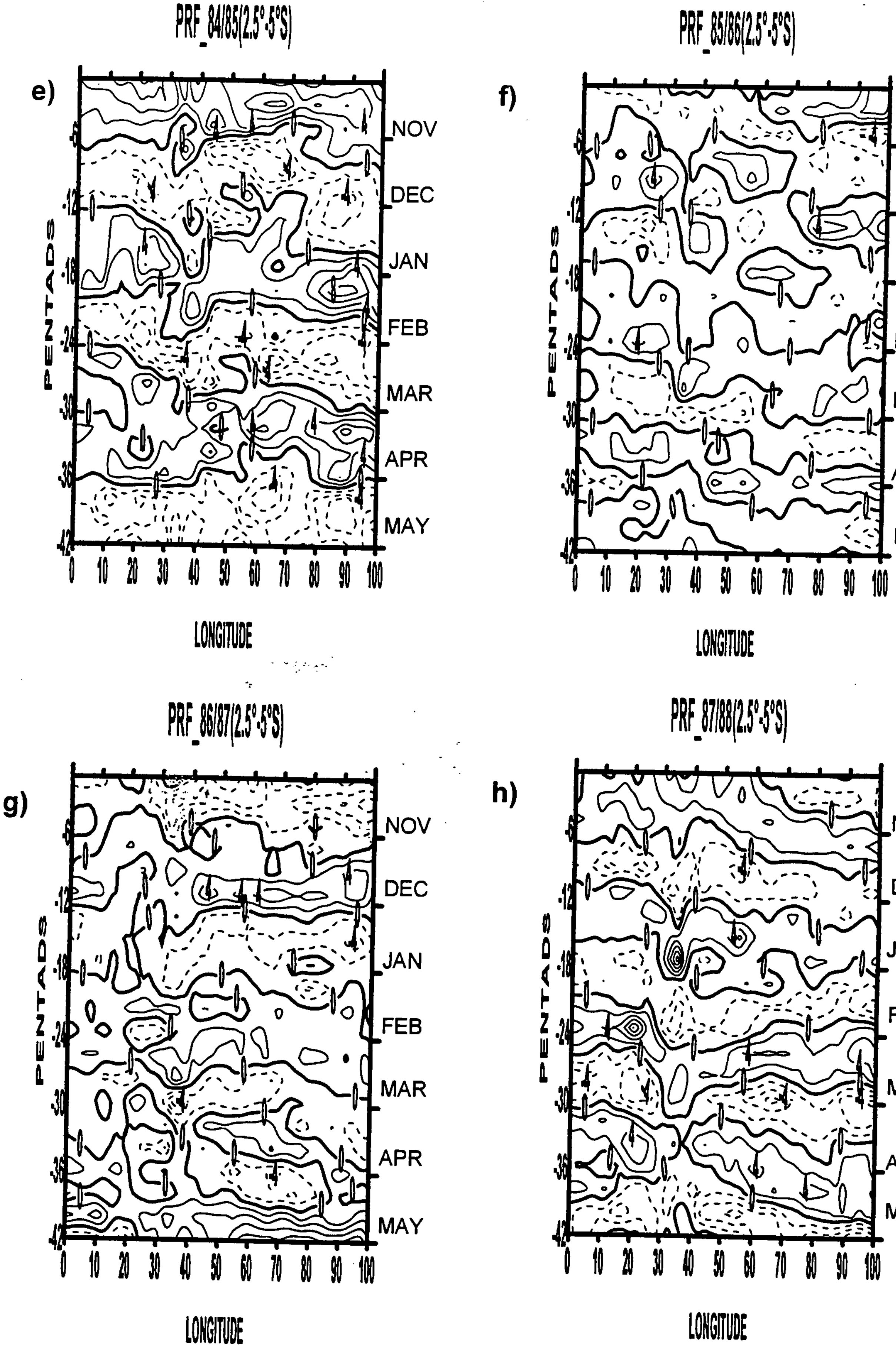

Figure 6.8 Continued: pentad 30 (i.e. Nov-May 1980/81 to 1992/93) with time mean removed, Solid (dashed) contours indicate positive (negative) anomalies, contour interval 2 mm

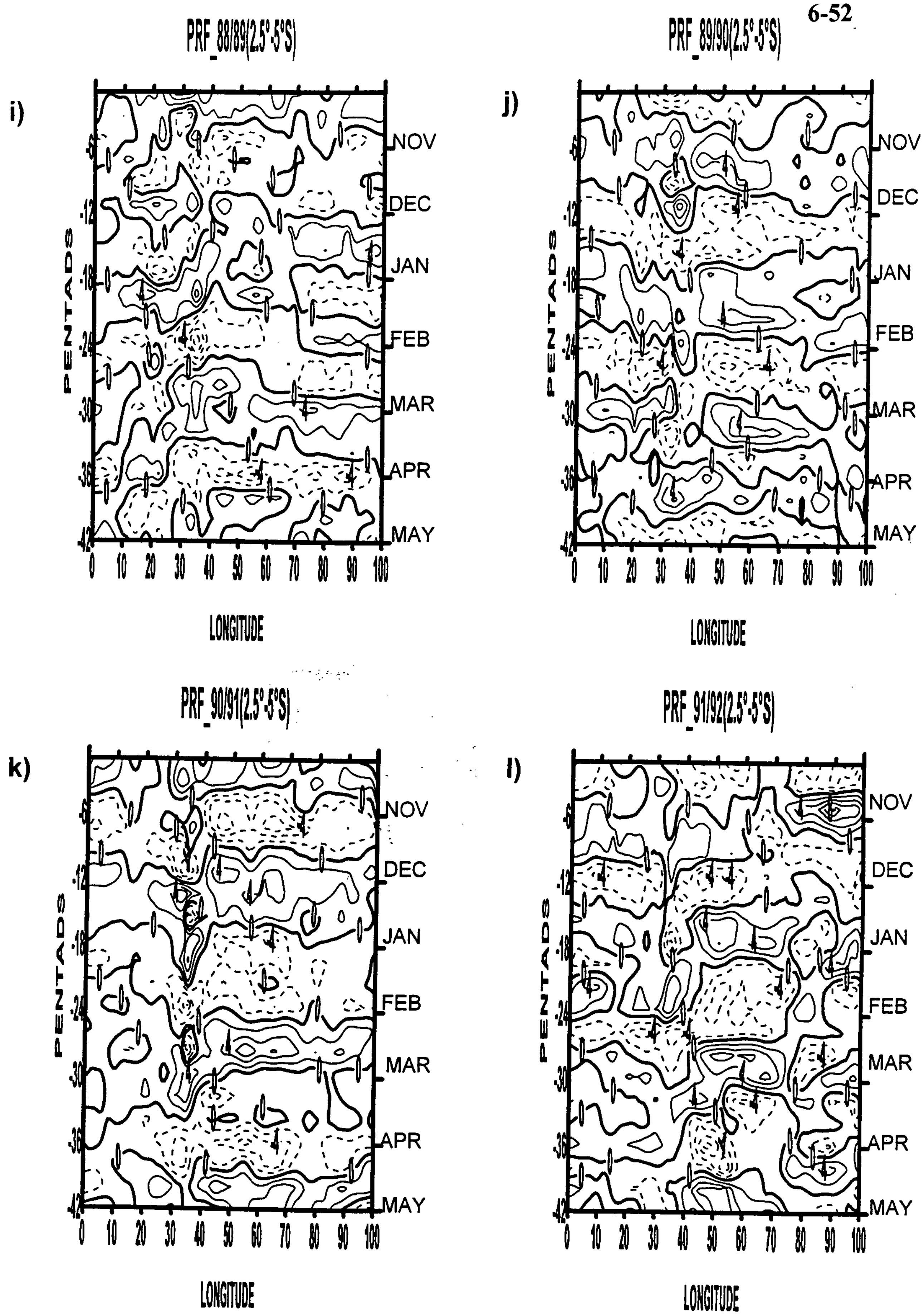

Figure 6.8 Continued:

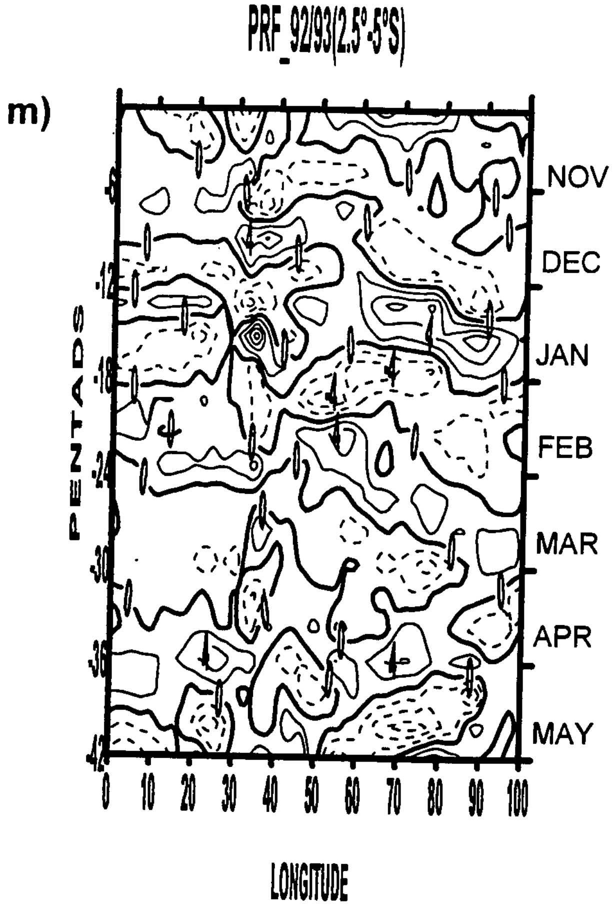

Figure 6.8 Continued:

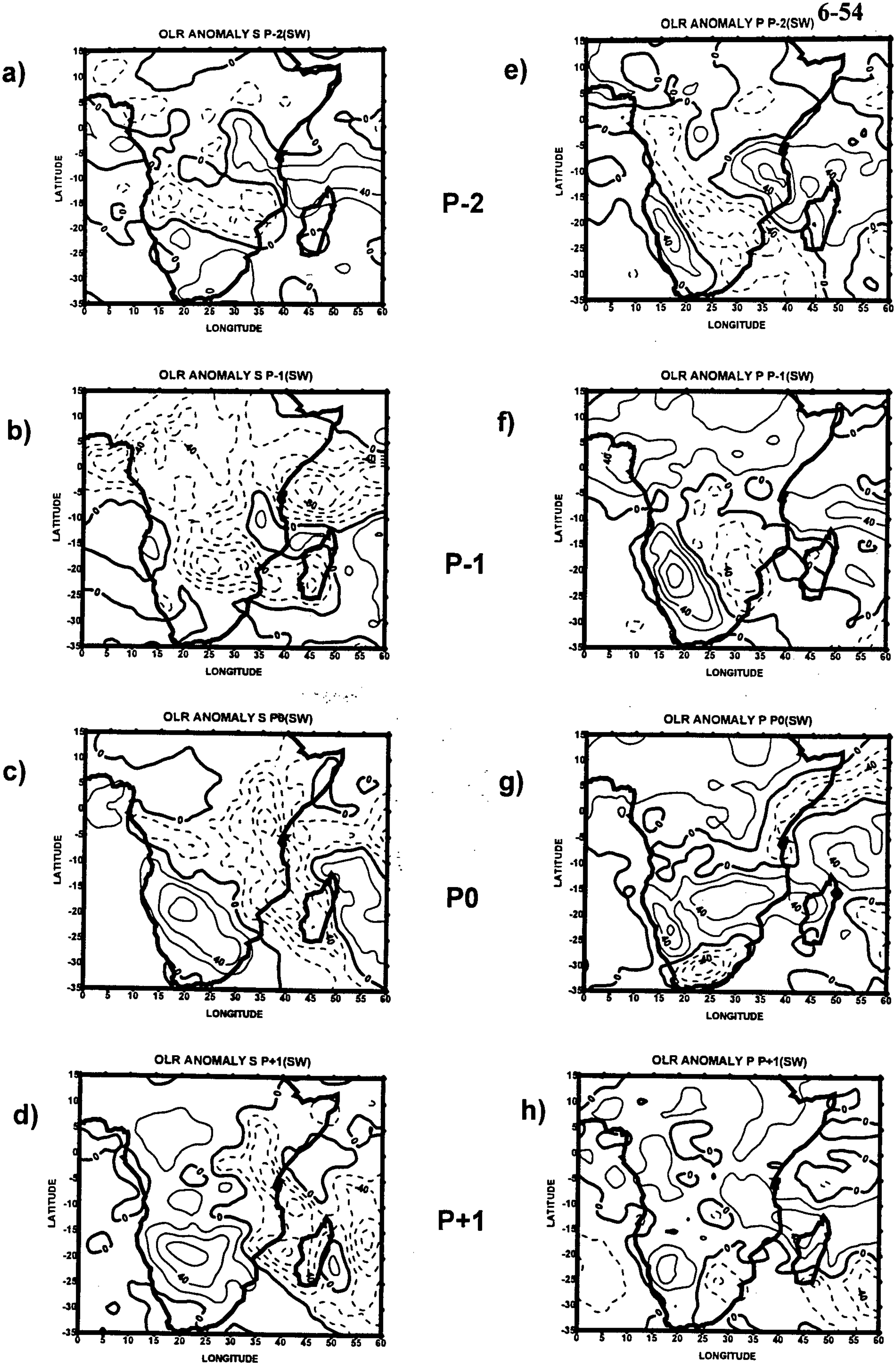

Figure 6.9: OLR anomaly for P-2 to P0. (a-d) sequence from pentad 01 to pentad 04 1993: (e-h) sequence from pentad 14 to pentad 17 1981, contour interval 20 W m^{-2}

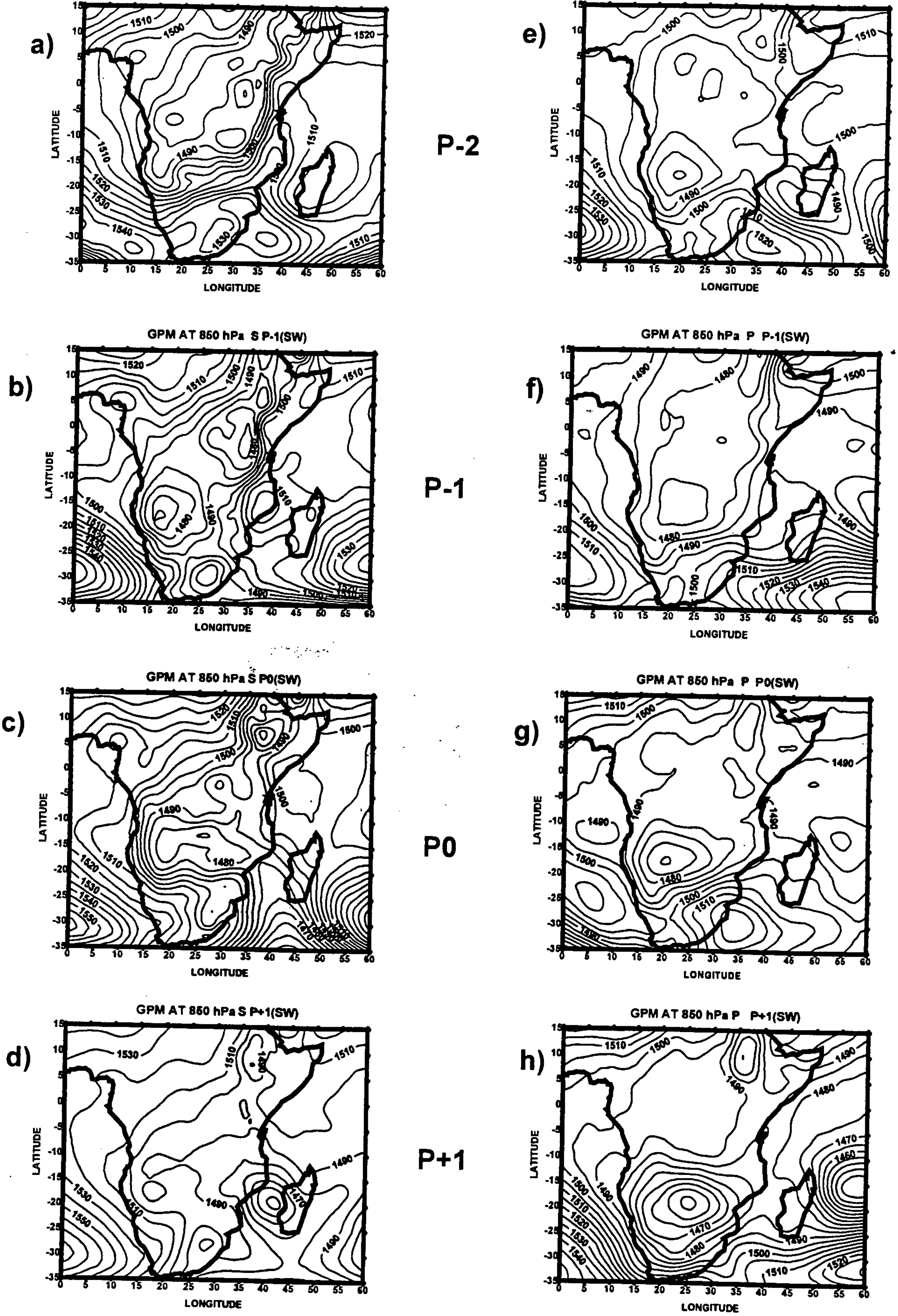

Figure 6.10: Geopotential heights at 850 hPa for P-2 to P+1. (a-d) sequence from pentad 01to pentad 04 1993; (e-h) sequence from pentad 14 to pentad 17, 1981; contour interval 5 gpm.

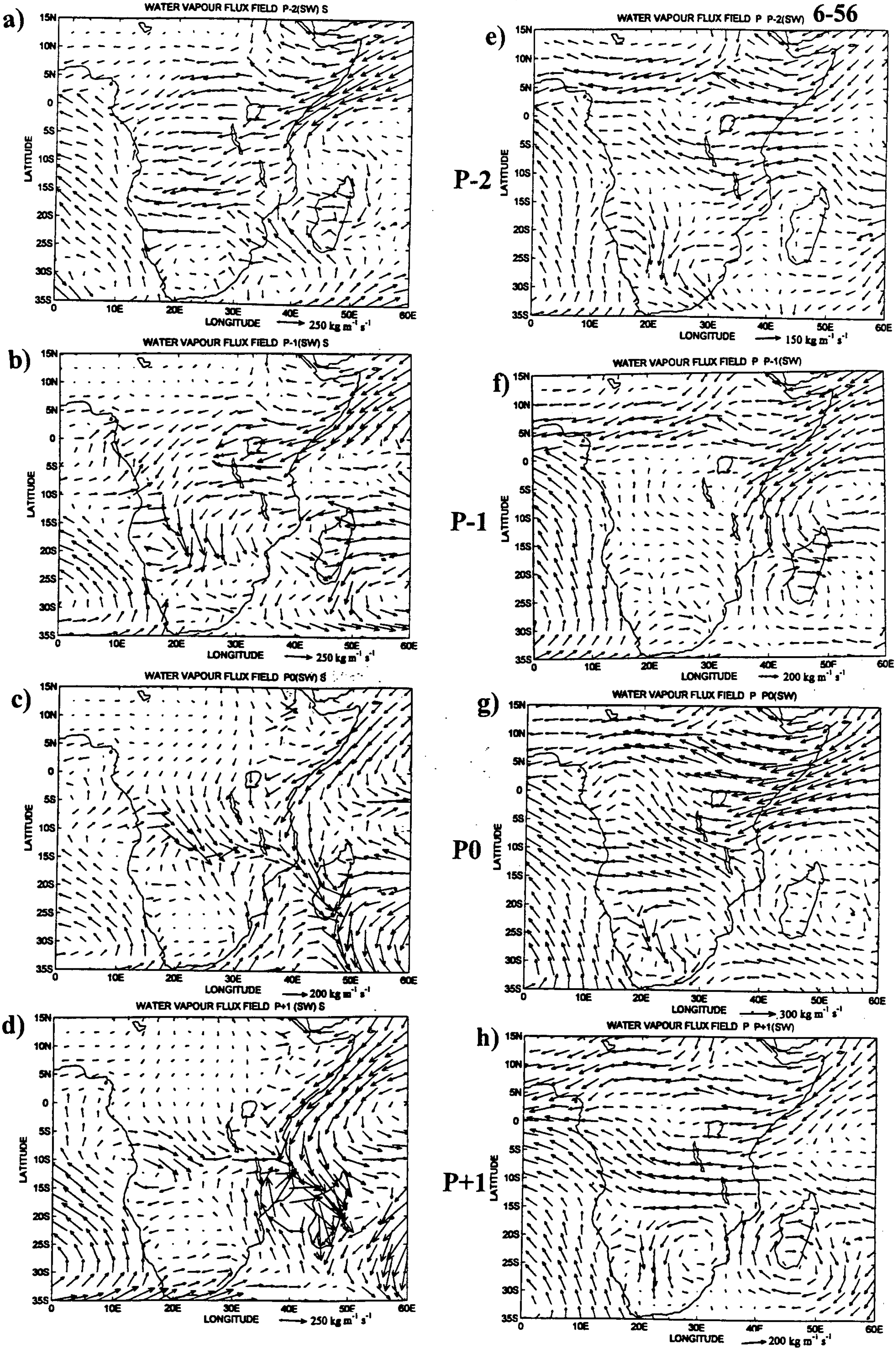

Figure 6.11: WVF integrated from surface to 500 hPa for P-2 to P+1. (a-d) Sequence from pentad 01 to 04 of 1993; (e-h) sequence from pentad 66 to pentad 69 of 1981.

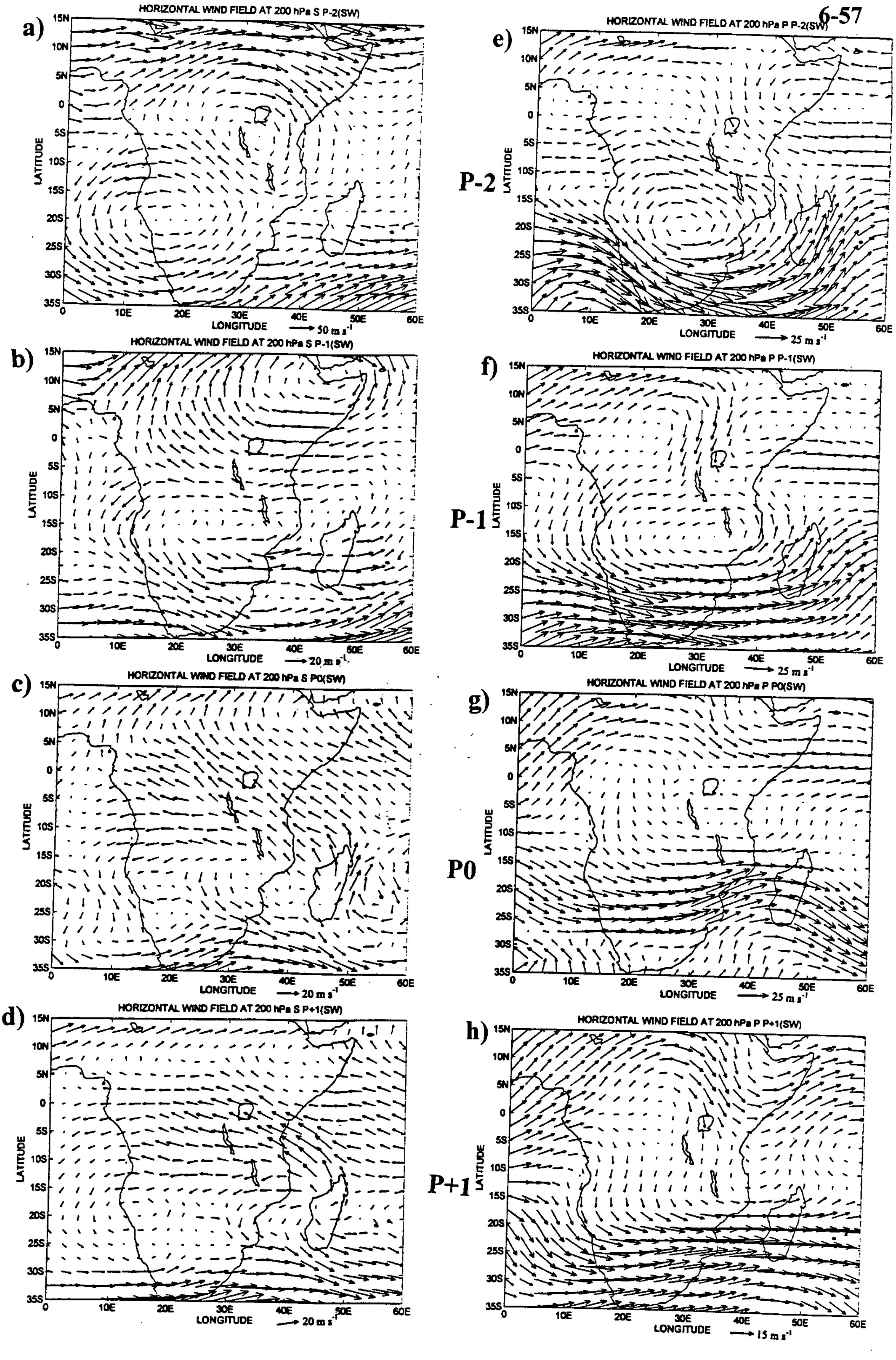

Figure 6.12: Wind flow pattern at 200 hPa for P-2 to P+1. (a-d) sequence from pentad 01 to 04 of 1993; (e-h) sequence from pentad 66 to pentad 69 of 1981.

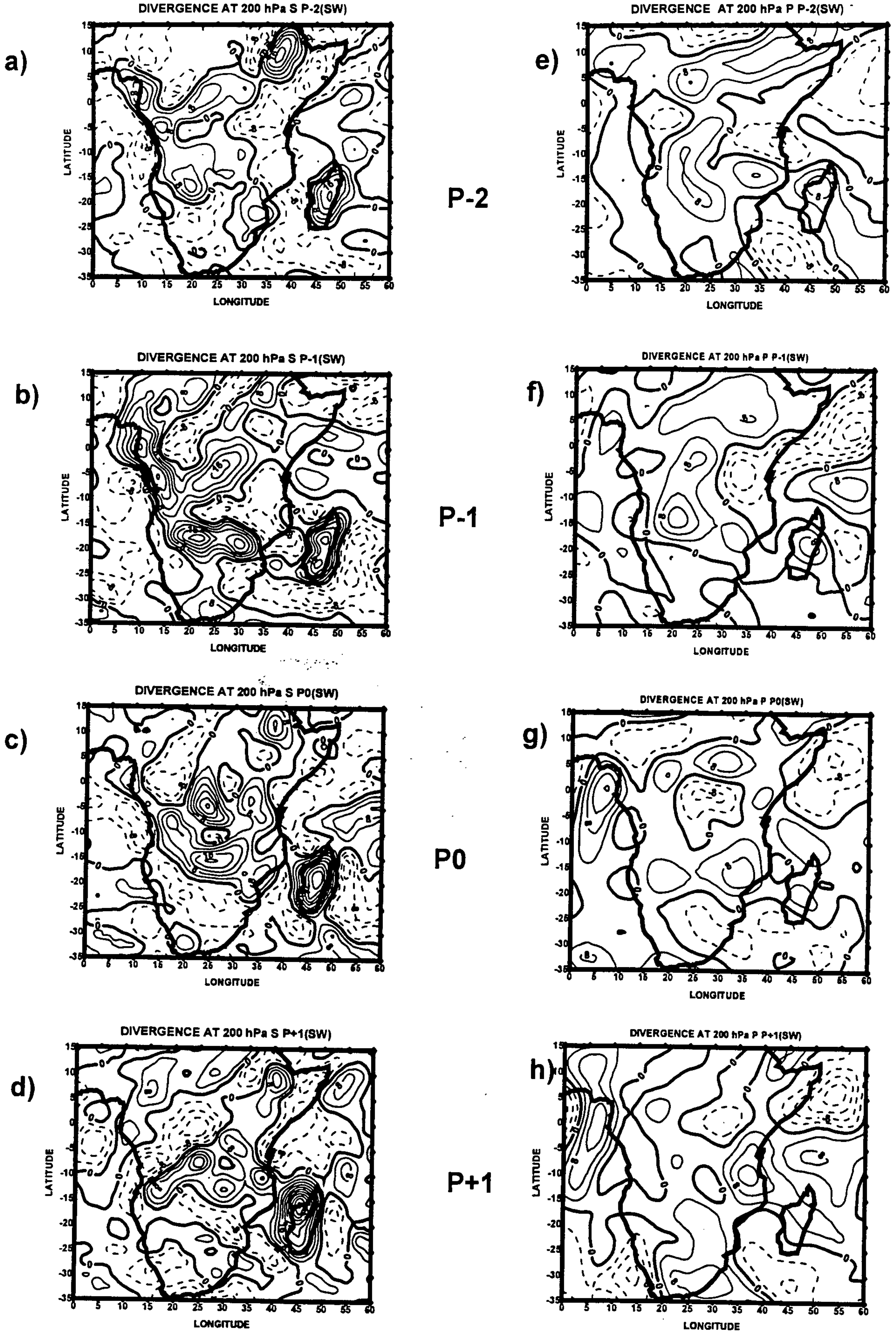

Figure 6.13: Divergence at 200 hPa for P-2 to P+1. (a-d) sequence from pentad 01 to pentad 04 1993; (e-h) sequence from pentad 66 to pentad 69 1981, contour interval 4×10^{-6} s^{-1}

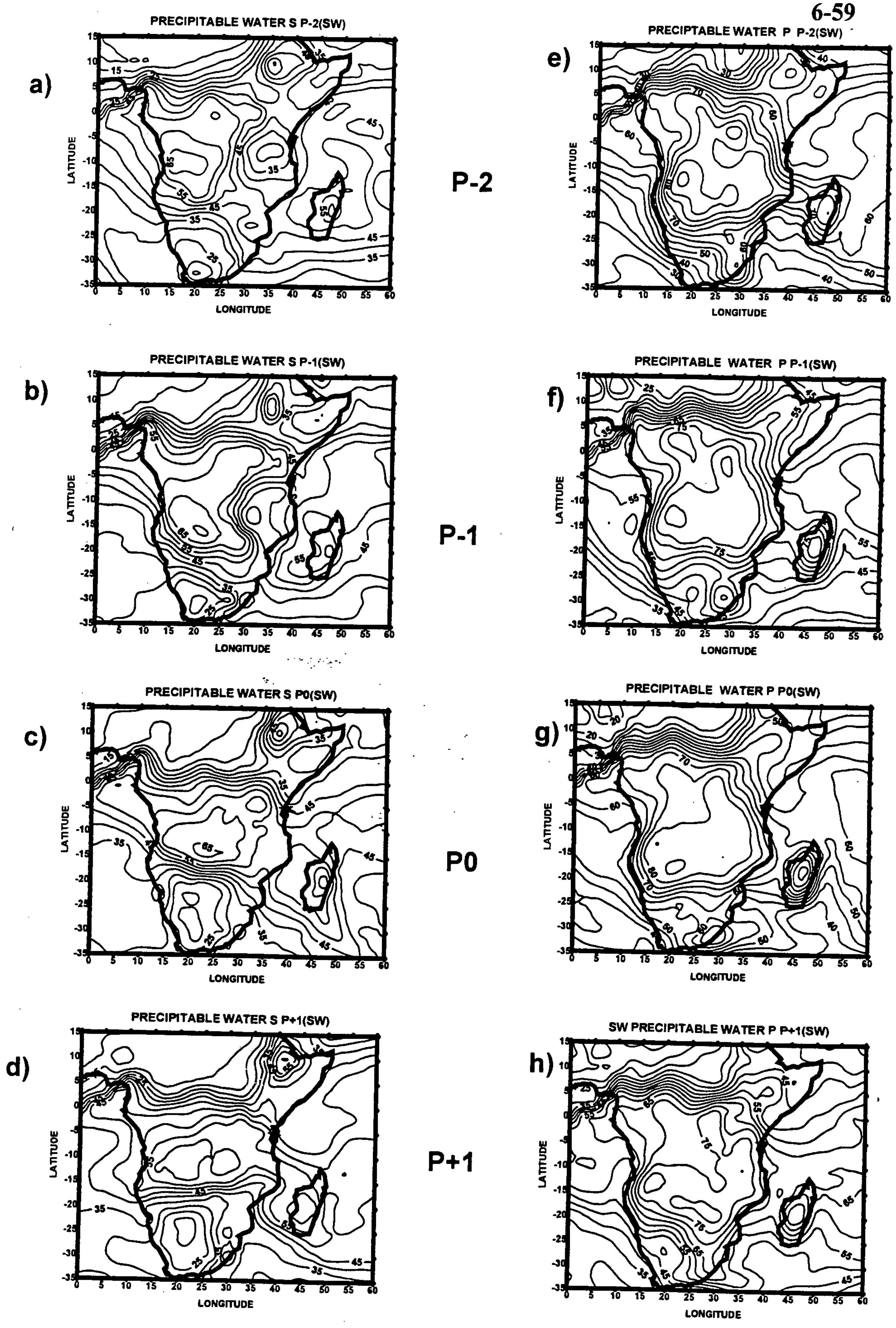

Figure 6.14: Precipitable water integrated from 1000 hPa to 300 hPa for P-2 to P+1. (a-d) sequence from pentad 01 to pentad04 1993; (e-h) sequence from pentad 66 to pentad 69 1981, contour interval 5 mm

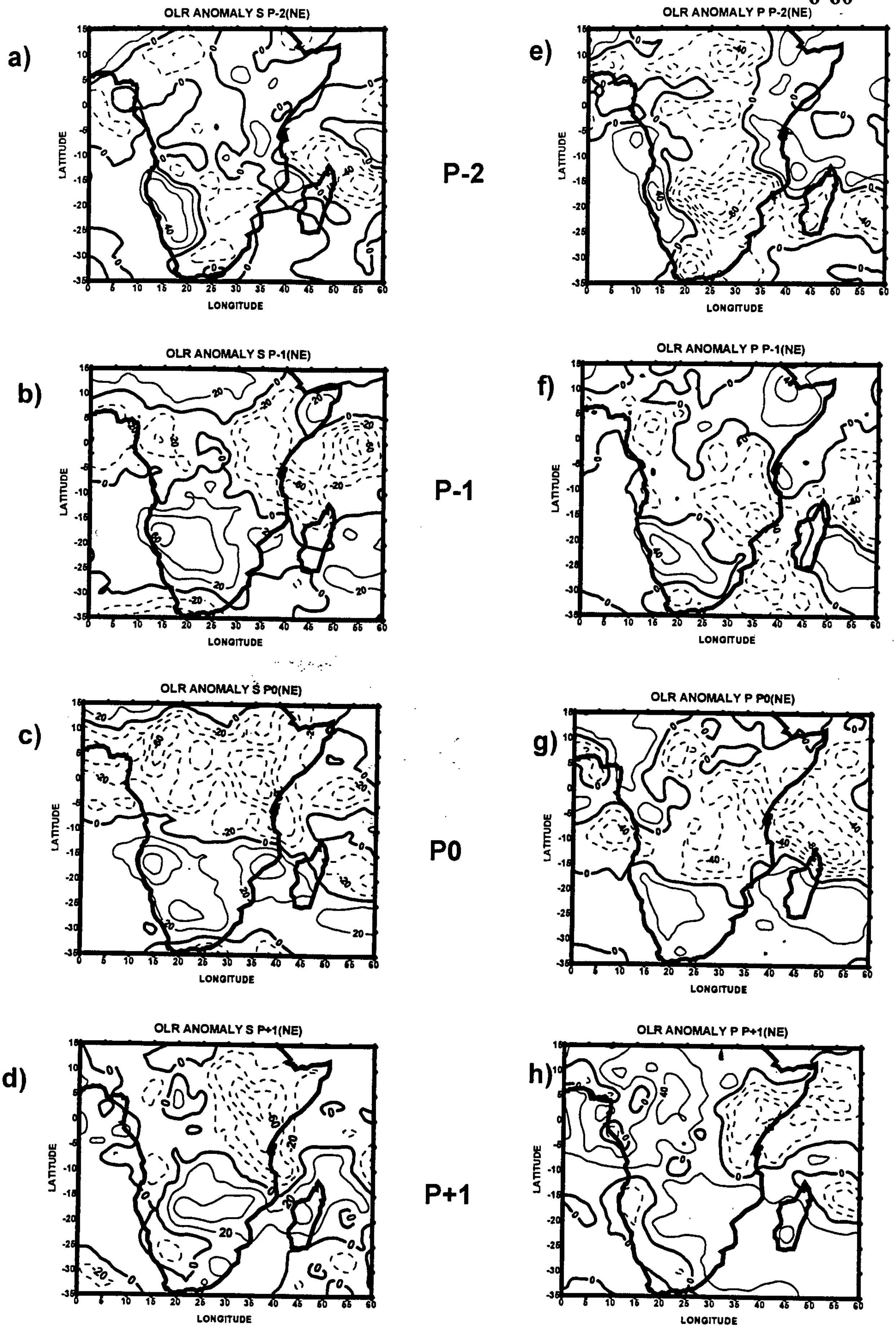

Figure 6.15: OLR anomaly for P-2 to P+1. (a-d) sequence from pentad 09 to pentad 12 1990. (e-h) sequence from pentad 20 to pentad 23 1988 eastward propagating convective system; contour interval 20 W m^{-2}

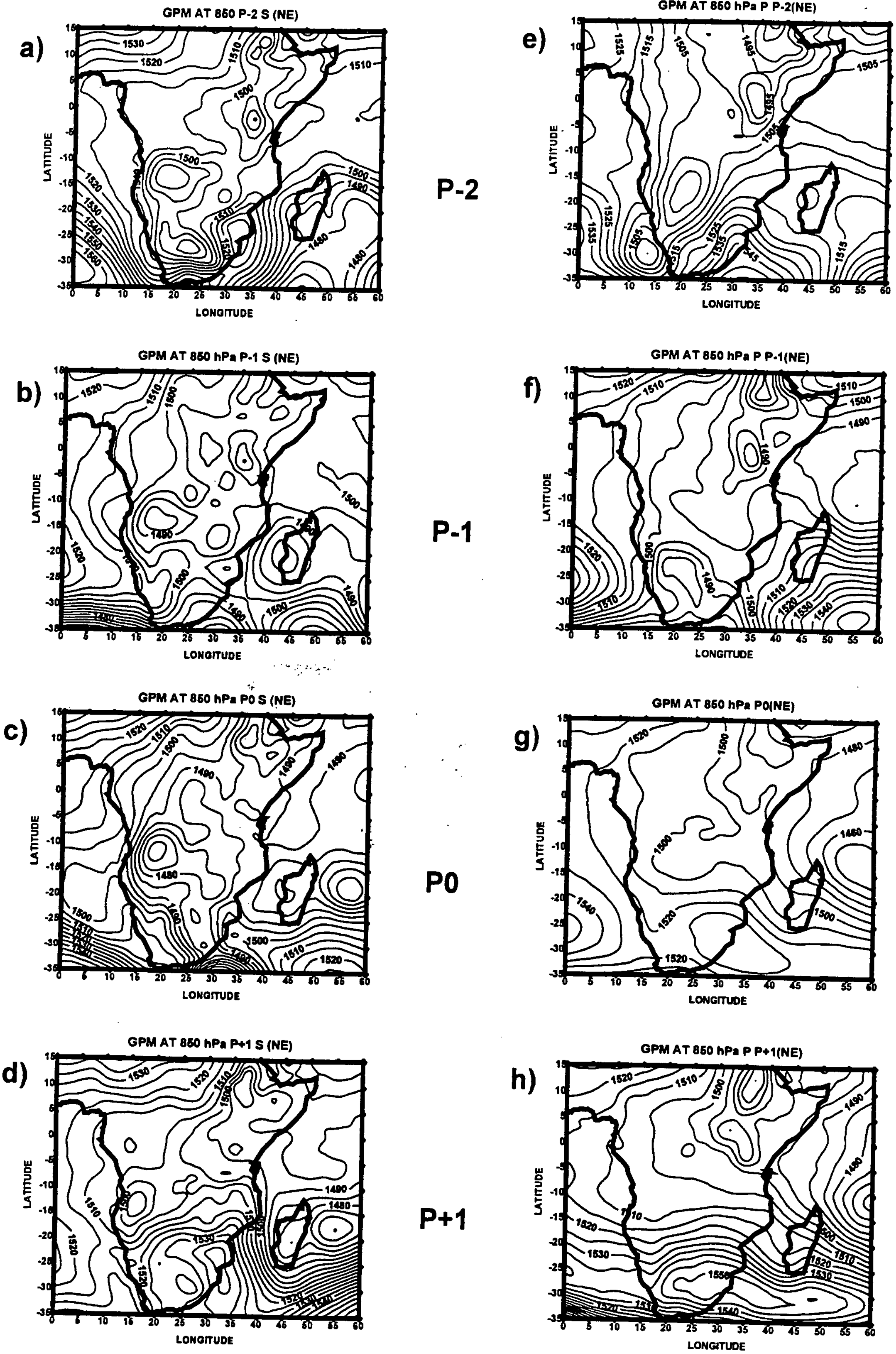

Figure 6.16: Geopotential heights at 850 hPa level for P-2 to P+1. a-d sequence from pentad 9 to pentad12 of 1990; e-h sequence from pentad 14 to pentad 17, of 1988. Contour interval 5 gpm

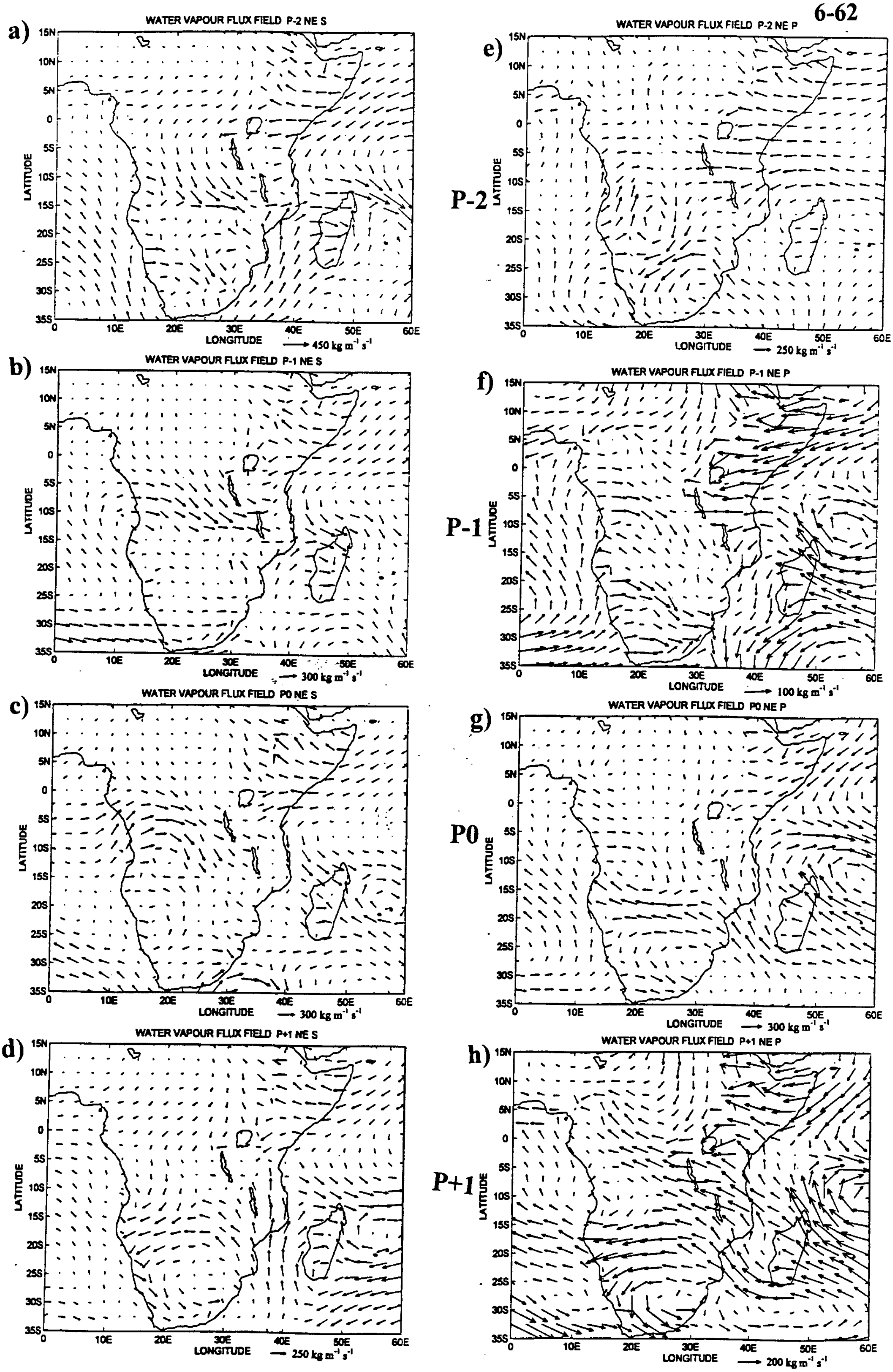

Figure 6.17: WVF integrated from surface to 500 hPa for P-2 to P+1. (a-d) sequence from pentad 9 to 12 of 1990; (e-h) sequence from pentad 14 to pentad 17 of 1988.

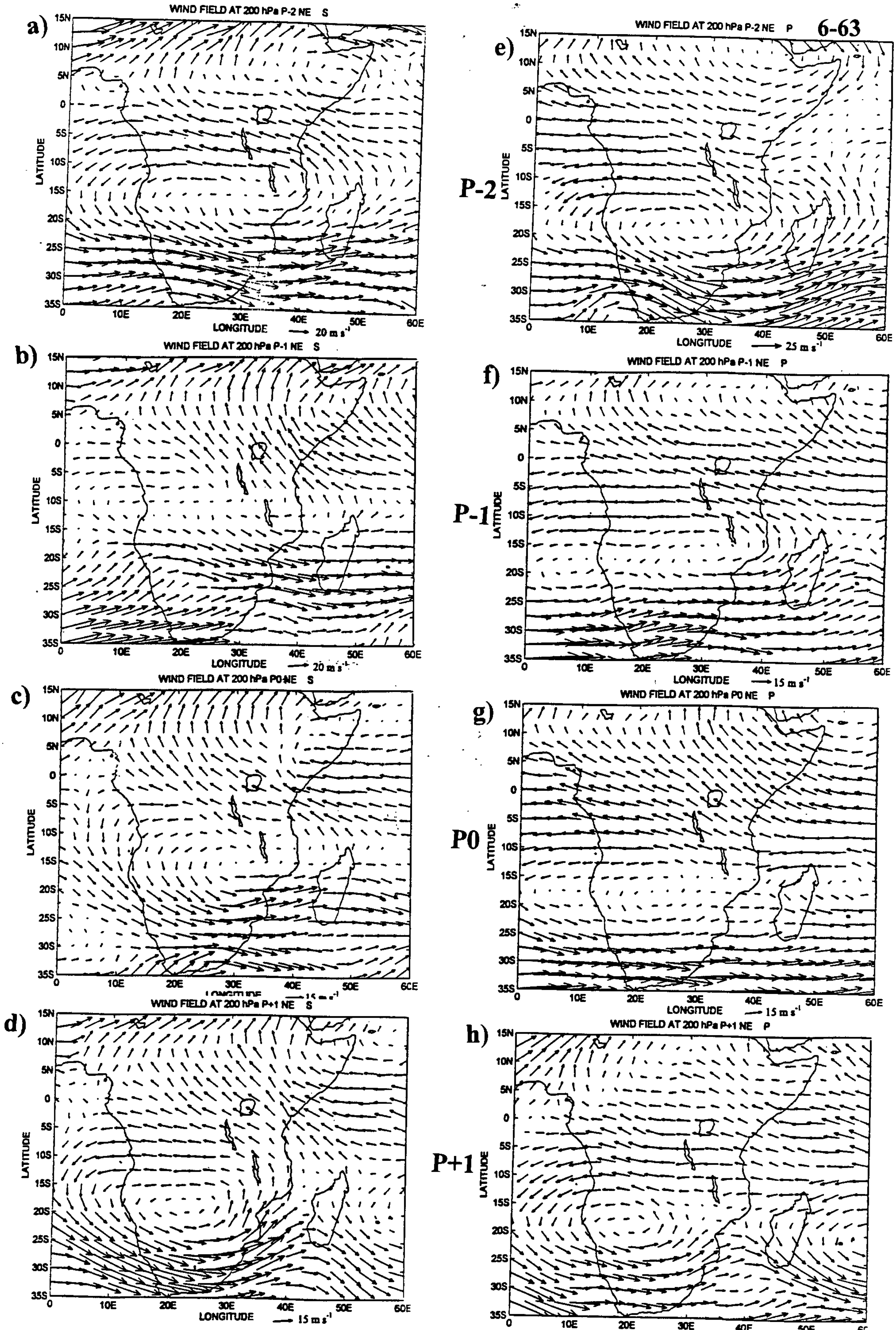

Figure 6.18: Wind flow pattern at 200 hPa for P-2 to P+1. (a-d) sequence from pentad 9 to 12 of 1990; (e-h) sequence from pentad 14 to pentad 17 of 1988.

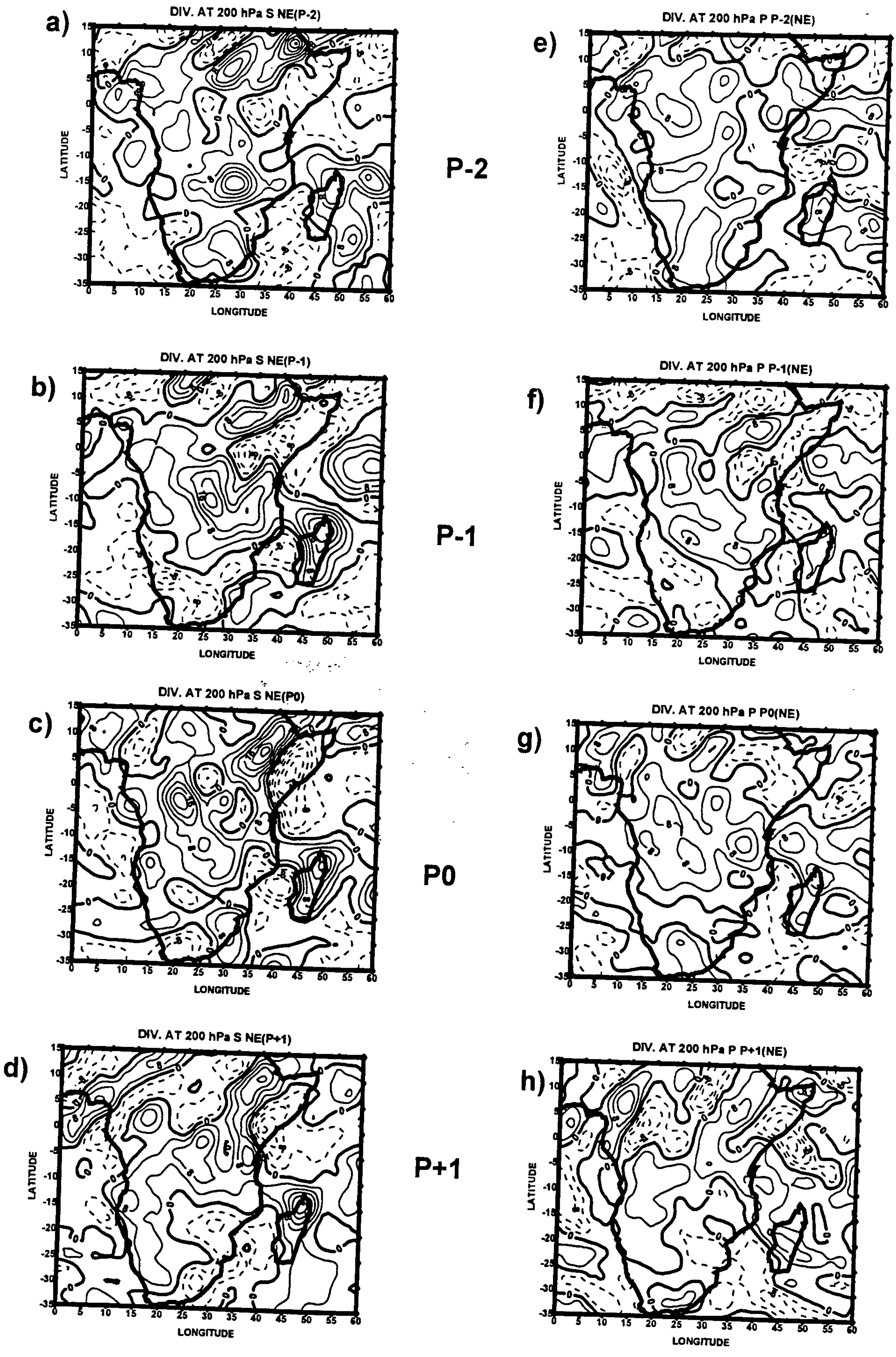

Figure 6.19: Divergence at 200 hPa for P-2 to P+1: a-d sequence from pentad 9 to pentad 12 of 1990; e-h sequence from pentad 14 to pentad 17 of 1988. Contour interval 4×10^{-6} s^{-1}

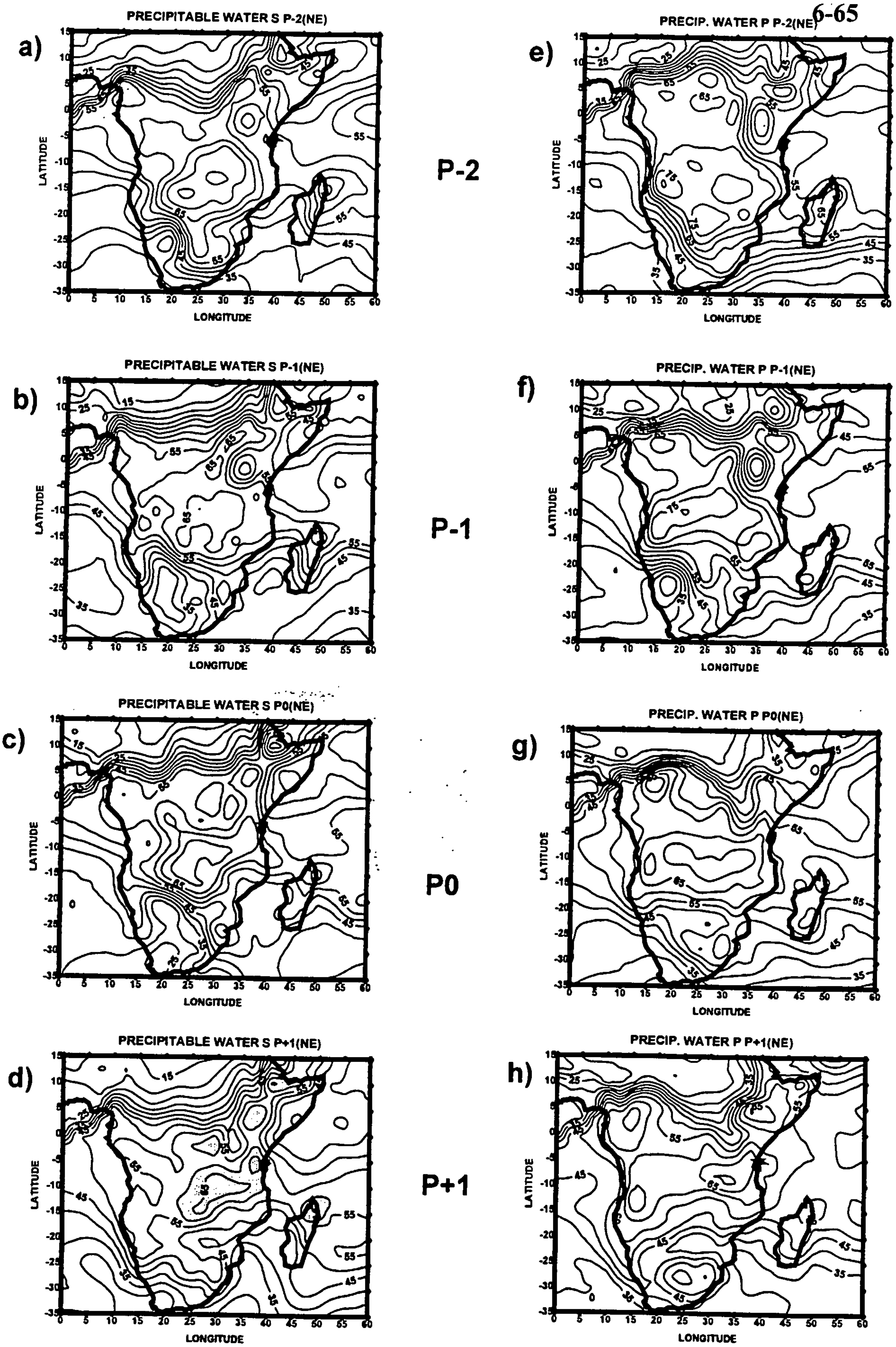

Figure 6.20: Precipitable water for P-2 to P+1; (a-d) sequence from pentad 9 to pentad 12 of 1990 (e-h) sequence from pentad 14 to pentad 17 of 1988. Contour interval 5 mm

CHAPTER 7

SUMMARY AND CONCLUSIONS

7.1 Introduction

Relationships of seasonal and inter-annual rainfall with global meteorological phenomena like ENSO (El Nino Southern Oscillation), SSTs (Sea Surface Temperatures), QBO (Quasi-Biennial Oscillation) etc. have been documented in many earlier studies. Little effort was placed on the study of rainfall variability in Tanzania at the intraseasonal time scale. One of the aims of this thesis was to identify and describe the main characteristics of the intraseasonal convective variability over northeastern and southwestern Tanzania during the MAM and DJF rainy seasons, in both frequency and spatial domains. Secondly the study aimed to identify kinematic and thermodynamic features associated with the intraseasonal convective variability using pentad OLR and ECMWF data. The third aim was to identify the characteristic nature of propagating convective systems transiting the two areas and investigate kinematic and thermodynamic features associated with these propagating convective systems. Time series plots and spectral analyses were performed on the derived area-averaged pentad OLR indices to determine convective variability and convective periodicities with dominant spectral peaks at intraseasonal time scale. Based on OLR pentad indices time series, spatial composites for the onset of convection and the most active convective phase were analysed. Horizontal and vertical section composites of kinematic and thermodynamic fields were analysed in order to understand features which are associated with active convection and its precursor. Time-longitude or Hovmoller plots along 5 and 10°S of band filtered OLR, zonal winds at 850 hPa and 200 hPa levels, and precipitable water anomalies revealed the propagating nature and coupling of local circulation and convection. One important type was an eastward propagating Madden Julian Oscillation (MJO), whilst westward and quasi-stationary types also occured.

7.2 Summary

7.2.1 Chapter 3

-the time series plots of pentad OLR indices demonstrated the existence of more active and less active convective phases within rainy seasons. Year to year variations of amplitude and periodicity of convection have been noted;

-spectral peaks were found in the 2-8 pentad range. Spectral peaks with periods above 6 pentads could be linked to the MJO and those in 4-6 pentad period range could be linked to tropical and mid latitude waves;

- the northeastward propagation of convection was found to be linked with mid-latitude frontal troughs.

7.2.2 Chapters 4 and 5

Deep convection was found to be associated with:

- the development of weak westerlies at low levels over the Congo basin and relaxation of the northeasterly monsoon over the western Indian Ocean in the case of southwestern sub-region in DJF;
- convergence of northeasterly monsoon and south-easterly trade winds over the coast of Tanzania and Kenya during MAM over the northeastern sub-region;
- increasing speed of tropical easterly wind and diffluent cross equatorial southeasterlies at 200 hPa level
- increase in precipitable water
- warming up of the middle troposphere by about 1.5°K

7.2.3 Chapter 6

Time-longitude diagrams revealed propagating and non-propagating features in the 2.5°-5°S and 7.5°-10°s latitude bands. More organised propagating features were revealed after short period oscillations with periods 2 to 3 pentads were removed by filtering. Westward propagating features were found to be generally weak and short lived.

Eastward propagating convective systems were found to be coupled with

- westerly winds at 850 hPa level
- relatively strong easterly winds at 200 hPa
- positive precipitable water, though on some occasions the coupling was weak;

The phase speed of eastward propagating convective systems (negative OLR anomalies) was found to be between 1.7-8 m s^{-1} and the periods of occurrence of large scale active events was found to be between 5 to 11 pentads, with the average period of about 6 pentads i.e. 30 days. The large scale active eastward propagating events were found to be generally separated by less convection (positive OLR anomalies). Active eastward propagating convective systems are large scale features which can be traced in the two latitude bands, i.e. 2.5°-5°S and 7.5°-10°S at the same time. Some intraseasonal convective systems start over the continent of Africa with small amplitude and propagate eastward to the Indian Ocean where their amplitude increases. The systems appear disorganised over the coast of East Africa. This could be due to the diverging northeasterly flow in the north and the ridging in the south.

On the basis of the findings in this study we propose schematic diagrams to represent flow patterns during the active convective phase for DJF in the southwestern sub-region and MAM in the northeastern sub-region.

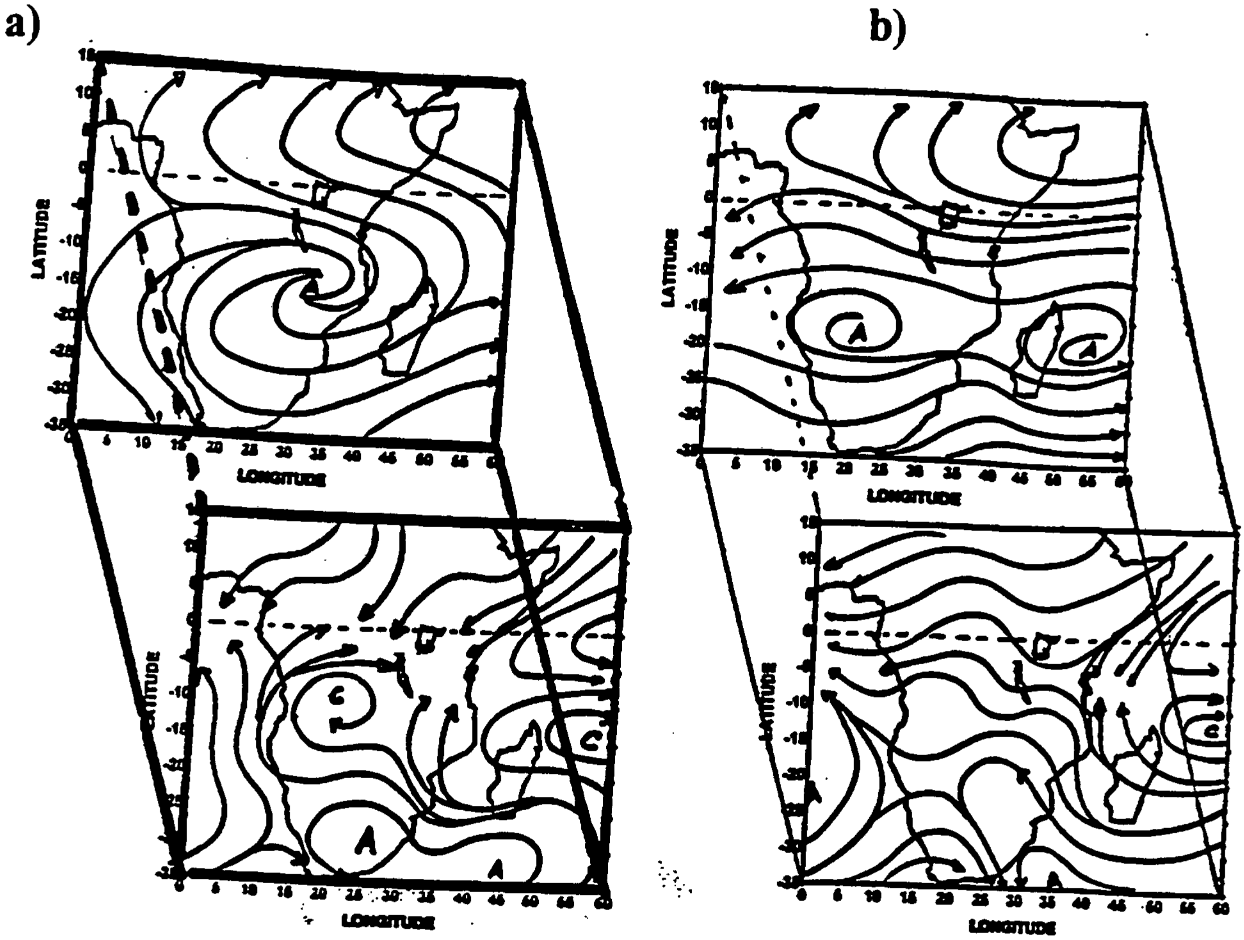

Figure 7.1: Schematic of large-scale circulation features associated with deep convection in Tanzania. The upper and lower panels represents the 200 hPa and the 850 hPa flow patterns respectively. (a) represents DJF season, (b) represents MAM season

7.3 Conclusions

Intraseasonal convective oscillation signals have been found over Tanzania. Further detailed studies could establish the causes of changes in the amplitude and period of oscillation of convection. This will be a step towards finding statistical patterns and predictors for intraseasonal rainfall which is important for the planning of agricultural activities. The predictions can also be of vital importance to dam and other water resources managers in the monitoring of dam levels, distribution of water for irrigation, etc. This study is particularly important to hydrologists as the large scale distribution of rainfall will mean that most of the river catchments are covered by rainfall at same time.

Some weakness in the present study should however, be mentioned.

- the OLR pentad indices were confined to 2 seasons, so convective periods above 6 pentads could not be resolved.

-composite vertical motions could be biased by differences in ECMWF data assimilation from 1980 to 1994. Signals in the convection variabilities were evident, although poor observational coverage over tropical regions is a source of bias.

- the sample size for compositing was small, so affecting pattern stability.

Recommendations:

This thesis has contributed to the understanding of intraseasonal convective oscillation characteristics with associated kinematic and thermodynamic processes over northeastern Tanzania during the 'masika' (MAM) season and over southwestern Tanzania during the DJF season. A similar study, covering the northeastern areas of Tanzania for the 'vuli' (OND) season, was done by Kabanda, (1995). A detailed study of the causes of year to year variations of amplitudes and periods at intraseasonal time is required in order to find the causes. The knowledge will lay a ground work for the formulation of intraseasonal rainfall prediction models. Vertical section analysis have shown that the large amplitude changes of zonal wind speed occur at the 700 hPa level. Weather forecasters should thus operationally use analyses of meteorological parameters at the 700 hPa level to take advantage of strong signals at this level.

ACKNOWLEDGEMENTS

I wish to thank my supervisors, Professor Mark R. Jury (Head of the Geography and Environmental studies, University of Zululand) and Professor Geoff Brundrit (Head of the Oceanography Department, University of Cape Town) for their tireless support, guidance and suggestions throughout this study. Valuable and constructive comments and suggestions were available at different stages of my study from Associate Professor Frank A. Shillington. Constructive criticisms and suggestions from Professor Bin Wang (University of Hawaii, Department of Meteorology) and Dr. Roland Madden (NCAR) are acknowledged. I am grateful to Henry Mulenga and Mark Majodina for their helpful discussions and suggestions during the whole period of this research work.

Many thanks goes to the Water Research Commission (WRC) for funding this research work. I am grateful to the Director General and staff of the Directorate of Meteorology, Tanzania for all the assistance given to me before and during the course of this study.

The author wishes to thank all staff members of the Oceanography Department for their support during this study. In short I can just say; they created a conducive environment for my study.

I finally wish to thank my family for their constant encouragement and accepting in separation during the whole period of this study.

References

Alusa. A., and M. Mushi, 1973: A study of the onset, duration and cessation of the rains in East Africa. Proceedings of the Fifth Specialist Meeting on Applied Meteorology in East Africa, Nairobi, Kenya, 133-140.

Anyamba, E. K., 1992: some properties of a 20-30 day oscillation in tropical convection. J. Afr. Met. Soc. **1**, 1-19.

Asnani, G. C., 1993: Tropical Meteorology. Noble Printers, Pune- India, 1202 pp.

Bengtsson, L. and Shukla, J., 1988: Integration of Space and In situ Observations to study Global Climate Change, Bulletin of American Meteorological Society, **69**, 10, 1130-1143.

Bolton, D., 1980: The computation of Equivalent Potential temperature, Mon. Wea. Rev. **108**, 1046-1053.

Chang, C-P., and H. Lim, 1988: Kelvin wave- CISK: A possible mechanism for the 30-50 day oscillation. J. Atmos. Sci., **45**, 1709-1720.

Chen, T. and Tzeng, R., 1990: Global Scale Intraseasonal and Annual Variation of Divergent-Water vapour Flux, Meteorology and Atmospheric Physics, **44**, 133-151.

Dixon, W. J.; M. B. Browon; L. Engelman; R. I. Jennrich, 1990: BMDP Statistical Software, University of California Press

EAMD, 1963: Climatic seasons of East Africa. E. A. Met. Dept. Report No. 8, 4pp

EAMD, 1963: The weather of East Africa, East African Meteorological Department. Pamphlet series No. 7, 13pp

Griffiths, J., 1959: The variability of annual rainfall in East Africa. Bulletin of American Society, **44**, 361-362

Hartmann, D. L. Michelsen, and S.A. Klein, 1992: Seasonal variations of Tropical intraseasonal oscillations: A 20-25 day oscillation in the western Pacific. J Atmos. Sci., **49**, 1277-1289.

Hastenrath s., Nicklis A. and Greischer L., 1993: Atmospheric- hydrospheric mechanisms of climate anomalies in the western equatorial Indian ocean, Journal of Geographical research, **98**, 20219-20235.

Hendon, H. H and Liebmann, 1990: The Intraseasonal (30-50) Oscillation of the Australian Summer Monsoon, J. Atmos. Sci., Vol. **47**, No. 24, 2904-2923.

Hendon, H. H., 1988: A simple model of the 40-50 day oscillation. J. Atmos. Sci., **45**, 569-584.

Hills, R., 1979: The structure of the Inter-Tropical Convergence zone in the Equatorial African rainfall. Transaction of the Institute of British geographers. 4, 329-352 pp.

Holton, J. R., 1973: An introduction to dynamic Meteorology. Academic press, Ney York, 319 pp.

Hoskins, B. J., H. Hsui; I. N. Janes; M. Masutani; P.D.Sardeshmukh, and G.H. White, 1989: Diagnostics of the global atmosphere circulation based on ECMWF analysis 1979-1989, WMO/TD-No. 326.

Jury M.R and McQueen C., 1993: Climatic atlas of climatic determinants for Tanzania.

Jury M.R and Levey K, 1993: The climatology and characteristics of drought in the Eastern Cape of South Africa, International Journal of climatology, **13**, 629-6491.

Jury, M. R., B. Parker, and D Waliser, 1994: Evolution and Variability of the ITCZ in the SW Indian Ocean: 1988-1990, Theor. Appl. Climatol. **48**, 187-194.

Jury, M. R., B. Pathack, G. Campbell, B. Wang, and W. Landman., 1991: Transient convective waves in the Tropical SW Indian Ocean. Meteorol. Atmos. Phys., **47**, 27-36.

Jury, M. R., B. Pathak and D. Waliser, 1994: satellite OLR and microwave data as a proxy for summer rainfall over sub-equatorial Africa and adjacent Oceans. Int. J. Climatol., 257-269.

Kabanda, T. A., 1995: Seasonal and Intraseasonal dynamics and Precursors of rainfall over northern Tanzania. MSc. Thesis, University of Cape Town, Cape Town, South Africa.. 155 pp

Knutson , T. R., and K. M. Weickmann, 1987: 30-60 day atmospheric circulations: Composite life cycles of convection and circulation anomalies. Mon. Wea. Rev., **115**, 1407-1436.

Knutson, T. R., and K. M. Weickmann, 1987: 30-60 day atmospheric circulations: Composite life cycles of convection and circulation anomalies. Mon. Wea. Rev., **115**, 1407-1436

Kuboto, S., and S. Lida, 1954: Statistical characteristics of the atmospheric disturbances. Meteor. and Geophys. **5**, 22-34.

Lau, K.-M and L. Peng, 1987: Origin of Low Frequency (intraseasonal) Oscillations in the Tropical Atmosphere. Part I: basic Theory, Journal of the Atmospheric Sciences, **44**, 6, 950-972.

Levey, K. M., 1993: Intraseasonal oscillations of convection over southern Africa. MSc. Thesis, University of Cape Town, Cape Town, South Africa. 226 pp.

Lyons, S. W., 1991: Origins of Convective variability over equatorial Southern Africa during Austral Summer, Bulletin of American Meteorological Society. **4**, 23-39.

Madden, R. A., 1986: Seasonal Variation of the 40-50 day oscillation in the tropics. J. Atmos. Sci., **43**, 3138-3158.

Madden, R. A., and P. R. Julian, 1971: Detection of a 40-50 day oscillation in the zonal wind in the tropical Pacific. J. Atmos. Sci., **28**, 702-708.

Madden, R. A., and P. R. Julian, 1972: Description of global-scale circulation cell in the tropics with a 40-50 day period. J. Atmos. Sci., **29**, 1109-1123.

Makarau, A., 1994: Intra-seasonal oscillatory modes of the southern Africa summer circulation., PhD Thesis, University

Malkus, J. S., and Riehl, H., 1960: On the dynamics and energy transformations in steady-state hurricanes, Tellus, **12**, 1-20.

Mason, S. J., 1993: Sea Surface temperatures and south African Rainfall Variability, PhD Thesis, university of Witwatersrand, 235 pp.

Murakami, T., 1987: Intraseasonal atmospheric teleconnection patterns during northern hemisphere summer. Mon. Wea. Rev., **115**, 2133-2154.

Murakami, T., 1988: Intraseasonal atmospheric teleconnection patterns during northern hemisphere winter. J. Clim., 117-131.

Murakami, T., and T. Nakazawa, 1985: Tropical 45-day oscillations during the 1979 Northern Hemisphere summer. J. Atmos. Sci., **42** 1107-1122

Murakami, T.; Long-Xun Chen; AN Xie and Madan L. Shretha., 1986: Eastward propagation of 30-60 day Perturbations as revealed from Outgoing Longwave Radiation Data. Journal of the Atmospheric Sciences, **43**, No. 10, 961-971.

Nassor, A., 1994: Monsoon Surges, Tropical cyclones, and extreme events in the NW Madagascar. MSc. Thesis, University of Cape Town.

Nicholson, S.E, 1983: sub-Saharan rainfall in years 1976-80: evidence of continued drought. Mon. Wea. Rev., **111**,1646-1654.

Niita, T., Nakagomi, Y. Suzuki, Hasegawa, N., and Kadokura A., (1985): Global Analysis of the lower Tropospheric Disturbances in the Tropics During the Northern Summer of the FGGE year; Part 1: Global features of the disturbances; J. Met. Soc. of Japan, **63**, No. 1, 1-16

Numerical Algorithims group Limited, 1990: NAG Fortran Library, Introductory Guide, Mark 14, Wilkinson house, Jordan road, OXFORD, UK.

Nyenzi, B. S., 1984: Equatorial zonally moving disturbances which contributed to the East African long rains March to May 19979, MSc. Thesis, Florida state University 73 pp.

Nyenzi, B. S., 1988: Mechanism of the East African variability., PhD Thesis , Florida state University 184 pp.

Ogallo, L. J, and Suleiman, K.A, 1987: Rainfall characteristic in East Africa during El-Nino year. Proc. First Technical Conference on Met Research in eastern and southern Africa. Nairobi, Kenya, 6-9 January 1987, 76-80.

Ogallo, L. J., 1988: Relationship between seasonal rainfall in East Africa and Southern Oscillation, Journal of Climatology, **8**, 31-43.

Ogallo, L. J., 1989: The spatial and temporal patterns of the East African seasonal rainfall derived from principle component analysis, Royal Meteorological Society, 145-167.

Parker, B. A., 1994: Composite structure of tropical cyclones in the Indian Ocean. Msc. Thesis, University of Cape Town, Cape Town South Africa.

Preston-Whyte, R. A. and Tyson, P.D., 1988: The Atmosphere and weather of South Africa, Oxford University Press, Cape Town, 374 pp

Rui, H. and Wang, B., 1990: development characteristics and dynamic structure of tropical intra-seasonal convection anomalies. J. Atmos Sci, **47**,357-379.

Rui, H., and B. Wang., 1990: Development Characteristics and Dynamic Structure of Tropical Intraseasonal Convection Anomalies, J. Atmos. Sci., **47**, 357-379.

Semazzi, H. F. M., 1980: Stationary barotropic flow induced by a mountain over a tropical belt. Mon. Wea. Rev. **108**, 922-930.

Steiner, E. J., 1989: Moisture convergence during a convergence flare up in the tropics, Proceedings of the fourth AMS conference on satellite Meteorology and oceanography, 154-157.

Underhill, L. G., 1981: Introstat, Third edition. Department of Mathematical Statistics, university of Cape Town.Juta and Co., LTD., 383 pp

Vincent, D.G; T. Sperling; A. Fink; S. Zube and P. Speth, 1991: Intraseasonal Oscillation of Convective Activity in the Tropical Southern hemisphere: May, 1984-April, 1986, J. Clim., **4**, 40-53

Wang, B., and Rui, H.,1990: Synoptic Climatology of Transient Tropical Intraseasonal convectional Anomalies: 1975-1985, Meteorology and Atmospheric Physics, **44**, 43-61.

Weickmann, K. M., G. R. Lussky, and J. E. Kutzbach, 1985: Intraseasonal (30-60 day) fluctuations of outgoing longwave radiation and 250 mb stream function during northern winter. Mon. Wea. Rev., **113**, 941-961.

Weickmann, K.M. and S.J. khalsa., 1990: The shift of convection from the Indian ocean to the western Pacific ocean during a 30-60 Day Oscillation, Monthly weather review. **118**, 964-978.

Zhu, B., and B. Wang, 1993: The 30-60 day convective seesaw between the tropical Indian and western pacific oceans. J. Atmos. sci., **50**, 184-199

Zipser, E. J., and K. L. Mohr, 1997: Convective intensity over south America, Africa, and The Maritime continent: Quantitatuve camparison ising ice scattering signatures. Preprints of the Fifth International Conference on Southern Hemisphere Meteorology and Oceanography, AMS 7-11 April 1997, 200-201.

APPENDIX A

PENTAD	MONTH	DATE	PENTAD	MONTH	DATE
01	JAN	01-05	38	JUL	05-09
02	JAN	06-10	39	JUL	10-14
03	JAN	11-15	40	JUL	15-19
04	JAN	16-20	41	JUL	20-24
05	JAN	21-25	42	JUL	25-29
06	JAN	26-30	43	JUL-AUG	30-03
07	JAN-FEB	31-04	44	AUG	04-08
08	FEB	05-09	45	AUG	09-13
09	FEB	10-14	46	AUG	14-18
10	FEB	15-19	47	AUG	19-23
11	FEB	20-24	48	AUG	24-28
12	FEB-MAR	25-01	49	AUG-SEPT	29-02
13	MAR	02-06	50	SEPT	03-07
14	MAR	07-11	51	SEPT	08-12
15	MAR	12-16	52	SEPT	13-17
16	MAR	17-21	53	SEPT	18-22
17	MAR	22-26	54	SEPT	23-27
18	MAR	27-31	55	SEPT-OCT	28-02
19	APR	01-05	56	OCT	03-07
20	APR	06-10	57	OCT	08-12
21	APR	11-15	58	OCT	13-17
22	APR	16-20	59	OCT	18-22
23	APR	21-25	60	OCT	23-27
24	APR	26-30	61	OCT-NOV	28-01
25	MAY	01-05	62	NOV	02-06
26	MAY	06-10	63	NOV	07-11
27	MAY	11-15	64	NOV	12-16
28	MAY	16-20	65	NOV	17-21
29	MAY	21-25	66	NOV	22-26
30	MAY	26-30	67	NOV-DEC	27-01
31	MAY-JUN	31-04	68	DEC	02-06
32	JUN	05-09	69	DEC	07-11
33	JUN	10-14	70	DEC	12-16
34	JUN	15-19	71	DEC	17-21
35	JUN	20-24	72	DEC	22-26
36	JUN	25-29	73	DEC	27-31
37	JUN-JUL	30-04			